Departamento de Física Teórica
Universidad Autónoma de Madrid

Instituto de Física Teórica
UAM/CSIC

The quest for neutrino interactions at future oscillation facilities

Memoria de Tesis Doctoral realizada por
Pilar Coloma Escribano
y presentada ante el Departamento de Física Teórica
de la Universidad Autónoma de Madrid
para la obtención del Título de Doctora en Ciencias

Tesis Doctoral dirigida por **Andrea Donini,**
Investigador Científico del Instituto de Física Teórica UAM/CSIC

Junio de 2011

Motivaciones y Objetivos

El Modelo Estándar (ME) es una teoría cuántica de campos renormalizable que respeta la simetría gauge $SU(3)_C \times SU(2)_L \times U(1)_Y$ [1–4]. Hasta ahora, ha descrito con gran éxito las interacciones fuerte y electrodébil observadas entre partículas elementales, que tienen lugar mediante el intercambio de bosones vectoriales. Sin embargo, sabemos *a priori* que no es una teoría completa, dado que no es capaz de incorporar una descripción cuántica de la gravedad de manera consistente. Si bien esta es la evidencia más fuerte de que el ME es tan sólo una versión efectiva de una teoría más completa a alta energía, presenta otros problemas adicionales que también apuntan en la misma dirección.

Desde el punto de vista experimental, existen fuertes evidencias en este sentido. Por un lado, para explicar las curvas de rotación de las galaxias, los datos de lentes gravitatorias y las medidas de la Radiación de Fondo de Microondas de COBE y WMAP [5,6] es necesaria la presencia de una gran cantidad ($\sim 25\%$) de materia no bariónica en el Universo, llamada *materia oscura*. Por otro lado, las medidas de la relación entre la distancia y el corrimiento al rojo de algunas supernovas evidencian la aceleración del Universo [7]. Para acomodar los datos experimentales y conseguir una expansión acelerada del Universo, es necesario introducir una gran cantidad de *energía oscura* ($\sim$ 70%) en las ecuaciones de Friedmann-Robertson-Walker. Una manera para introducir esta energía oscura es a través de una constante Λ en el lagrangiano que, en presencia de gravedad, se vuelve no trivial. A dicha constante, de origen desconocido, se la denomina *constante cosmológica*. Una hipótesis bastante aceptada es que Λ podría estar relacionada con la energía del vacío del ME. Sin embargo, la estimación de la misma difiere, en el mejor de los casos, en más de 50 órdenes de magnitud respecto del valor experimental. En definitiva, el ME no es capaz de explicar ni la materia oscura ni la energía oscura, que componen aproximadamente un 95% de nuestro Universo.

Desde un punto de vista teórico, el ME presenta algunos problemas adicionales. En primer lugar, no consigue explicar de manera consistente los vacíos de la teoría. Además del problema de la constante cosmológica y su relación con el vacío en presencia de gravedad, en QCD nos encontramos con el problema de violación de CP fuerte [8]. Los efectos no perturbativos de la teoría generan un término en el lagrangiano de QCD que viola explícitamente P y CP: $\theta F_{\mu\nu}\widetilde{F}^{\mu\nu}$. Dicho término se podría reabsorber mediante una rotación de sabor si los quarks no tuvieran masa, pero deja de ser así con quarks masivos. Las medidas experimentales del momento dipolar eléctrico del neutrón establecen la cota $\theta < 3 \times 10^{-10}$ [9], pero el ME carece de una simetría que pueda explicar un valor tan pequeño.

Estos problemas parecen indicar, por tanto, que el ME es una teoría efectiva de otra más completa a alta energía. De ser así, el sector escalar del ME estaría afectado por un segundo problema teórico: el *problema de la jerarquía*. En el ME, el bosón de Higgs es necesario para proporcionar masas a los bosones gauge durante la ruptura espontánea de la simetría electrodébil, preservando la invarianza gauge y la renormalizabilidad de la teoría. Al mismo tiempo, le da masas a los fermiones cargados mediante acoplos de Yukawa, puesto que se encuentran permitidos por la simetría gauge. Siendo un bosón escalar, su masa no se encuentra protegida por ninguna simetría del ME, y por tanto es de esperar que reciba correcciones radiativas de orden cuadrático con la escala en la cual el ME pierde su validez como teoría efectiva debido a la presencia de nueva física, $\delta m^2 \propto \Lambda^2$. Sin embargo, las cotas de trivialidad para la masa del Higgs sugieren que su valor debe estar en torno a la escala electrodébil [10–12]. De hecho, las medidas de precisión en LEP apuntan incluso a valores relativamente pequeños [13], $m_H < 167$ GeV (95% CL). Si suponemos que el ME es válido hasta la escala de Planck ($\sim 10^{19}$ GeV), esto implicaría necesariamente un ajuste muy fino de los parámetros del modelo de modo que las contribuciones radiativas a la masa del Higgs se cancelaran y ésta quedara en torno a la escala electrodébil. Esto es lo que se conoce como el problema de la jerarquía [14, 15]. Este problema podria estarnos indicando que la nueva física no

se encuentra muy por encima de la escala electrodébil, o que incorpora un mecanismo (simetría) de manera que las correcciones radiativas a la masa del Higgs se cancelan de forma exacta.

En tercer lugar, el ME tampoco nos proporciona una explicación para la asimetría materia-antimateria del Universo. La simetría entre partículas y antipartículas es una de las bases de la física actual: el teorema de conservación de CPT establece que, dada una partícula cualquiera existe otra con su misma masa y anchura de desintegración, pero con carga opuesta [4]. Sin embargo, nuestro Universo está compuesto casi por entero de materia y no de antimateria. La explicación más natural de este hecho es que durante la expansión del Universo tuvo lugar un proceso conocido como *bariogénesis*, que favoreció la producción de partículas sobre antipartículas mediante procesos que violan el número bariónico B. Para que dicho proceso tenga lugar se deben verificar las tres condiciones de Sakharov [16]: (1) debe violar B; (2) debe tener lugar fuera del equilibrio térmico; (3) debe violar C y CP. Aunque en principio el ME contiene los ingredientes necesarios para dar lugar a bariogénesis, no es capaz de expicar una asimetría tan fuerte como la que se observa hoy en día.

Por último, nos encontramos con el *problema del sabor*. El ME presenta una estructura muy compleja en sabor, marcada sobre todo por grandes diferencias entre las masas de los fermiones. Una vez las oscilaciones de neutrinos y la mezcla en el sector leptónico están bien establecidas y soportadas por fuertes evidencias experimentales, es necesario ampliar el contenido del ME para darles cabida de alguna manera. Esto tiene dos consecuencias importantes que agravan el problema del sabor: la primera es que las masas de los neutrinos resultan extremadamente pequeñas en comparación con las del resto de los fermiones; la segunda es que la mezcla en el sector leptónico sigue un patrón completamente distinto al del observado en el sector bariónico. Por tanto, el ME cuenta con un conjunto de acoplos de Yukawa cuyos valores se extienden a lo largo de doce órdenes de magnitud, y con un patrón para la mezcla entre familias que difiere ampliamente entre los sectores bariónico y leptónico. El problema del sabor consiste en entender si hay o no un mecanismo que genere este complicado patrón de mezcla y que pueda quizá explicar el número de generaciones del ME.

El sector de los neutrinos precisamente nos abre una ventana a algunos de estos problemas y, en general, hacia nueva física por encima de la escala electrodébil. En primer lugar, las oscilaciones de neutrinos demuestran que son partículas masivas, y se hace necesaria la inclusión de su correspondiente término de masa en el lagrangiano. Esto constituye, *per se*, una evidencia de la existencia de física más allá del ME, ya que para incluir las masas de los neutrinos se hace necesario incluir nuevas partículas en el modelo. Cada una de estas extensiones del ME podría, además, tener consecuencias en otras áreas de la física de partículas. Por ejemplo, los modelos tipo *See-Saw* [17–19] contienen una fuente importante de violacion de $B-L$ y fases adicionales de violación de CP, que podrían ayudar a explicar bariogénesis a través de *leptogénesis* [20]. Además, la posibilidad de que existan más de tres especies de neutrinos no ha sido descartada aún. Las especies restantes serían neutrinos estériles desde el punto de vista electrodébil, y su presencia en la naturaleza sólo sería detectable a través de la mezcla con los neutrinos activos o por su influencia en cosmología. Multitud de experimentos han sido diseñados para estudiar esta posibilidad mediante oscilaciones con detectores cercanos, cuyo objetivo es explorar las oscilaciones entre neutrinos con diferencias de masa en torno al eV. De hecho, las recientes anomalías observadas en LSND y MiniBooNE parecen reforzar esta hipótesis en algún sentido. Por otro lado, las últimas observaciones de WMAP, en combinación con los datos de lentes gravitacionales y las abundancias primordiales de elementos ligeros, parecen sugerir la existencia de más de tres neutrinos ligeros. Una consecuencia muy interesante de algunos modelos con neutrinos estériles (con masas en torno al keV) es que proporcionan un posible candidato a materia oscura. Por último, existe toda una multitud de modelos de sabor propuestos para explicar los patrones de mezcla entre familias. El sector de los neutrinos podría arrojar mucha luz sobre estos modelos, ayudando a discriminar entre

unos y otros.

Resulta por tanto evidente que entender bien el problema del sabor y cómo se produce la mezcla en el sector leptónico podría ayudarnos a explicar algunos de los problemas que sufre el ME. Para ello, es necesario obtener una medida de los parámetros de mezcla que aún se desconocen, así como reducir el error en los parámetros que ya han sido medidos. En este sentido la medida del tercer ángulo de mezcla, θ_{13}, resulta de gran importancia, ya que nos abre una ventana hacia la violación de CP en el sector leptónico. Además, si θ_{13} resultara ser cero, sería extremadamente difícil obtener una medida de la jerarquía que siguen los estados de masa. Hasta ahora, los experimentos de oscilaciones de neutrinos han arrojado mucha luz sobre la matriz de mezcla leptónica y sobre los valores de sus masas. En caso de que θ_{13} resultara ser extremadamente pequeño, éste se hallaría por debajo del alcance de la presente generación de experimentos, y se haría necesaria una nueva generación especialmente diseñada para medir θ_{13} y, si fuera posible, la fase de violación de CP y la jerarquía de los estados de masa. Estamos entrando, por tanto, en una nueva era para la física de neutrinos. Cuatro tipos de futuros experimentos, con el objetivo de medir los parámetros desconocidos del sector leptónico, se encuentran ahora mismo bajo discusión: Reactores, "Super-Beams", "β-beams " y "Neutrino Factories".

La primera parte del trabajo recogido en esta tesis consiste en el estudio de las posibilidades que tendrían distintos setups de Super-Beams y β-beams para determinar θ_{13}, δ y la jerarquía de los estados de masa, considerando únicamente las interacciones del ME extendido con las masas de neutrinos. En una segunda parte, consideramos además la posible existencia de operadores efectivos provenientes de nueva física y sus efectos a baja energía. En este contexto, estudiamos qué cotas se podrían establecer en una "Neutrino Factory" sobre los parámetros que acompañan a dichos operadores, así como las posibilidades de medir violación de CP procedente de nueva física.

El esquema que hemos seguido es el siguiente. En el capítulo 1, hacemos una introducción teórica general al contenido de partículas del ME y los mecanismos más simples para generar masas para los neutrinos. Hacemos, además, una breve introducción general al formalismo de operadores efectivos y los operadores de dimensión más baja que podrían tener algún efecto en física de neutrinos a baja energía. En el capítulo 2, hacemos un resumen sobre los distintos tipos de experimentos, pasando por la desintegración β del tritio, la desintegración doble β sin neutrinos en el estado final, las observaciones en cosmología y los experimentos de oscilaciones. Por último, introducimos de manera muy breve las anomalías experimentales recientes. En los capítulos 3, 4 y 5 presentamos nuestro trabajo. Los resultados del capítulo 4 se corresponden con los resultados de los artículos [21] y [22] , publicados en la revista científica *Journal of High Energy Physics*, mientras que los resultados presentados en el capítulo 5 son bastante recientes y aún están pendientes de publicación [23, 24]. Finalmente, presentamos nuestras conclusiones en el capítulo 6.

Motivations and Goals

The Standard Model (SM) is a renormalizable quantum field theory which is invariant under the gauge symmetry $SU(3)_C \times SU(2)_L \times U(1)_Y$ [1–4]. So far, it has been able to describe with great success the observed strong and electroweak interactions between elementary particles, which take place through the exchange of vector gauge bosons. However, we know *a priori* that the SM is not a full theory, since it is not able to incorporate in a consistent way a quantum theory of gravity. Even though this is the most accute evidence which indicates that the SM is only a low energy version of another theory at higher energies, it presents additional problems which also point in the same direction.

Strong experimental evidences claim for the existence of physics Beyond the Standard Model (BSM). On the one hand, in order to explain the rotational curves of galaxies, data for gravitational lensing and the measurements on the Cosmic Microwave Background obtained by COBE and WMAP [5, 6] a great amount ($\sim 25\%$) of non-baryonic matter should be present in the Universe. This is the so-called *dark matter*. On the other hand, the measurements on the relation between the distance and redshift of some supernovae are evidencing the acceleration of the Universe [7]. In order to accomodate the experimental data and obtain an accelerated expansion of the Universe, a large amount of *dark energy* ($\sim 70\%$) has to be necessarily introduced in the Friedmann-Robertson-Walker equations. One possible way to do this is by means of a constant term in the lagrangian, Λ, which becomes non-trivial in presence of gravity. Such constant is commonly known as *the cosmological constant*. The origin of this constant remains presently unknown. A quite accepted hypothesis is that Λ could be related to the vacuum energy of the SM. Nevertheless, a *naïve* estimate of this energy differs at least in more than 50 orders of magnitude with respect to the experimental value. To sum up, the SM is not able to explain neither the dark matter nor the dark energy, which roughly amount to a 95% of our Universe.

From a more theoretical point of view, the SM presents further issues. Firstly, it cannot explain in a consistent way the vacua of the theory. In addition to the cosmological constant and its presumed relationship with the vacuum of the theory in presence of gravity, in QCD we find the *strong CP problem* [8]. Non-perturbative effects of the theory generate an explicitely C- and CP-violating term in the lagrangian: $\theta F_{\mu\nu}\widetilde{F}^{\mu\nu}$. Such a term can be reabsorbed by means of a rotation in flavour space assuming massless quarks. However, this is no longer true in the presence of quark masses. Experimental measurements on the neutron electric dipole moment stablish a bound on the value for θ at $\theta < 3 \times 10^{-10}$ [9]. Again, the SM does not provide an explanation for such a small value.

These problems seem to indicate, thus, that the SM is an effective version of another theory at higher energies. If this is true, the scalar sector of the SM would be affected by a second theoretical problem: the *hierarchy problem*. In the SM, the Higgs boson is needed in order to give masses to the electroweak bosons after the Electro-Weak Symmetry Breaking (EWSB). The Higgs mechanism preserves gauge invariance and the renormalizability of the theory. At the same time, it gives masses to the fermions through the Yukawa terms, which are allowed by the gauge symmetry. The Higgs being a scalar boson, its mass is not protected by any of the symmetries of the SM. Therefore, any New Physics (NP) beyond the Electro-Weak (EW) scale is expected to produce quadratic corrections to its mass, $\delta m^2 \propto \Lambda^2$, where Λ is the scale at which the new degrees of freedom become relevant. However, triviality bounds on the Higgs mass suggest that its value should be around the EW scale [10–12]. Indeed, the precision measurements obtained at LEP even point to relatively small values [13], $m_H < 167$ GeV (95% CL). If we make the assumption that the SM is valid up to the Planck scale ($\sim 10^{19}$ GeV), this would necessarily imply a very precise *fine-tuning* of the parameters of the model so that the radiative contributions to the Higgs mass cancel out. This is what is usually known as the hierarchy problem [14, 15]. The

hierarchy problem could be pointing to the existence of NP not very far away from the EW scale. Another possibility could be that the NP incorporates a specific mechanism (symmetry) leading to the exact cancelation of the radiative corrections to the Higgs mass.

In third place, the SM does not provide an explanation for the baryon asymmetry of the Universe. The symmetry between particles and antiparticles is one of the bases of modern physics: the CPT theorem stablishes that, for a given particle there exists an antiparticle with identical mass and decay width but with opposite charges [4]. However, our Universe is mainly made of matter and not antimatter. The most accepted explanation for this is that during the early expansion of the Universe a process known as *baryogenesis* took place. Such process would have favored the creation of particles with respect to the creation of antiparticles through processes which violate the baryon number B. As a result, the asymmetry we observe nowadays was generated. In order for baryogenesis to take place, the three Sakharov conditions [16] need to be satisfied: (1) the process must violate B; (2) it must take place out of thermal equilibrium; (3) the C and CP discrete symmetries must be violated. Even though the SM contains all the ingredients for baryogenesis to take place, it is not able to explain the large asymmetry observed nowadays.

Eventually, there is the *flavour problem*. The SM presents a very complex flavour structure, with great differences between the masses of the different fermions. Once neutrino oscillations and the mixing in the lepton sector have been clearly stablished by overwhelming experimental evidences, it is necessary to enlarge the matter content of the SM in order to accomodate neutrino masses. This has two main consequences which aggravate the flavour problem: firstly, neutrino masses turn out to be extremely small in comparison with those of the rest of the fermions; (2) secondly, the mixing in the leptonic sector follows a very different pattern to the one observed in the baryonic sector. As a consequence, the SM presents a set of Yukawa couplings whose values are placed along twelve orders of magnitude, and a different mixing pattern in the leptonic and quark sectors. The flavour problem addresses the question of whether there is a mechanism behind such a complicated mixing pattern, and if such mechanism is also able to explain the number of fermion generations in the SM.

The neutrino sector is precisely opening a window to some of these problems and, in general, to NP above the EW scale. Firstly, neutrino oscillations demonstrate that neutrinos are massive. The inclusion of a mass term for them in the lagrangian is mandatory. This is, *per se*, an evidence of NP since new particles need to be added to the SM particle content. Each of these extension could, at the same time, have consequences in other areas of particle physics. For instance, the *See-Saw* models contain an important source of violation of $B - L$ as well as additional CP violating phases [17–19]. Both could help to baryogenesis through *leptogenesis* [20]. Besides, the existence of more than three neutrino species has not been discarded yet. The extra neutrino species would be sterile from the electroweak point of view, and their presence in Nature could only be observed through their mixing with the active species or their consequences in cosmology. Plenty of experiments have been designed in order to study this possibility including near detectors. The main purpose of such facilities would be to explore oscillations between neutrinos with squared-mass differences around the eV. In fact, recent anomalies observed at the LSND and MiniBooNE experiments seem to favor this hypothesis in some sense. On the other hand, the latest results from WMAP, in combination with gravitational lensing results and the primordial abundances of light elements, seem to suggest the existence of more than three light neutrino species. A very interesting consequence of some models of NP including sterile neutrino species (with masses around the keV) would be the availability of a candidate for dark matter. Finally, there is a whole plethora of flavour models proposed in order to explain the mixing pattern between fermion families. The neutrino sector could be particularly illuminating for these models and could help to discriminate between them.

Therefore, it turns out that the understanding of the flavour problem and the mixing in the

leptonic sector could be of great help in order to undestand some of the rest of the problems of the SM. In order to do so, it is necessary to obtain a measurement on the yet unknown mixing parameters, as well as to reduce the present uncertainties on the parameters which have already been measured. In this sense a measurement of the third mixing angle, θ_{13}, turns out to be of great importance. In first place, it opens a window to CP violation in the leptonic sector. In addition, if θ_{13} turns out to be zero a measurement on the hierarchy of neutrino masses would be very hard to obtain. So far, neutrino oscillation experiments have shed much light on the leptonic mixing matrix and neutrino masses. In case θ_{13} turns out to be extremely small, this would be beyond the reach of the present and forthcoming generations of neutrino experiments. A new generation, specially designed in order to obtain a measurement on θ_{13} and, if possible, the CP violating phase and the mass hierarchy, would be needed. We are entering a precision Era in neutrino physics. Four kinds of future neutrino oscillation experiments are currently being under consideration: Reactors, Super-Beams, β-beams and Neutrino Factories.

The first part of this thesis consists on the study of the possibilities that several Super-Beam and β-beam setups would have in order to determine θ_{13}, δ and the mass hierarchy. This analysis is performed considering only the interactions of the SM extended with neutrino masses. In a second part of the work, we have also considered the possible existence of effective operators originated from NP beyond the SM and their effects at low energies. In this context, we study which bounds could be placed at a Neutrino Factory over the parameters which are associated to these operators in the lagrangian, as well as the possibilities of observing a CP violating signal coming from NP.

The structure of the manuscript is the following. In Ch. 1, a general introduction to the SM particle content and the simplest mechanisms which can account for neutrino masses is presented. In addition, we introduce very briefly the formalism of effective operators and the lowest dimension operators which could give an observable effect in low energy neutrino physics. In Ch. 2, we summarize the experimental landscape in neutrino physics. We briefly review the experiments on tritium double beta decay, neutrinoless double beta decay, the results from cosmological observations and the main neutrino oscillation experiments. Finally, we introduce the recent (unexplained) experimental anomalies. Chapters 3, 4 y 5 are dedicated to present our results. The results presented in Ch. 4 correspond to the results obtained in Refs. [21] and [22] and have been published in the Journal of High Energy Physics, whereas the results presented in Ch. 3 and Ch. 5 are expected to be published in the near future [23, 24]. Eventually, in Ch. 6 we summarize and draw our conclusions.

Contents

1 The origin of neutrino masses **1**

1.1 The gauge group of the SM and its particle content . . . 1
1.2 Mechanisms to generate neutrino masses . . . 4
1.3 Diagonalization of the mass lagrangian. The U_{PMNS} matrix . . . 9
1.4 Neutrino oscillations . . . 10
1.4.1 Oscillations in vacuum with N families . . . 11
1.4.2 Oscillations in matter . . . 14
1.5 Higher dimension operators . . . 17

2 Experimental landscape in neutrino physics **21**

2.1 The absolute scale of neutrino masses . . . 21
2.1.1 Limits from electroweak decays . . . 21
2.1.2 Cosmological bounds . . . 22
2.1.3 Bounds from neutrinoless double β-decay . . . 22
2.2 Neutrino oscillation experiments . . . 23
2.2.1 Oscillations in the solar regime . . . 24
2.2.2 Oscillations in the atmospheric regime . . . 26
2.2.3 The three neutrino oscillation framework . . . 27
2.3 The degeneracy problem . . . 29
2.4 The next generation of experiments . . . 33
2.5 Experimental anomalies . . . 35
2.5.1 LSND and MiniBooNE . . . 36
2.5.2 The reactor anomaly . . . 36
2.5.3 The MINOS anomaly . . . 37
2.5.4 Hints from cosmology for sterile neutrinos . . . 38

3 Super-Beams **41**

3.1 The setups . . . 41
3.1.1 The baselines . . . 41
3.1.2 The beam . . . 42
3.1.3 The detectors . . . 43
3.2 Simulation details . . . 44
3.2.1 Detector simulations . . . 45
3.2.2 Main backgrounds . . . 46
3.2.3 Observables . . . 47
3.3 Optimisation studies . . . 48
3.3.1 NC background in LENA . . . 48
3.3.2 Quasi-elastic events in GLACIER . . . 48

3.3.3 Systematic errors . . . 50
3.3.4 Intrinsic beam backgrounds . . . 50
3.3.5 Running times . . . 51
3.3.6 τ detection . . . 53
3.4 Comparison for different baselines . . . 53
3.4.1 Sensitivity to θ_{13} . . . 54
3.4.2 CP discovery potential . . . 56
3.4.3 Sensitivity to the mass hierarchy . . . 56

4 The double baseline β-beam **59**
4.1 The β-beam concept . . . 60
4.2 The accelerator design . . . 62
4.2.1 Choice of $\beta^{\pm}$-emitters . . . 62
4.2.2 Choice of γ . . . 64
4.2.3 Fluxes and cross sections . . . 64
4.2.4 The Storage Ring . . . 66
4.2.5 The atmospheric background for a high-γ β-beam . . . 70
4.3 The detector design . . . 71
4.3.1 The choice of the two baselines . . . 71
4.3.2 Signal event rates: the matter resonance at 7000 Km . . . 72
4.3.3 Detector technologies . . . 73
4.3.4 Backgrounds, efficiencies and systematic errors for the MIND detector . . . 76
4.4 Results . . . 77
4.4.1 Results for the two-baseline ^{8}Li /^{8}B β-beam (setup A) . . . 77
4.4.2 Results for the optimized two-baseline β-beam (setup B) . . . 82
4.4.3 Comparison with other high-energy future proposals . . . 87

5 NSI at Neutrino Factories **89**
5.1 Neutrino Oscillations with Non-Standard Interactions . . . 90
5.2 The Neutrino Factory . . . 91
5.2.1 Neutrino Factory setups . . . 93
5.3 Input parameters and marginalization procedure . . . 95
5.4 Sensitivities achieved mainly through the $\nu_e \to \nu_\mu$ and $\nu_e \to \nu_\tau$ channels . . . 96
5.4.1 Impact of the NSI on the measurement of θ_{13} . . . 97
5.4.2 Sensitivity to $\epsilon_{e\mu}$ and $\epsilon_{e\tau}$ . . . 98
5.5 Sensitivities achieved mainly through the $\nu_\mu \to \nu_\mu$ channel . . . 100
5.5.1 Sensitivity to $\epsilon_{\mu\tau}$ . . . 100
5.5.2 Sensitivity to the diagonal NSI parameters . . . 100
5.6 Discovery potential for CP violation in the $(\phi_{e\mu}, \phi_{e\tau}, \delta)$ space . . . 101
5.6.1 Non-standard CP violation in the absence of νSM CP violation . . . 103
5.6.2 $\delta_{\rm CP}$ fraction: Non-standard CP violation in presence of νSM CP violation . 106

5.6.3 CP volume fraction 109

6 Summary and Conclusions **113**

7 Resumen y Conclusiones **117**

A The acceleration and storage chain **123**
A.1 Proton Driver 123
A.2 Ion production 123
A.3 Acceleration stage 124

B Oscillation probabilities **127**
B.1 Oscillation probabilities in the standard approach 127
B.1.1 The $\nu_e \to \nu_\mu$ appereance channel 127
B.1.2 The $\nu_e \to \nu_\tau$ appearance channel 128
B.1.3 The $\nu_\mu \to \nu_\mu$ disappearance channel 128
B.2 Oscillation probabilities in presence of NSI 129

C Statistical procedure **133**
C.1 The statistical procedure used in Secs. 5.4 and 5.5 133
C.2 The statistical procedure used in Sec. 5.6 135

Bibliography **139**

1

The origin of neutrino masses

In this chapter we introduce some of the minimal extensions of the SM which can account for neutrino masses. In Sec. 1.4.2 the SM particle content and its properties are presented; in Sec. 1.2 the simplest possibilities for the inclusion of neutrino masses in the Standard Model and the $d = 5$ Weinberg operator are introduced; Sec. 1.3 is dedicated to introduce the leptonic mixing matrix; in Sec. 1.4 the general formulae for oscillations and matter effects in a two family model are derived; finally, in Sec. 1.5 higher dimensional operators able to produce neutrino masses and Non-Standard Interactions at low energies are introduced.

1.1 The gauge group of the SM and its particle content

The gauge symmetry group of the Standard Model (SM), $SU(3)_C \times SU(2)_L \times U(1)_Y$, determines the number and general properties of the gauge fields which mediate its interactions. The fermionic matter content of the SM, an external input, is classified in three families or generations. The quantum numbers are the same for the three families, since the particles in each family correspond to the same irreducible representations of the gauge group. Tab. 1.1 summarizes the fermionic particle content of the SM, including the quantum numbers of each particle and the irreducible representation to which it belongs.

The SM also includes a scalar field called the Higgs boson, which behaves as a singlet under $SU(3)_C$, as a doublet under $SU(2)_L$ and has hypercharge $Y = 1/2$ (see Tab. 1.1). The Higgs boson is needed in the SM in order to give masses to the $W^\pm$ and Z gauge bosons without spoiling the renormalizability of the theory. We know that the SM gauge group is broken into the subgroup $SU(3)_C \times U(1)_{em}$, since the gauge bosons in the electroweak sector are massive while photons and gluons remain massless. This is done through the spontaneous ElectroWeak Symmetry Breaking (EWSB), when the Higgs boson takes a vacuum expectation value (*vev*):

$$\phi \longrightarrow \langle \phi \rangle = \frac{1}{\sqrt{2}} \begin{pmatrix} 0 \\ v \end{pmatrix}.$$

Three out of the four degrees of freedom of the Higgs boson are absorbed by the vector bosons in the EW sector. As a result, the W and the Z get a mass through the Higgs mechanism, while the photon remain massless. The masses of the gauge bosons at tree level are related to the Higgs *vev* as[1] $M_W = (g^2 v^2)/2$; $M_Z = (g^2 + g'^2)v^2/2$, where $g = e/\sin\theta_W$ and $g' = e/\cos\theta_W$. Direct measurement of the vector boson masses give $M_W^2 = 80.398 \pm 0.025\,\text{GeV}$, $M_Z^2 = 91.1876 \pm 0.0021\,\text{GeV}$ [25], which automatically implies $v \sim \mathcal{O}(250)$ GeV.

[1] These relations are modified at the loop level, though.

Particle			Quantum numbers		
1^{st} Family	2^{nd} Family	3^{rd} Family	$SU(3)_C$	$SU(2)_L$	$U(1)_Y$
$\begin{pmatrix} u \\ d \end{pmatrix}_L$	$\begin{pmatrix} c \\ s \end{pmatrix}_L$	$\begin{pmatrix} t \\ b \end{pmatrix}_L$	3	2	1/6
$\begin{pmatrix} \nu_e \\ e \end{pmatrix}_L$	$\begin{pmatrix} \nu_\mu \\ \mu \end{pmatrix}_L$	$\begin{pmatrix} \nu_\tau \\ \tau \end{pmatrix}_L$	1	2	$-1/2$
u_R	c_R	t_R	3	1	2/3
d_R	s_R	b_R	3	1	$-1/3$
e_R	μ_R	τ_R	1	1	-1
ϕ			1	2	1/2

Table 1.1: Quantum numbers for the different representations of the gauge group, associated to the Higgs boson and the fermions belonging to each family in the SM. Fermion families are ordered attending to their masses: the third one is the most massive, while the first one contains the lightest fermions. Left-handed particles (first two columns) are generally denoted with uppercase letters (Q_L, L_L), while lowercase is used to refer to right-handed particles (q_R, l_R). Notice the convention $Q = T_3 + Y$, where Q, T_3 and Y refer to electric charge, thrid component of the isospin and hypercharge of a given particle, respectively.

The Higgs boson has not been observed yet and its mass is also unknown. In the SM, the Higgs mass is given by $m_H = \sqrt{\lambda}v$, where λ is the Higgs self-coupling parameter and v is the Higgs *vev*. While v can be determined through the masses of the gauge bosons, λ is presently unknown and, therefore, the value of m_H cannot be derived directly. Direct searches at LEP have placed a lower bound at $m_H > 114.4$ GeV (95% CL) [13]. However, triviality bounds point to the Higgs mass being below $\sim 600 - 700$ GeV (see, for instance, Ref. [26] for a nice review on theoretical bounds to the Higgs mass). Furthermore, precision electroweak data from LEP measurements point to relatively low values [13], $m_H < 167$ GeV (95% CL), a range which will be fully explored at the LHC in the near future. Such a tiny window for the Higgs mass is the source of a long-standing problem of the SM. The Higgs mass is not protected from becoming large by any symmetry of the SM. Indeed, if we assume that the SM is an effective theory, the Higgs mass is expected to receive quadratic corrections from any scale of New Physics (NP) above the electroweak scale: $\delta m_H \propto \Lambda^2$. In this case, the Higgs mass should be at the order of the scale Λ at which the NP takes in. Clearly, if the NP arises at the Planck or at the GUT scales, for instance, a strong *fine tuning* of the coefficients associated to the quantum corrections to the Higgs mass will be needed in order to bring it down to the EW scale. This problem is known as the *hierarchy problem*, and it is usually invoked to suggest that NP should lie at $\mathcal{O}$(TeV) at most.

It is worth to note that the Higgs boson plays a double role in the SM: while it is introduced in order to give masses to the gauge bosons through the EWSB, at the same time it *accidentally* produces mass terms for all the fermions in the model (with the sole exception of the neutrinos, for which right-handed particles are not present and Yukawa terms cannot be constructed). Since Yukawa terms such as $Y_d Q_L d_R \phi$ are allowed by the gauge symmetry, they have to be included in the lagrangian. These also generate mass terms for the fermions once the EWSB takes place, as it will be shown in the next section in detail. Therefore, the lagrangian of the SM can be written as:

$$\mathcal{L} = \mathcal{L}_k + \mathcal{L}_g + \mathcal{L}_H + \mathcal{L}_Y \,,$$

where $\mathcal{L}_k$ contains the kinetic terms for all fermions, $\mathcal{L}_g$ the gauge interactions, $\mathcal{L}_H$ the scalar potential associated to the Higgs, and $\mathcal{L}_Y$ the Yukawa couplings for all fermions. The allowed ranges for the fermion masses of the three families in the SM are summarized in Tab. 1.2. Dedicated searches for particles belonging to a fourth family have been performed in several experiments, with negative results. The following lower bounds for the masses of charged fermions belonging to a fourth family can be derived from them at the 95%CL [25]:

$$\begin{aligned} m_{\tau'} &> 100.8\,\text{GeV} \\ m_{t'} &> 256\,\text{GeV} \\ m_{b'} &> 128\,\text{GeV} \end{aligned}$$

Notice that the Higgs boson could be either a fundamental or an effective field, but it is absolutely necessary to break the gauge group and give mass to the vector bosons. In fact, the Higgs boson contained in the SM is the minimal possibilily able to give masses to the W and Z gauge bosons and all the fermions, but larger scalar sectors have also been considered in theories beyond the SM, such as, for instance, the two-Higgs-doublet models (see, for instance, Ref. [27] for a recent review).

Finally, it is worth to mention that two accidental discrete symmetries appear in the SM: these are the baryon and lepton numbers, B and L. It is remarkable that, although both B and L are anomalous, $B - L$ is a non-anomalous symmetry of the SM. This is the main reason why in some theories beyond the SM the gauge group is enlarged including a $U(1)_{B-L}$ additional local symmetry, which would imply an unobserved additional neutral gauge boson [28–30].

First Family (MeV)	Second Family (MeV)	Third Family (GeV)
$m_e = 0.510998910 \pm 1.3 \times 10^{-8}$	$m_\mu = 105.6583668 \pm 3.8 \times 10^{-6}$	$m_\tau = 1.77682 \pm 1.6 \times 10^{-4}$
$m_u = 2.49^{+0.81}_{-0.79}$	$m_c = 1270^{+70}_{-110}$	$m_t = 172 \pm 0.9 \pm 1.3$
$m_d = 5.05^{+0.75}_{-0.95}$	$m_s = 105^{+25}_{-35}$	$m_b = 4.19^{+0.18}_{-0.06}$

Table 1.2: Allowed ranges at 1σ CL for the masses of the charged fermions of the three families in the SM [25]. The $u-$, $d-$ and $s-$ quark masses are estimates of the so-called "current quark masses" in a mass independent substraction scheme such as $\overline{MS}$ at a scale $\mu = 2$ GeV. The estimates of $u-$ and $d-$ quark masses are controversial and remain under active investigation. The $c-$ quark mass is the "running" mass ($\mu = m_c$) in the $\overline{MS}$ scheme. The range $1.0 - 1.4$ GeV for the $\overline{MS}$ mass corresponds to $1.47 - 1.83$ GeV for the pole mass. The $b-$ quark mass is the "running" mass ($\mu = m_b$) in the $\overline{MS}$ scheme. In this case, the range $4.13 - 4.37$ GeV for the $\overline{MS}$ mass corresponds to $4.71 - 4.98$ GeV for the pole mass. The value for the top mass quoted here is an average of top mass measurements of Tevatron-Run-I and Run-II that were published at the time when Ref. [25] was prepared.

1.2 Mechanisms to generate neutrino masses

Due to the gauge properties of the Higgs boson, the following interaction terms need to be introduced in the lagrangian, since they are allowed by the gauge symmetry of the SM:

$$-\mathcal{L}_Y = Y_d \overline{Q}_L \phi d_R + Y_u \overline{Q}_L \widetilde{\phi} u_R + Y_l \overline{L}_L \phi l_R + h.c.\,,$$

where $\widetilde{\phi} = i\sigma_2 \phi^*$.

After EWSB takes place, as the Higgs gets a *vev* all the quarks and charged leptons acquire their masses through these interaction terms in the lagrangian:

$$\mathcal{L}_Y \longrightarrow \sum_{\psi=q,l} Y_\psi \frac{v}{\sqrt{2}} (\overline{\psi}_L \psi_R + h.c.) = m_\psi \overline{\psi}\psi$$

The couplings Y_ψ are the Yukawa couplings, whose values are determined through the measurement of fermion masses. As we have just seen, this mechanism needs the existence of right-handed singlets to give masses to the fermions.

Note that right-handed particles necessarily have to be included in the SM particle content, because the strong and electromagnetic interactions are not chiral. However, this is not the case for neutrinos, since they do not interact neither strongly nor electromagnetically. Right-handed neutrinos, thus, are not needed to explain the observed weak interactions phenomena. Therefore, when the SM was built they were not included in its particle content.

As a consequence, in the absence of a ν_R, neutrinos cannot acquire mass through a Yukawa term. This was not a problem when the SM was formulated, as neutrino masses had not been observed yet. However, the first evidence of physics Beyond the Standard Model (BSM) came with the discovery of neutrino oscillations [31,32]. Since the observed pattern of oscillations can only be explained if at least two of the neutrino masses are non-vanishing, a mechanism to generate them

must be added to the SM. In order to do so, the particle content of the SM needs to be enlarged. This can be done in several ways.

Imposing exact L conservation: Dirac neutrinos.

A straightforward option to generate neutrino masses consists in the inclusion of right-handed neutrinos in the SM particle content. In this case, neutrinos acquire their masses just as the rest of the fermions, through their corresponding Yukawa terms in the lagrangian:

$$\mathcal{L}_{\rm Y}^{\nu} = Y_{\alpha\beta}^{\nu}\overline{L}_{L\alpha}\widetilde{\phi}\nu_{R\beta} + h.c. \tag{1.1}$$

However, notice that right-handed neutrinos are singlets of the gauge group. As a consequence, an additional Majorana mass term of the form $M\overline{\nu}_R^c\nu_R$ could in principle be added to $\mathcal{L}_{\rm mass}^{\nu}$, since it is compatible with the gauge symmetries of the SM. However, such a term is L violating. Since L is respected in the SM, one possibility would be that it is also respected by any possible extension of physics BSM.

In this approach, after EWSB the lagrangian would be:

$$\mathcal{L}_{mass}^{\nu} = \underbrace{\frac{v}{\sqrt{2}}Y_{\alpha\beta}^{\nu}}_{m_{\alpha\beta}^{\nu}}\,\overline{\nu}_{L\alpha}\nu_{R\beta} + h.c.\,,$$

where Y_ν is a $n \times n'$ hermitian matrix containing the Yukawa couplings, where n and n' are the number of left- and right-handed neutrinos, respectively. Notice that, in order to reproduce neutrino masses in the observed range, $m_\nu \sim \mathcal{O}(10^{-2})$ eV, extremely small Yukawa couplings are needed: $Y_\nu \sim \mathcal{O}(10^{11})$. It is commonly argued that such small values for the couplings are "unnaturally" small, since the Yukawa couplings for the rest of the fermions adopt values which are in the range $\left[10^{-6}, 1\right]$. In particular, it is suggestive that neutrino Yukawa couplings are roughly 6 orders of magnitude below those of their multiplet counterparts, the charged leptons. A possible interpretation for this is that neutrinos acquire their masses through a different mechanism related to NP beyond the SM, which suppresses their masses with respect to those of the charged leptons. However, it should also be noticed that this "naturalness" problem is not exclusive of the neutrino sector: as it can be seen from Tab. 1.2, charged fermion masses span over 6 orders of magnitude, with some hierarchy present between the ranges in the different families. Therefore, it could also be possible that a mechanism responsible of the flavour structure in the SM explains its fermionic spectrum.

Imposing partial L conservation: Light Majorana neutrinos.

A second possibility arises if we consider the L symmetry to be slightly violated in the full theory[2]. Since it is an accidental symmetry of the model which appears due to the particle content of the SM before neutrino masses were included, we can decide not to preserve it anymore. In this approach, a Majorana mass term for the right-handed neutrinos should be added to the neutrino mass lagrangian,

$$-\mathcal{L}_{\rm Y}^{\nu} = Y_{\alpha\beta}^{\nu}\overline{L}_{L\alpha}\widetilde{\phi}\nu_{R\beta} + \frac{1}{2}M\overline{\nu}_R^c\nu_R + h.c.\,, \tag{1.2}$$

[2]In some models, such as the one proposed in Ref. [33], for instance, Majorana terms are allowed whereas L conservation is imposed at the same time. This can be done assigning appropriate values of L to the new particles in the model.

M being a $n' \times n'$ complex matrix, in general. It should be noticed, however, that a trivial rotation can always be performed for the ν_R states in such a way that the Majorana mass matrix M turns out to be diagonal with real positive entries.

After EWSB, the mass lagrangian in Eq. (1.2) can be rewritten as:

$$-\mathcal{L}^{\nu}_{\text{mass}} = \frac{1}{2}\,\overline{n}^{c}_{L}\mathcal{M}^{*}n_{L} + \text{h.c.}\,,$$

where

$$n_L = \begin{pmatrix} \nu_L \\ \nu^c_R \end{pmatrix}\,.$$

For n leptonic generations, $\mathcal{M}$ is the $2n \times 2n'$ neutrino mass matrix

$$\mathcal{M} = \begin{pmatrix} 0 & \frac{v}{\sqrt{2}}Y_\nu \\ \frac{v}{\sqrt{2}}Y^T_\nu & M \end{pmatrix}\,. \tag{1.3}$$

Finally, Majorana masses M_{ii} run with the renormalization scale, Λ, as:

$$\frac{dM_{ii}}{d\Lambda} \propto M_{ii}\sum_{\alpha}|Y_{\alpha i}|^2\,. \tag{1.4}$$

As it can be seen, the renormalization running of the Majorana mass is proportional to the Majorana mass itself. It is thus "protected" by chiral symmetry. If M is small, the running guarantees that quantum corrections will be small, too. This observation applies to any particular choice of M, which is therefore stable under renormalization[3]. Thus, small Majorana masses enlarge the symmetries of the lagrangian since L conservation is recovered in the limit $M \to 0$, and at the same time they are protected from becoming large by the chiral symmetry.

Allowing large L violation: The See-Saw models.

A third possibility would be to allow for a large violation of L. Following this approach, there is nothing now which prevents our Majorana masses in Eq. (1.2) from becoming large. Indeed, from Eq. (1.4) it can be seen that M is stable under renormalization, regardless of its value. Therefore, in principle M can also be large. In this approach, if we follow the procedure described above and diagonalize the mass matrix in Eq. (1.3) in the limit where $M \gg v$, the following expression for light neutrino masses is obtained:

$$m^{light}_{\nu} = \frac{v^2}{2}Y_\nu\frac{1}{M}Y^t_\nu\,. \tag{1.5}$$

By doing this, the smallness of neutrino masses is automatically explained due to a suppression with the mass of the heavy neutrino, and extremely small Yukawa couplings are not needed anymore. The smallness of neutrino masses is provided in this case by the theory, which introduces a suppression with the scale of NP $\Lambda \gg v$. Consequently, these kind of models are called "See-Saw" models [17, 18, 34, 35].

An alternative approach which gives the same expression for neutrino masses consists in integrating out the heavy fields in the theory, since $M \gg v$, and working in the effective theory

[3]This case is quite different from the case of the Higgs mass, for which we have seen that quantum corrections are quadratically sensitive to the UV cut-off.

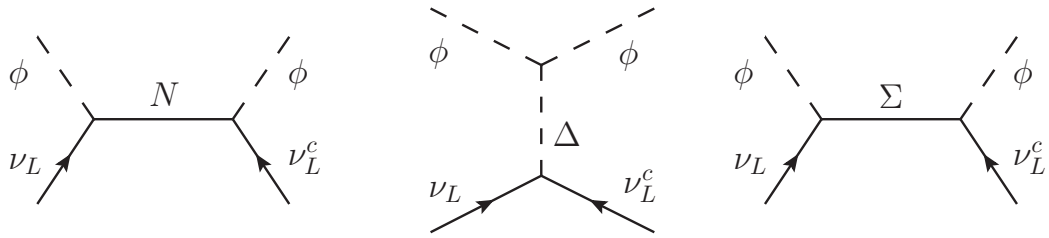

Figure 1.1: Feynman diagrams associated to the type I (left), type II (middle) and type III (right) See-Saw mechanisms. When the heavy particle that is acting as a mediator is integrated out, the Weinberg operator is generated in the low energy regime.

at low energies. Doing this in the theory described above, we obtain the following dimension 5 operator:

$$\mathcal{L}^{d=5} = (\overline{L}_{L\alpha}\widetilde{\phi})(Y_\nu \frac{1}{M} Y_\nu^t)_{\alpha\beta}(\widetilde{\phi}^t L^c_{L\beta}),$$

where $L_{L\alpha}$ stands for the leptonic doublet and $\psi^c = C\overline{\psi}^t$, C being the charge conjugation operator. This is the so-called Weinberg operator [36], which will give rise to neutrino masses after EWSB. It is important to notice that this is the only gauge invariant $d = 5$ operator which can be constructed within the SM particle content. In addition, notice that its inclusion in the lagrangian violates the $B-L$ symmetry. Since the SM preserves the $B-L$ symmetry, quantum corrections cannot generate such a term at any order in perturbation theory. It cannot be generated due to non-perturbative effects, either, since $B - L$ is non-anomalous.

The most general expression for this operator would be the following:

$$\mathcal{L}^{d=5} = \frac{c^{d=5}_{\alpha\beta}}{\Lambda}(\overline{L}_{L\alpha}\widetilde{\phi})(\widetilde{\phi}^t L^c_{L\beta}),$$

where the energy scale Λ is needed in order to keep correct dimensions in the lagrangian. In the previous case, Λ corresponds to the mass of the heavy neutrino (type I See-Saw, [35, 37]), and the expression in Eq. (1.5) for the light neutrino masses is easily recovered at low energies. However, this is not the only possible extension of the SM which gives rise to the Weinberg operator. The inclusion of a heavy scalar triplet (type II See-Saw, [38–40]) or a heavy fermionic triplet (type III See-Saw, [41]) would also produce the same effective lagrangian at low energies, although in these cases different expressions for the light neutrino masses would be obtained since more parameters are involved in the lagrangian at high energies. The three diagrams associated to the three types of See-Saw mechanisms, which originate the Weinberg operator after the heavy particles are integrated out can be seen in Fig. 1.1.

Several reasons make the See-Saw mechanism very appealing from the theoretical point of view. Firstly, it provides a "natural" explanation for the smallness of neutrino masses due to the suppression with the mass of the heavy particles: therefore, small Yukawa couplings are not needed anymore. At the same time, it constitutes a window to a scale of NP at energies much above the electroweak scale. Finally, these kind of models provide, in principle, the necessary ingredients for leptogenesis to take place since they involve new sources of CP violation and a large violation of L at temperatures above the electroweak scale [20].

Notice the strong interplay that takes place between the neutrino Yukawa couplings and the

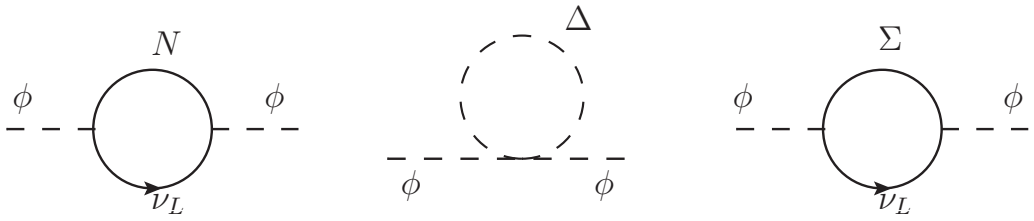

Figure 1.2: 1-loop contributions to the Higgs mass for the type I (left), type II (middle) and type III (right) See-Saw models.

scale of NP, Λ. Neutrino masses obtained from the Weinberg operator take the form:

$$m_\nu \sim c^{d=5} Y^t Y \frac{v^2}{\Lambda} ,$$

where the exact expression for $c^{d=5}$ depends on the particular model of NP giving rise to the Weinberg operator at low energies. For illustration, let us consider the type I See-Saw. If a neutrino Yukawa coupling of $\mathcal{O}(1)$ (like the coupling for the top quark) is assumed, in order to obtain neutrino masses in the correct ballpark Λ needs to be placed at the GUT scale. This possible relation between the neutrino sector of the SM and new particles at the GUT scale is extremely suggestive from the theoretical point of view, since it opens the possibility of obtaining bariogenesis through leptogenesis. However, the scale of NP could also be lowered to the TeV range if smaller Yukawa couplings of $\mathcal{O}(10^{-6})$ (like the coupling for the electron) are assumed.

On the other hand, while in See-Saw models neutrino masses are generated at tree-level, notice that the Weinberg operator could be also generated at the one-loop level [42–46]. In this case, the coefficient of the Weinberg operator in the expansion would have an extra suppression due to the loop:

$$c^{d=5} \sim \frac{1}{16\pi^2} Y^t Y .$$

In this case, even with large Yukawa couplings of $\mathcal{O}(1)$ the NP scale could be placed at the TeV. Notice that this interplay may become even more complicated when a particular model of NP is considered, if the associated expression of $c^{d=5}$ can involve additional parameters.

Finally, it should also be taken into account that large Majorana masses lead to a destabilization of the electroweak scale (in absence of a mechanism to cancel them out, such as supersymmetry, for instance), since Majorana fermions produce quadratic corrections to the Higgs mass. In Fig. 1.2, the 1 loop contributions to the Higgs mass for the three types of See-Saw can be seen. For instance, the contribution for the type I See-Saw (left diagram in Fig. 1.2 can be written as [47]:

$$\delta m_H^2 \sim \frac{1}{v^2}(4m_t^2 - 2M_W^2 - M_Z^2 - m_H^2)\Lambda^2 . \tag{1.6}$$

Therefore, even if in principle large scales may be preferred in order to provide adequate conditions for leptogenesis, for instance, at the same time they appear to be disfavoured since they worsen the hierarchy problem.

1.3 Diagonalization of the mass lagrangian. The U_{PMNS} matrix

In the previous section we have focused on the mass terms in the neutrino lagrangian. However, they need to be diagonalized. In this section it will be shown that, analogously to what happens in the quark sector, the rotation matrices cannot be fully reabsorbed.

Let us take first the case where n' singlets ($\nu_{R\alpha}$) are added to the SM particle content and exact lepton number conservation is imposed. In this case, the full neutrino lagrangian after EWSB can be written as:

$$\mathcal{L}^\nu = \mathcal{L}^\nu_k + \mathcal{L}^\nu_{CC} + \mathcal{L}^\nu_{NC} + \mathcal{L}^\nu_m \,,$$

being[4]:

$$\begin{aligned} \mathcal{L}^\nu_k &= i\overline{\nu}_{L\alpha}\not{D}\nu_{L\alpha} + i\overline{\nu}_{R\alpha}\not{\partial}\nu_{R\alpha}\,, \\ \mathcal{L}^\nu_{CC} &= -\frac{g}{\sqrt{2}}\left(\overline{l}_{L\alpha}\,\gamma^\mu\,\nu_{L\alpha}W^+_\mu + h.c.\right)\,, \\ \mathcal{L}^\nu_{NC} &= -\frac{g}{\cos\theta_W}\,\frac{1}{2}\,\overline{\nu}_{L\alpha}\,\gamma^\mu\,\nu_{L\alpha}Z^0_\mu\,, \end{aligned}$$

where greek indices refer to flavour space, and summing over repeated indices is assumed.

The mass lagrangian would correspond to the one in Eq. (1.1), which can be diagonalized through the bi-unitary transformation:

$$\left\{\begin{array}{lcl} \nu_{L\alpha} &=& V^*_{\alpha i}\nu_i\,, \\ \nu_{R\beta} &=& V_{\beta i}\nu_i\,. \end{array}\right.$$

A similar transformation can be performed to diagonalize the charged lepton masses:

$$\left\{\begin{array}{lcl} l_{L\alpha} &=& \widetilde{V}^*_{\alpha i}l_i\,, \\ l_{R\beta} &=& \widetilde{V}_{\beta i}l_i\,. \end{array}\right.$$

After diagonalization, the V and $\widetilde{V}$ cancel with their adjoints in the kinetic and mass terms, since they are unitary. However, in the charged current lagrangian the mixed product will remain:

$$\mathcal{L}^\nu_{CC} = -\frac{g}{\sqrt{2}}\sum_\alpha \widetilde{V}_{j\alpha}V^*_{\alpha i}\left(\overline{l}_{Lj}\,\gamma^\mu\,\nu_{iL}W^+_\mu + h.c.\right)\,. \tag{1.7}$$

Here, latin indices correspond to mass eigenstates, and greek indices to flavour eigenstates. A redefinition of the lepton mass eigenstates as the flavour ones allows to rewrite Eq. (1.7) as:

$$\mathcal{L}^\nu_{CC} = -\frac{g}{\sqrt{2}}U^*_{\alpha i}\left(\overline{l}_{L\alpha}\,\gamma^\mu\,\nu_{iL}W^+_\mu + h.c.\right)\,, \tag{1.8}$$

where $U = \widetilde{V}^\dagger V$ is the so-called U_{PMNS} (Pontecorvo-Maki-Nakagawa-Sakata) matrix [48–51]. Notice that the U_{PMNS} matrix is physical and therefore can be measured experimentally. It is in addition expected to be unitary, since it is the product of two unitary matrices. For $n = 3$ and $n' \leq 1$, the mixing matrix is a 3×3 matrix, and therefore it is parametrized by a total of 3 angles

[4]Notice that, since the ν_R are $SU(3)_C \times SU(2)_L \times U(1)_Y$ singlets, the covariant derivative reduces to $D_\mu = \partial_\mu$ in the kinetic energy term.

and 6 phases. In general, it is also assumed to be unitary. If neutrinos are Dirac particles 5 out of the 6 phases can be reabsorbed by means of a rotation in flavour space, and only one of them remains in the parametrization: this is the CP violating phase δ.

For the three-family case, the matrix is usually parametrized as [25]:

$$U_{PMNS} = \begin{pmatrix} 1 & 0 & 0 \\ 0 & c_{23} & s_{23} \\ 0 & -s_{23} & c_{23} \end{pmatrix} \begin{pmatrix} c_{13} & 0 & s_{13}e^{-i\delta} \\ 0 & 1 & 0 \\ -s_{13}e^{i\delta} & 0 & c_{13} \end{pmatrix} \begin{pmatrix} c_{12} & s_{12} & 0 \\ -s_{12} & c_{12} & 0 \\ 0 & 0 & 1 \end{pmatrix},$$

where $c_{ij} \equiv \cos\theta_{ij}$, $s_{ij} \equiv \sin\theta_{ij}$.

In case neutrinos also have a Majorana mass only three of the phases can be reabsorbed in a rotation in flavour space, and thus the U_{PMNS} matrix can be written as:

$$U^{Maj}_{PMNS} = U_{PMNS} \cdot \mathrm{diag}(1, e^{i\alpha_1}, e^{i\alpha_2})\,. \tag{1.9}$$

The values for the U_{PMNS} matrix elements are [52]:

$$|U_{PMNS}| \sim \begin{pmatrix} 0.8 & 0.5 & 0-0.15 \\ 0.4 & 0.5 & 0.7 \\ 0.4 & 0.5 & 0.7 \end{pmatrix}.$$

When a comparison is made with its analogous in the quark sector, V_{CKM} [25]:

$$V_{CKM} \sim \begin{pmatrix} 0.97 & 0.23 & 0.003 \\ 0.23 & 0.97 & 0.04 \\ 0.008 & 0.04 & 0.99 \end{pmatrix},$$

the second piece of the flavour puzzle appears. The mixing matrix in the quark sector is almost diagonal, showing a strong hierarchy for the mixing between particles belonging to different generations. On the contrary, all the matrix elements in the $PMNS$ matrix are of the same order of magnitude (with the sole exception of U_{e3}). In particular, they seem to follow a tribimaximal pattern [53]. This has been widely discussed in the literature (see, for instance, Ref. [54] and references therein), since a tribimaximal mixing matrix for the leptonic sector is obtained, for instance, in models where discrete flavour symmetries are imposed. Finally, it should be mentioned the huge uncertainties over the $PMNS$ matrix elements, to be compared with their analogous in the quark sector, of $\mathcal{O}(1\%)$.

1.4 Neutrino oscillations

The existence of a physical mixing matrix in the leptonic sector has two main consequences: first of all, leptons can change flavour as it occurs in the quark sector and, secondly, neutrinos can oscillate[5]. Oscillations are quantum mechanics interference phenomena which consist in the conversion of a particle of one flavour into another with different flavour after traveling a certain distance L. A clear indication of neutrino oscillations is precisely the L/E dependence, which distinguishes them from lepton flavour violating interactions, for instance. In this section, the neutrino oscillation probabilities for N families will be derived for the vacuum case, and then the potential for neutrinos traveling through matter will be introduced. The two neutrino oscillation formulas in

[5]Oscillations do not take place in the quark sector due to strong interactions. However, oscillation phenomena occur for K and B mesons.

matter will be presented, while we refer the reader to App. B for the expanded probabilities in the three family case. Nothing in this section is different from the classical references (see, for instance, Ref. [55] and references therein).

1.4.1 Oscillations in vacuum with N families

We can consider that a neutrino is produced as a wave packet localized around the source position $x_0 \equiv (t_0, \vec{x}_0)$ in a flavour eigenstate ν_α, which is a superposition of the mass eigenstates ν_i. Then, at another point $x \equiv (t, \vec{x})$ the neutrino will have evolved freely as:

$$|\nu_\alpha(x)\rangle = \sum_j U_{\alpha j} \int \frac{d^3k}{(2\pi)^3} f_j(\vec{k}) e^{-ik_j(x-x_0)} |\nu_j\rangle \,, \tag{1.10}$$

where U is the U_{PMNS} mixing matrix, and $k_j \equiv (k_{0,j}, \vec{k})$ is the four-momenta associated to ν_j.

An important remark should be done at this point regarding the use of flavour eigenstates with respect to mass eigenstates. Flavour eigenstates are neither momentum nor energy eigenstates[6]. A first consequence which is derived from this fact is that each wave packet corresponding to a mass eigenstate propagates with a different group velocity, $v_k = p_k/E_k$. Therefore, they separate as they travel towards the detector. In order for oscillations to take place, the different mass eigenstates must be able to interfere at the detector. This is only possible if the separation between the wave packets at the detector is smaller than the size of the wave packet. An additional consequence due to the difference between flavour and mass bases is the quantum entanglement existing between the particles involved in neutrino production and the neutrino mass eigenstates. Therefore, a careful treatment of the process, taking into account the rest of particles resulting from the production process, should be done. In Ref. [56] a detailed analysis, taking this into account, was performed. It was shown that the detailed properties of the states involved in neutrino production play no role in the analysis of neutrino oscillations, provided that the spatial separation of the wave packets associated to the mass eigenstates allows them to interfere at the detector. Therefore, in the following we will ignore the production process of the neutrino.

Since the mass eigenstates form an orthonormal basis, the transition amplitude $\nu_\alpha \to \nu_\beta$ will be, at a point x:

$$\mathcal{A}_{\alpha\to\beta}(x) = \langle \nu_\beta | \nu_\alpha(x) \rangle = \sum_j U_{\alpha j} U^*_{\beta j} \int \frac{d^3k}{(2\pi)^3} f_j(\vec{k}) e^{-ik_j(x-x_0)} \,. \tag{1.11}$$

For the sake of simplicity, in the following we will work in one dimension only, assuming that the detector is placed at $x = (t, L)$. This is a good approximation, since neutrino oscillation experiments require the neutrino to propagate far from the production point. Therefore, only the particles which propagate in that direction will be detected. We will also set $x_0 = (0, 0)$. Thus, the transition amplitude can be written as:

$$\mathcal{A}_{\alpha\to\beta}(L, t) = \sum_j U_{\alpha j} U^*_{\beta j} \int \frac{dk_z}{(2\pi)} f_j(k_z) e^{-ik_{0,j}t + ik_z L} \,, \tag{1.12}$$

where $k^2_{0,j} = k^2_z + m^2_j$.

[6] Neutrino flavour eigenstates are states with more or less well-defined energy, but they are not momentum eigenstates and therefore need to be treated as wave-packets with a certain spread in momentum. Ignorance of this fact could lead to wrong statements, such as the violation of energy-momentum conservation in neutrino oscillations.

The oscillation probability is obtained by squaring the amplitude (1.12). Since we do not know the time of the neutrino detection, an integration over t is also needed[7]:

$$\begin{aligned} P(\nu_\alpha \to \nu_\beta) &= \int dt \left|\mathcal{A}_{\alpha\to\beta}(L,t)\right|^2 \\ &\sim \sum_{i,j} U_{\alpha j} U^*_{\beta j} U^*_{\alpha i} U_{\beta i} \int dk_z \int dk'_z \int dt\, f_j(k_z) f^*_i(k'_z) e^{i(k_{0,j}-k'_{0,i})t} e^{i(k_z-k'_z)L}\,. \end{aligned}$$

Notice that no normalization factors have been included so far. These will be included later through a normalization of the probability to 1.

Since neutrinos are relativistic in the range of energies which are relevant for neutrino oscillation experiments, the neutrino energy can be safely approximated as $k_{0,i} = \sqrt{k_z^2 + m_i^2} = k_z + \mathcal{O}(m_i^2/k_z^2)$. After integration over t and k'_z, and neglecting the corrections $\mathcal{O}(m_i^2/k_z^2)$, the following expression for the oscillation probability is obtained:

$$\begin{aligned} P(\nu_\alpha \to \nu_\beta) \;\sim\; & \sum_{i,j} U_{\alpha j} U^*_{\beta j} U^*_{\alpha i} U_{\beta i} \times \\ & \int dk_z \left\{ f_j(k_z) f^*_i(k_z) e^{-i(\frac{\Delta m^2_{ij}}{2k_z})L} + f_j(k_z) f^*_i(-k_z) e^{i(2k_z)L} \right\}, \end{aligned}$$

where $\Delta m^2_{ij} \equiv m^2_j - m^2_i$. We have neglected all the corrections with the only exception of the exponent in the first term, since L is expected to be large enough to avoid the suppression with $1/k_z$. The second term in the oscillation probability disappears if we make the general assumption that the neutrino wave packets have finite size, much smaller than L. After integrating over k_z and normalizing the probability to 1, the following expression for neutrino oscillations is obtained:

$$\begin{aligned} P(\nu_\alpha \to \nu_\beta) = \sum_i |U_{\alpha i}|^2 |U_{\beta i}|^2 + 2 \sum_{\substack{i,j \\ i<j}} \mathrm{Re}\left(U_{\alpha i} U^*_{\beta i} U^*_{\alpha j} U_{\beta j}\right) \cos\left(\frac{\Delta m^2_{ij} L}{2E}\right) + \\ + 2 \sum_{\substack{i,j \\ i<j}} \mathrm{Im}\left(U_{\alpha i} U^*_{\beta i} U^*_{\alpha j} U_{\beta j}\right) \sin\left(\frac{\Delta m^2_{ij} L}{2E}\right), \end{aligned} \tag{1.13}$$

where $k_z \simeq E$ has been assumed for the oscillation phase.

Applying now the unitarity of the U_{PMNS} matrix and some trigonometrical equivalences, we get the final oscillation formula for neutrinos:

$$\begin{aligned} P(\nu_\alpha \to \nu_\beta) = \delta_{\alpha\beta} - 4 \sum_{\substack{i,j \\ i<j}} \mathrm{Re}(U_{\alpha i} U^*_{\beta i} U^*_{\alpha j} U_{\beta j}) \sin^2\left(\frac{\Delta m^2_{ij}}{4E} L\right) + \\ + 2 \sum_{\substack{i,j \\ i<j}} \mathrm{Im}(U_{\alpha i} U^*_{\beta i} U^*_{\alpha j} U_{\beta j}) \sin\left(\frac{\Delta m^2_{ij}}{2E} L\right). \end{aligned} \tag{1.14}$$

The antineutrino oscillation probability can be obtained from this one, assuming CPT is conserved:

$$P(\overline{\nu}_\alpha \to \overline{\nu}_\beta) = P(\nu_\beta \to \nu_\alpha)\,.$$

[7] The distance from the source to the detector is a well-known parameter in neutrino oscillation experiments. On the contrary, the exact time at which the neutrino is produced is not known.

Changing $\alpha \leftrightarrow \beta$ in the probability, all terms remain unchanged except the last one, which flips sign:

$$\mathrm{Im}(U^*_{\alpha i}U_{\beta i}U_{\alpha j}U^*_{\beta j}) = -\mathrm{Im}(U^*_{\beta i}U_{\alpha i}U_{\beta j}U^*_{\alpha j})\,.$$

Taking this into account, the antineutrino oscillation probability is written as:

$$P(\overline{\nu}_\alpha \to \overline{\nu}_\beta) = \delta_{\alpha\beta} - 4\sum_{\substack{i,j\\ i<j}} \mathrm{Re}(U^*_{\alpha i}U_{\beta i}U_{\alpha j}U^*_{\beta j}) \sin^2\left(\frac{\Delta m^2_{ij}}{4E}L\right) - \\ -2\sum_{\substack{i,j\\ i<j}} \mathrm{Im}(U^*_{\alpha i}U_{\beta i}U_{\alpha j}U^*_{\beta j}) \sin\left(\frac{\Delta m^2_{ij}}{2E}L\right)\,. \tag{1.15}$$

From the comparison of Eqs. (1.14) and (1.15), we can see that if U_{PMNS} turns out to have a non-vanishing CP-violating phase δ, then the probabilities for neutrino and antineutrino oscillation between the same flavour states will not coincide. It should also be noted that, for the two-family case, δ can be reabsorbed through a rotation in the flavour basis.

Due to the unitarity of the PMNS matrix all possible combinations $\mathrm{Im}(U^*_{\alpha i}U_{\beta i}U_{\alpha j}U^*_{\beta j})$ can be expressed in terms of only one of them, in the three family case:

$$\left|\mathrm{Im}(U^*_{e2}U_{\mu 2}U_{\mu 3}U^*_{e3})\right| = c_{12}s_{12}c_{23}s_{23}c^3_{13}s_{13}\sin\delta \equiv J\,,$$

which is the so-called Jarlskog invariant [57]. Note that the Jarkslog invariant will be automatically zero if any of the mixing angles turns out to be zero. Therefore, in this case there would not be any possibility of observing CP violation in the leptonic sector.

On the other hand, it can be easily checked that the Majorana phases cancel out in the oscillation probabilities. From Eq. (1.9), it follows that:

$$\begin{aligned} U^{Maj}_{\alpha 1} &= U_{\alpha 1} \\ U^{Maj}_{\alpha 2} &= U_{\alpha 2}e^{i\alpha_1} \\ U^{Maj}_{\alpha 3} &= U_{\alpha 3}e^{i\alpha_2} \end{aligned}$$

Since these relations are independent from the flavour index, both Majorana phases disappear from the oscillation probabilities. Thus, oscillation experiments are completely unable to distinguish whether neutrinos are Dirac or Majorana particles.

Some final remarks should be done at this point regarding this particular derivation for neutrino oscillation probabilities:

(i) it is important to notice that the neutrino oscillation probability has been derived here within the assumption that they are relativistic. However, this assumption is not really necessary. In Ref. [56] it was found that, as long as the separation between the wavepackets associated to each mass eigenstates is smaller than the size of the wave packets, interference phenomena and quantum oscillations may take place, without any further assumptions on the masses or the momenta of the particles involved in the process. The following oscillation phase is derived in that case:

$$\phi = t\frac{\Delta m^2_{ij}}{E_i + E_j}\,. \tag{1.16}$$

This result is more general, and thus can be applied to K and B oscillations as well. In particular, for relativistic neutrinos $t \sim L$ and the phase in Eq. (1.13) is recovered. Moreover,

the condition of interference for the wave packets at the detector also guarantees the independence of neutrino oscillations from the particular production process [56]. Therefore, it can be argued that, in some sense, the oscillation phase (1.16) is "universal". A detailed review of the quantum mechanics formalism for neutrino oscillations can be found, for instance, in Refs. [56, 58, 59].

(ii) a slight correction to the relation $t = L$ is due to the finite time interval in which the wave packets overlap with the detection process and to the finite coherence time of the detection process. The probability in Eq. (1.14) should be averaged over the resulting total time interval Δt_D for the detection process. However, since this time is characteristic of a microscopic process, it is always much smaller than the macroscopic propagation time, $t \simeq L$. Since neutrino oscillations are observable only if $(\Delta m^2_{ij}/2E)t \sim \mathcal{O}(1)$, the correction $(\Delta m^2_{ij}/2E)\Delta t_D$ is always negligible. In other words, the phase of the oscillation remains practically constant during the detection process, and averaging it over the detection time interval is equivalent to the approximation $t = L$.

1.4.2 Oscillations in matter

Neutrino oscillations may be modified when neutrinos travel through matter, due to their interactions with nuclei and electrons. If a neutrino interacts with matter N times, the resulting cross section will be proportional to the sum of the squared amplitudes of each interaction:

$$\sum_{i=1}^{N} \left|\mathcal{M}_i\right|^2 \propto N G_F^2 \,.$$

However, the suppression due to G_F is large, and therefore the resulting effect will be small. An alternative approach is to consider the neutrino as a wave passing through matter. If the wavelength λ is large compared to the interatomic spacing, the effect of the medium can be described by introducing a refraction index. If λ is also small compared to the size of the scatterer, so that diffraction can be ignored, one can describe the propagation of a neutrino through matter by geometrical optics[8]. The transmitted wave is formed by a superposition of amplitudes from atoms lying within a distance of order λ:

$$\left|\sum_{i=1}^{N} \mathcal{M}_i\right|^2 \propto \left|N G_F\right|^2 .$$

This is the so-called *forward coherent scattering*. Notice that not all possible interactions of neutrinos in matter will contribute to this amplitude. The coherent interference will only take place if the neutrino flavour does not change through its propagation through matter. The processeses which satisfy this condition are depicted in Fig. 1.3. Notice that, while NC processes affect the three flavour eigenstates, the only flavour which will interact via a CC process is ν_e, since only electrons are present in matter (while muons and taus are not). As a consequence, matter effects will affect each flavour eigenstate differently.

The forward scattering amplitude, $F_{\nu_l f}(0)$, is related to the refraction index of neutrinos in matter as [60]:

$$n_{\nu_l} = 1 + 2\pi \sum_f F_{\nu_l f}(0) \frac{N_f}{p^2} \,, \tag{1.17}$$

[8] The wavelength for a neutrino of momentum p is $\lambda = h/p \sim 200(1\text{MeV}/p)(10^{-13}\text{cm})$. Therefore, both conditions will usually be satisfied.

where p is the momentum of the neutrino, $l \equiv e, \mu, \tau$, and N_f corresponds to the number density of fermions, f being the constituents of matter, $f \equiv p, n, e$. This relation is valid for homogeneous, isotropic media and for scattering amplitudes sufficiently smaller than $n-1$. On the other hand, the refraction index can be related to the potential in matter as:

$$n_{\nu_l} \simeq 1 + \frac{V_{\nu_l}}{p} + \mathcal{O}(\frac{m_\nu}{p}) \,. \tag{1.18}$$

Thus, from the comparison of Eq. (1.17) and Eq. (1.18), the effective matter potential for a neutrino traveling through matter is obtained:

$$V = 4\pi \sum_f F_{\nu_l f}(0) N_f \,. \tag{1.19}$$

The forward scattering amplitude for a relativistic neutrino interacting with a target at rest in an unpolarized medium can be computed from the electroweak lagrangian as [61, 62]:

$$F_{\nu_l f}(0) = \mp \frac{1}{\pi} \frac{G_F E}{\sqrt{2}} g^f \,, \tag{1.20}$$

where g^f is the coupling constant associated to the electroweak current. In our case, $g^f = 1$ for CC interactions, while $g^f = I_3^f - Q^f \sin\theta_W$ for NC interactions, with I_3^f and Q^f being the third component of the isospin and the electric charge of the fermion f, respectively.

From Eq. (1.20) and Eq. (1.19), the resulting potential can be obtained:

$$V \simeq \sqrt{2} G_F N_f g^f \,.$$

We can now compute the contributions to the potential associated to the interactions depicted in Fig. 1.3. The contribution associated to charged current interactions (right diagram) with neutrinos gives [62]:

$$V_e = \sqrt{2} G_F N_e \,,$$

where the $\pm$ sign corresponds to neutrinos and antineutrinos, respectively.

For the potential associated to neutral current interactions (left diagram) we get, on the other hand:

$$V_{nc} = \sqrt{2} G_F \sum_f N_f \left[I_3^f - \sin^2\theta_W Q^f \right] \,,$$

where f stands for the constituents of matter (*i.e.*, protons, neutrons and electrons). Once all charges are substituted, and assuming that $N_p = N_e$ (neutral matter), the contributions due to protons and electrons cancel out. Therefore, only the neutron contribution remains:

$$V_{nc} = -\sqrt{2} G_F \frac{N_n}{2} \,.$$

Notice that neither muon nor tau neutrinos interact with matter via W exchange (right diagram of Fig. 1.3), since the probability of a significant coherent scattering on μ or τ in matter is practically zero. Because of this, the potential these neutrinos feel is exclusively due to their interaction by means of a Z boson (left diagram in Fig. 1.3).

Once we change to the mass basis, the full hamiltonian, including the matter potential, is written as:

$$H = \frac{1}{2E} \begin{pmatrix} m_1^2 & 0 & 0 \\ 0 & m_2^2 & 0 \\ 0 & 0 & m_3^2 \end{pmatrix} + U \begin{pmatrix} V_e & 0 & 0 \\ 0 & 0 & 0 \\ 0 & 0 & 0 \end{pmatrix} U^\dagger + U \begin{pmatrix} V_{nc} & 0 & 0 \\ 0 & V_{nc} & 0 \\ 0 & 0 & V_{nc} \end{pmatrix} U^\dagger \,, \tag{1.21}$$

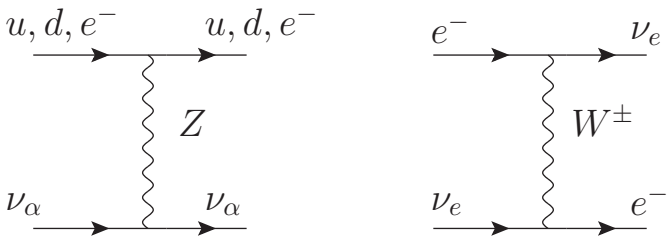

Figure 1.3: Feynman diagrams contributing to the forward coherent scattering between neutrinos ($\alpha = e, \mu, \tau$) and the constituents of matter.

where U is the PMNS mixing matrix. Notice that since the neutral current contribution to the potential, V_{nc}, is diagonal, it can be substracted from the hamiltonian. Therefore, the only contribution that will have a physical effect will be that associated to electron neutrinos, V_e.

The hamiltonian in Eq. (1.21) needs to be diagonalized in order to obtain the eigenvalues needed to compute the transition amplitude. This diagonalization is rather complicated if we consider 3 families (approximate expressions can be found in App. B), but it can be easily solved in the two-family case:

$$\begin{aligned} P(\nu_\alpha \to \nu_\beta) &= \sin^2 2\theta_M \sin^2\left(\tfrac{\Delta m^2_M L}{4E}\right) \\ P(\nu_\alpha \to \nu_\alpha) &= 1 - P(\nu_\alpha \to \nu_\beta)\,, \end{aligned} \tag{1.22}$$

where Δm^2_M and θ_M are the effective squared mass difference and mixing angle in matter. In turn, these can be expressed as functions of the squared mass difference and the mixing angle for two families in vacuum, Δm^2 and θ:

$$\begin{cases} \Delta m^2_M &\equiv \Delta m^2 \sqrt{\sin^2 2\theta + (\cos 2\theta \mp x)^2}\,, \\ \sin^2 2\theta_M &\equiv \dfrac{\sin^2 2\theta}{\sin^2 2\theta + (\cos 2\theta \mp x)^2}\,, \\ x &\equiv \dfrac{2EV_e}{\Delta m^2}\,, \end{cases} \tag{1.23}$$

where the $\mp$ corresponds to neutrinos and antineutrinos, respectively.

In the following, we will always refer to matter with constant density[9] (as it is the case for neutrinos traveling through the Earth). An interesting phenomenon arises for the particular case where:

$$x = \pm\cos 2\theta \Leftrightarrow E = \pm\frac{\Delta m^2}{2V_e}\cos 2\theta\,, \tag{1.24}$$

since in this case the parameters in Eq. (1.23) take the values:

$$\begin{aligned} \sin^2 2\theta_M &= 1 \\ \Delta m^2_M &= \Delta m^2 \sin 2\theta\,. \end{aligned} \tag{1.25}$$

[9]The case where neutrinos travel through matter with variable density, as it is the case for neutrinos produced in the Sun, is not discussed in the present manuscript. We address the interested reader to Ref. [55] and references therein.

Therefore, a resonance takes place for certain values of the neutrino energy, and the effective mixing in matter is maximal even if that is not the case in vacuum. This dramatic amplification of a small mixing angle in vacuum into a very large one in matter is the so-called Mikheyev-Smirnov-Wolfenstein (MSW) effect [60, 63, 64]. Notice that this resonance takes place only for neutrinos or only for antineutrinos, depending on the value of $\mathrm{sgn}(\Delta m^2)$. Therefore, this can be used as a powerful tool to obtain a measurement on the mass hierarchy, as it will be shown in Sec. **??** for the three family case.

1.5 Higher dimension operators

Effects of NP at high energy manifest at low energies through an infinite set of non-renormalizable effective operators of dimension $d > 4$, which are invariant under the SM gauge group. These are weighted by inverse powers of the NP scale Λ:

$$\mathcal{L}^{eff} = \mathcal{L}_{SM} + \frac{1}{\Lambda}\delta\mathcal{L}^{d=5} + \frac{1}{\Lambda^2}\delta\mathcal{L}^{d=6} + \dots , \tag{1.26}$$

where $\mathcal{L}_{SM}$ is the SM Lagrangian which contains all gauge invariant operators of dimension $d \leq 4$. Therefore, in general it would be expected that any NP above the EW scale produced additional signatures at low energies beyond neutrino masses. Since the effects of such operators scale with inverse powers of Λ, however, their effects at low energies are expected to be smaller as the dimension of the operator increases. Therefore, if no further assumption is given, in general it is expected that the greatest effects come from the lowest dimension operators. The $d = 5$ operator was discussed in Sec. 1.2. In the following, we will discuss the $d = 6$ operators, which are the next more relevant ones according to their dimensionality.

$d = 6$ operators

According to dimensionality, after the Weinberg operator the next relevant operators are the $d = 6$ ones. We are interested in operators leading to effects in neutrino physics. Therefore, here we will only consider operators involving leptons.

Before the W and Z bosons were discovered, electroweak processes were described by an effective theory: the Fermi theory for electroweak interactions [65]. This theory was needed in order to account for three electroweak processes observed at low energies: β decays of nuclei, muon decays and muon capture by nuclei. It described in a correct way the electroweak processes at energies much smaller than the EW scale through the inclusion of (non-renormalizable) four fermion operators. In this range of energies, the W and Z propagators are contracted and the full diagram is reduced to a four fermion point-like interaction (see Fig. 1.4). The strength of the coupling for each of the three examples mentioned above seemed to be equal: this was the origin of the Fermi coupling constant, G_f.

Following the same approach, we could try to introduce all $d = 6$ operators which violate flavour in the SM at low energies. The so-called "Non-Standard neutrino Interactions" (NSI) approach consists in the parametrization of all possible effects of NP in the neutrino sector in a phenomenological way, including all the effective four fermion operators which can lead to effects in neutrino oscillations. These can affect neutrino production, detection or propagation processes, depending on their particular structure.

NSI affecting production and detection come from charged current processes, and the neutrino flavour is identified through the measured charged lepton. These interactions can take place

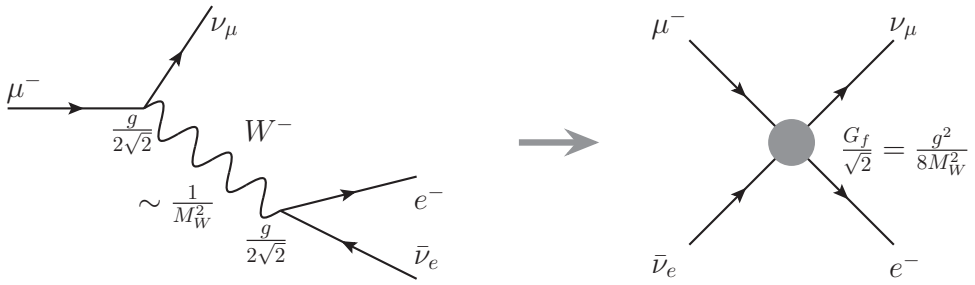

Figure 1.4: Left: SM diagram for muon decay. Right: resulting vertex in the Fermi effective theory at low energies after the W is integrated out.

either with leptons or with quarks. General leptonic NSI are given by the effective lagrangian:

$$\delta\mathcal{L}^l_{\rm NSI} = -2\sqrt{2}\,G_F\varepsilon^{\alpha\beta,P}_{\gamma\delta}\left(\bar{l}_\alpha\gamma^\mu P l_\beta\right)\left(\overline{\nu}_\gamma\gamma_\mu P_L\nu_\delta\right)\ , \tag{1.27}$$

where $P \equiv P_{L,R} = (1 \mp \gamma_5)/2$, G_F is the Fermi constant, and greek indices correspond to flavour indices (e, μ, τ). Notice also that for charged current NSI $\alpha \neq \beta$ and, due to hermiticity, $\varepsilon^{\alpha\beta P}_{\gamma\delta} = \varepsilon^{\alpha\beta P*}_{\gamma\delta}$.

In a similar way, charged current NSI with quarks are given by the effective lagrangian:

$$\delta\mathcal{L}^q_{\rm NSI} = -2\sqrt{2}\,G_F\varepsilon^{qq',P}_{\gamma\delta}V_{qq'}\left(\overline{q}\gamma^\mu P q'\right)\left(\bar{l}_\alpha\gamma_\mu P_L\nu_\beta\right) + h.c.\ , \tag{1.28}$$

where q and q' are up- and down-type quarks, and $V_{qq'}$ refers to the corresponding element of the CKM matrix. Obviously, only $q = u$ and $q' = d$ are of practical interest for neutrino production and detection processes, since neutrinos are produced through meson and muon decays and are observed through their interactions with nuclei.

Finally, NSI affecting neutrino propagation are described through the inclusion of the following four fermion effective operators:

$$\delta\mathcal{L}^{prop}_{\rm NSI} = -2\sqrt{2}\,G_F\sum_{f,P}\varepsilon^{fP}_{\alpha\beta}\left(\overline{\nu}_\alpha\gamma^\mu P_L\nu_\beta\right)\left(\overline{f}\gamma_\mu P f\right)\ , \tag{1.29}$$

where f stands for the index running over fermion species in Earth matter, $f = e, u, d$.

Any model of NP giving rise to these operators should meet the necessary requirement of gauge invariance under the SM gauge group, though [66–70]. This leads to another remarkable point: the set of effective operators which generate neutrino NSI is tightly related to its analogous in the charged lepton sector, which is much more constrained experimentally. For instance, the NSI operator for $f = e$ in Eq. (1.29) could be originated from the following gauge invariant one:

$$-2\sqrt{2}\,G_F\sum_{f,P}\varepsilon^{fP}_{\alpha\beta}\left(\overline{L}_\alpha\gamma^\mu_L L_\beta\right)\left(\overline{L}_e\gamma_{\mu,L}L_e\right)\ , \tag{1.30}$$

which would produce after EWSB, in addition to the mentioned NSI operator, another one which would contribute to the $\mu \to eee$ process (for $\alpha = \mu, \beta = e$). Since this is experimentally very constrained, this imposes tight bounds on the coefficients associated to the NSI operators. It is thus very hard to build a particular model giving large NSI effects in neutrino oscillations without violating stringent experimental bounds on processes involving charged leptons. It is also clear

that, for any particular model of NP, once the corresponding set of low-energy effective operators is derived, relations between their coefficients are expected to take place and (usually) additional bounds apply.

On the other hand, a model independent approach could be followed instead. In this case, all effective four-fermion operators which can affect neutrino oscillations have to be included at once, and the experimental bounds are used to constrain their coefficients independently. Bounds obtained this way are usually looser, but apply to a wide variety of high-energy extensions of the SM. Constraints obtained this way on NSI parameters in propagation are very mild, generically at $\mathcal{O}(10^{-1})$ or even order unity [67, 71]. However, from the theoretical point of view, such large values of the NSI parameters are not really expected. This is easily understood if one tries to find a model of NP responsible for NSI effects without enlarging the low-energy SM particle content.

Finally, higher dimension operators with $d = 6+2n$ will produce corrections to the effects of $d = 6$ operators. However, these will be further suppressed with the ratio v^2/Λ^2. If these operators are produced at tree level, these corrections will take the form:

$$\varepsilon \sim \frac{1}{\Lambda^2}\left[c^{d=6} + \sum_{n=1} c^{d=6+2n}\frac{v^{2n}}{\Lambda^{2n}}\right] .$$

Therefore, unless a certain symmetry is imposed in order to forbid the $d = 6$ operators in the effective lagrangian, the effects from higher dimension operators will be subleading.

Can these operators lead to sizable effects at low energies?

We have already mentioned that the relative importance of the operators involved in the effective theory at low energies scale with inverse powers of Λ. Therefore, their effects at low energies are expected to be smaller as the dimension of the operator increases. However, we have implicitely assumed here that the NP which originates this infinite set of operators is unique. An alternative (and interesting) possibility would be that the scales of NP which give rise to these operators at low energies are different for some of them.

As an illustrative example, let us consider the $d = 5$ and $d = 6$ operators. While the only $d = 5$ operator which can be constructed within the SM particle content is the Weinberg operator, there is a whole set of $d = 6$ operators [72] which can be contructed with the SM fields. An important common feature that all the $d = 6$ operators share is that they preserve $B - L$, while the Weinberg operator does not. Therefore, it may be "natural" (in some sense) to consider that the NP which produce these operators is associated to different energy scales. If we consider the case of four fermion operators for instance, these give rise, in general, to lepton flavour violating processes. In this case, a reasonable assumption could be that the scale where lepton flavour violation is relevant, Λ_{LFV}, differs from the one associated to lepton number violation, Λ_{LNV}. Consequently, the effective lagrangian may be written as:

$$\mathcal{L}^{eff} = \mathcal{L}_{SM} + \frac{1}{\Lambda_{LNV}}\delta\mathcal{L}^{d=5} + \frac{1}{\Lambda^2_{LFV}}\delta\mathcal{L}^{d=6} + \dots . \tag{1.31}$$

In principle, for this lagrangian effects coming from such $d = 6$ operators could still be *relatively* large (and therefore measurable) as long as the condition $\Lambda_{LFV} \ll \Lambda_{LNV}$ is fullfilled (see, for instance, Ref. [73], or Ref. [47] in the context of minimal seesaw models). A natural proposal is that, if in the new theory the Majorana character is associated to some tiny parameter which breaks $B-L$, the coefficient associated to the Weinberg operator is necessarily proportional

to it, and consequently suppressed. This does not have to be the case for dimension 6 operators, which are unrelated to the $B - L$ symmetry. An interesting example in this sense is the type II See-Saw, for instance, or the so-called inverse See-Saw models [74], where a suppression parameter is automatically included.

However, and as we have already mentioned, this is very difficult to achieve since gauge invariance imposes tight relations between the operators in the neutrino and the charged lepton sector (see, for instance, Refs. [69] and [68] where the possibility of obtaining large gauge invariant neutrino interactions is discussed in detail).

2

Experimental landscape in neutrino physics

This chapter is dedicated to give an overview of the current experimental landscape in neutrino physics: in Sec. 2.1, a brief discussion on the absolute scale of neutrino masses is performed, and the bounds obtained from the main experiments are summarized; in Sec. **??** the three neutrino oscillation framework is introduced, and the current experimental values for the neutrino oscillation parameters are presented; in Sec. 2.3 we explain the "degeneracy problem"; in Sec. 2.4 the main future neutrino oscillation facilities are introduced; finally, in Sec. 2.5 a brief review of the most important (yet unexplained) anomalies observed in neutrino experiments (with respect to the 3 neutrino scenario) are presented.

2.1 The absolute scale of neutrino masses

It is important to note that, since oscillation experiments depend on squared-mass differences, no information on the absolute mass scale of neutrinos can be extracted from them. However, indirect bounds on their masses can be derived from electroweak decays and cosmology. Additional bounds can also be derived from neutrinoless double beta decay experiments, in case neutrinos are Majorana particles.

2.1.1 Limits from electroweak decays

Accurate measurements of the end-point energy in the spectrum of certain electroweak decays can be used to place direct bounds on the *effective neutrino masses* for the flavour eigenstates, defined as:

$$m_\alpha^2 \equiv \sum_i |U_{\alpha i}|^2 m_i^2 \,.$$

A tight direct limit for the electron neutrino mass can be derived from the measurements of tritium β decay [25, 75, 76]:

$$m_{\nu_e} < 2\,\text{eV}\,(95\%\,\text{CL})$$

The KATRIN experiment [77], which is expected to start running in 2012, will improve this bound an order of magnitude ($m_{\nu_e} < 0.2$ eV at 90% CL [78]).

For the other two neutrinos direct limits are much weaker[1], though. These can be obtained from the measurement of the end-point in the spectrum of their charged counterparts in the decays

[1] In Ref. [79], a slightly more restrictive bound for the muon neutrino mass was obtained, $m_{\nu_\mu} < 170$ keV (90% CL). However, this bound is very sensitive to small changes on the pion mass, the muon momentum and their errors.

$\pi^+ \to \mu^+ \nu_\mu$ and $\tau^+ \to \pi^+ \nu_\tau$ [25]:

$$m_{\nu_\mu} < 190\,\text{keV}\,(90\%\,\text{CL}) \quad (2.1)$$
$$m_{\nu_\tau} < 18.2\,\text{MeV}\,(95\%\,\text{CL}) \quad (2.2)$$

2.1.2 Cosmological bounds

Additional (more stringent) bounds on the absolute scale of neutrino masses can be obtained from cosmological measurements on the formation of large scale structures. Notice that atoms form in the so-called *recombination era* ($T < 1$ eV) of the early Universe, when the density fluctuation of photons is still related to that of baryons. Observation of the anisotropies in the Cosmic Microwave Background (CMB) indicate that such fluctuations are $(\delta\rho/\rho) \leq 10^{-5}$ [5], but such a small value is not enough to explain the formation of the observed large scale structures in the present Universe. Non-baryonic matter, on the other hand, plays a very important role in structure formation[2]. This can be used to place bounds on neutrino masses, for instance. Take into account that, as long as neutrinos are relativistic (*i.e.*, as long as $T > m_\nu$) no fluctuations can grow, since they can *free-stream* and wash-out perturbations at all scales within the horizon. Therefore, the formation of large scale structures is directly related to the moment when neutrinos become non-relativistic, and consequently, this imposes a bound on the masses of the active neutrino species [6, 80]:

$$\sum_i m_i < 0.54\,\text{eV}\,(95\%\,\text{CL}).$$

This value corresponds to the result obtained from the latest data from WMAP for the CMB, combined with the data from weak lensing measurements, supernovae and baryonic acoustic oscillations. The ΛCDM cosmological model has been assumed[3].

2.1.3 Bounds from neutrinoless double β-decay

Another process that would help in the determination of the absolute scale of neutrino masses is the so-called *neutrinoless double beta decay* ($0\nu\beta\beta$ decay):

$$(A, Z) \to (A, Z+2) + e^- + e^- \,.$$

It is worth noticing that, since it is a lepton number violating process, it can only take place if neutrinos have Majorana masses (see Sec. 1.2). Its amplitude can be written as:

$$A_{0\nu\beta\beta} \propto \sum_i U_{ei}^2 m_i M^{0\nu\beta\beta}(m_i)\,,$$

where m_i is the mass of the neutrino which is mediating the process, U_{ei} is the matrix element of the PMNS matrix, and $M^{0\nu\beta\beta}$ is the nuclear matrix element, which takes into account the nuclear transition between the initial and final states. The observation of $0\nu\beta\beta$ decay would not only be an experimental evidence of the Majorana nature of neutrinos, but it would also place a bound on their masses. The usual bound derived in the literature is obtained summing over the contributions due to active neutrinos and implicitly neglecting the contribution of extra degrees of freedom. In

[2] In particular, cold dark matter plays a very important role in the formation of large scale structures.

[3] Notice that this value strongly depends on the particular cosmological model under consideration and the data included in the analysis. For instance, if the supernovae and baryon acoustic oscillation observations are not included in the analysis, this bound is relaxed to $\Sigma_i m_i < 1.1$ eV [25].

this case, the only contribution comes from neutrinos with $m_i^2 \ll p^2$, where p is the momentum exchanged in the process between the two nuclei, $p^2 \simeq -(100\,\mathrm{MeV})^2$. Then, the nuclear matrix element can be approximated to be independent of the neutrino mass, $M^{0\nu\beta\beta}(m_i) \simeq M^{0\nu\beta\beta}(0)$, and the amplitude of the process is simply proportional to:

$$A_{0\nu\beta\beta} \propto M^{0\nu\beta\beta}(0) m_{ee},$$

with

$$m_{ee}^2 = \left| \sum_{i=1}^{N_{light}} m_i U_{ei}^2 \right|^2 ,$$

where N_{light} is the number of light neutrino species ($m_i^2 \ll p^2$). In the particular case of $N_{light} = 3$, we get:

$$m_{ee}^2 = \left| m_1 c_{12}^2 c_{13}^2 + m_2 s_{12}^2 c_{13}^2 e^{2i\alpha_1} + m_3 s_{13}^2 e^{2i\alpha_2} \right|^2 , \tag{2.3}$$

where $c_{ij} = \cos\theta_{ij}$, $s_{ij} = \sin\theta_{ij}$ and the α_i are combinations of the Dirac and Majorana phases. It is important to notice, though, that if there exist extra neutrinos with masses $M^2 \sim p^2$, the corresponding expression for m_{ee} will be different (see Ref. [81] for details).

$0\nu\beta\beta$ decay has already been explored for different nuclei by several collaborations [82–89], but no signal has yet been observed[4] on the effective $0\nu\beta\beta$ decay neutrino mass, leading to the upper bound [82]:

$$|m_{ee}| < 0.34\,\mathrm{eV}\,(90\%\,\mathrm{CL}).$$

New projects [93–103] are expected to explore the parameter space down to $|m_{ee}| < \mathcal{O}(10^{-1} - 10^{-2})\,\mathrm{eV}^2$ [104].

2.2 Neutrino oscillation experiments

Oscillation neutrino experiments can be classified according to their L/E ratio. This fixes the range of squared-mass differences that a given experiment can explore. Notice that the oscillatory pattern of the probabilities is given through the following combinations of parameters:

$$\phi_{ij} \equiv 1.27 \frac{\Delta m_{ij}^2(\mathrm{eV}^2) L(\mathrm{Km})}{E_\nu(\mathrm{GeV})} ,$$

where the prefactor 1.27 arises when $\Delta m_{ij}^2 \equiv m_i^2 - m_j^2$, L and E are expressed in terms of eV^2, Km and GeV, respectively.

Without any loss of generality, one can choose the mass differences so that Δm_{21}^2 is always positive. For the second mass difference, Δm_{31}^2, there are two possible mass orderings denoted as *normal* and *inverted* (see Fig. 2.1): these correspond to the two possible values of the sign of Δm_{31}^2. Normal ordering is related to hierarchical masses, $m_1 \ll m_2 \ll m_3$, for which $m_2 \simeq \sqrt{\Delta m_{21}^2}$ and $m_3 \simeq \sqrt{\Delta m_{32}^2}$. On the other hand, the inverted ordering implies that $m_3 \ll m_1 \simeq m_2$. A third possibility would be a mass spectrum with quasi-degenerate masses, $m_1 \simeq m_2 \simeq m_3 \gg \Delta m_{21}^2, \Delta m_{32}^2$. Notice that the angles θ_{ij} can be taken without loss of generality to lie in the first quadrant, $\theta_{ij} \in [0, \frac{\pi}{2}]$, while the CP phase is defined in the interval $\delta \in [-\pi, \pi]$. Other conventions are also possible, though [105].

[4] There is a claim for a signal from part of the Heidelberg-Moscow collaboration, though [90, 91]. However, this measurement is quite controversial because: (1) it has not been confirmed by any other experiment yet; (2) it is in conflict with cosmological bounds on neutrino masses [6, 92].

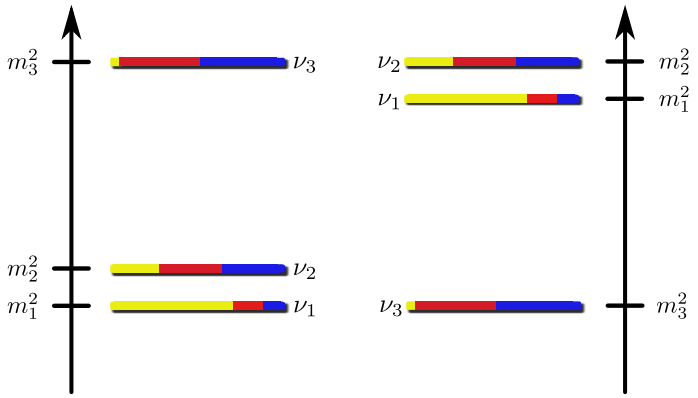

Figure 2.1: Neutrino mass patterns compatible with the current data from neutrino oscillations. Left hand diagram shows normal mass ordering, while the right hand side shows the inverted one. Each color corresponds to the amount of each neutrino flavour that is involved in each mass eigenstate (yellow, red and blue correspond to e, μ and τ, respectively). Notice that, as we have already commented in Sec. 2.1, the absolute scale of neutrino masses remains unknown.

If for a certain L/E one of the oscillation phases ϕ_{ij} is of order one, then the oscillation probabilities can be safely approximated to the two-family case. The appearance oscillation probability in this case is written as:

$$P_{2f}^{app} \simeq \sin^2 2\theta_{eff} \sin^2 \left(\Delta m^2_{eff} \frac{L}{4E} \right) , \tag{2.4}$$

while the disappearance probability reads:

$$\begin{aligned} P_{2f}^{dis} &= 1 - P_{2f}^{app} \\ &\simeq \sin^2 2\theta_{eff} \sin^2 \left(\Delta m^2_{eff} \tfrac{L}{4E} \right) , \end{aligned} \tag{2.5}$$

where θ_{ij} and Δm^2_{ij} have been replaced by two effective parameters, θ_{eff} and Δm^2_{eff}. Notice that in the two-family approximation the probabilities are CP-conserving. Therefore, they are valid for both neutrinos and antineutrinos.

2.2.1 Oscillations in the solar regime

Neutrinos coming from the Sun have been detected using a wide variety of radiochemical techniques [32, 106–111], as well as in Čerenkov (WC) detectors [112–117].

WC detectors are sensitive only to the Elastic Scattering (ES) process[5]:

$$\nu_e + e^- \to \nu_e + e^- \qquad \text{(ES)}$$

Contrary to the standard WC detectors (such as SK), the SNO experiment [32,110,118–120] is a second generation WC detector, where D_2O is used instead of water as the detection medium. Therefore, SNO could observe not only ES processes, but also CC and NC interactions:

$$\begin{aligned} \nu_e + d &\to p + p + e^- \qquad \text{(CC)} \\ \nu_x + d &\to p + n + \nu_x \qquad \text{(NC)} \end{aligned}$$

[5]Muon and tau neutrinos also interact via ES processes. However, their interaction rates are very suppressed with respect to that for electron neutrinos in the range of energies for solar neutrino experiments.

This allows to obtain a solar model-independent test of neutrino oscillations by comparing the charged- and neutral-current interaction rates: while the CC interaction is sensitive only to electron neutrinos, the NC interaction is sensitive to all active neutrino flavours ($x \equiv e, \mu, \tau$). This means that, if solar (electron) neutrinos change into other active flavours, then the interaction rate via ES will be smaller than the interaction rate due to NC processes, $\phi^{\rm ES}(\nu_e) < \phi^{\rm NC}(\nu_x)$. The measurement on the ES interaction rate at SNO was observed to be consistent with the observed rate at Super-Kamiokande [32], whereas the total flux of active neutrinos was observed to be in agreement with the predictions of the Standard Solar Model [121]:

$$\phi(\nu_x) = 5.44 \pm 0.99 \times 10^6 {\rm cm}^{-2}{\rm s}^{-1}\,,$$

thus providing the first compelling evidence of a non-electron flavour component in the solar neutrino flux measured at the Earth. The results were consistent with oscillations ($\nu_e \to \nu_\mu, \nu_\tau$) in the so-called "solar regime", replacing θ_{eff} and Δm^2_{eff} in Eq. (2.5) by θ_{sol} and Δm^2_{sol}.

More recently, the Borexino solar neutrino experiment [122], which is located at the LNGS laboratory at Gran Sasso, presented new data. At Borexino, neutrinos are detected via ES processes in a scintillator detector with a very low energy threshold. This allows to detect solar monocromatic ^{7}Be neutrinos (with $E_\nu = 0.862$ MeV) for the first time. Notice that in the energy range above 3 MeV, neutrino oscillations are dominated by matter effects, while vacuum effects are dominant below 0.5 MeV. The measurement of P_{ee} in both oscillation regimes is important in order to discard exotic explanations of neutrino oscillations. The results obtained from the Borexino experiment reject the no oscillation hypothesis at 4σ CL [123]. However, they show some tension with the present best-fit for the rest of solar oscillation experiments. This could be pointing out to some new effect to be unveiled at this L/E.

Neutrino oscillations in the solar regime can also be observed at reactor experiments. At nuclear reactors, neutrinos procuded in the reactor core have their energies in the MeV range. In these kind of experiments, neutrinos are detected through inverse β-decay:

$$\bar\nu_e + p \to e^+ + n\,.$$

which has a lower energy threshold of about 2.6 MeV. The signature for this reaction is a delayed coincidence between the detection of a prompt e^+ and the signal from the neutron capture. If the distance from the reactor to the detector is such that $E\,({\rm MeV})/L\,(100\,{\rm km}) \sim 10^{-5}\,{\rm eV}^2$, then neutrino oscillations in the solar regime will be observed at the detector. This is the case of the KamLAND experiment [124–126], where neutrinos produced in several reactor cores are detected at a liquid scintillator detector placed at an average distance $L \sim \mathcal{O}(150)$ km. Results from KamLAND constitute a confirmation of neutrino oscillations in the solar regime using a different source.

Recently, both the Super-Kamiokande and the KamLAND collaborations have released new data [127,128]. From the combination of both the solar and KamLAND data, the currently allowed ranges at 3σ CL for the solar parameters are [128]:

$$\begin{aligned} \tan^2\theta_{sol} &= 0.444^{+0.036}_{-0.030} \\ \Delta m^2_{sol} &= (7.50^{+0.19}_{-0.20}) \times 10^{-5}\,{\rm eV}^2 \end{aligned} \qquad (2.6)$$

In Fig. 2.2, the allowed regions in the ($\tan^2\theta_{12}$, Δm^2_{21}) plane, for the combination of the solar and KamLAND latest data, are shown [128]. As it can be seen from the plot, KamLAND measurements have noticeably reduced the uncertainty on the solar mass difference, while the allowed range for the mixing angle is basically set by the solar experiments.

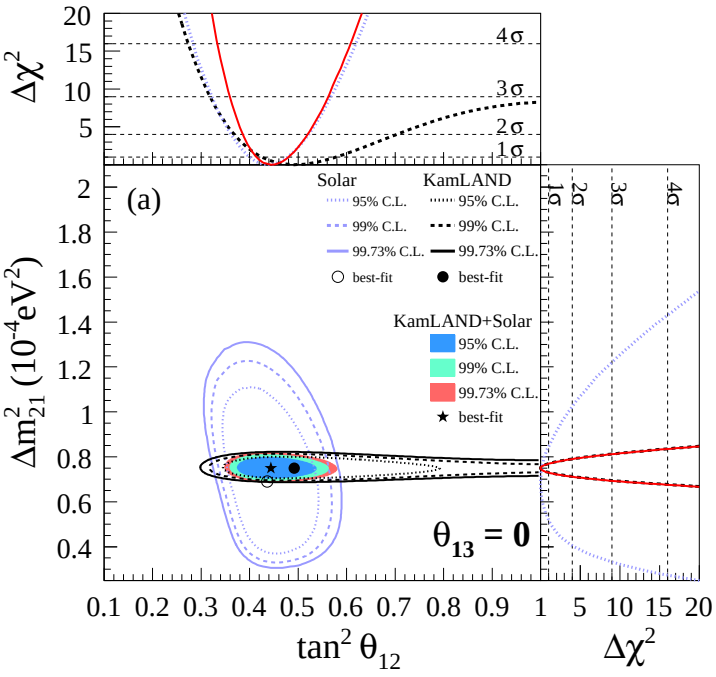

Figure 2.2: Allowed regions projected in the $(\tan^2\theta_{12}, \Delta m^2_{21})$ plane, for the solar and KamLAND latest data, from the analysis in the two-family oscillation approach. The shaded regions show the results from the combined analysis from the solar and KamLAND data. The side panels show the $\Delta\chi^2$ profiles projected onto the $\tan^2\theta_{12}$ and Δm^2_{21} axes, where the red lines show the results from the combined analysis. This figure was taken from [128].

2.2.2 Oscillations in the atmospheric regime

For $E/L \gg 10^{-5}\,\mathrm{eV}^2$, terms oscillating with ϕ_{13} and ϕ_{23} frequencies dominate over ϕ_{21}, and the experiment becomes sensitive to θ_{23} and Δm^2_{32}. This regime is called the "atmospheric regime", because it was first studied using the neutrino flux produced by cosmic rays hitting the outer layers of the Earth atmosphere. Again, in this regime the oscillation probability can be approximated to the two-family case (see Eq. (2.5)), this time replacing θ_{eff} and Δm^2_{eff} by θ_{atm} and Δm^2_{atm}.

Oscillations from neutrinos produced in the atmosphere have been observed by several experiments: Kamiokande [129], Super-Kamiokande [31, 130–132], IMB [133], Soudan2 [134] and MACRO [135]. The typical values obtained for the atmospheric parameters in these experiments are $\Delta m^2_{atm} \sim 2.5 \times 10^{-3}\,\mathrm{eV}^2$ and $\sin^2 2\theta_{atm} \sim 1$.

More recently, conventional neutrino beams have also explored the atmospheric mixing parameters. At conventional neutrino beams, neutrinos are produced from pion and kaon decays in a decay pipe aimed at the detector:

$$\begin{aligned} \pi^+ &\rightarrow \mu^+ + \nu_\mu\,, \\ K^+ &\rightarrow \mu^+ + \nu_\mu\,. \end{aligned} \tag{2.7}$$

Neutrinos produced in conventional beams have energies in the range $\left[10^{-1}, 10\right]\,\mathrm{eV}^2$. Therefore, if a detector is placed at $L \sim 10^2$ Km, oscillations in the atmospheric regime can be explored. This is precisely the case of the K2K [136] and the MINOS [137] collaborations. Both of them have reported

the observation of neutrino oscillations in the atmospheric regime [138–141], thus confirming the phenomenon with a different source. The most precise measurement on the atmospheric mass splitting comes from the analysis of the data from the MINOS experiment, while for the mixing angle Super-Kamiokande gives the best result. The currently allowed ranges for the atmospheric parameters at 90% CL [141]:

$$\begin{aligned} \sin^2 2\theta_{atm} &> 0.90 \\ \Delta m^2_{atm} &= (2.32^{+0.12}_{-0.08}) \times 10^{-3}\mathrm{eV}^2 \end{aligned} \tag{2.8}$$

This very large value for θ_{23} indicates a strong mixing between the second and the third families: atmospheric oscillations, therefore, take place mainly in the channel $\nu_\mu \to \nu_\tau$. All neutrino oscillation experiments listed above have observed disappearance signals in the atmospheric regime. A third conventional beam experiment has been designed in order to explore the appearance signal due to $\nu_\mu \to \nu_\tau$ oscillations: the OPERA experiment [142–144]. At OPERA, the CNGS beam is aimed from CERN to the detector placed in the undergound Gran Sasso Laboratory (LNGS), 730 km away from the neutrino source at CERN. Very recently, the OPERA collaboration has observed a candidate event [145].

Finally, atmospheric oscillations can also be observed at nuclear reactors. If a detector is placed at a distance L from the reactor core such that $E/L \sim 2.5 \times 10^{-3}\,\mathrm{eV}^2$, the experiment will be sensitive to the atmospheric mass difference. In this case, though, the mixing angle which plays a role in the probability is the third mixing angle, θ_{13}, due to the initial flavour of the beam. Oscillations in this regime can also be approximated to the two-family case (Eq. (2.5)), replacing θ_{eff} and Δm^2_{eff} by θ_{13} and Δm^2_{31}, respectively. The present limit on θ_{13} was set by the CHOOZ experiment [146, 147] at $\sin^2\theta_{13} < 0.15$ (90% CL).

2.2.3 The three neutrino oscillation framework

From the results of solar [148], atmospheric [149] and reactor neutrino oscillation experiments [150] it is obvious that the minimal joint description of solar and atmospheric evidences requires that all three known neutrinos take part in oscillations, (see Refs. [151, 152] for recent fits).

The strong hierarchy between the two squared-mass differences and the very small value of the third mixing angle θ_{13} imply that even though the transition probabilities present an oscillatory behaviour with two oscillation lengths, in present experiments such interference effects can be neglected. However, when both terms are of the same order, the two-family approximation cannot be used anymore, and three-family oscillation probabilities must be used instead. Notice that it is in this last case when the CP-violating phase δ can play a role, since additional mixing effects due to the third mixing angle θ_{13} appear (remember that, as it was shown in Ch. 1, CP-violation due to neutrino mixing can only be observed if oscillations take pleace between three non-degenerate generations at least). It is worth to mention that all solar and atmospheric experiments discussed so far are "disappearance experiments" (with the only exception of the OPERA experiment): a neutrinos of a certain flavour are measured at the detector, and the survival probabilities are determined since the initial flux composition is known. On the other hand, some of the presently running and most of the newly proposed terrestrial experiments are "appearance experiments", which are statistically more sensitive to small, θ_{13}-governed probabilities. Notice that in this this kind of experiments the L/E ratio can be tuned in order to maximize the sensitivity of a given experiment to the third mixing angle.

For instance, θ_{13} allows atmospheric oscillations to occur in both the $\nu_\mu \to \nu_\tau$ and $\nu_\mu \to \nu_e$ channels (and, similarly, $\nu_e \to \nu_\tau$ and $\nu_e \to \nu_\mu$). However, the oscillation amplitudes for channels involving ν_e are controlled by the size of $\sin^2\theta_{13} = |U_{e3}|^2$. Therefore, these channels will be

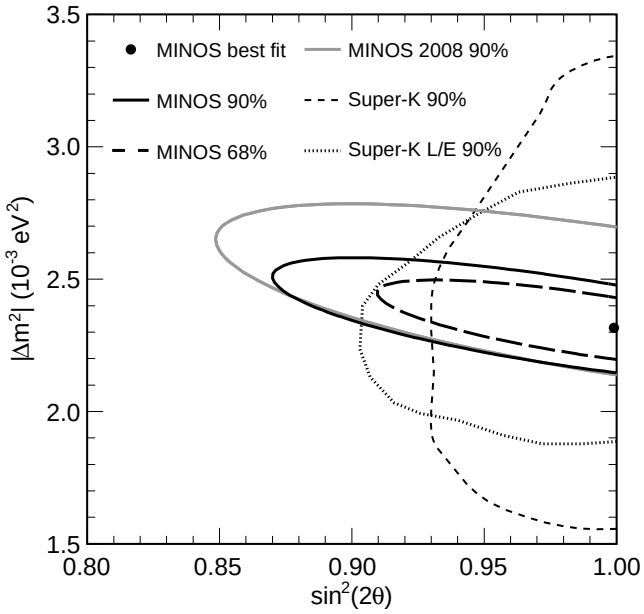

Figure 2.3: Allowed regions projected in the $(\sin^2\theta_{23},\, \Delta m^2_{32})$ plane, around the best fit values for the mass splitting and mixing angle in Eq. (2.8) obtained from the analysis of the latest MINOS data. For comparison, the contours from previous measurements [132, 140] are also shown. This figure was taken from [141].

dominated by θ_{13} and the number of events at the detector will be small compared to the signals in solar or atmospheric oscillation experiments. Furthermore, because of matter effects the probability is different for normal and inverted hierarchies. This effect can be a decrease or an increase in the expected number of events (with respect to the $\theta_{13} = 0$ prediction), depending on the value of $|\,\Delta m^2_{31}\,|$. Therefore, we see that our ability to determine the mass hierarchy through appearance experiments will also depend on the value of θ_{13}. It becomes, thus, a priority in neutrino oscillation experiments, since a non-vanishing θ_{13} opens a window to possible measurements on δ and the mass hierarchy[6].

The full understanding of the leptonic mixing constitutes one of the main neutrino-physics goals for the next decade. Several reactor [156–158] and accelerator [159,160] neutrino experiments are currently running, or will start running in the near future, to search for positive signals of non-zero θ_{13}. Strategy for exploration of the remaining two unknown parameters in the leptonic mixing, δ and the mass hierarchy, heavily depends upon whether they succeed or fail to detect non-zero θ_{13}. If these experiments fail to observe any positive signal for non-zero θ_{13}, more powerful experiments

[6]The mass hierarchy could be determined by other means, though. For instance, in Ref. [153,154] the possibility of measuring the neutrino mass hierarchy through the $P_{\mu\mu}$ channel was considered. Even though such a measurement is experimentally very challenging, it would provide an alternative way to measure the mass hierarchy in case $\theta_{13} = 0$. On the other hand, an inverted hierarchy would also have an impact on $0\nu\beta\beta$ searches and cosmology [155].

involving bigger detectors and improved beams in order to pin down this elusive mixing angle will be needed. The main unknown parameters in the leptonic sector which could be determined through oscillation experiments are the following:

- the mixing angle θ_{13};
- the value of the CP violating phase δ;
- the right order of the mass eigenstates (normal or inverted hierarchy), that is, the sign of Δm^2_{31};
- possible deviations of θ_{23} from maximal mixing;
- in case that $\theta_{23} \neq 45°$, the θ_{23} octant.

The determination of these parameters is definitely the first step towards the understanding of the flavour puzzle. On the other hand, it should also be noted the present uncertainties in the measurement of the solar and atmospheric parameters, much larger than their analogous in the quark sector. These should also be reduced in order to approach an understanding of the flavour mixing in the SM.

The latest derived ranges for the six parameters at 1σ (3σ) are summarized in Tab. 2.1, which has been taken from [152]. It is worth to mention that the current best fit value for θ_{13} is found to be different from zero, something which has been widely discussed in the literature in the last few years. For instance, in [161] a hint for non-zero θ_{13} was already pointed out as a result of the slight tension existing between solar and KamLAND data. In [151], a reanalysis of the solar and KamLAND data was performed, including new releases of data and variations on the solar fluxes as well as the Gallium capture cross-section. It was found that the inclusion of solar data tends to lower the statistical significance of the hint for $\theta_{13} \neq 0$, while the results from ν_e appearance in MINOS [162] and the new Super-Kamiokande results [163] increase it. In all cases, the statistical significance was found to be between 1σ and 2σ, though. More recently, in Ref. [152], another fit was obtained including both the latest solar [117, 127, 163] and MINOS [141, 164] data (including both ν and $\bar{\nu}$), as well as the improved calculations on reactor antineutrino fluxes [165, 166]. Also in this case, the statistical significance of the hint for $\theta_{13} \neq 0$ was found to be above 1σ and, depending on the set of data included in the fit, even above 2σ.

2.3 The degeneracy problem

In the three family case, there are 18 possible oscillation channels. However, using some symmetry properties these can be expressed in terms of only two of them [167]:

- the 9 antineutrino oscillation probabilities can be obtained from the 9 neutrino oscillation probabilities, assuming CPT invariance: $\mathrm{P}(\nu_\beta \to \nu_\alpha) = \mathrm{P}(\bar{\nu}_\alpha \to \bar{\nu}_\beta)$;
- replacing $\delta \to -\delta$ in $\mathrm{P}(\nu_\alpha \to \nu_\beta)$ its T-conjugate is obtained, $\mathrm{P}(\nu_\beta \to \nu_\alpha)$;
- using the unitarity of the U_{PMNS} matrix, three more relations between the probabilities can be found;
- finally, from the parametrization chosen for the PMNS matrix, it follows that the exchange of a ν_μ for a ν_τ in a probability can be done simply by replacing $c_{23} \to -s_{23}$ and $s_{23} \to c_{23}$.

Parameter	Best fit $\pm 1\sigma$	2σ	3σ
Δm^2_{21} $[10^{-5}\text{eV}^2]$	$7.59^{+0.20}_{-0.18}$	7.24–7.99	7.09–8.19
Δm^2_{31} $[10^{-3}\text{eV}^2]$	2.45 ± 0.09 $-(2.34^{+0.10}_{-0.09})$	$2.28 - 2.64$ $-(2.17 - 2.54)$	$2.18 - 2.73$ $-(2.08 - 2.64)$
$\sin^2\theta_{12}$	$0.312^{+0.017}_{-0.015}$	$0.28 - 0.35$	$0.27 - 0.36$
$\sin^2\theta_{23}$	0.51 ± 0.06 0.52 ± 0.06	$0.41 - 0.61$ $0.42 - 0.61$	$0.39 - 0.64$
$\sin^2\theta_{13}$	$0.010^{+0.009}_{-0.006}$ $0.013^{+0.009}_{-0.007}$	≤ 0.027 ≤ 0.031	≤ 0.035 ≤ 0.039

Table 2.1: Current best-fit values for the neutrino oscillation parameters and their allowed ranges at 1, 2 and 3σ, taken from Ref. [152]. For Δm^2_{31}, $\sin^2\theta_{23}$, and $\sin^2\theta_{13}$ the upper (lower) row corresponds to normal (inverted) neutrino mass hierarchy. The new reactor anti-neutrino fluxes taken from [165] have been considered, and short-baseline reactor neutrino experiments ($L \lesssim 100$ m) have been included in the fit.

However, as we have already seen in Sec. **??**, there are still two unknown parameters in the mixing matrix. Moreover, the mass hierarchy and the precise value of the atmospheric mixing angle remain also unknown. Since some of these unknowns belong to the same terms in the oscillation probabilities, degenerate solutions are expected to take place. Let us consider now the neutrino oscillation probability in Eq. (B.1) to explain this point in detail. The problem arises when one tries to adjust the experimental data to the oscillation probability. If we assume the "true" values to be $(\bar{\theta}_{13}, \bar{\delta})$, the equation:

$$P^+_{e\mu}(\bar{\theta}_{13}, \bar{\delta}) = P^+_{e\mu}(\theta_{13}, \delta) \tag{2.9}$$

has a continuous number of solutions. The set of points in the (θ_{13}, δ) plane satisfying this equation is called an "equiprobability curve".

In order to find out which point of the curve is the true solution, a combination of the measurements for neutrinos and antineutrinos can be done. In this case, the system will have two equations (one for neutrinos, the other for antineutrinos) and two unknowns. Therefore, two different solutions are expected to take place: these are the "true" solution and the "intrinsic clone" [168].

Let us consider, for instance, $P^{+,\text{mat}}_{e\mu}$, Eq. (B.1) in App. **??**, to illustrate this point in detail. An expansion of the golden neutrino probability in Eq. (B.1) to second order in θ_{13}, would return the following expression:

$$P^+_{e\mu}(\theta_{13}, \delta) = 4X^\mu_+\theta^2_{13} + 2Y^\mu_+\theta_{13}\cos\left(\delta - \frac{\Delta_{31}L}{2}\right) + Z^\mu, \tag{2.10}$$

where the coefficients $X^\mu_\pm$ and $Y^\mu_\pm$ are independent of θ_{13} and δ, and the solar term Z^μ is the same for neutrinos and antineutrinos. After substituting Eq. (2.10) in Eq. (2.9), the equiprobability

curve for neutrinos in the (θ_{13}, δ) plane is obtained:

$$\begin{aligned}\theta_{13} &= -\frac{Y_+^\mu}{4X_+^\mu}\cos\left(\delta - \frac{\Delta_{31}L}{2}\right) \\ &\pm \left\{\left(\frac{Y_+^\mu}{4X_+^\mu}\cos\left(\delta - \frac{\Delta_{31}L}{2}\right)\right)^2 + \frac{1}{4X_+^\mu}(P_{e\mu}^+(\bar{\theta}_{13}, \bar{\delta}) - Z^\mu)\right\}^{1/2}. \end{aligned} \tag{2.11}$$

Eq. (2.11) provides the whole set of points in the (θ_{13}, δ) plane which satisfy Eq. (2.9). A repetition of the same exercise for antineutrinos produces another equiprobability curve. This will be the same as in Eq. (2.11), after the replacements: $\delta \to -\delta$, $X_+^\mu(Y_+^\mu) \to X_-^\mu(Y_-^\mu)$. To find out if the equiprobabilities intersect at values of (θ_{13}, δ) different from the "true" values, we have to equal Eq. (2.11) to the corresponding one for antineutrinos and solve it for δ. These solutions are called the "intrinsic clones" [168].

For small baseline experiments, this procedure is considerably simplified, as matter effects are negligible and one can use the vacuum limit for the probabilities ($V \to 0$). For instance, for atmospheric oscillations in vacuum the intrinsic clone is located at $(\bar{\theta}_{13}, \pi - \delta)$ [168].

A good method in order to solve this degeneracy is to combine the results obtained at several energies. However, if the spread in energy is not large enough, the equiprobability curves will meet at both the true solution and also (approximately) at the intrinsic clone. This can be clearly seen in Fig. 2.4, where several equiprobability curves are shown for different energies in the range $[5, 50]$ GeV, for $L = 7332$ km. All the curves meet at both the true solution $(\bar{\theta}_{13} = 5°; \bar{\delta} = 60°)$ and the intrinsic clone $(\theta_{13} \sim 6°; \delta \sim -100°)$, with the sole exception of the curve corresponding to $E_\nu = 5$ GeV, which breaks the degeneracy. A statistical analysis of these data sets would give two minima in the ^{2}: the absolute one, located at the true solution, and a local minimum around the intrinsic clone (with less statistical significance). The degeneracy is broken when the value of the ^{2} at the degeneracy is sufficiently increased so that the true solution can be unambiguously identified.

Notice, however, that the instrinsic degeneracy is not the only possible degeneracy that can take place. Here it has been implicitly assumed that the right values of the Δm^2_{32} sign and the θ_{23} octant are known. However, since this is not the case, there are three more ways in which the true solution can be confused with a clone:

the sign degeneracy: this degeneracy appears when trying to find out the hierarchy by looking at the probability [169, 170]. For instance, the golden channel probability in the vacuum limit, Eq. (**??**), remains unaffected under the change: $(\delta, s_{atm}) \to (-\delta, -s_{atm})$, with $s_{atm} = sign(\Delta m^2_{32})$. However, this is not true if we look at the probability in matter, Eq. (B.1) in App. **??**. In Ch. 4 it will be shown how matter effects play a very important role in solving this degeneracy.

the octant degeneracy: from Eq. (**??**) we see that there are two possible values for the mixing angle θ_{23} that are compatible with the data because they give the same value for the probability [171]: θ_{23} and $\frac{\pi}{2} - \theta_{23}$.

mixed degeneracies: these arise from the combination of the latter two, because the sign and octant affect at the same time to the same terms in the probability [172].

From this, we can conclude that for the true pair of values $(\bar{\theta}_{13}, \bar{\delta})$ we will have **eight possible additional values** which will correspond to the same probability [172]. This eight-fold degeneracy can be reduced or even solved in some cases [172, 174–178], by combining the results from different oscillation channels, energies and/or baselines, or using results from different experiments.

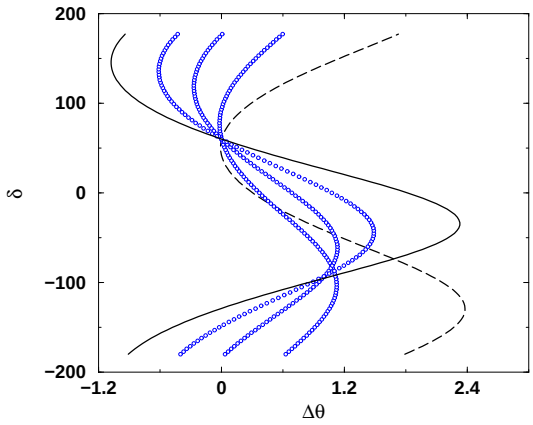

Figure 2.4: Equiprobability curve for antineutrinos, being $\bar{\theta}_{13} = 5°$, $\bar{\delta} = 60°$, $E_\nu \in [5, 50]$GeV and $L = 7332$ Km. The dashed line corresponds to $E_\nu = 5$ GeV, the solid line to $E_\nu = 45$ GeV; the dotted lines lie between these two. This figure was taken from [173].

The Magic Baseline as a powerful degeneracy solver

It has been shown [172,179] that the first two degeneracies can be evaded, in principle, by choosing the baseline of the experiment equal to the characteristic refraction lenght due to Earth matter [60]. This translates into the condition:

$$\sin\left(\frac{VL}{4E}\right) = 0\,, \tag{2.12}$$

where V is the matter potential from Sec. 1.4.2. Notice that, if this condition is fullfilled, the δ dependent terms in the probabilities in matter vanish (see App. **??**). In this case, a clean determination of θ_{13} and $\mathrm{sgn}(\Delta m^2_{31})$ would be possible, since the intrinsic and sign degeneracies are broken. The condition in Eq. (2.12) is equivalent to:

$$\frac{\rho}{[g/cm^3]}\frac{L}{[km]} \simeq 32725\,,$$

where ρ is the matter density. According to the Preliminary Reference Earth Model (PREM) [180–182], this condition is satisfied for:

$$L \simeq 7690\,\mathrm{km},$$

which is also called the *magic baseline* [172, 179]. The position of the magic baseline depends mainly on the density profile of the Earth and not on the oscillation parameters or the energy of the beam[7].

In Fig. 2.5 the effect of the magic baseline is shown. The neutrino oscillation probabilities for the golden channel are depicted as a function of the neutrino energy. Results are shown in the right panel for a value of L close to the magic baseline, $L = 7500$ km, while the left panel shows the oscillation probability at $L = 2000$ km from the source. The mixing angle θ_{13} has been set to 5°, while several lines, corresponding to $\delta = 0, \pm\pi/2, \pi$, have been depicted in order to show the δ-dependence on the probabilities. It can be easily seen from the right panel in the figure that the

[7] A mild dependence on the oscillation parameters and energy creeps in for large values of θ_{13} [183,184], though.

probabilities at $L = 7500$ km are almost independent from δ. In addition, it is remarkable that the probability is strongly enhanced around $E_\nu \sim 6$ GeV. As it will be shown in Ch. 4, this particular feature of the golden oscillation probability for baselines around 7000 km turns out to be a very powerful tool for solving the sign degeneracy at certain β-beam setups.

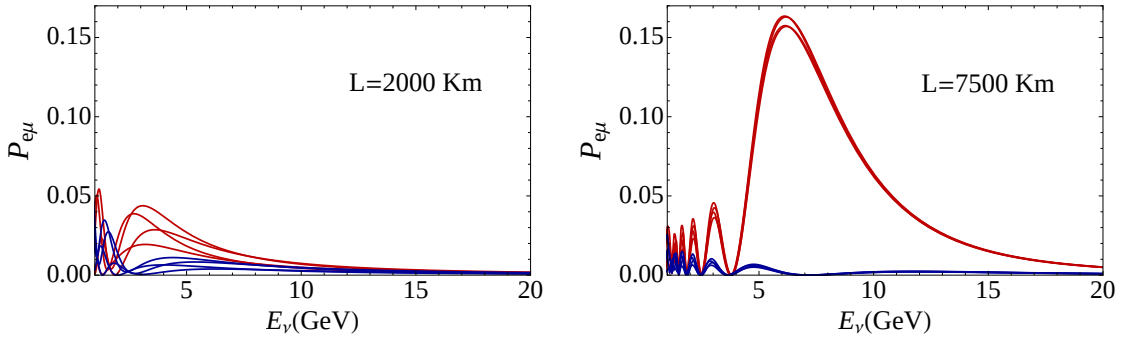

Figure 2.5: Golden neutrino probabilities for normal (red) and inverted (blue) hierarchies, at 2000 km (left) and 7500 km (right) from the source, as a function of the neutrino energy. Several lines, corresponding to different values of δ, are shown. The mixing angle θ_{13} has been set to 5°.

An additional relevant feature can be observed from the comparison of the two panels in Fig. 2.5: a strong enhancement of the probabilitiy at 7000 km takes place for neutrinos around $E_\nu \sim 6$ GeV, only under the assumption of normal hierarchy (red lines in the right panel). This is a resonant effect which takes place because the density encountered by the (anti)neutrinos at this baseline allows for the denominators $B_\mp = |V \mp \Delta_{23}|$ in Eq. (B.1) to cancel for $E_\nu \sim 6$ GeV if the mass hierarchy is normal (inverted). Even if the conditions under which Eq. (B.1) was expanded are not satisfied in this case, the exact oscillation probability shows a resonant enhancement when this condition is met [185]. The advantage of tuning the beam energy to the resonant one is two-fold: first, the increase in the oscillation probability compensates the loss of events due to the very long baseline, increasing the statistics at the far detector and improving its sensitivity to smaller values of $\sin^2 2\theta_{13}$; second, the resonance only occurs for (anti)neutrinos if the mass hierarchy is normal (inverted), therefore providing an extremely good probe of the mass ordering. The resonant behaviour of the golden probability at 7000 km will be fully exploited in the β-beam setups studied in Ch. 4, since the peak of the neutrino spectrum produced from the β-decay of ^{8}Li and ^{8}B ions boosted at $\gamma = 350$ perfectly matches that of the resonance.

2.4 The next generation of experiments

The full understanding of the leptonic mixing matrix constitutes, together with the discrimination of the Dirac/Majorana character of neutrinos and with the measurement of their absolute mass scale, the main neutrino-physics goal for the next decade.

As we have just seen, the joint determination of θ_{13}, δ and $\mathrm{sgn}(\Delta m^2_{31})$ is extremely difficult due to degeneracies and correlations arising between them. A further problem arises from our present imprecise knowledge of atmospheric parameters, whose uncertainties are far too large to be neglected when looking for such tiny signals as those expected in appearance experiments [186]. If θ_{13} lies beyond the reach of the present generation of neutrino oscillation experiments, new

facilities will be needed in order to address its measurement. The future generation of oscillation experiments is focused on the simultaneous measurement of θ_{13} and δ. Therefore, most of the future proposals imply the combination of different experiments and facilities to solve degeneracies. The new generation of experiments can be divided in four classes: Reactors, Super-Beams, Neutrino Factories and β-beams . We introduce the main future reactor experiments here, whereas Super-Beams, β-beams and Neutrino Factories will be discussed in detail in the following chapters. The work presented in this thesis perfectly matches the main purposes of two european projects: LAGUNA and EUROnu. Their main goals are also introduced here.

New Reactor experiments

Reactor experiments have already been used to determine the solar mixing parameters [150], to test the mixing angle θ_{13} [146] and to test oscillations to sterile neutrino species [187, 188]. As it was already commented in Sec. **??**, the present limit on θ_{13} has been set by the CHOOZ experiment [146, 147] at $\sin^2\theta_{13} < 0.15$ (90% CL). The main source of systematic error in the Chooz experiment is due to uncertainties of the original neutrino flux emitted by the reactor. In order to reduce these errors, the design of future reactor experiments includes at least two identical detectors, placed at different baselines. The main disadvantage of this kind of experiments is that they are limited to electron antineutrino disappearance, which is independent from δ. On the other hand, this may be useful in order to obtain a clean measurement of θ_{13}, since degeneracies and correlations will not take place. Three future reactor experiments are currently under construction: Daya Bay [157], Double Chooz [156, 189, 190] and RENO [158]. The detectors technology in these cases are liquid scintillators loaded with Gadolinium in order to facilitate neutron capture.

Daya Bay is a nuclear power plant located at about 70 km northeast of the Hong Kong airport in China. It is expected to explore the third mixing angle down to $\sin^2\theta_{13} \geq 0.01$ (90% CL). The nuclear power complex has two pairs of reactor cores, and another pair is currently under construction. It is located in a mountainous region that provides natural overburden to shield the underground antineutrino detectors from cosmic rays, the main background in this kind of experiments. Two experimental halls near the reactor cores will measure the neutrino flux, while one far hall is located near the oscillation maximum. From a total of 8 identical antineutrino detectors, two will be placed at each of the near sites, while the remaining four will be placed at the far site [191].

Double Chooz is located in the same site as Chooz, in the northeast of France, very close to the Belgian border. Two identical detectors are already under construction: these will be placed at 400 m and 1050 m from the reactor cores. The Double Chooz project is divided into 2 phases: the first phase (which started at the end of 2010) will last ~ 1.5 years, with only the far detector running. During this phase, it is expected to achieve the sensitivity of Chooz after about one month of data taking, and after 1.5 years it is expected to reach the limit $\sin^2 2\theta_{13} \geq 0.06$ (90% CL). In a second phase, which is expected to start by the middle of 2012, the two detectors will be taking data for 3 years, and the experiment is expected to reach the limit $\sin^2 2\theta_{13} \geq 0.03$ (90% CL) [192].

The RENO experiment is located on the site of Yonggwang nuclear power plant in the southwestern part of Korea, at around 250 km from Seoul. Again in this case, two identical detectors are being constructed at 290 m and 1380 m from the reactor cores. This experiment is expected to reach the limit $\sin^2 2\theta_{13} \geq 0.02$ (90% CL) [193].

The LAGUNA and EUROnu design studies

In orther to determine the feasibility and optimal performance of the present candidates for a future oscillation facility, a tight cooperation between phenomenologists and experimentalists is mandatory. It is precisely with this purpose that the LAGUNA and EUROnu projects were started.

The Large Apparatus for Grand Unification and Neutrino Astrophysics (LAGUNA) project [194–196] is a European design study for the development of a kiloton-scale underground particle detector. The detector will be a multi-purpose facility with a broad physics reach - searching for proton decay, detecting astrophysical neutrinos, and it will also be used as part of a Long-Baseline Neutrino Oscillation (LBNO) experiment. The LAGUNA-LBNO study focuses on assessing the potential of three different detector technologies (liquid argon, liquid scintillator, Water Čerenkov) and seven possible baselines within Europe. The neutrino beam is assumed to originate from CERN, Geneva, and the baseline will be determined by the position of the detector. The work presented in Ch. 3 is a detailed study of the performance of all possible setups under consideration in LAGUNA, including variations on the performance parameters for each detector in order to find out which ones are more relevant for the overall performance of the facility. Therefore, it constitutes an important part within the LAGUNA-LBNO design study.

EUROnu is a European Commission FP7 Design Study for a *High Intensity Neutrino Oscillation Facility in Europe* [197, 198]. It started in 2008 and will run for 4 years. Its primary aims are to study three possible future neutrino oscillation faciltiies in Europe and do a cost and performance comparison between them. These facilities are a Super-Beam from CERN to Fréjus, a β-beam with high-Q ions and the NF. In addition, EUROnu will look at the performance of the baseline detectors for each facility and determine their physics reach. The work presented in Ch. 4 and Ch. 5 is embedded in the EUROnu project.

2.5 Experimental anomalies

Up to now, we have been focused on a three-family oscillation scenario. However, the existence of additional (sterile) neutrino species has not been discarded yet. In addition to the solar, atmospheric and reactor neutrino oscillation experiments, additional experiments with very short baselines have been performed in order to look for possible sterile neutrino species [199]. Amongst these very short baseline experiments we find Bugey [187], CDHS [200,201], CHORUS [202], KARMEN [203], LSND [204], MiniBooNE [205, 206] and NOMAD [207, 208]. In all of them, the L/E ratio was tuned in order to look for oscillations driven by a squared-mass difference in the range $\Delta m^2 \gtrsim 1\text{eV}^2$.

Several of these experiments have observed different anomalies, which could be pointing to the existence of a fourth neutrino (see, for instance, Ref. [209] for a recent analysis). In addition to this, different results in neutrino and antineutrino modes have been observed, not only in very short baseline experiments, but also in the MINOS experiment [139,210], which is currently taking data. The joint analysis of these anomalies seems to indicate the presence of new particles together with some additional source of CP violation [209, 211], though more exotic explanations involving, for instance, CPT violation [212] or Lorentz violation [213] have also been considered. Furthermore, the results from cosmology obtained from the latest observations at WMAP seem to favour the existence of additional effective neutrino degrees of freedom.

2.5.1 LSND and MiniBooNE

The LSND experiment took data from 1993 to 1998 at LANSCE, in Los Alamos. At LSND, neutrinos travelled for about 30 meters to the detector. The LSND collaboration announced an excess in the $\bar{\nu}_\mu \to \bar{\nu}_e$ appearance probability at 3.3σ of order 10^{-3} [214]. Such oscillation was also observed in the CP conjugate channel, $\nu_\mu \to \nu_e$ [215]. Both signals could be explained with oscillations between two-families with a squared-mass difference $\Delta m^2 = 1.2$ eV^2 and a mixing angle such that $\sin^2 2\theta = 0.003$.

Notice that this value for Δm^2 is not compatible with the rest of squared-mass differences measured in atmospheric and solar experiments in the 3 family scheme (see Tab. 2.1). Therefore, in order to explain the LSND anomaly one has to invoke an extension of the three-neutrino mixing scenario, introducing either a mechanism to generate a third squared-mass difference or a new form of flavour transition beyond oscillations. Nevertheless, statistical significance of the signal is rather low. Furthermore, it is worth to note that such a signal was discarded by the KARMEN and the NOMAD experiments. KARMEN [203] was located at the neutron spallation source, ISIS, at the Rutherford Appleton Laboratory, and took data between 1997 and 2001. The KARMEN experiment had very similar settings to LSND but a shorter baseline ($L \sim 17$ m), and did not detect such a signal. The NOMAD experiment, on the other hand, was designed to search for $\nu_{e,\mu} \to \nu_\tau$ signals from neutrino oscillations in the CERN wide-band beam. With an average distance between the neutrino source and the detector of ~ 600 m and a L/E ratio of 0.025 Km/GeV, the NOMAD experiment was sensitive to squared-mass differences $\Delta m^2 > 1\text{eV}^2$. Also in this case, no evidence for ν_τ appearance was found.

In order to test LSND results, Fermilab started a new experiment with an identical setup: MiniBooNE. Its results were consistent with the LSND signal in the context of $\bar{\nu}_\mu \to \bar{\nu}_e$ oscillations [205]. However, the signal has not been confirmed by the MiniBooNE search in the CP-conjugate channel [204], $\nu_\mu \to \nu_e$, where the data has been found to be within the expected background. A remarkable feature is the low energy excess for $E_\nu \leq 475$ MeV both in the neutrino and antineutrino modes [206, 216]. In Fig. 2.6, the low energy excess for the neutrino mode is depicted, as a function of the neutrino energy. For comparison, results obtained assuming oscillations into a sterile neutrino are also shown for several values of the mixing angle and the squared-mass difference. This low energy excess makes it even more difficult to find a plausible explanation for the data. For instance, in [209], it was shown that a five neutrino model (with two squared-mass differences in the $\Delta m^2 \sim 1\text{eV}^2$ range) would in principle be able to explain both anomalies, with the exception of the low energy event excess for which an alternative explanation would be needed. In the same reference, it was shown that a four neutrino model (3+1) would be strongly disfavoured by the data, since in this case it is not possible to obtain CP violation.

2.5.2 The reactor anomaly

In preparation for the Double Chooz reactor experiment [192], the specific reactor antineutrino fluxes have been reevaluated [165, 166]. New (improved) reactor antineutrino spectra have been obtained for ^{235}U, ^{239}Pu, ^{241}Pu and ^{238}U. These calculations rely on detailed knowledge of the decays of thousands of fission products, while previous estimates used a phenomenological model [217,218]. New calculations result in an increase of the antineutrino flux of about a 3%. For all reactor experiments at $L < 100$ m from the reactor core [187, 219–225], the average ratio N_{obs}/N_{pred} was previously observed to be in reasonable agreement with the non-oscillation hypothesis, though slightly lower than expected in some cases. However, with the new fluxes this ratio shifts to 0.943 ± 0.023, leading to a deviation from unity at 98.6% CL [166]. This might indicate that these experiments would have observed a deficit according to these new fluxes [152, 166].

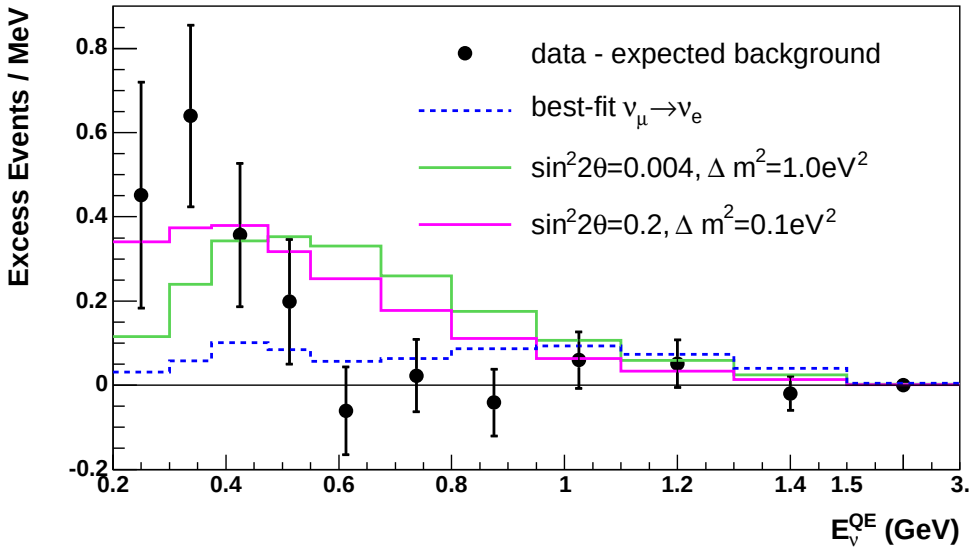

Figure 2.6: Low energy excess observed in the neutrino running mode in the MiniBooNE experiment. For comparison, the results obtained assuming oscillations into a sterile neutrino are also shown for several values of the mixing angle and the squared-mass difference. This figure has been taken from [216].

It is remarkable that the neutrino results from MiniBooNE [205] and the gallium neutrino sources experiments[8] [226] seem to observe ν_e at similar L/E. These anomalies have been already discussed in the literature [166, 226], suggesting again a possible oscillation into a fourth sterile neutrino.

2.5.3 The MINOS anomaly

In MINOS, interactions of neutrinos produced in the Fermilab NuMI beamline are observed at a near detector and at a far detector, located at 735 km from the source. MINOS is the first experiment to probe $\sin^2 2\theta_{13}$ beyond the CHOOZ limit [189].

Recently, the MINOS collaboration has presented their results for antineutrino disappearance data [210], which can be seen in Fig. 2.7. The contour obtained in [141] for ν_μ disappearance at MINOS, as well as the results derived in [52] for a global fit to atmospheric disapperance data are also shown for comparison. It is surprising that the results for neutrino and antineutrino oscillations are compatible only at the 90% CL, and in a very small region of the parameter space. However, it is also important to notice that the statistics for antineutrinos is still well below that for neutrinos (1.71×10^{20} POT for antineutrinos, to be compared with 7.25×10^{20} POT for neutrinos).

In Ref. [226], for instance, some tension between the neutrino data (from the combined analysis of MiniBooNE and Gallium experiments) and the antineutrino data (from the combined analysis of reactor experiments) was already pointed out, and the possibility of having different mixing angles in the neutrino and antineutrino sector was considered. Possible explanations

[8] A possible anomaly has been also pointed out for the Gallium radioactive source experiments [226]. In these experiments, the number of measured events is about 2.7σ smaller than the prediction.

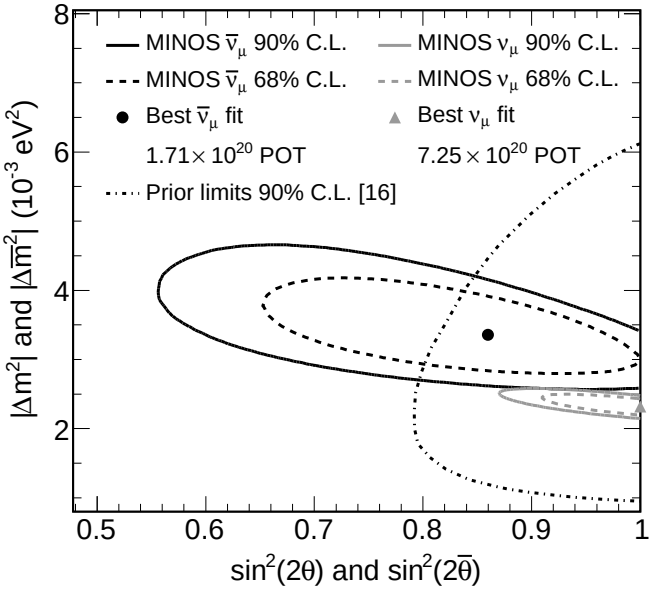

Figure 2.7: Allowed regions for the $\bar{\nu}_\mu$ oscillation parameters from a fit to the data obtained by the MINOS collaboration. Indirect limits taken from [52] and the MINOS allowed region for ν_μ oscillation [141] are also shown for comparison. This figure was taken from [210].

for a different behaviour in the neutrino and antineutrino sectors include Non-Standard Interactions [227] or active-sterile neutrino mixing [209]. However, the violation of fundamental symmetries of the SM, such as Lorentz violation or CPT violation, have also been considered (see, for instance, Refs. [212, 213]). A third possibility would be a model with an additional $L_\mu - L_\tau$ gauge symmetry [228].

2.5.4 Hints from cosmology for sterile neutrinos

A system is said to be in thermal equilibrium when the state of the system does not change with time. In an expanding Universe, the temperature is constantly changing. Therefore, in order to be in thermal equilibrium, the interaction rate of the particles in the Universe needs to be faster than the expansion rate of the Universe. When this condition fails to hold, the particles are said to *decouple* or *freeze-out*. This imposes a relation between the temperature at which particles decouple and the effective number of relativistic degrees of freedom of the Universe at the time of decoupling, g_* [229]:

$$T^3 \sim 1.66 g_*^{1/2} \frac{G_F^2}{M_P} ,$$

where G_F and M_P are the Fermi constant and the Planck mass, respectively. Assuming that neutrinos are relativistic at the time of decoupling, and that there are only three light neutrino species, this implies that the temperature (time) at which they decouple is $T_D \simeq 1$ MeV ($t \simeq 1$ s). However, if there are more species of neutrinos the decoupling temperature would be higher. A

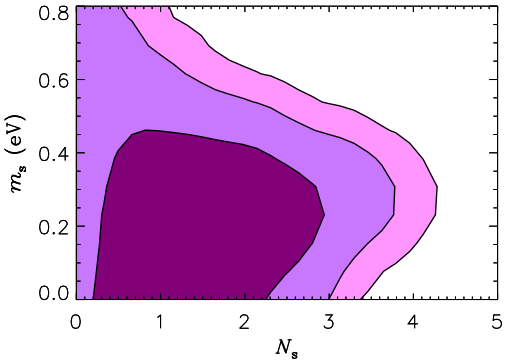

Figure 2.8: $2D$ marginalized 68%, 90% and 95% confidence regions for the neutrino mass and thermally excited number of degrees of feedom N_s ($N_{eff} = 3.046 + N_s$). Ordinary neutrinos have been taken to be massless, while sterile states have a common mass scale m_s. This figure was taken from [233].

higher decoupling temperature for neutrinos implies a higher neutron to proton ratio at the time of nucleosynthesis, since:

$$\frac{n_n}{n_p} = e^{-(m_n - m_p)/T} ,$$

Consequently, higher abundances of light elements (D,^{3}He,^{4}He and ^{7}Li) would be expected. Thus, it is clear that the observed abundances[9] imply a bound on the number of relativistic neutrino species at the time of decoupling.

From the latest data from the WMAP collaboration in combination with additional large scale structure data [6], the effective number of thermally excited neutrino degrees of freedom is found to be:

$$N_{eff} = 4.34^{+0.86}_{-0.88} (68\%\,\mathrm{CL}).$$

A similar study including the Sloan Digital Sky Survey data release 7 halo power spectrum found $N_{eff} = 4.78^{+1.86}_{-1.79}$ at 95% CL [232].

If low-mass sterile neutrinos exist and mix with active neutrinos, they can be thermally excited by the interplay of oscillations and collisions. In particular, for the eV mass range and the relatively large mixing angles needed to explain the oscillation experiments, the sterile states are good candidates to explain the extra degrees of freedom. In Ref. [233], the number of thermally excited sterile neutrinos was taken to be an adjustable parameter, such that $N_{eff} = 3.046 + N_s$, N_s being the extra sterile states. The results obtained for the case where ordinary neutrinos are taken to be massless, while the sterile states have a common mass scale m_s (which is left as a free parameter), are shown in Fig. **??**. The main conclusion that can be drawn from the plot is that sterile neutrinos are not excluded by present cosmological observations if they are not too heavy, and an extra thermal degree of freedom would be even welcome in order to accomodate the Big Bang Nucleosynthesis data.

Finally, it is worth to mention that in 2011 the Planck experiment will measure N_{eff} with a factor of 4 improved accuracy with respect to present data [234, 235].

[9] It is worth to mention here that the observed primordial abundances for the majority of light elements are in agreement with the predictions of Big Bang Nucleosynthesis, save one exception: that of ^{7}Li is approximately two to three times less than what the theory predicts [230]. This is usually referred to as the "Lithium problem" [231].

3
Super-Beams

Super-Beams (SB) produce intense ν_μ beams produced from pion and kaon decays. A SB is taken to be a conventional neutrino beam [] driven by a proton driver with a beam power in the range 2-5 MW [236, 237]. Two main experiments of this kind have already been approved. The T2K experiment [238], aiming from J-PARC to Super-Kamiokande at a distance of $L = 295$ km, has already started taking data. The NOνA experiment [160], on the other hand, will exploit a totally active liquid scintillator and is expected to start taking data in 2013 [239]. The main advantage of NOνA with respect to T2K is its larger baseline, which provides the experiment with some sensitivity to the mass hierarcy (provided that θ_{13} is sufficiently large). Besides the LAGUNA design study, some other SB proposals for the next generation of neutrino experiments (which are currently under discussion) are: T2HK [240], the SPL [241, 242] and, more recently, a Wide-Band Super-Beam (WBB) in the US (LBNE [243, 244]).

In this chapter we evaluate the physics potential of a SB based at CERN when exposed to a massive detector placed at one of seven possible underground locations within Europe. The chapter is organized as follows. In Sec. 3.1 the seven possible locations and the three detector technologies (liquid argon, liquid scintillator and Water Čerenkov) are introduced. Sec. 3.2 is dedicated to explain the simulation details in detail, including the specific details that have been used to simulate the detectors. We also include the definition of the main observables that will be used to describe the performance of the setups. In Sec. 3.3 we show the dependence of the results for the liquid argon and liquid scintillator detectors against variations of several factors in the simulations. These include systematic errors, efficiencies for quasi-elastic (QE) events, the NC backgrounds and the running-time for each polarity, for instance. Finally, in Sec. 3.4 we present a comparison of the performance of each detector technology for each of the seven possible baselines.

3.1 The setups

In this section we introduce the three main factors which determine the SB setups that will be studied in the rest of this chapter: the seven possible sites in Europe capable of hosting a very massive neutrino detector; the beam composition and its optimization for the different possible locations; and the three detectors under consideration within the LAGUNA design study.

3.1.1 The baselines

For the purposes of minimising backgrounds, the detector must be situated underground. Therefore, the choice of the baseline is limited to locations where there is already an existing mine capable of accommodating a large-scale detector, or to locations where it would be possible to expand an

Location	Distance from CERN [km]	1^{st} osc max [GeV]
Fréjus (France)	130	0.26
Canfranc (Spain)	630	1.27
Umbria (Italy)	665	1.34
Sierozsowice (Poland)	950	1.92
Boulby (UK)	1050	2.12
Slanic (Romania)	1570	3.18
Pyhäsalmi (Finland)	2300	4.65

Table 3.1: Potential sites under consideration within the LAGUNA design study [196]. The seven possible locations for the detectors are shown, as well as their distances from CERN and the energies corresponding to the first oscillation peak at these baselines (ignoring matter effects).

existing mine. The practical considerations of building a gigantic detector deep underground include engineering, construction, safety and transportation issues, all of which are considered in the LAGUNA design study. The possible locations of the detectors, their distances from CERN and the energies at the first oscillation maximum corresponding to each baseline (ignoring matter effects) are shown in Table 3.1.

3.1.2 The beam

The range of energies matching the first oscillation peak for each of the possible locations for the detector (see Tab. 3.1) points to the use of a SB. The main advantage of SBs, compared to other proposals such as β-beams or NF, is that the technology required to produce the beam is relatively well-known [245], whereas their major disadvantage is the intrinsic beam background. SB fluxes have been provided by A. Longhin [246]. For each baseline, the beam has been optimized in order for the peak to be as close as possible to the first oscillation maximum indicated in Tab. 3.1. The spectra for the ν beam optimized for 130 km and 665 km baselines are shown in the left and right panels of Fig. 3.1, respectively, as a function of the neutrino energy. Notice the different energy range in the two panels due to different optimization of the beam in order to match different oscillation peaks.

As it can be seen in the figure, together with the dominant neutrino flavour (ν_μ) a small but unavoidable mixture of $\bar{\nu}_\mu$, $\bar{\nu}_e$ and ν_e is also produced (the spectrum for the $\bar{\nu}$ beam is very similar). The contamination becomes larger as the energy of the beam is increased, as it can be seen from the comparison between the two panels in the Fig. 3.1.. This limits the SB sensitivity to $\nu_\mu \to \nu_e$ oscillations. The intrinsic ν_e contamination, which grows with increasing neutrino energy, must be kept as low as possible. One way to achieve this is setting the neutrino beam axis tilted by a few degrees with respect to the vector pointing from the source to the far detector. This is the case of both T2K [238] and NOνA [160]. Off-axis neutrino fluxes are significantly smaller, though, and therefore are not optimal for very long baselines ($\mathcal{O}(1000 - 2000)$ km), such as the ones envisaged by the LBNE or the LAGUNA-LBNO proposals, for instance.

A second feature which can be seen from the comparison between the fluxes depicted in the left and right panels is the much lower flux for the 130 km baseline with respect to the flux for 665 km. The lower flux is explained because a proper collimation of the beam is much more difficult to achieve for lower beam energies.

In the standard setup, 2 years of ν running and 8 years of $\bar{\nu}$ running are assumed: such an asymmetric configuration is needed in order to compensate the much lower fluxes obtained in the antineutrino running mode, as well as to compensate the much smaller cross section for antineutrinos with respect to neutrinos. With this configuration of running times, roughly the same number of neutrino and antineutrino events will be observed at the detector. This will be further discussed in Sec. 3.3.

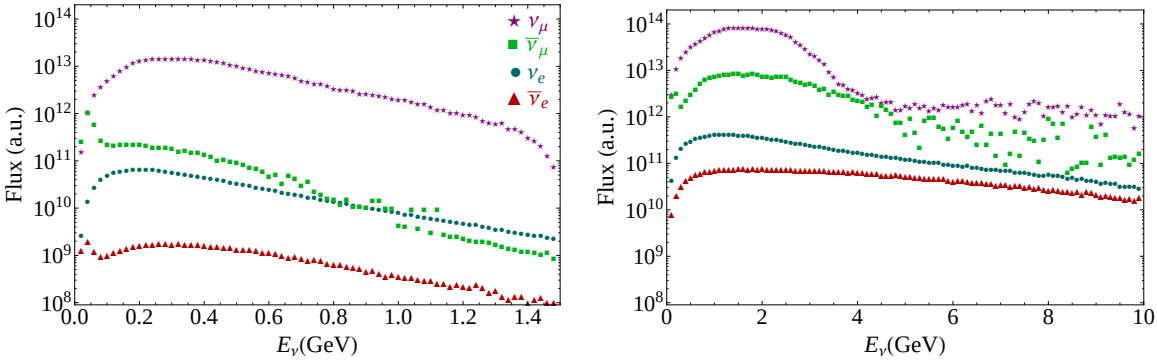

Figure 3.1: Optimized flux for the 130 km (left) and 665 km (right) baselines, produced at the CERN high-power PS2 (50 GeV protons with 3×10^{20} protons on target per year) in the neutrino mode. Fluxes are shown at 100 Km from the source, in arbitrary units and as a function of the neutrino energy [246].

3.1.3 The detectors

The final component of the experiment is the detector. Although a detector with charge identification would be helpful in order to reduce the intrinsic background, in principle it is not necessary. Due to the low energy range for these kind of experiments, an appropriate detector should have a very low energy threshold and large efficiencies for QE events. On the other hand, it should also be able to reduce the NC background produced from pion decays to a negligible level. Three different technologies are currently under discussion:

GLACIER (Giant Liquid Argon Charge Imaging ExpeRiment [247]) consists of a 100 kton liquid argon detector. Among the many ideas developed around the use of liquid noble gases, the Liquid Argon Time Projection Chamber (LAr TPC) certainly represents one of the most challenging and appealing designs. Images taken with a LAr TPC are comparable with pictures from bubble chambers. It offers a very low energy threshold (of few MeV for electrons and few tens of MeV for protons), good suppression for the NC background coming from pion decays and good signal efficiencies. Its main drawback is its efficiency to detect QE events, which is not clear yet. As it will be shown in Sec. 3.3, this is crucial in order to have a good CP discovery potential for this kind of detectors.

LENA (Low Energy Neutrino Astronomy [248–250]) consists of a 50 kton liquid scintillator detec-

tor optimized for the detection of low-energy neutrinos and for the search for proton decay. It is based on the same technology developed for the BOREXINO detector [251]. Their good energy resolution, low energy threshold and high light yield makes them very suitable for being exposed to SBs or β-beams . Their main disadvantage, on the other hand, is their limitations to reject the NC bacgkground coming from pion decays at the detector.

MEMPHYS (MEgaton Mass PHYSics [252]) consists of a 440 kton water Čerenkov (WC) detector. Three detector designs for Mton WC detectors are currently being carried out: Hyper-Kamiokande in Japan [240], UNO in the USA [253] and MEMPHYS in Europe. The WC detector technology is the cheapest and the most suitable to instrument very large detector masses. However, WC detectors are not suited to measure high energy neutrino interactions in the multi-GeV energy range. A further limitation comes from the confusion between single electron or gamma rings and high-energy π^0's giving two overlapping rings.

The construction of one of these very massive underground detectors has additional advantages to those derived from long baseline neutrino oscillation experiments. The three detector technologies listed above could also be used to detect neutrinos produced in the atmosphere, neutrinos coming from astrophysical sources (neutrinos produced in supernovae explosions, relic supernovae neutrinos, solar neutrinos) and geoneutrinos (antineutrinos originated from the β-decay of radioactive elements inside the Earth). In addition, they could improve further the experimental sensitivity to proton decay and allow to probe non-minimal SU(5) models as well as other types of GUTs.

3.2 Simulation details

In order to probe the power of future experiments, we need to *simulate* data. First, we simulate the "true" distribution of events as a function of the neutrino energy for a given set of input values. Then, we try to fit that distribution of events with the corresponding one obtained for a certain set of "test" values. Moreover, neutrinos are detected through the observation of secondary particles. The detection of these secondary particles helps to reconstruct the original event, with a certain efficiency. The reconstructed event will hopefully be a good approximation to the original event. However, the whole sample of reconstructed events will not correspond to the original sample because no detector is perfect. The main consequence from this is that, sometimes, two samples that have been generated with different input values (the "true" and the "test" values) are statistically compatible. The question we need to address is how these limitations and errors affect our ability to obtain information about the true neutrino events.

A software package which has been precisely designed to do so is the General Long-Baseline Experiment Simulator (GLoBES) [254,255], which has been used for all the simulations described in this chapter. The matter density has been taken in agreement with the Preliminary Reference Earth Model (PREM) profile from Refs. [**?**,180,182], assuming an uncertainty of 5%[1]. Marginalization has been performed over the solar and atmospheric oscillation parameters, including gaussian priors around their input values consistent with the present allowed regions at 1σ (see, for instance, Ref. [152] for a recent global fit). Normal mass hierarchy has been assumed for all the results shown in the following sections unless stated otherwise. Nevertheless, we have checked that the results for the inverted hierarchy are very similar to these (under the inversion of $\delta \to -\delta$).

[1] This is a conservative estimate. For instance, in Ref. [256] a $\sim 2\%$ uncertainty was found on the matter density along the CERN - Pyhäsalmi baseline.

3.2.1 Detector simulations

The particular details that have been used to simulate each detector are summarised in Tab. 3.2. The LAr detector details are in agreement with Refs. [257] and [258]. The migration matrices for the LAr detector have been provided by L. Esposito and A. Rubbia [259]. Specifications for the LENA detector have been obtained from Refs. [260, 261] and [262].

A detailed simulation of the WC detector when exposed to a multi-GeV neutrino beam is lacking, and therefore its performance is yet unclear for high neutrino energies. We have followed Refs. [257] and [263]. The migration matrices for a WC exposed to a multi-GeV SB have been kindly provided by the LBNE collaboration [264]. However, these migration matrices are optimized in the high-energy range and may be too pessimistic for our shorter baseline setups. This is particularly relevant for the $L = 130$ km baseline, since in this case the peak of the spectrum is below the low energy threshold of the LBNE migration matrices (0.5 GeV). Therefore, for the $L = 130$ km setup we have used the same migration matrices and efficiencies as in Ref. [265].

In Sec. 3.3 it will be shown how the performance of these detectors is affected against variations on some of the parameters shown in Tab. 3.2.

A final comment should be done at this point regarding the inclusion of atmospheric data in the simulations. Atmospheric data could be helpful in solving degeneracies, specially in the case of very low baseline setups where no matter effects are present and the sign degeneracy cannot be solved (see, for instance, Ref. [265]). No atmospheric data has been included in any of our simulations, though.

Detector	M (kton)	ϵ_{CC}	ϵ_{QE}	NC backgr.	Energy resolution	E (GeV)
GLACIER	100	90%	80%	0.5%	Migr. Matr. [259]	[0.1, 10]
LENA	50	90%	70% (e) 85% (μ)	[0.5, 5] %	$\sigma_{CC}(e,\mu) = 0.05E$ $\sigma_{QE}(e,\mu) = 0.10E$	[0.5, 7]
WC ($L > 130$)	440	40%	40%	5%	Migr. Matr. [265]	[0.5, 10]
WC ($L = 130$)		$\sim 70\%$	$\sim 70\%$		Migr. Matr. [264]	[0.1, 1]

Table 3.2: Parameters used in the simulations of each of the LAGUNA detectors. See text for details.

Finally, in Fig. 3.2 the QE and non-QE cross sections for neutrinos (solid) and antineutrinos (dashed) are depicted as a function of the energy [266,267]. Blue and green lines correspond to the non-QE and QE cross sections, respectively, divided by the neutrino energy. As it can be seen from the plot, QE events dominate in the very low energy range, while they decay very quickly above 1 GeV. Above 2 GeV, the fraction of QE events is very small, and most of the events are non-QE. This is particularly relevant for WC detectors. WC detectors perform very well in the QE event region, where only one ring is produced by the scattered particle. However, their efficiencies start to deteriorate very quickly as neutrinos enter in the non-QE region of the cross section, because deep inelastic processes produce multiple rings which need to be correctly identified.

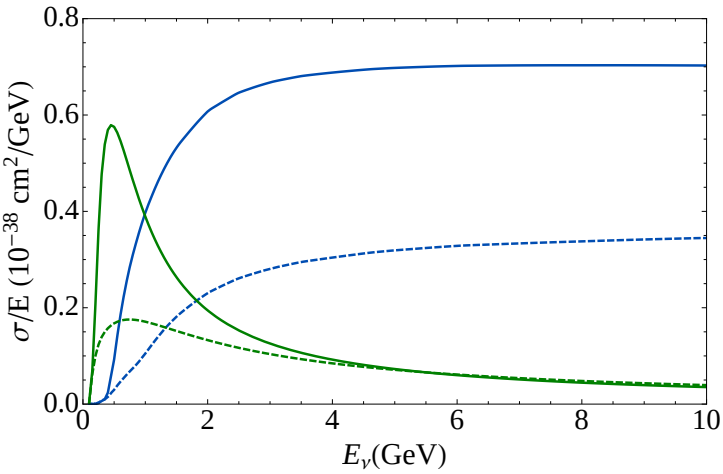

Figure 3.2: Cross sections (divided by the neutrino energy) for neutrinos (solid) and antineutrinos (dashed), as a function of the neutrino energy [266, 267]. Blue and green lines correspond to the cross sections for non-QE and QE events, respectively.

3.2.2 Main backgrounds

All the LAGUNA detectors are capable of identifying electrons and muons; therefore the $\nu_\mu \rightarrow \nu_\mu$ and $\nu_\mu \rightarrow \nu_e$ channels, and their CP conjugates, can be observed. The main background contributions for these channels arise from:

- Intrinsic ν_e ($\bar{\nu}_e$) beam background (see Fig. 3.1): this is the main background to the primary SB channel, the $\nu_\mu \rightarrow \nu_e$ channel. The problem is that it is impossible to distinguish between a ν_e which is the product of an oscillated ν_μ (signal), and one which was produced as a ν_e in the beam (background). The rejection of this background stems purely from the ability to predict or measure the intrinsic ν_e ($\bar{\nu}_e$) component of the beam. Theoretical predictions can be made based on measurements from fixed-target experiments and, ideally, from the use of a near-detector which measures the un-oscillated beam spectrum. NOvA [160] and T2K [238] estimate that they can reduce this component of their background to $\sim 50\%$ of the total ν_e ($\bar{\nu}_e$) content using these methods. We will assume this value in our simulations unless otherwise specified.

- Intrinsic $\bar{\nu}_\mu$ (ν_μ) background in ν_μ ($\bar{\nu}_\mu$) beam: this forms $\sim 10\%$ of the beam as can be seen from Fig. 3.1. As there are no plans to magnetize any of the LAGUNA detectors, there is no way of distinguishing between positively and negatively charged leptons, and therefore it is not possible to distinguish between neutrino and anti-neutrino events. In case CP is conserved, this is not relevant as ν and $\bar{\nu}$ will behave the same way. However, one of the primary aims of the experiment is to detect the presence of CP violation. Therefore, it is crucial to distinguish between ν and $\bar{\nu}$ and this background needs to be minimized. We estimate that a background of 50% of the total content is realistic, given current knowledge of neutrino beam fluxes and planned future experiments.

- Neutral-current events: π^0's can be produced in high-energy NC events and then decay into two photons. If the two rings overlap, the event is often misidentified as an electron. This is not a significant background for liquid argon which has a very good efficiency for the

detection of photons, but is more problematic for WC detectors, and possibly also for liquid scintillators. In addition to this, single π^+/π^- NC events are a background for the muon appearance signals.

- An additional background is in principle expected to come from neutrinos produced in the atmosphere - the so-called *atmospheric background*. This background would be particularly harmful in the low energy range (approximately below 1 GeV) and therefore it could be an issue for some SB and low-γ β-beam setups. However, it can be avoided by imposing stringent duty cycles for the beams. In Ref. [265], it was shown that, for the envisaged duty cycles of 2.4×10^{-4} at the SPL, this background is negligible in the SB case. For β-beams , though, further investigation is still needed to find out the actual duty cycles that could be reached in the storage ring (see Ch. 4 for details).

3.2.3 Observables

To compare different options and to understand which of them is the one to be pursued as a future neutrino facility, a list of observables to be measured has been defined: θ_{13}; the CP-violating phase δ; the sign of the atmospheric mass difference (hereafter called s_{atm}); the deviation from $\theta_{23} = 45°$; and the θ_{23}-octant (if $\theta_{23} \neq 45°$). Aside from these measurements, a new facility should also reduce the present errors on atmospheric and solar parameters. We now define the main observables that will be used in the following to address the performance of the different setups[2]:

the sensitivity to θ_{13}: this is defined as the ability of a certain experiment to rule out the $\theta_{13} = 0$ hypothesis in the fit, after marginalizing over all the other parameters. In other words, the sensitivity to θ_{13} gives the limiting value of θ_{13} for which the data can statistically distinguish a positive θ_{13}-driven oscillation from the $\theta_{13} = 0$ prediction.

the CP discovery potential: this is defined as the ability of a certain experiment to rule out the CP conservation hypothesis ($\delta = 0$ and $180°$), after marginalizing over all the other parameters.

the sensitivity to sgn(Δm^2_{31}): this is defined as the ability of a certain experiment to rule out the wrong hierarchy, after marginalizing over the rest of parameters. For each setup, there is a limiting value of θ_{13} below which the predictions for the wrong hierarchy cannot be separated from the data corresponding to the right hierarchy.

These observables are mainly accesible through the $\nu_e \to \nu_\mu$ and the $\nu_\mu \to \nu_e$ channels (together with their CP-conjugates), so they are common observables for β-beams and SBs. Therefore, they will also be used to describe and compare the performance of the β-beam setups discussed in Ch. 4.

In general, results will be presented in the $\sin^2 2\theta_{13}$-δ plane. However, sometimes it is also useful to present the results showing the amount of values of δ for which a given observable can be measured, the so-called *CP-fraction*. The concept of CP-fraction was introduced in Refs. [268, 269] to compare in a condensed form the performances of different proposals regarding the measurement of a given observable. It translates into a loss of information about the specific values of δ for which the sensitivity to a given observable is achieved but allows a better comparison of the relative performance of the different facilities. Therefore, results will be presented in any of the following planes, depending on the particular features that should be pointed out in each case:

[2] In some of the cited references these definitions can suffer minor changes.

- in the $\sin^2 2\theta_{13}$-δ plane;
- as a function of $\sin^2 2\theta_{13}$ and the fraction of the δ parameter space for which a given observable can be measured.

Unless otherwise stated, results will be shown at a statistical significance of 3σ (1 d.o.f.) and in logarithmic scale in the $\sin^2 2\theta_{13}$-axis.

3.3 Optimisation studies

In this section we study the properties of the beam and detector which affect the sensitivity of the experiment. We studied several variables: systematic errors, the intrinsic beam background, the possibility of τ detection, the different detection properties for quasi-elastic and non-quasi-elastic events, the time spent running in neutrino and anti-neutrino mode, and the effect of neutral-current backgrounds.

3.3.1 NC background in LENA

The main limitation for the LENA detector is its ability to reject the NC background which originates from the wrong identification of π^0's at the detector, which is not clear yet. Therefore, in the following we will present our results for the LENA detector in the most optimistic and the most pessimistic situations: in the former case, we assume a NC background rejection capability comparable to that for the GLACIER detector (that is, only a 0.5% of the NC events cannot be properly identified as background events); while in the latter we assume a 10 times worse NC rejection capability (that is, a 5% of the NC events cannot be properly identified as background events). In Fig. 3.3, we present a comparison of the results obtained for the CP discovery potential of the LENA detector for these two values, as well as for several values in between: 1%, 2% and 3%. The minimum value of θ_{13} for which CP violation can be observed is severely affected by the NC background, the worsening of the performance being roughly proportional to the amount of NC background that cannot be rejected at the detector.

3.3.2 Quasi-elastic events in GLACIER

Quasi-elastic (QE) and non-quasi-elastic (nQE) events have different event topologies and therefore different detection properties. The typical energy of a QE event is $\lesssim 1.5$ GeV although there are still QE events at higher energies. The information from low-energy events contributes mainly to the sensitivity to CP violation because matter effects (which can mimic CP violation) are proportional to the neutrino energy. Therefore, the detection of QE events will be most valuable for CP discovery. Results are only shown for the LAr detector, where the QE detection efficiencies could be an issue. In Fig. 3.4 we show the effect of the QE efficiencies on the CP discovery potential for the LAr detector placed at Pyhäsalmi. As it can be seen from the figure, the effect is remarkable. Even though the minimum value of θ_{13} for which CP violation can be established remains practically unaffected (the greatest worsening takes place around $\delta \sim -90°$, where $\sin^2(2\theta_{13min})$ changes from $\sim 5 \times 10^{-3}$ to 7×10^{-3}), the amount of values of δ for which CP violation can be discovered is considerably reduced when the QE events are removed from the whole sample of events (see right panel in Fig. 3.4). Notice, however, that only the QE efficiencies for the detection of electrons is relevant; the rate of detection of QE muons is unimportant since disappearance channels are insensitive to CP violation.

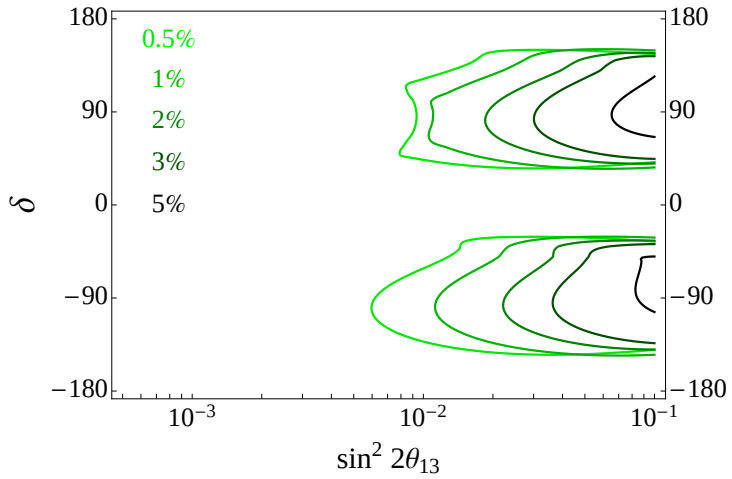

Figure 3.3: Effect of the NC background rejection capability of the LENA detector on the CP discovery potential. The legend indicates the percentage of NC events at the detector which cannot be rejected. Results are presented for the detector placed at Pyhäsalmi.

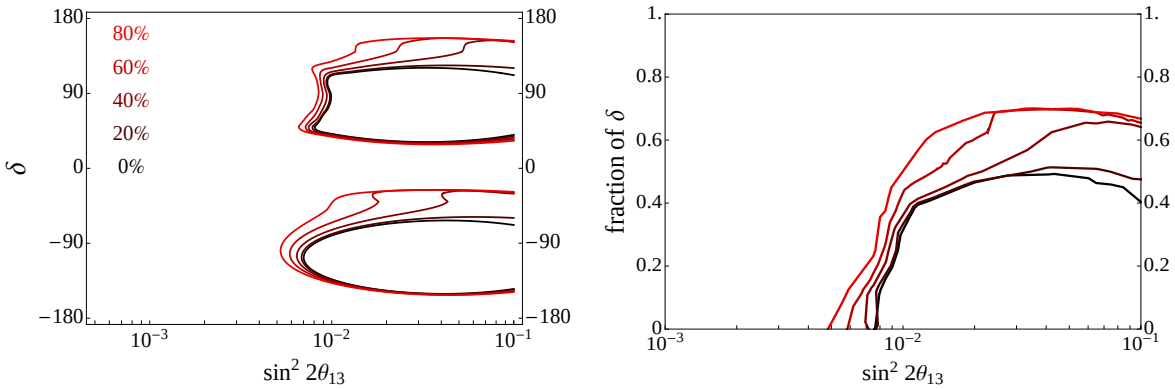

Figure 3.4: Effect of different QE efficiencies on CP discovery potential for the LAr detector placed at the Pyhäsalmi baseline. Left panel shows the results in the δ-$\sin^2 2\theta_{13}$ plane, while for the right panel the results are shown as a function of $\sin^2 2\theta_{13}$ and the fraction of the δ parameter space for which CP violation can be discovered.

3.3.3 Systematic errors

The dominant sources of systematic errors are those associated to the predictions of the beam flux composition and the interaction cross-sections at the detector. The effects due to systematic errors can be separated into those affecting the signal, and those affecting the predictions for the backgrounds. We show in Fig. 3.5 the dependence on the results against variations on the systematic errors both for the signal and the background. Results are shown for the LAr detector placed at the Pyhäsalmi mine in Finland, but qualitatively similar results are expected for the other detectors and baselines. The CP discovery potential and the sensitivity to θ_{13} are shown for several combinations of the systematic errors that have been taken for the signal and the background, as indicated in the legend. In our baseline configuration, a 5% systematic error is assumed over the signal and background, in agreement with Ref. [270] (light blue lines). We find that the magnitude of the systematic errors is crucial for both the sensitivity to θ_{13} and the CP discovery potential.

Two main effects due to systematics can be observed in the CP discovery potential: first, the amount of values of δ for which CP violation can be discovered in the large θ_{13} region is mainly affected by the systematics in the signal; second, the minimum value of θ_{13} for which CP violation can be observed is mainly affected by the background systematics. These features are quite general, and can also be observed in Secs. 3.3.2 and 3.3.1: while signal efficiencies help to improve the δ-fraction, background levels affect the minimum value of θ_{13} for which CP violation can be discovered.

Finally, the systematic errors on the signal affect the sensitivity to θ_{13} almost independently on the value of δ, whereas an increase in the background systematic errors only produces a worsening of the sensitivity in the region where $\delta \sim +90°$.

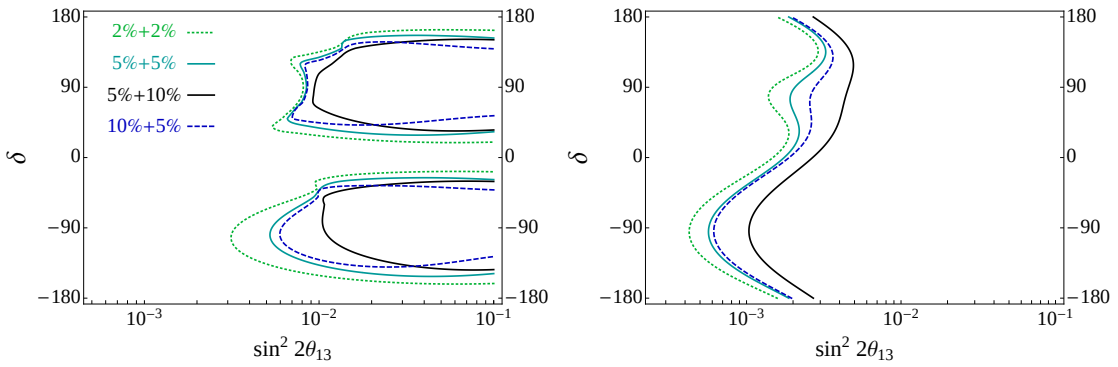

(a) CP discovery potential.

(b) Sensitivity to θ_{13}.

Figure 3.5: Effect of systematic errors on the CP discovery potential (left) and θ_{13} discovery potential (right) for the LAr detector placed at Pyhäsalmi. The first and second values indicated in the legend correspond to the systematic errors assumed over the signal and background, respectively.

3.3.4 Intrinsic beam backgrounds

As it was already mentioned in Sec. 3.1, the intrinsic beam background is one of the limiting factors of a SB experiment. It is thus important to maximise our knowledge of the beam content, either by using a near-detector, or by performing dedicated fixed-target experiments. The reason for this can be seen in Fig. 3.6 where we show how different levels of the beam background (ranging from 10% to 50%) affect the CP discovery potential of the experiment. Results are shown for the LAr

detector located at Pyhäsalmi, but qualitatively similar results are expected for the other detectors and baselines. The improvement is most prominent around the region $\delta = -90°$, whereas the sensitivity around $\delta = +90°$ is limited instead by the ability of the setup to solve the degeneracies in that region.

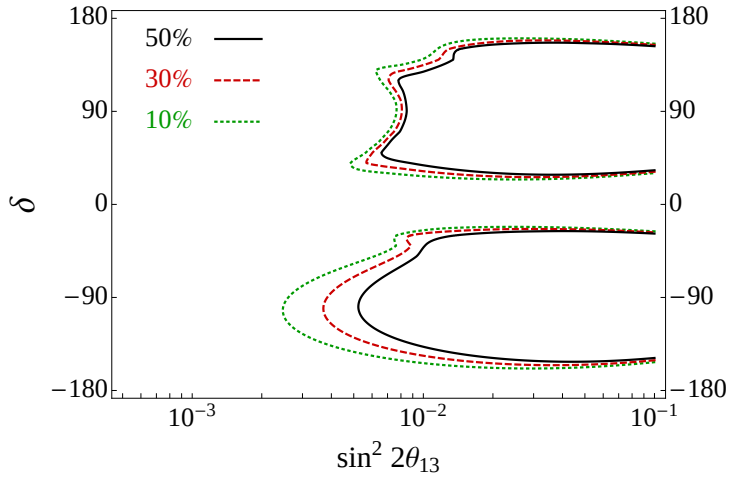

Figure 3.6: Effect of intrinsic beam backgrounds on the CP discovery potential for the LAr detector placed at Pyhäsalmi. The legend indicates the percentage of events coming from the beam contamination that cannot be rejected at the detector.

3.3.5 Running times

As mentioned in Sec. 3.1 the running times for the neutrino and anti-neutrino beams are asymmetric because of the different compositions of the beams, as well as to compensate the much smaller antineutrino cross section (see Fig. 3.2). The default configuration of 2 years running in neutrino mode and 8 years in anti-neutrino mode leads to an approximately equal number of neutrino and anti-neutrino events. This is crucial for the CP discovery potential of the facility, since CP violation would be observed through a different behaviour for neutrinos and antineutrinos.

It is worth to note that neutrinos and anti-neutrinos provide sensitivity to θ_{13} in different regions of the parameter space - neutrinos provide sensitivity in the region of positive δ, whereas antineutrino events are useful in the region of negative δ (the situation is precisely the opposite for an inverted hierarchy). This can be clearly seen in Fig. 3.7, where we show how the sensitivity to θ_{13} is affected by the running times for each polarity. Results are shown for several configurations of the neutrino and antineutrino running times, as indicated in the legend. Results are shown for the LAr detector placed at Pyhäsalmi, but qualitatively similar results are expected for the rest of baselines and detectors.

In Fig. 3.8 we show the effect of the neutrino and anti-neutrino running times on the CP discovery potential. The CP discovery potential is shown for several configurations of the neutrino and antineutrino running times, as indicated in the legend. It is clear that both ν and $\bar{\nu}$ events are necessary to optimise the CP discovery potential of the facility, whereas in the case where only neutrinos or only anti-neutrinos are considered the CP discovery potential is severly worsened.

Finally, from the comparison of Fig. 3.7 and Fig. 3.8 it can be seen that the asymmetric running times for ν and $\bar{\nu}$ mode are mostly useful in order to gain some sensitivity to θ_{13} in the

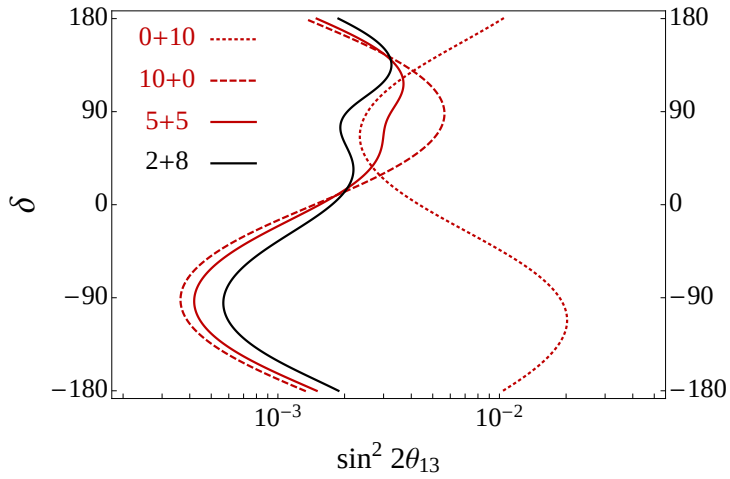

Figure 3.7: CP discovery potential for several configurations of the neutrino and anti-neutrino running times, for the LAr detector placed at Pyhäsalmi. The first and second numbers in the legend indicate the neutrino and antineutrino running times, respectively.

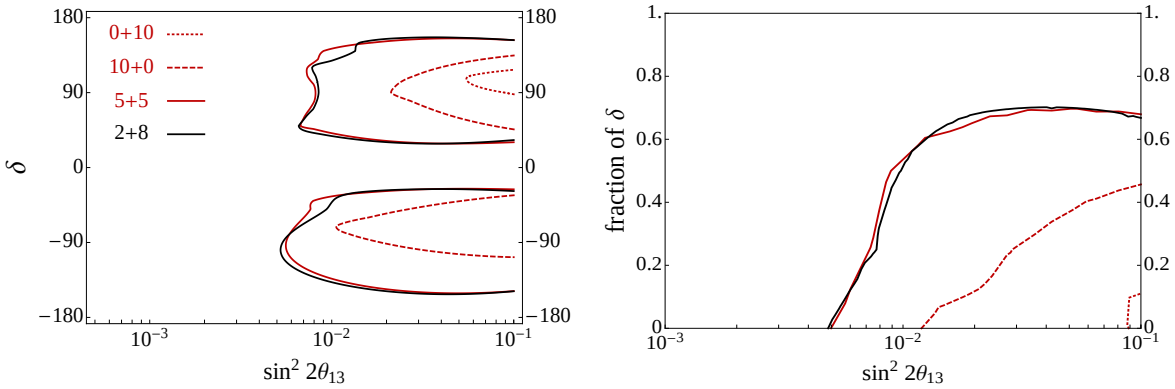

Figure 3.8: CP discovery potential for several configurations of the neutrino and anti-neutrino running times, for the LAr detector placed at Pyhäsalmi. Left panel shows the results in the δ-$\sin^2 2\theta_{13}$ plane, while for the right panel the results are shown as a function of $\sin^2 2\theta_{13}$ and the fraction of the δ parameter space for which CP violation can be discovered. The first and second numbers in the legend indicate the neutrino and antineutrino running times, respectively.

regions of positive δ (with respect to the symmetric configuration, $5+5$). However, the results for the CP discovery potential do not change much.

3.3.6 τ detection

It is possible that a liquid argon or liquid scintillator detector will be able to detect and identify tau leptons in addition to electrons and muons, making it possible to observe the ν_τ and $\bar{\nu}_\tau$ appearance channels. However, τ detection is experimentally very challenging and is therefore only of benefit if the additional events produce a significant improvement to the performance. Since the peak energy of the highest energy beam (for the 2285 km baseline) is only slightly above the ν_τ detection threshold of 3.5 GeV, only a very small amount of τ production is kinematically feasible. In Tab. 3.3, we show the total number of expected τ and $\bar{\tau}$ events at a 100 kton detector with perfect efficiency and energy resolution, placed at Pyhäsalmi, after one year of exposure per polarity. Results are shown for normal hierarchy and for $\theta_{23} = 45°$. For comparison, the number of ν_μ and $\bar{\nu}_\mu$ events at the detector is also shown. Even though the LAr and LENA detectors may have some detection efficiency for τ particles, this would certainly be below 50%. This means that the actual number of events would be even smaller than the numbers listed in the table. We have numerically checked that the effect of τ detection in the performance of the setup is negligible, even in the very optimistic case where a 50% efficiency is assumed.

N_{ν_μ}	$N_{\bar{\nu}_\mu}$	N_{ν_τ}	$N_{\bar{\nu}_\tau}$
8189	3442	753	346

Table 3.3: Total number of tau events for a 100 kton detector with perfect efficiency placed at Pyhäsalmi, after one year of exposure per polarity. Results are shown for normal hierarchy and for $\theta_{23} = 45°$. For comparison, the total number of ν_μ and $\bar{\nu}_\mu$ events are also shown.

3.4 Comparison for different baselines

The performance of any neutrino oscillation experiment depends strongly on the length of the baseline: it is a well-established fact that matter effects, as first discussed by Wolfenstein [60], alter oscillation probabilities relative to the vacuum case. The effect increases as the baseline and/or the density of the medium through which the neutrino is propagating is increased. Matter effects are also proportional to the neutrino energy (see Sec. 1.4.2). This phenomenon is exploited by long-baseline neutrino oscillation experiments in order to determine the neutrino mass hierarchy (normal or inverted). Matter effects are also needed in order to achieve a good CP discovery potential; otherwise, the hierarchy degeneracies will considerably worsen the results. Finally, the sensitivity to θ_{13} is the observable which is most robust against the presence of degeneracies and, consequently, matter effects are not so relevant in this case. Therefore, the dependence on the baseline for this observable is not so strong, whereas the specific details of each detector play a more important role.

Therefore it is vital that we assess and compare the performances of each of the LAGUNA baselines, listed in Tab. 3.1, in addition to each of the detectors. We present our results in terms of the observables defined in Sec. 3.2.3: (1) sensitivity to θ_{13}; (2) CP discovery potential; (3)

sensitivity to the mass hierarchy. The results will in general be presented as a function of $\sin^2 2\theta_{13}$ and the fraction of values of δ for which a certain observable can be measured, at a statistical significance of 3σ (1 d.o.f). In some cases, they may also be presented in the $\sin^2 2\theta_{13}$-δ plane, in order to illustrate some particular features of the figures. Since two of the LAGUNA baselines are very close in length (630 km and 665 km), their results are very similar. Therefore we have decided to present the results for the 665 km baseline only, since the ones corresponding to 630 km are virtually identical.

In addition, we note that the ability to reject NC background events in LENA is still in the process of being studied and is as yet unknown. As it was shown in Sec. 3.3.1, the level of the NC background plays a large role in the final sensitivities. Therefore in this section we show the results obtained in the scenario that the LENA detector can reject NC events down to 0.5% (as for LAr), and one in which the NC background takes a higher value of 5% (as for WC).

3.4.1 Sensitivity to θ_{13}

In Fig. 3.9, the results for the sensitivity to θ_{13} are presented for the six baselines and for the four detectors under consideration. As already mentioned, this is the observable which is least affected by the presence of degeneracies, and therefore the baseline dependence is not very relevant. It can be clearly seen, though, that the results obtained when the detector is placed at Fréjus ($L = 130$ km) are considerably worse than for the rest of the baselines. This is mainly because the flux for the Fréjus baseline is roughly an order of magnitude below those for the rest of the baselines, as it was already commented in Sec. 3.1.

An interesting feature can be observed from the comparison of the upper plots in Fig. 3.9, which correspond to the LAr (left) and LENA (right) detectors. Notice from Tab. 3.2 that the energy range for the LENA detector goes up to 7 GeV, whereas for the LAr detector it reaches 10 GeV. However, the difference in performance for both detectors is not significant. It is also important to notice that, even though the mass for the LAr detector is larger by a factor of two, the effect due to its larger mass is unimportant. This is due to the extremely good energy resolution of LENA in the lower energy part of the spectrum, which makes its performance comparable to that of the LAr detector, even though its mass is smaller by a factor of two. This is something which will also play an important role in the CP discovery potential of the facilities, as will be shown in the next subsection.

The performance of the LENA detector when exposed to this kind of beam is, therefore, remarkable. However, its ability to reject NC events is yet not clearly understood. This is crucial in order to determine its ultimate performance. The impact of the NC background for the LENA detector can be seen from the comparison between the two right panels in Fig. 3.9. Both panels correspond to the performance of the LENA detector, but in the lower panel the NC background has been increased by a factor of 10 in the simulations. As a result, the sensitivity to θ_{13} is worsened roughly by a factor of 3.

In general, the longer the baseline, the better the sensitivity. However, it can be seen that this does not hold for the longest baseline (2285 km), especially for the LAr detector and LENA detector with a low NC background. This indicates that these two detectors perform sufficiently well and that they are statistics-limited. On the other hand, the flux at the detector scales with the distance from the source as L^{-2}. Since we have considered the same number of PoT for all possible locations, there is a limiting value of L for which the gain in sensitivity due to larger matter effects does not compensate for the flux loss. A possibility to overcome this could be to increase in the number of PoT, for instance.

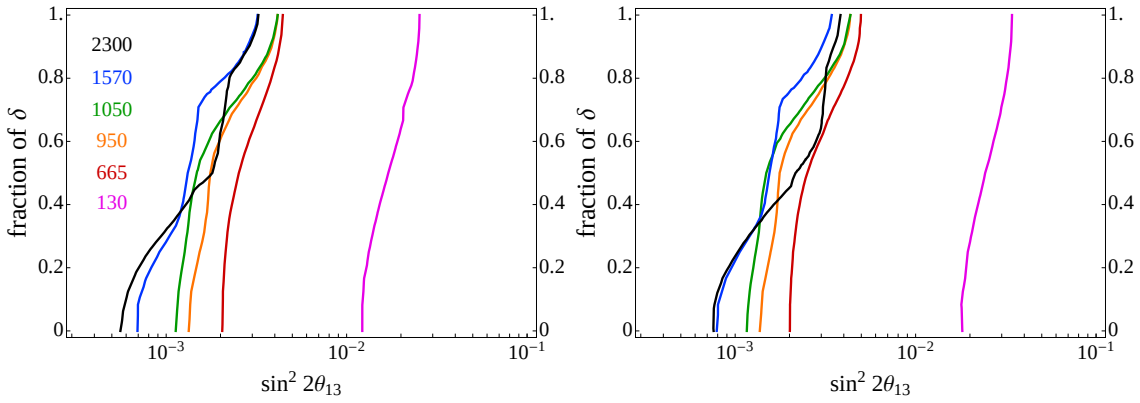

(a) GLACIER (b) LENA (0.5% NC)

(c) Water Čerenkov (d) LENA (5% NC)

Figure 3.9: Sensitivity to θ_{13} as a function of $\sin^2 2\theta_{13}$ and the fraction of possible values of δ for which the $\theta_{13} = 0$ hypothesis can be ruled out at 3σ (1 d.o.f.). Results are shown for the six baselines under study and for the four detectors under consideration.

3.4.2 CP discovery potential

In Fig. 3.10, the results for the CP discovery potential are presented. In can be seen that very long baselines always yield the best results for this observable. This is closely related to the presence of stronger matter effects for the longer baselines, although the same reasoning as explained in Sec. 3.4.1 applies to the 2285 km baseline, this time for all the detectors. In the region where $\delta \sim +90°$, the sign (hierarchy) degeneracies move to CP conserving values of δ and therefore the CP discovery potential of the facility is worsened. This can be avoided if the facility is also able to measure the sign and resolve these degeneracies. As a consequence, larger baselines are generally better for this observable. The situation is critical for the shortest baseline of $L = 130$ Km (CERN to Fréjus). In order to maximize the CP discovery potential of a certain experiment, one should try to tune the L/E ratio to the first oscillation peak. This maximizes the Y term in the probability (see Eq. (B.1) in App. B), which contains the δ-dependence, and at the same time the statistics at the detector are increased.

A particular feature is observed in the plots, precisely regarding the baseline dependence. Notice that, in principle, better results are obtained for higher energy setups. However, the results for the Pyhäsalmi baseline are outperformed by those obtained at the 1570 km baseline, regardless of the particular detector technology. In order to understand this, several things have to be taken into account simultaneously: (1) the cross section in the non-QE range increases linearly with the energy, so higher energies imply a larger number of events at the detector; (2) larger energies imply also larger matter effects, which can mimic CP violation effects and diminish the actual CP discovery potential of the facility; (3) the flux at the detector scales with the distance from the source as L^{-2}. In our case, it seems that higher neutrino energies and larger baselines are preferred; however, for the Pyhäsalmi baseline the increase in the cross section with the neutrino energy cannot compensate neither the flux loss nor the (too large) matter effects, and the CP discovery potential starts to be worsened.

As it was already mentioned in Sec. 3.3.2, QE events are very important for CP discovery potential whereas high energy events do not play a significant role for this observable. This can be seen from the comparison between the upper panels in Fig. 3.10, which correspond to the LAr (left) and LENA (right) detectors. Notice that the energy range for the LENA detector goes up to 7 GeV, whereas for the LAr detector it reaches 10 GeV. However, the difference in the CP discovery potential that can be reached with both detectors is not significant. It is also important to notice that, even though the mass for the LAr detector is larger by a factor of two, the effect due to its larger mass is not very relevant. This is due to the extremely good energy resolution of LENA in the lower energy part of the spectrum, which makes its performance comparable to that of the LAr detector, even though its mass is smaller by a factor of two.

Again in this case, we show the impact of the NC background for the LENA detector in the two right panels in Fig. 3.10. As a result of the higher NC background, in the lower right panel the CP discovery potential is considerably worse. Not only is the limiting value of $\sin^2 2\theta_{13}$ reduced by around an order of magnitude (as it was the case for the sensitivity to θ_{13}), but also the fraction of values of δ for which CP violation can be observed has been considerably reduced. This effect is particularly relevant for the detector placed at Pyhäsalmi - since it is mainly limited by statistics, its performance is considerably reduced when larger backgrounds are included in the simulations.

3.4.3 Sensitivity to the mass hierarchy

Finally, in Fig. 3.11, we present the results for the sensitivity to the mass hierarchy. A normal hierarchy has been assumed in all cases. We have checked that the results for an inverted hierarchy are very similar to these, but with the interchange $\delta \to -\delta$. Consequently, the fraction of values of

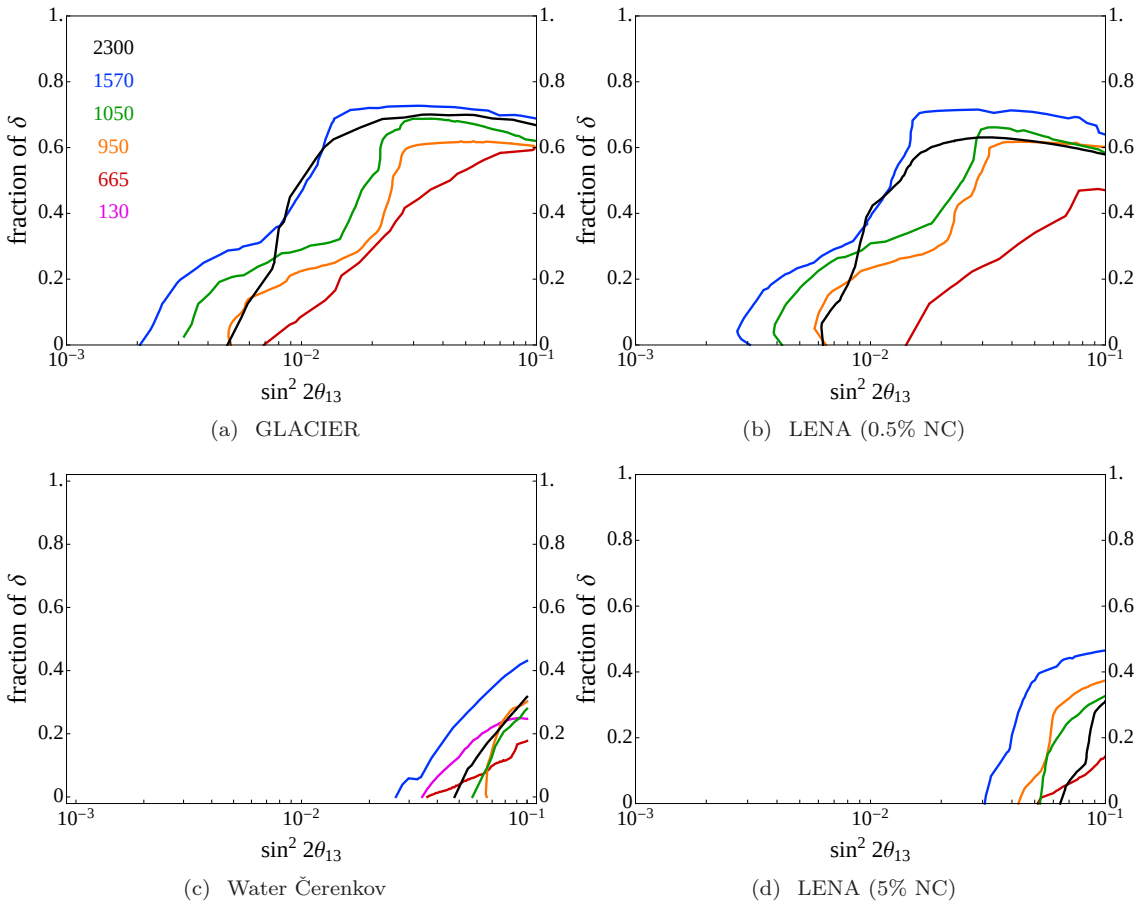

(a) GLACIER (b) LENA (0.5% NC)

(c) Water Čerenkov (d) LENA (5% NC)

Figure 3.10: CP discovery potential as a function of $\sin^2 2\theta_{13}$ and the fraction of possible values of δ for which the CP conservation hypothesis ($\delta = 0$ or π) can be ruled out at 3σ (1 d.o.f.).

δ for which the wrong hierarchy can be ruled out remains unaffected when an inverted hierarchy is assumed; therefore these results will not be presented here.

Unlike the other two observables, the choice of baseline is critical in this case in determining the performance of the facility. Thus it is always true that the longer the baseline, the better the performance - it can clearly be seen from the figure that the best results are obtained when the detector is placed at the Pyhäsalmi baseline, regardless of the detector technology. On the other hand, the results for the CERN-Boulby and CERN-Sierozsowice baselines are remarkably similar, since their baselines only differ in 100 km. The worst results, in turn, are obtained for the shorter baselines: no sensitivity at all is obtained if the detector is placed at Fréjus ($L = 130$ km), whereas in the case of Canfranc/Umbria ($L \sim 665$ km) some sensitivity can be achieved for some values of δ.

Again, the performances of the LAr and LENA detector (in the absence of NC backgrounds) are very similar, as it was in the case of the sensitivity to θ_{13} and for the CP discovery potential. However, around a factor of 3 is lost when the NC background is increased from 0.5% to 5% for the LENA detector.

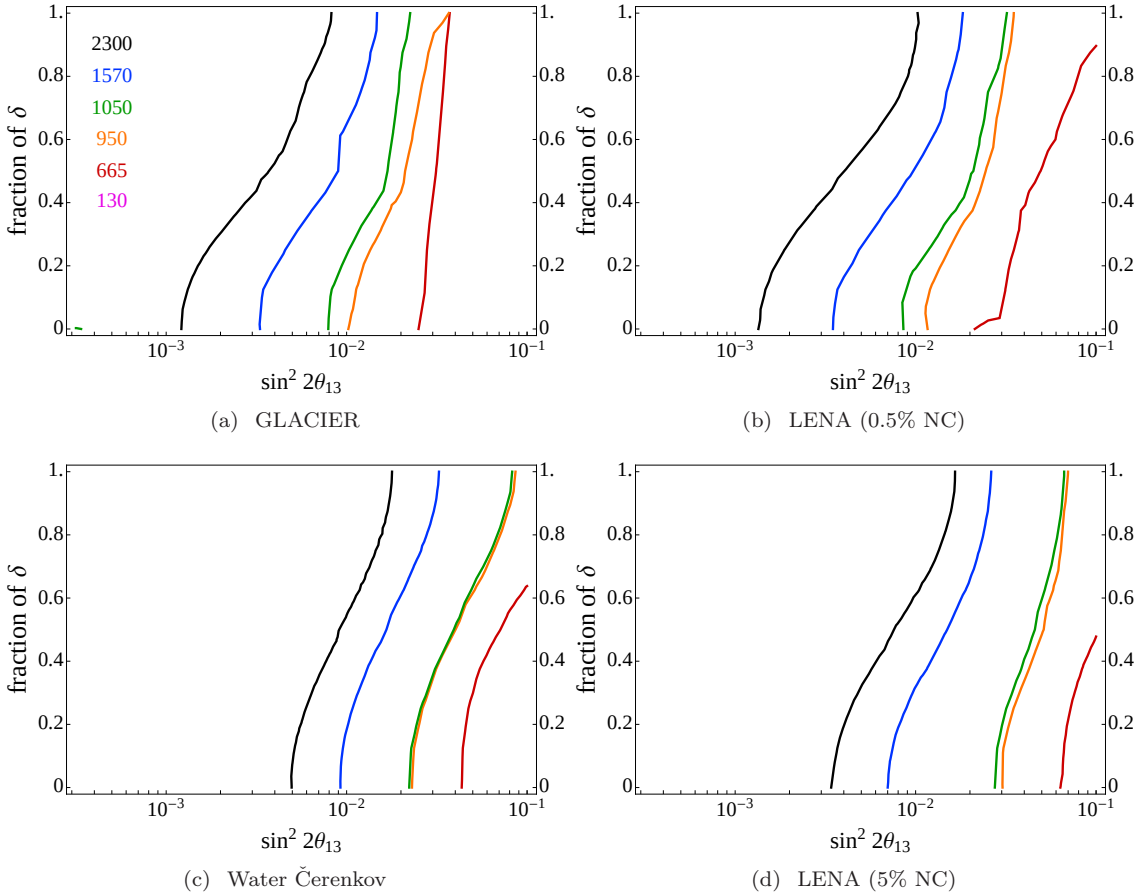

(a) GLACIER (b) LENA (0.5% NC)

(c) Water Čerenkov (d) LENA (5% NC)

Figure 3.11: Sensitivity to the mass hierarchy as a function of $\sin^2 2\theta_{13}$ and the fraction of possible values of δ for which the wrong hierarchy can be ruled out at 3σ (1 d.o.f.). A normal hierarchy has been assumed.

4

The double baseline β-beam

In this chapter, we present the results of Refs. [21] and [22], where we studied the performance of two different two-baseline high-γ β-beam setups. We face the same physics case considered for the IDS-NF, that is, a very small value for θ_{13} out of reach for the present and forthcoming generation of neutrino oscillation experiments (*i.e.*, $\theta_{13} \leq 3^\circ$). The two setups proposed here are the natural conclusion of a series of theoretical, experimental and accelerator achievements:

- In Ref. [271] the idea of accelerating radioactive ions and store them so as to produce intense $\nu_e(\bar{\nu}_e)$ beams was advanced. In the original proposal, ^{6}He/^{18}Ne ions were boosted at $\gamma \sim 100$ using existing infrastructures at CERN, producing $\nu_e(\bar{\nu}_e)$ beams aimed at a 1 Mton WC detector to be located in a newly excavated cavern at the Fréjus underground laboratory, $L =$ 130 Km down the source. The physics reach of this setup was studied in Ref. [174, 272, 273].

- In Refs. [274, 275] it was proposed to accelerate the same two ions, ^{6}He and ^{18}Ne, at a much higher γ ($\gamma = 350$ and 580, respectively), aiming again at a 1 Mton WC detector to be located at a newly excavated cavern at the Canfranc underground laboratory, $L = 650$ Km from the source. Such a high Lorentz boost factor could only be attained at CERN using new infrastructures. Alternatively, the TeVatron could be used for the last acceleration stage (see, *e.g.*, Ref. [276]). This setup greatly outperforms the "low"-γ one discussed above and could compete with NF–based setups in the sensitivity to CP violation.

- In Ref. [277,278], the "ionization cooling" technique to produce intense ^{8}Li and ^{8}B beams was proposed (the latter being out of reach with standard ISOL-type targets). The feasibility of this method will be studied in full detail in the framework of the EURO-ν Design Study [197].

- In Ref. [176], some of the authors of this paper proposed the use of a "cocktail" of ^{8}Li/^{8}B and ^{6}He/^{18}Ne β-beams at $\gamma = 100$ (the maximum that can be achieved with existing CERN infrastructures) illuminating a 1 Mton WC detector located at $L = 650$ Km, so as to solve some of the parametric degeneracy from which the measurement of (θ_{13}, δ) is afflicted. This setup is only useful in the case of large θ_{13}, due to its statistical limitations.

- In Refs. [279,280], the possibility of using a high-γ ^{6}He/^{18}Ne β-beam illuminating a (MINOS-like) 50 Kton magnetized iron detector located at $L = 732$ Km down the source was explored. The existing cavern at the Gran Sasso underground laboratory could be used for such a compact detector. This setup is also statistically limited, though.

- Eventually, in Refs. [184, 185] a $\gamma = 350$ ^{8}Li/^{8}B β-beam illuminating a 50 Kton magnetized iron detector (INO [281,282]) located at $L = 7100$ Km down the source was proposed, to take advantage of the resonant matter effects so as to measure $\mathrm{sgn}(\Delta m^2_{31})$ for $\sin^2 2\theta_{13} \geq 10^{-3}$.

The main difference of using ^{8}Li/^{8}B instead of ^{6}He/^{18}Ne ions is that the end-point energy of the ^{8}Li/ ^{8}B β-decays is $E_0 \sim 13$ MeV (to be compared with $E_0 \sim 3.5$ MeV for ^{6}He/^{18}Ne). With a Lorentz boost factor of $\gamma = 350$, a (relatively) high mean neutrino energy in the laboratory frame, $E_\nu \sim 6$ GeV is achievable. At these neutrino energies $P_{e\mu}$ picks up near-resonant matter effects and becomes very large and a very good sensitivity to the mass hierarchy is foreseen [184,185,283]. Both of the setups studied here take advantage of this fact. A baseline optimization study [284] showed that indeed the magic baseline is the best place to measure the mass hierarchy and θ_{13} if a β-beam fueled with ^{8}B and ^{8}Li ions is used. A further consequence of having an energetic neutrino flux is that we can safely use dense detectors with a good muon identification efficiency, as an alternative to the WC technology.

However, this baseline is also very close to the "magic baseline" [168,179], at which matter effects cancel the dependence of the oscillation probability on δ. As a consequence, the sensitivity to δ is lost and another baseline, appropriately chosen in order to match the first oscillation peak, is needed to gain sensitivity to δ. In setup A for ^{8}Li /^{8}B accelerated at $\gamma = 350$ the value for this baseline turns out to be $L = 2000$ Km. For setup B ^{6}He /^{18}Ne are used instead to aim at the shorter baseline, accelerated at $\gamma = 350$ too. In this case, the baseline which matches the first oscillation peak is much shorter, $L = 650$ Km. Setup B takes advantage, on the one hand, of the strong sensitivity that can be achieved with a ^{6}He /^{18}Ne β-beam to CP violation while, on the other, the ^{8}Li /^{8}B β-beam takes advantage of the resonance at the magic baseline, thus providing a good sensitivity to the mass hierarchy.

This chaper is organized as follows. In Sec. 4.1 the β-beam is introduced. In Secs. 4.2 and 4.3 we describe the technical details of both setups. Sec. 4.2 is dedicated to the technical details regarding the acceleration of the ions, mainly: the choice of β-emitters, γ, the fluxes and cross sections and the storage ring design. The atmospheric background is also discussed here, since its relevance will be determined by the energy of the beam and the suppression factor in the decay ring. Sec. 4.3 is dedicated, on the other hand, to discuss the relevant aspects for the technology and location of the detectors: the choice of the two baselines, the detector details, the matter resonance at 7000 km, the efficiencies, systematic errors and the rest of backgrounds. Finally, in Sec. 4.4 we present the results for both setups, including a comparison with other high-γ β-beam facilities. For technical details related to the production, acceleration and storage of the ions we refer the interested reader to App. A.

4.1 The β-beam concept

The β-beam concept was first introduced in [271]. It involves producing a huge number of β-unstable ions, accelerating them to some reference energy, and allowing them to decay in the straight section of a storage ring aiming at a far detector, resulting in a very intense and pure ν_e or $\bar{\nu}_e$ beam. Golden transitions, $\nu_e \to \nu_\mu$ and $\bar{\nu}_e \to \bar{\nu}_\mu$, can then be measured through muon observation at the detector.

It shares with the NF two main advantages with respect to conventional beams (where neutrinos are obtained via pion decay): a) the neutrino flux is pure (for a β-beam , only ν_e or $\bar{\nu}_e$ neutrinos are present in the flux), thus decreasing the beam-induced background, and b) the neutrino spectrum can be exactly computed, thus strongly reducing flux systematics.

Three main variables determine the properties of the facility: the type of ion used, and in particular the end-point kinetic energy of the electron in the center-of-mass frame for the β decay, E_0; the relativistic Lorentz boost factor γ (energy divided by mass) of the ion; and the baseline, L.

The unpolarized[1] neutrino flux per solid angle in a detector located at distance L from the source, aligned with the boost direction of the parent ion is [274]:

$$\left.\frac{d\Phi}{dSdy}\right|_{\theta\simeq 0} \simeq \frac{N_\beta}{\pi L^2}\frac{\gamma^2}{g(y_e)} y^2(1-y)\sqrt{(1-y)^2-y_e^2}, \tag{4.1}$$

with $0 \leq y = \frac{E}{2\gamma E_0} \leq 1 - y_e$, $y_e = m_e/E_0$ and

$$g(y_e) \equiv \frac{1}{60}\left\{\sqrt{1-y_e^2}(2-9y_e^2-8y_e^4) + 15y_e^4 \log\left[\frac{y_e}{1-\sqrt{1-y_e^2}}\right]\right\}. \tag{4.2}$$

In this equation, m_e is the electron mass, E the energy of the final state neutrino in the laboratory frame and N_β the total number of ion decays per year. The average neutrino energy in the laboratory frame is $\langle E\rangle = \gamma E_0$. In Fig. 4.1, the β-beam fluxes obtained at 100 km from the source are shown, as a function of the neutrino energy, for the four ion candidates. As it can be seen from the figure, due to their different end-point energies the neutrinos produced from ^{8}Li and ^{8}B decays are peaked at higher energies by a factor of 4, roughly. On the other hand, the spectrum is much broader for ^{8}Li and ^{8}B decays than in the ^{6}He and ^{18}Ne case, where all neutrinos are produced more or less with the same energy.

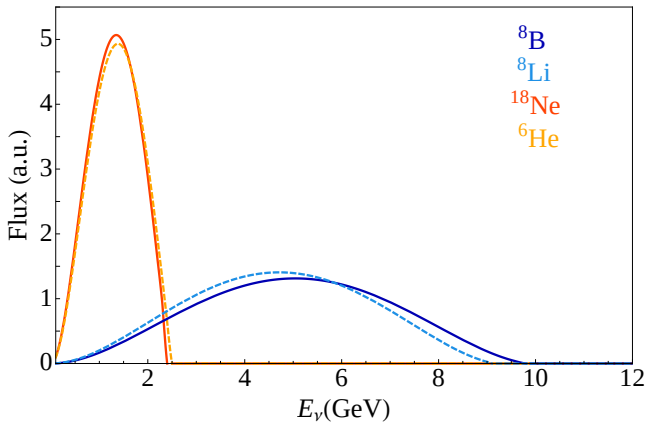

Figure 4.1: β-beam fluxes (in arbitrary units) corresponding to each of the four ion candidates boosted to $\gamma = 350$ as a function of the neutrino energy, measured at 100 km from the source.

The key parameter in the optimization of the β-beam flux is the relativistic γ factor. Notice that, for a fixed number of decaying ions and a fixed baseline, the number of CC muon events in the detector increases with γ and linearly decreases with E_0. This can be derived from Eq. (4.1) as follows: in the hypothesis of linear dependence of the total neutrino-nucleon CC cross-section on the neutrino energy[2] and for L/E tuned to the n-th $\nu_e \to \nu_\mu$ oscillation peak, the number of events expected at the detector is [271]:

[1]The possibility of using a neutrino beam coming from a polarized source has been studied in the context of a NF, but not for a β-beam . The flux for neutrinos produced from a polarized source has extra terms which could help to increase the statistical significance of a CP violating signal in the case of a NF [285, 286]. It would be interesting to study that option also in the β-beam scenario. In this case, polarization would only be possible for high-Q β-beams , since ^{8}Li /^{8}B have spin $S = 2$ whereas ^{6}He /^{18}Ne have $S = 0$.

[2]Notice, however, that this is not suitable for neutrino energies below 1 GeV, where the cross-section energy dependence is E^k with $k \geq 1$. This is, on the other hand, the typical range of energies considered for low-γ β-beams .

$$N_{events} \propto N_\beta \left(\frac{\Delta m^2}{2n-1}\right)^2 \frac{\gamma}{E_0}\,. \tag{4.3}$$

According to Eq. (4.3), it seems that ions with low E_0 should in principle be preferred. The choice of the isotope is, however, a compromise between production yield, E_0, and the half-life of the ion, $T_{1/2}$: isotopes should be sufficiently long-lived to avoid strong losses in the acceleration phase, but must decay fast enough to generate a neutrino beam of sufficient flux. A fourth relevant parameter is the atomic number, Z: assuming a limited space charge capacity of the acceleration chain, low-Z ions can be stored in larger number than high-Z ions (thus affecting N_β). The following isotopes have been identified as good candidates: ^{6}He for $\bar{\nu}_e$ production and ^{18}Ne to produce ν_e, both of them with $E_0 \sim \mathcal{O}(\text{MeV})$. Another pair of ions with larger E_0 have been also considered: ^{8}Li and ^{8}B. Notice that, at the same γ/L, the neutrino flux produced from high-Q ions is typically three to four times more energetic than those produced in ^{6}He/^{18}Ne decays. This can be very helpful in order to determine the mass hierarchy through matter effects. However, in order to match the oscillation peak, larger baselines are needed as the energy of the beam increases. This implies a loss in the flux, which is inversely proportional to L^2. A detailed discussion on the properties of the β-emitters will be performed in Sec. 4.2.1.

4.2 The accelerator design

In this section, we will discuss in detail the different features related to accelerator requirements. These include the choice of the ions and an introduction to their main characteristics (Sec. 4.2.1), the γ factor (Sec. 4.2.2), the achievable fluxes (Sec. 4.2.3) and possible alternatives for the storage ring original design (Sec. 4.2.4). Finally, the atmospheric background, which can be reduced with an appropriate bunching of the ions in the storage ring, is also discussed in Sec. 4.2.5.

4.2.1 Choice of $\beta^\pm$-emitters

Three parameters that are crucial to determine the choice of the optimal β-emitters are E_0, the ion half-life $T_{1/2}$ and Z. First of all, from Eq. (4.3) it can be seen that the lower the end-point energy E_0, the larger the statistics. Secondly, the ion half-life $T_{1/2}$ must be long enough to accelerate the ions to the desired energy and short enough to allow a large number of them to decay in the storage ring such as to produce an intense neutrino beam. Eventually, assuming a limited space charge capacity of the storage ring, low-Z isotopes can be stored in larger number than high-Z isotopes [287].

It is well known (see for instance [284] for a discussion) that for two different isotopes producing a beam, if one demands the same spectral shape of the neutrino flux, *i.e.* the same peak energy and normalization, then the following relations hold:

$$\frac{N_\beta^{(1)}}{N_\beta^{(2)}} \simeq \left(\frac{E_0^{(1)}}{E_0^{(2)}}\right)^2, \quad \frac{\gamma^{(1)}}{\gamma^{(2)}} \simeq \frac{E_0^{(2)}}{E_0^{(1)}} \qquad \Rightarrow \qquad \frac{N_\beta^{(1)}}{N_\beta^{(2)}} \simeq \left(\frac{\gamma^{(2)}}{\gamma^{(1)}}\right)^2,$$

where $E_0^{(i)}$ is the end-point energy of the ion-decay, and where the effect of the electron mass has been neglected. Clearly, the higher the end-point energy of the β-decay of an ion, the lower the γ needed to reach a given neutrino energy in the lab frame. Recall that the maximum energy of the neutrino in the lab frame is given by $E_\nu^{max} = 2\gamma E_0$, where the electron mass has been neglected. Therefore, it is easier to reach higher neutrino energies using ions with higher end-point energy.

Element	A/Z	$T_{1/2}$ (s)	E_0 (MeV)	Decay Fraction
^{18}Ne	1.8	1.67	3.41	92.1%
			2.37	7.7%
			1.71	0.2%
^{8}B	1.6	0.77	13.92	100%
^{6}He	3.0	0.81	3.51	100%
^{8}Li	2.7	0.83	12.96	100%

Table 4.1: A/Z, half-life and end-point energies for two β^+-emitters (^{18}Ne and ^{8}B) and two β^--emitters (^{6}He and ^{8}Li). All different β-decay channels for ^{18}Ne are presented [288].

At the same time, however, to have the same number of events in the far detector for two sets of ions with different E_0 boosted at the same γ, we need larger number of useful ion decays for source ions with higher E_0. For our candidate source ions we can see that the following conditions hold

$$N_\beta^{B+Li} \simeq 12 \cdot N_\beta^{Ne+He}\,, \quad \gamma^{Ne+He} \simeq 3.5 \cdot \gamma^{B+Li},$$

in order to obtain the same neutrino flux spectrum.

Experimental challenges on both N_β and γ are in fact intimately related to a large extent. The boost directly depends on the amount of acceleration possible. The number of useful ion decays, on the other hand, is affected by losses during the acceleration process and hence impacts the amount of acceleration possible. Another important way N_β and γ get related is through the design of the storage ring. Higher boost factors of the source ions make them harder to bend. Thus, for the same magnetic field strength, a larger curved section of the storage ring is required to bend ions boosted at high γ than at low γ. Unless the straight sections are increased proportionally, the fraction of stored ions that decays in the straight sections of the ring (the so-called "livetime" $\ell \equiv L_s/L_r$) decreases. This will be discussed in detail in Sec. 4.3.

In Tab. 4.1 we remind the relevant parameters for four ions: ^{18}Ne and ^{6}He, ^{8}Li and ^{8}B. As it was stressed in the literature (starting with Ref. [271]), ^{6}He has the right half-life to be accelerated and stored such as to produce an intense $\bar{\nu}_e$ beam using existing CERN infrastructures. According to the prescriptions given above, ^{18}Ne has been identified as the best candidate as β^+-emitter, although its half-life is twice that of ^{6}He. Other ions were originally discarded for different reasons: for example, ^{33}Ar is too short-lived to be accelerated to the desired energy ($T_{1/2} = 0.17$ s). As it can be seen in Tab. 4.1, ^{8}Li and ^{8}B are good alternatives to ^{6}He and ^{18}Ne as β^-- and β^+-emitters, respectively. ^{8}Li has similar half-life, Z and A/Z to ^{6}He, thus sharing the key characteristics needed for the bunch manipulation. ^{8}B has a lifetime similar to that of ^{8}Li and ^{6}He. Its A/Z is similar to that of ^{18}Ne, instead, although its Z is much smaller (which could in principle allow to store a larger amount of ions in the PS and in the SPS). This ion, however, is difficult to produce with standard ISOLDE techniques [289] (it reacts with many elements typically used in ISOL targets and ion sources and it is therefore barely released). For this reason it was originally discarded as a possible β^+-emitter.

A detailed study of the attainable production rate of ^{8}Li and ^{8}B using ISOLDE techniques is lacking. Intense fluxes of both ions could be in principle produced using the "ionization cooling"

technique proposed in Ref. [277], that is currently being studied in the framework of the EURO-ν Design Study [197]. It is not difficult to produce an intense ^{8}Li flux: using a thin Ta foil ISOL target, it is possible to produce 6×10^8 ^{8}Li ions per μC, to be compared with 6×10^6 ^{6}He ions per μC [290]. The case of ^{8}B is different, though: this ion was previously discarded as a β^+-emitter since it is extremely difficult to produce at a sufficient rate with ISOLDE techniques. However, using the "ionization cooling" technique, sustained ^{8}Li and ^{8}B production is supposed to be at reach through the reactions $^7\mathrm{Li} + \mathrm{D} \to {}^8\mathrm{Li} + \mathrm{p}$ and $^6\mathrm{Li} + {}^3\mathrm{He} \to {}^8\mathrm{B} + \mathrm{n}$ [289]. We will assume in the following that ^{8}Li/^{8}B ion fluxes can be produced at least as efficiently as ^{6}He/^{18}Ne ones. In Sec. 4.2.3 the different fluxes under consideration will be presented in more detail.

4.2.2 Choice of γ

In principle, larger γ values are preferred mainly due to two reasons: (1) according to Eq. (4.3), larger boost factors provide larger statistics at the detector; (2) the neutrino energy is proportional to γ, and the cross section at the detector increases with the neutrino energy.

Four classes of β-beam setups have been considered so far: $\gamma \simeq 10$ ("very low" γ) [291,292], $\gamma \sim 100$ ("low" γ), with a typical baseline of $L \sim \mathcal{O}(100)$ Km for ^{18}Ne and ^{6}He [174,265,272–274] or $L \sim \mathcal{O}(700)$ for ^{8}B and ^{8}Li [176,278]; $\gamma \sim 300$ ("high" γ), with $L \sim \mathcal{O}(700)$ Km [269,274, 275,279,280] for ^{18}Ne and ^{6}He or $L \sim \mathcal{O}(7000)$ for ^{8}B and ^{8}Li [184,185,283]; and $\gamma \geq 1000$ (very "high" γ), with baselines of several thousands kilometers, comparable with those suggested for the NF [269,274,293].

The three higher γ ranges are related to different CERN-based facilities: the SPS, with $\gamma \leq 250$; the SPS+, with $\gamma \leq 600$; and the LHC, with $\gamma \geq 1000$. The SPS+ is not built yet: it would be a new synchrotron that would use fast cycling superconducting magnets, located in the SPS tunnel. Such a facility should be able to accelerate particles up to 1 TeV. Injecting protons into the LHC at 1 TeV strongly reduces the dynamic effects of persistent currents and stabilizes the operation of the collider. This would ease operation of the LHC and permit to increase luminosity up to 10^{35} cm^{-2}s^{-1} and, if needed, prepare it to double the operating energy ("DLHC" phase) [294]. Using the SPS+ as a final stage of acceleration for a β-beam is not in conflict with LHC operations, since the SPS+ operates as injector only for a small fraction of its duty time (in the LHC filling phase).

After this work was completed the construction of the SPS+ was cancelled, though. A similar facility would be mandatory in order to accelerate ions to high-γ values such as the ones that are being considered here. Therefore, in the following we will assume that the SPS+ (or a similar machine) can be built, and present our results accordingly. Indeed, the SPS+ as the final booster of the β-beam is not the only possibility that can be envisaged to reach the multi-GeV regime. After injection of the ions from the SPS to the LHC, a mini-ramp of the LHC itself would bring the ions at $\gamma = 350$. Differently from the previous case, this option would however require allocation of a significant fraction of the LHC duty cycle for neutrino physics, and it could be in conflict with ordinary collider operations. A third option could be to use the TeVatron at FermiLab as the last acceleration stage (see, for example, Ref. [276]).

4.2.3 Fluxes and cross sections

The original β-beam proposals assumed useful fluxes of 1.1×10^{18} and 2.9×10^{18} decays per year for ^{18}Ne and ^{6}He respectively when accelerated to $\gamma = 100$. These fluxes have been considered as "goal" and are commonly assumed in the literature [272,274,275]. Similar "goal" numbers regarding ^{8}B and ^{8}Li are lacking. However, preliminary studies on the production rates of ^{8}B and ^{8}Li show

that they are both produced more easily than ^{18}Ne and ^{6}He respectively. This is particularly true for neutrinos produced from the decay of ^{8}B since the production of ^{18}Ne is very challenging.

Lacking a detailed study of the achievable ^{8}Li and ^{8}B fluxes, for setup A we consider three possible values for the β-beam flux[3]:

- "Nominal flux"
  In this case, 2×10^{18} total decays per year per baseline for both ^{8}Li and ^{8}B are considered. These fluxes are close to the "goal fluxes", *i.e.* 2.9×10^{18} and 1.1×10^{18} decays per year for ^{6}He and ^{18}Ne.
- "Medium flux"
  In this case, fluxes of 5×10^{18} total decays per year per baseline for both ions are assumed.
- "Ultimate flux"
  For this most optimistic scenario, fluxes of 10×10^{18} total decays per year per baseline for both ions are considered.

For setup B, only the ultimate flux is considered, for all ions. Please notice that the useful number of ion decays is obtained by multiplying the total number of decays by the storage ring *livetime*, and therefore is expected to be roughly around a 30%. For instance, it should be noticed that for the original ring design proposed in Ref. [271], with a livetime $l = 0.36$, the goal fluxes of 2.9×10^{18} and 1.1×10^{18} useful decays per year actually correspond to $\sim 8 \times 10^{18}$ and $\sim 3 \times 10^{18}$ total decays per year for ^{6}He and ^{18}Ne , respectively[4]. The livetime, though, depends on the exact design of the storage ring, and needs to be optimized for the particular ion species and the γ at which they are accelerated. This will be discussed in detail in Sec. **??**.

We remind that an intense ^{8}Li (but not ^{8}B) beam could be produced using well-studied ISOLDE techniques. An interesting option could be to start a first phase with an intense $\bar{\nu}_e$ flux aiming at the two detectors for a five year period, whilst building the facility needed to produce the ^{8}B beam that would be used in the second phase.

As it is shown in App. A, no specific drawback in the acceleration and storage phase for using Li/B instead of the standard He/Ne ions is expected. For this reason, we assume that the "nominal flux" could be safely used at this setup, if shown to be achievable for standard setups. An increase of the ion flux up to the "ultimate flux" is believed to be possible (see Ref. [295]). Notice, moreover, that due to the higher energy of this setup compared to standard He/Ne options, the atmospheric neutrino background is expected to be significantly lower and a larger number of bunches can be thus injected into the storage ring, as it will be explained at the end of this section.

We have considered identical fluxes for ^{8}Li and ^{8}B ions, in the absence of a clear indication of a significant asymmetry in the ion production stage (differently from the He/Ne case, see Appendix). Notice that for setup B, where the four ion species are considered, only the "ultimate flux" will be considered, for the four ions. Finally, the total running time which has been considered for both setups is 10 years. This is translated into 5 years of data taking per ion circulating in the storage ring for setup A, whereas it needs to be reduced to 2.5 years in setup B, since four different ions will circulate in the ring.

The ν and $\bar{\nu}$ cross-sections on iron have been taken from Ref. [296]. Notice that, for both of the setups proposed here, most of the neutrinos have multi-GeV energies, and therefore the νN

[3] Notice that we consider identical fluxes for the two detectors. As it will be explained in Sec. 4.3, this does not mean that the number of ions circulating in the storage ring must be twice the number considered for single detector setups.

[4] At the time when this work was published, it was uncertain if these fluxes could be achievable or not. Recent studies [289] seem to indicate that these values can be in principle achieved at least for ^{6}He and ^{18}Ne , and quite probably for ^{8}Li too. The case of ^{8}B , though, is more complicated and needs further research.

cross-sections are dominated by the deep inelastic part. Thus, the details of the different cross-sections present in the literature are not as relevant as it was in the case for lower energies neutrino beams (see, for instance, Ref. [297] for a recent discussion on how the present uncertainties in the neutrino-nucleon cross-sections can have serious impact on the performance of low-energy neutrino oscillation facilities).

4.2.4 The Storage Ring

Two geometries for the β-beam storage ring have been considered in the literature so far: the racetrack geometry and the triangle geometry. Both geometries have been considered also in the framework of the NF studies, see Ref. [298]. The original storage ring design, proposed by Piero Zucchelli back in 2002 [271] was conceived to store ^{6}He and ^{18}Ne ions boosted at $\gamma = 100$ (the maximum boost achievable using the PS and the SPS at CERN being $\gamma = 150$ for ^{6}He and $\gamma = 250$ for ^{18}Ne, respectively). The main parameters for this ring, which will be referred to as "Ring 1" hereafter, are summarized in the first column in Tab. 4.2. This ring was designed to bend ions boosted to $\gamma = 100$. However, more powerful magnets are needed in order to bend ions accelerated to $\gamma = 350$. In the same table some possible alternative designs, which include 8.3 T magnets, are also shown. "Ring 2" and "Ring 3" keep the same length for the straight sections as in the original design, while for the ring labelled as "Short Ring" this length has been considerably shortened.

	Ring 1	Ring 2	Ring 3	Short Ring	IDS-NF
Magnets	5 T	8.3 T	8.3 T	8.3 T	–
Radius (m)	300	633	569	633	65
ℓ	0.36	0.28	0.29	0.17	0.37
L_s (m)	2500	2500	2500	998	599
L_t (m)	6885	8974	8531	5970	1606

Table 4.2: Main parameters which describe some possible designs for a racetrack storage ring for a β-beam . For comparison, we also show the corresponding parameters for the IDS-NF muon storage ring, taken from Ref. [299]. ℓ corresponds to the livetime in Eq. (4.4).

The ratio between the number of useful ion decays and the total number of ion decays in the whole ring is given by the *livetime*. It can be obtained as the ratio between the straight section of the ring which is aiming at the detector and its total length, $\ell = L_s/L_t$. For a ring with racetrack geometry, this corresponds to:

$$\ell_{racetrack} = \frac{L_s}{2\pi R + 2L_s}\,, \tag{4.4}$$

where L_s and R correspond to the length of the straight section aiming at the detector and the curvature radius, respectively. As it can be seen from Tab. 4.2, the original racetrack design for the ^{6}He $/^{18}$Ne $\gamma = 100$ β-beam had a livetime of $\ell = 0.36$. The situation changes when different ions are stored in the ring, or higher boost are considered. Higher boost factors make ions more difficult to bend, and therefore larger magnetic fields and/or larger curvature radius are required. On the other hand, slightly smaller curvature radii are required to bend ^{8}Li $/^8$B with respect to ^{6}He $/^{18}$Ne , due to their different A/Z (see Tab. 4.1).

On the other hand, the livetime for a triangular ring is obtained as:

$$\ell_{triangle} = \frac{2L_s}{2\pi R + 3L_s}\,. \tag{4.5}$$

In setup A, ^{8}Li /^{8}B ions are boosted to $\gamma = 350$. If LHC 8.3 T dipolar magnets are used instead of 5 T magnets, the radius needed to bend the ions in this case can be obtained by rescaling the radius in the original design:

$$R' = 300 \times \left(\frac{5}{8.3}\right)\left(\frac{350}{100}\right)\left(\frac{2.7}{3}\right) = 569\,\mathrm{m}\,, \tag{4.6}$$

where the last factor is needed because of the different A/Z ratio.

From Eq. (4.5), a triangular ring with three straight sections with $L_s = 2500$ m and three arcs with $R = 569$ m curvature radius would have $\ell = 0.46$. With this geometry, the total length of the ring is $L_t \sim 10$ km, not much larger than in the original proposal. It should also be taken into account that, in this case, 23% of the total number of ion decays will be aimed at each detector. This may be advantageous with respect to the case where two racetrack rings are built. In this case, since the total number of ions that can be produced would have to be split in half and stored in each of the two rings, only a 30% of the total number of ion decays would be useful. This is the storage ring geometry which has been chosen for setup A.

For setup B the situation is different, though. Imagine that one of the long straight sections of a triangular ring aims at a detector located at $L = 7000$ km and that a second one aims at a detector located at $L = 650$ km. If we inject ^{6}He and ^{18}Ne ions in the storage ring and let them decay, neutrinos produced in the straight section aiming at the "near" detector give a very good sensitivity to θ_{13} and to the CP violating phase δ. On the other hand, neutrinos produced in the straight section aiming at the "far" detector will contribute scarcely to the measurement of the sign of the atmospheric mass difference, since their energy is too small to have a resonant behavior in matter and compensate the very long baseline (see Sec. **??**). A similar situation can be observed when ^{8}Li and ^{8}B ions are injected in the ring: those ions that decay aiming at the "far" detector produce a neutrino flux that provides a very good sensitivity to the mass hierarchy. On the other hand, those decaying in the straight section which is pointing to the "near" detector contribute very little to the measurement of θ_{13} and δ, since the neutrino flux is strongly off the oscillation peak and, consequently, their energy is too high for the oscillations to develop at the 650 km baseline. For this reason, it is easy to understand that no particular advantage arises in using a triangle geometry storage ring for setup B. We will thus consider two racetrack geometry storage rings instead, each of them with one of the straight sections aiming at one of the two detectors. Notice that this setup is similar to the one considered in the IDS-NF baseline proposal [298].

However, some technical difficulties have to be faced regarding the design of the storage ring. In Tab. 4.2 the main parameters for several possible storage rings are summarized. In the same table the corresponding parameters for the muon storage ring, in the case of a NF, are also shown for comparison. Notice the much more compact storage ring in the case of the NF, compared to the analogous device proposed for the β-beam . The different size is motivated by two important differences between the β-beam and the NF: first, shorter arcs are needed to bend muons with respect to ions, for similar magnetic fields; second, the occupancy of a β-beam ring must be very small to reduce the atmospheric background as stressed at the beginning of this section (*i.e.*, either we inject very few ions into the ring, or the size of the ring must be very large). The atmospheric background, however, is not a significant problem at the NF[5], the neutrino energy being of the

[5]Notice that the so-called "*low-energy NF*", proposed in Ref. [300, 301], could be affected by the same problem as the β-beam . In this case, the storage ring design for this facility should be modified accordingly.

Ions (γ)	^{6}He /^{18}Ne (100/100)	^{6}He /^{18}Ne (350/350)	^{8}Li /^{8}B (350/350)	^{8}Li /^{8}B (390/656)	IDS-NF	
Ring	Ring 1	Ring 2	Ring 2	Short Ring	IDS ring	
Baseline (km)	130	650	7000	7000	4000	7500
ϑ	0.6°	3°	34.5°	34.5°	18°	36°
Depth (m)	32	197	2132	1282	225	428

Table 4.3: Summary of the tilt angles and the total depth that would need to be reached if the storage rings described in Tab. 4.2 are used to aim at several baselines. Results are presented for the original ^{6}He /^{18}Ne $\gamma = 100$ proposal, as well as for several high-γ options. For comparison, the corresponding parameters for the IDS-NF setup [299] are also shown.

order of several GeVs (in this range of energy the atmospheric background is at least two orders of magnitude smaller than in the case of $\mathcal{O}(100)$ MeV neutrinos).

The original design of the storage ring for the β-beam must be modified when the boost factor γ is increased. In the second column in Tab. 4.3 the main parameters for this ring are summarized (Ring 2). In order to bend the ions more powerful magnets are preferred in this case. Notice that the length of the straight sections has been kept as in the original design. Since the radius is now much larger, though, the total length of the ring is increased, and as a consequence the livetime is reduced with respect to the original design, $\ell = 0.28$. If we use this ring to aim to a detector placed at 650 km from the source, it would have to be tilted $\vartheta = 3°$ with respect to the horizon. This can be seen from Tab. 4.3, where a summary of the tilt angles and maximum depths for different ring designs is presented, for different possible baselines. As it can be seen from the table, the maximum depth that the *Ring 2* would reach into the ground in this case would be $d = 197$m. From the comparison with the IDS-NF muon storage ring design, it emerges that this design is not unrealistic: albeit much longer than the ring conceived for the NF, the decay tunnel for this ring reaches the same depth d as the NF ring aiming at $L = 4000$ km.

However, if Ring 2 is used to aim at a detector located at $L = 7000$ km from the source, the maximum depth of the far end of the ring would be $d = 2132$ m (see Tab. **??**), something well beyond any realistic possibility. As it was stressed in the beginning of this section, however, two storage rings will be used in setup B to aim to the detectors located at $L = 650$ km and $L = 7000$ km. Therefore, it is possible to design two rings of different characteristics, each of them optimized for a different detector. In particular, the ring aiming at the magic baseline could be more compact than the other one.

One possibility could be to use the slightly more favorable Z/A ratio of ^{8}Li with respect to ^{6}He to build a ring with smaller curvature radius, Ring 3 (see Tab. 4.2). It is clear that the final depth would not be considerably reduced, although it would have a slightly better livetime, $\ell = 0.29$. A second, more interesting, possibility is to reduce the straight sections of the ring to reduce its longitudinal size, and correspondingly d, at the price of a reduced livetime. A relevant question is, then, how much can we reduce the livetime of the ring so as to increase its technical feasibility, but with only a small loss in the sensitivity to the mass hierarchy? Even more important, which loss of sensitivity to the mass hierarchy is acceptable without a significant loss of sensitivity to the CP violating phase δ?

An answer to these questions is offered by Tab. 4.4. Notice that in Ring 2 we can store ^{8}Li , ^{18}Ne and ^{8}B ions boosted up to $\gamma = 390$, 583 and 656, respectively. In Tab. 4.4, it can be observed that increasing the boosting factor of ^{8}Li and ^{8}B ions to the maximum γ for which these ions can still be stored into this ring, a significant increase of the number of events in the far detector can be achieved. Such increase depends on the hierarchy and on the fulfillment of the resonant condition of the oscillation probability in matter: for example, a 10% increase of the boost of ^{8}Li ions from $\gamma = 350$ to $\gamma = 390$ implies a 50% (25%) increase in the number of events observed at the detector for inverted (normal) hierarchy. Similar results are obtained for ^{8}B ions.

	$\gamma^{^8Li}$	350	360	370	380	390
+	$N_{ev}(\gamma)$	1.84	1.94	2.05	2.18	2.33
	$N_{ev}(\gamma)/N_{ev}(350)$		1.05	1.11	1.18	1.27
-	$N_{ev}(\gamma)$	55.80	62.46	69.40	76.54	83.86
	$N_{ev}(\gamma)/N_{ev}(350)$		1.12	1.24	1.37	1.50
	$\gamma^{^8B}$	583	600	617	633	650
+	$N_{ev}(\gamma)$	477.16	499.72	521.64	541.68	562.34
	$N_{ev}(\gamma)/N_{ev}(583)$		1.05	1.09	1.14	1.18
-	$N_{ev}(\gamma)$	15.20	16.58	17.99	19.34	20.79
	$N_{ev}(\gamma)/N_{ev}(583)$		1.09	1.18	1.27	1.37

Table 4.4: Number of muons observed at a 50 kton magnetized iron detector [281,282] with perfect efficiency located at 7000 km from the source after 5 years of data taking as a function of the boost factor of ^{8}Li (upper table) and ^{8}B ions (lower table), for $\theta_{13} = 5^\circ$ and $\delta = 90^\circ$. A livetime $\ell = 0.3$ has been assumed for the storage ring. The ratio of the number of events obtained with a given γ with respect to those obtained storing ^{8}Li (^{8}B) ions boosted at $\gamma = 350$ (583) is also shown.

The increase in the statistics can be used for two different purposes: the first possibility, of course, is to use it to achieve a higher sensitivity to the mass hierarchy. However, the sensitivity increase is not dramatic (as it should be expected, since for Gaussian statistics the sensitivity scales with the square root of the statistics). The second possibility, that could open the path to a feasible β-beam facility with long baseline, is to use the higher statistics to reduce significantly the size of the storage ring: the physics reach of a setup using Ring 2 with ^{8}Li ions boosted at $\gamma = 350$ is identical to the reach of a racetrack ring with a much shorter straight section, $L_s = 998$ m, if the ^{8}Li ions are boosted at $\gamma = 390$. This ring has been labelled as the "Short ring" (see Tab. 4.2). The maximum depth in this case is still much larger than what is needed for any of the NF rings (see Tab. **??**), but is almost 1 km shorter than for *Ring 2*. Note that for the higher energy ^{8}Li/^{8}B beams, the problem of atmospheric neutrino background is almost non-existent, as discussed before. Therefore, the reduction of the total ring size does not pose any serious threat to the experiment.

We therefore propose two storage rings of different design for setup B: Ring 2 to store ^{6}He and ^{18}Ne ions boosted at $\gamma = 350$, aimed at $L = 650$ km, whereas the Short Ring could be

used to store ^{8}Li and ^{8}B boosted at $\gamma = 390$ and 656, aiming at $L = 7000$ km.

Eventually, it is worth to mention that a more compact ring (with larger ℓ) could be obtained by increasing the magnetic field in the curved section, taking advantage of the R&D programme for LHC upgrades aimed to the development of high field magnets (with $B \in [11 - 15]$ T). If one assumes that magnetic field strengths of 15 T could be used for the storage ring [302], then ^{6}He ions boosted at $\gamma = 350$ could be stored in a ring with curvature radius $R = 350$ m. If the straight sections of the ring are kept fixed to $L_s = 2500$ m, the total length of the ring is $L_r = 7200$ m with a livetime $\ell = 0.35$. The longitudinal section of this ring would be 3200 m, with a maximal depth d at the far end of the ring when tilted at $\vartheta = 34.5°$ of 1812 m. If we now fill a ring equipped with the same magnets with ^{8}Li and ^{8}B ions boosted at $\gamma = 390/656$, we can still achieve a good sensitivity to the mass hierarchy reducing the livetime to $\ell = 0.17$ (as discussed above), corresponding to straight sections of length $L_s = 556$ m. Such a ring has a total length $L_r = 3311$ m, a longitudinal section of 1256 m and a maximal depth at the far end of the ring aiming at the magic baseline detector $d = 711$ m. This depth is not much larger than the depth required for the NF magic baseline ring, and hence it could represent an extremely interesting option to be investigated further.

Finally, activation of the ring in the baseline setup (^{6}He/^{18}Ne at $\gamma = 100$) is under study. Results presented at the last NuFact Conference seem to indicate that energy deposit at the end of the straight sections is under control [303]. Power losses and activation for ^{6}He/^{18}Ne at higher γ have not been computed in detail, however. In the case of ^{8}Li and ^{8}B ion beams, no detailed study has been performed for any γ. The β^--decay channel of ^{8}Li is $^8\text{Li} \rightarrow {}^8\text{Be} \rightarrow 2\alpha$. ^{8}B also decays into ^{8}Be and finally to two α's (it is the mirror nucleus of ^{8}Li). The two α's have the same A/Z as the ^{6}Li, and therefore the energy deposit should be located in the same part of the magnets at the end of the ring straight sections. It must be reminded that the ^{8}B β-decay spectrum is affected by several systematics errors that must be tamed before using it for a precision experiment (see Ref. [304]).

4.2.5 The atmospheric background for a high-γ β-beam

Atmospheric neutrinos interacting inside the detector or in its proximity give rise to muon events that can be confused with the signal. This background was studied at a β-beam , both for WC [274, 305] and iron detectors [276, 279, 280]. The number of muons produced by atmospheric neutrinos crossing the detector aligned with the β-beam flux was found to be of the order of tens of events per Kton per year. This background would completely dominate the oscillation signal (see Tab. 4.4). It is therefore mandatory to reduce it by a proper timing of the ion bunches.

In order to have a good time correlation of the signal with the neutrino flux produced at the source, the ions circulating in the storage ring must occupy a very small fraction of it. This is given by the "suppression factor" (S_f), defined as:

$$S_f = \frac{v \times \Delta t_{bunch} \times N_{bunch}}{L_{ring}} \tag{4.7}$$

where $v \simeq c$ is the ion velocity. For ^{6}He/^{18}Ne ions boosted at $\gamma = 100$ ($E \sim 300$ MeV), the suppression factor must be $S_f \sim 10^{-3}$ in order to overcome the atmospheric background. Such a tight S_f could be achieved with a challenging Δt_{bunch}=10 ns time-length, with a maximum of $N_{bunch} = 8$ bunches circulating at the same time. A suppression factor of $S_f \sim 5 \times 10^{-3}$ is currently at hand [289]. Further research is ongoing, though, to try to reduce it[6] down to 10^{-3}.

[6]More recently, the effect of the suppression factors was studied for several $\gamma = 100$ β-beam setups [306], where

At higher energies (*e.g.* $\gamma = 350$ for ^{6}He, $E \sim 1.2$ GeV), however, the atmospheric background is suppressed by about one order of magnitude with respect to $\gamma = 100$. S_f can thus be correspondingly relaxed. The average neutrino energy for high-γ ^{8}Li/^{8}B ion beams being $E \sim 6$ GeV, moreover, an extra suppression of the atmospheric neutrino background is expected with respect to the high-γ ^{6}He/^{18}Ne ion beams. As it can be seen from Fig. 2 of Ref. [131], for example, the atmospheric neutrino flux decreases about two orders of magnitude passing from 1 to 6 GeV. As a consequence, less demanding bunch time-lengths are acceptable for the setups proposed here, thus simplifying the storage ring design. For this reason, in the numerical analysis presented in Section 4.4 we have neglected the atmospheric neutrino induced background.

4.3 The detector design

In this section, the details of the setup related to the detector are discussed in detail. These include the choice of the two baselines (Sec. 4.3.1) and a discussion of the suitable detector technologies for a β-beam (Sec. 4.3.3). Finally, a discussion on backgrounds and systematic errors is also performed (Sec. 4.3.1).

4.3.1 The choice of the two baselines

As it was already shown in Sec. 2.3 (Ch. **??**), for very long baselines $L \sim \mathcal{O}(7000)$ km the δ-dependence in the oscillation probabilities vanish due to the proximity to the magic baseline, thus providing a very good sensitivity to θ_{13} due to the lifting of the intrinsic degeneracies. In addition to this, for neutrino energies around $E_\nu \sim 6$ GeV a resonant enhancement of the probability takes place only for neutrinos (antineutrinos) if the hierarchy is normal (inverted), thus providing a clean measurement of the mass hierarchy. In addition, the resonant enhancement in the oscillation probability compensates the loss of events due to the very long baseline, increasing the statistics at the far detector and improving its sensitivity to smaller values of $\sin^2 2\theta_{13}$.

For the second baseline the most important criterion is the measurement of CP violation, since a detector placed at 7000 km will be insensitive to δ. For that we want the second term to dominate in the probability. Moreover, matter effects can fake true CP violation stemming from the phase δ and, therefore, short baselines and low energies are better for those studies. The mean neutrino energy of neutrinos from ^{8}Li and ^{8}B decays at $\gamma = 350$ is $E_0\gamma \sim 6$ GeV, which translates to an on-peak baseline of $L \sim 1000 - 2000$ km. This is the short baseline considered for setup A. For setup B, since the end-point energies for ^{6}He and ^{18}Ne are roughly three times smaller than the ones for ^{8}Li and ^{8}B , the baseline corresponding to the first oscillation peak is expected to be three times smaller than the one for ^{8}Li and ^{8}B . The vacuum limit can be considered in this case in order to determine a more exact value. In the limit of $A \to 0$, maximizing the CP violating terms amounts to require that $\sin\Delta_{31} = 1$. For $\Delta m^2_{31} = 2.4 \times 10^{-3}$ eV^2 this implies $L/E = 515$ km/GeV. The mean neutrino energy of neutrinos from ^{6}He and ^{18}Ne decays at $\gamma = 350$ is $E_0\gamma \sim 1.2$ GeV. This translates to an on-peak baseline of $L = 618$ km matching perfectly the 650 km baseline between CERN and the Canfranc laboratory.

the atmospheric background is more problematic. The main outcome of that study can be summarized as follows: (1) the atmospheric background affects the performance of the β-beam in the region of small θ_{13}, but this is not the case for large θ_{13}; (2) a suppression factor below 10^{-4} is equivalent to no atmospheric background at all.

4.3.2 Signal event rates: the matter resonance at 7000 Km

In Tab. 4.5 we show the total expected event rates when each detector (assuming perfect efficiency) is exposed to the "ultimate flux" for one year of data taking, for several input values of $\sin^2 2\theta_{13}$, δ and the mass hierarchy. Results are shown for the WC detector placed at 650 km exposed to a $\gamma = 350$ ^{6}He /^{18}Ne β-beam (setup B), and the two 50 kton MIND detectors placed at 2000 (setup A) and 7000 km (setups A and B) exposed to a $\gamma = 350$ ^{8}Li /^{8}B β-beam . The rest of oscillation parameters have been fixed to the best-fit values in Ref. [152]. Notice that we the ν_e disappearance data will not be studied in any of our setups (see Ref. [283] for such a study at the L = 7000 Km baseline).

$\sin^2 2\theta_{13}$	sgn(Δm^2_{31})	δ	$N^{650}_{\nu_\mu}$	$N^{650}_{\bar{\nu}_\mu}$	$N^{2000}_{\nu_\mu}$	$N^{2000}_{\bar{\nu}_\mu}$	$N^{7000}_{\nu_\mu}$	$N^{7000}_{\bar{\nu}_\mu}$
0.01	+	90°	2759	198	114	4	31	1
		−90°	683	952	39	21	34	0
	-	90°	2101	321	49	18	1	14
		−90°	429	1249	10	53	1	13
0.001	+	90°	767	48	27	2	3	0
		−90°	109	286	3	7	4	0
	-	90°	657	41	16	1	0	2
		−90°	128	335	4	12	0	1

Table 4.5: Event rates for a detector with perfect efficiency after 1 year of exposure to 1×10^{19} ion decays. Results are shown for the WC detector placed at 650 km (setup B), and the two 50 kton MIND detectors placed at 2000 (setup A) and 7000 km (setups A and B), as well as for several choices of $\sin^2 2\theta_{13}$, δ and the mass hierarchy.

Notice the strong complementarity between the two baselines:

- The event rates both at the 650 km and the 2000 km baselines show a strong dependence on both the CP-violating phase δ and the sign of the atmospheric mass difference. Neutrino (antineutrino) events are enhanced for positive (negative) values of δ and normal (inverted) hierarchy. This strong dependence on both unknowns is also the source of strong degeneracies, when the effect of δ is able to compensate that of the mass hierarchy. Such a situation can be seen in the second and third rows of Tab. 4.5, where very similar event rates are found at the $L = 2000$ Km baseline for $\delta = -90°$ and $s_{atm} = +$ and for $\delta = 90°$ and $s_{atm} = -$. For this reason, with only one detector the sensitivity to the mass hierarchy would be limited to positive (negative) values of δ for a normal (inverted) hierarchy, where the effects of δ and the mass hierarchy push in the same direction (see eg. Fig. (19) of Ref. [307]).

- On the other hand, it can be seen that the event rates at the $L = 7000$ Km baseline are practically insensitive to the CP-violating phase δ (as this baseline is so close to the "magic baseline", where δ-dependence vanishes). The dependence on the mass hierarchy is, however, very strong, with a nearly resonant enhancement of the neutrino (antineutrino) oscillation

probability if the hierarchy is normal (inverted), regardless of the value of δ (see Refs. [184, 185, 283]).

The combination of both baselines can thus provide an unambiguous determination of both the CP violation phase and the mass hierarchy for large regions of the parameter space. This will be exploited both for setups A and B.

4.3.3 Detector technologies

Traditional technologies for ν production (conventional beams and superbeams) allow the investigation of the 1-3 sector of the leptonic mixing matrix through the appearance of ν_e and $\bar{\nu}_e$ at baselines $\geq$ 100 km, *i.e.* through the information encoded in the $\nu_\mu \to \nu_e$ and $\bar{\nu}_\mu \to \bar{\nu}_e$ transitions probabilities. In that context, optimal far detectors are low-density, massive electromagnetic calorimeters (liquid scintillators, WC or liquid Argon TPC's [308]).

On the other hand, both β-beams and NF exploit the T-conjugate channel $\nu_e \to \nu_\mu$ and $\bar{\nu}_e \to \bar{\nu}_\mu$. An important difference of the β-beam with respect to the NF is that in the former only $\nu_e(\bar{\nu}_e)$ are present in the beam, whereas in the latter both ν_e and $\bar{\nu}_\mu$ (or $\bar{\nu}_e, \nu_\mu$) are present. Therefore, in a β-beam –based experiment final lepton charge identification is not needed. Magnetization of the detector could in principle be removed from the detector, since at the β-beam no significant $\bar{\nu}_\mu$ flux that must be distinguished from the $\nu_e \to \nu_\mu$ signal is produced. Removing the magnetization of the detector can be used to reduce costs on the detector side, if it is not necessary to reduce possible backgrounds. In addition, it also allows for the use of large WC detectors, something impossible at the NF, where magnetized detectors are mandatory when looking for $\nu_e \to \nu_\mu$ oscillations. In both cases, calorimetric measurements are needed to reconstruct the neutrino energy[7].

For neutrinos produced by a β-beam with a (relatively) high energy ($E_\nu \sim 6$ GeV), the use of dense detectors is therefore possible. In particular, the choice of the passive material of the calorimeter depends on the typical range of the primary muon; the latter must be significantly larger than the interaction length to allow for filtering of the hadronic part and effective NC and ν_e CC selection. For neutrinos of energies greater than $\sim$1 GeV, iron offers the desired properties. As a consequence, the energy reached at the SPS+ can be exploited to switch from a low-Z to a high-Z/high-density calorimeter also in the case of the β-beam . The use of iron detectors avoids the need for large underground excavations, which are mandatory for β-beams of lower ν energies. Since these detectors are capable of calorimetric measurements, they can be exploited even better than WC to obtain spectral informations. Several techniques can be employed for the design of the active detectors of large mass iron calorimeters. A detailed study of a magnetized iron detector suitable for a $\gamma = 350$ ^{6}He/^{18}Ne β-beam was performed in Ref. [279].

Iron detectors are not expected to reach, anyhow, the granularity of liquid argon TPC's or the megaton-scale mass of a WC. Hence, in spite of the underground location, they cannot be used for proton decay measurements and low-energy astroparticle physics.

Most known detector technologies have been considered in the literature exposed to a β-beam . Each of these detectors offers the best performance only within a certain neutrino energy range. The main features of MIND, TASD and WC detectors are summarized in Tab. 4.6. A detailed report card on the detector performance in terms of energy threshold, energy resolution, backgrounds, statistics and costs is required for deciding the best detector option. The detector choice is also directly dictated by the energy of the β-beam .

For the ^{18}Ne and ^{6}He β-beam , it was argued in Ref. [269] that a WC would be best

[7] The only notable exception concerns "monochromatic Beta Beams" [309–312] based on ions decaying through electron capture. Energy reconstruction with these beams serves to suppress backgrounds, though.

Detector Characteristics	MIND [282, 313] (Only $\mu^{\pm}$)	TASD [160] (Both $\mu^{\pm}$ & $e^{\pm}$)	WC [275]
Fiducial Mass	50 kton	50 kton	500 kton
E_{min}	1 GeV	0.5 GeV	0.5 GeV
Bin Size	$\in$ [0.6, 2.3] GeV	0.2 GeV	0.25, 0.5 GeV
Background Rejection	0.0001	0.001	$\in$ [0.0001, 0.001]
Signal error (syst.)	2.5%	2.5%	2.5%
Background error (syst.)	5%	5%	5%
Detection Efficiency (ϵ)	$\in$ [5, 70] %	80% ($\mu^{\pm}$) & 20% ($e^{\pm}$)	$\in$ [20, 50] %
Energy Resolution (σ)	0.15 E(GeV)	$0.03\sqrt{\text{E(GeV)}}$ for $\mu^{\pm}$ $0.06\sqrt{\text{E(GeV)}}$ for $e^{\pm}$	$\lesssim$0.15E(GeV)
Charge Id Efficiency (f_{ID})	Yes	No	No

Table 4.6: Comparison of the typical detector characteristics expected for the three most popular β-beam detectors.

for $\gamma \leq 300$, while for larger boost factors one should use the TASD detector. In fact, most studies have used megaton scale water Čerenkovdetectors as detector option for a $L \leq 1000$ km [174, 176, 274–276, 314, 315]. In Refs. [316, 317] the idea of observing high γ β-beam neutrinos with magnetized iron detectors was introduced for the first time. This prospect was further used in Refs. [184, 185, 318, 319] and later in Refs. [284, 320]. We show in Tab. 4.6 the comparative catalogue of detector characteristics. The first relevant difference between the different technologies is the energy threshold: both the TASD [160] and water Čerenkovdetectors [275] have a very low energy threshold and are, hence, ideal for neutrino beams of relatively low energy (up to a few GeV). Magnetized iron detectors of the MIND type [313] (see also [282]), on the other hand, are a good option only for higher energy beams. The energy resolution of TASD is impressive up to a few GeV, whereas that of water Čerenkovdetector is good, but only for the energy regime which has a predominance of quasi-elastic events (E1 GeV). Eventually, iron detectors energy resolution is limited by the present segmentation design. The background rejection fraction, on the other hand, is seen to be best for the magnetized iron detector. It is in fact expected to be better for magnetized iron by at least an order of magnitude compared to water Čerenkovand TASD. Scaling of the detector mass is difficult for TASD and magnetized iron detectors beyond 50 kton, whereas megaton scale water Čerenkovdetectors are currently under study [238,252]. Notice, however, that a 50 kton magnetized iron detector represents, at present, the cheapest option between the three detectors technologies and design considered in Tab. 4.6.

Based on the comparative performance of the detectors and our physics goals we make the following choices: (1) for setup B, since the short baseline is the optimal one to perform CP violation studies, and since CP measurements are better at lower energies with ^{18}Ne and ^{6}He as source ions than at higher energy with ^{8}Li and ^{8}B [320], it is preferable to have a detector with lower threshold and good energy resolution. Therefore, the choice would be between TASD and WC detectors. Another two-baseline setup, using ^{8}B and ^{8}Li as source for a 50 kton magnetized iron detector at the magic baseline and ^{18}Ne and ^{6}He as the source for a 50 kton Totally Active Scintillator Detector (TASD) at $L = 730$ km was proposed in [320]. The sensitivity reach for this setup was seen to be remarkable, and for very high values for the number of useful radioactive ion decays and γ, even comparable to the NF. Notice, however, that a WC can be made much larger than TASD, implying larger satistics. Therefore, we opt for a water Čerenkovdetector with 500 kton fiducial mass at the shorter baseline (as in Refs. [274, 275]). This detector could be housed at Canfranc, for example, at a distance of 650 km from the β-beam at CERN; (2) for $\gamma = 350$, neutrinos produced in the decay of ^{8}B and ^{8}Li are much more energetic, $E \sim 6$ GeV. In this range of energies, inelastic processes dominate and therefore multiring events are produced, for which WC efficiencies are very poor. We prefer to use a magnetized iron detector at this baseline. A candidate for this detector at the magic baseline could be the ICAL@INO detector in India [281,282] which is at a distance of 7152 km from CERN, and which will soon go under construction. We will assume 50 kton of detector mass for this detector, though it is possible that INO will be upgraded to 100 kton. In setup A, we will consider an additional identical iron detector located at 2000 km from the source.

In order to simulate the response of the WC and magnetized iron detectors when exposed to the β-beam fluxes, we follow the analyses performed in Refs. [274] and [313]. The efficiencies and beam-induced backgrounds expected in a water Čerenkovdetector for the $\gamma = 350$ β-beam fluxes from ^{18}Ne and ^{6}He decays are given in [274] as migration matrices that we use to simulate our "near" detector. Unfortunately, a similarly detailed analysis of the performance of the iron detector exposed to the β-beam fluxes is lacking. We therefore follow the efficiencies and backgrounds derived in [313] for the NF fluxes instead (see, also, Ref. [321]). Notice that this is a very conservative assumption since charge ID is not mandatory in a β-beam , unlike for the NF, given the purity of the beam. Moreover, the NF spectrum is much wider than the β-beam one and reaches

much higher energies. Higher energy events, in turn, can induce neutral current interactions that feed down background to lower energies. The largest uncertainties in the performance of the iron detector are on the efficiencies and backgrounds for the events of lowest energy, around $1-5$ GeV. However, the main role of the iron detector considered in this setup is to observe the resonant enhancement of the oscillation probability that happens around $6-7$ GeV to measure the mass hierarchy. Therefore, the performance of the proposed setup does not depend critically on the efficiency and background of the lowest energy events, unlike in the IDS-NF baseline design where these events are crucial to solve degeneracies and improve the sensitivity to CP violation for large θ_{13}. We will illustrate the mild dependence of the performance of the setup on the energy threshold of the detector in the next section.

4.3.4 Backgrounds, efficiencies and systematic errors for the MIND detector

The β-beam flux illuminating the detector can be considered, with a very high accuracy, a pure ν_e beam. An undesired ν_μ and $\bar{\nu}_\mu$ beam contamination could in principle originate from the daughter ions produced in the β-decay that collide with the storage ring magnets, acting as a fixed target. This background was studied in Ref. [271] for ^{6}Li ions and it is smaller than 10^{-4}. The beam contamination induced by ^{18}F and ^{8}Be ions has not been studied in detail, but it is supposed to be similar to that of ^{6}Li, and thus negligible.

When looking for $\nu_e \to \nu_\mu$ oscillations at a β-beam , the main source of beam background are ν_e CC interactions (with a non-observed electron) or NC interactions in which a pion or some other meson produced in the hadronic shower mimics a muon track. Another, sub-dominant, possible background source are ν_e CC (again, with a non-observed electron) or NC interactions in which a charmed-meson is produced that eventually generates a muon through a semileptonic decay. It is clear that measuring the charge of the muon will strongly reduce both backgrounds (for $\nu_e N \to e^- D^+ X$, the final μ^+ has opposite charge with respect to the signal, $\nu_\mu N \to \mu^- X$).

A full simulation of the response of a magnetized iron detector to a high-γ β-beam is lacking. In Ref. [279] the signal identification efficiency of such a detector for ^{6}He boosted at $\gamma = 350$ and ^{18}Ne boosted at $\gamma = 580$ (*i.e.* for a neutrino energy around 1 GeV) was found to be of the order of 50-60%. On the other hand, in the framework of the ISS report [322], a detailed study of the MIND detector exposed to the NF beam (*i.e.* for a neutrino energy around 30 GeV) has been presented, finding a ν_μ identification efficiency in the energy range of interest as high as 70%. More recently, improved efficiencies[8] for the MIND detector in the energy range below 10 GeV have been obtained [321]. These are crucial for our study, since our the oscillation probability has a maximum around 6 GeV.

In Ref. [279], it was found that the probability for the background to mimic a CC-like event is around 1%. A rather large beam-induced background was therefore expected for this setup, as the consequence of the limited pion rejection capability of this detector compared with more challenging β-beam or NF detector designs. This large background was mainly caused by the (relatively) low energy of the neutrinos. At the typical neutrino energy of a ^{8}Li/^{8}B $\gamma = 350$ β-beam , these backgrounds are much easier to suppress in iron calorimeters. Consistently, in Ref. [185] this background was completely neglected, on the basis of the simulations by the INO collaboration. Moreover, in Refs. [313, 324, 325] the fractional backgrounds for a 50 GeV NF beam targeting an iron calorimeter were found to be around or below 10^{-4} for the region around 5

[8] The migration matrices for the golden channels have also been obtained very recently. However, they are not completely understood yet. It seems that a systematic "pull" of the reconstructed neutrino energy took place in the montecarlo simulation which results, for instance, in an significant overflow of events above 25 GeV [321, 323].

GeV. Since in our setup there is no such a strong down-feed of the background from high energy neutrinos, we expect 10^{-4} to be a pessimistic upper limit for the beam-induced background.

In the numerical analyses presented for the MIND detector in setups A and B, event rates have been divided into nine bins between 1.5 and 10.5 GeV, with $\Delta E = 1$ GeV. The detector energy resolution has been implemented through a gaussian resolution function with $\sigma = 0.15 \times E$. For setup A we considered constant efficiencies of 65%, while for setup B we considered the identification efficiencies in [321] and a constant fractional background equal to 10^{-5} of the unoscillated events per bin. We have also studied the impact of the beam background on the physics performance of the setup increasing the fractional background up to 10^{-4}, showing explicitly that the effect is small for any of the considered observables.

4.4 Results

In this section, we present the results for the two β-beam setups that have been considered in this chapter, according to the observables defined in Sec. 3.2.3 (see Ch. 3). To probe possible deviations from maximal mixing of the atmospheric mixing angle and eventually measure its octant in case it turns out not to be maximal, very precise measurements of θ_{23} are required. For this task the best sensitivities are achieved through the $\nu_\mu \to \nu_\mu$ and $\nu_\mu \to \nu_\tau$ channels. These channels are not accessible through β-beams , though, since only ν_e's are present in the beam[9]. Therefore, in this chapter we will focus in the measurement of the parameters which are accesible through the golden channel, which can provide excellent sensitivities to θ_{13}, δ and the mass hierarchy.

Sec. 4.4.1 is dedicated to present the results obtained for setup A. These include the results for the three observables introduced in Sec. 3.2.3, as well as some plots showing the performance when different features of the setup are varied, such as the number of ion decays in the storage ring, the systematic errors and the size of the detector placed at the magic baseline. Results for setup B are presented in Sec. 4.4.2. In this case, the results will be presented in two cases: (1) considering two storage rings of the same size aiming at the two detectors; (2) considering a shorter ring aiming at the far detector. A comparison with the results obtained for setup A will also be included. Finally, in Sec. 4.4.3 a comparison between the performance of setups A and B and other high-energy facilities in the literature is presented.

In the first two subsections, results will be presented in the plane $\sin^2 2\theta_{13}$-δ, in logarithmic scale, whereas in the last subsection the results will be shown as a function of $\sin^2 2\theta_{13}$ (in logarithmic scale) and the fraction of possible values of δ for which a given observable can be measured.

4.4.1 Results for the two-baseline ^{8}Li /^{8}B β-beam (setup A)

Lacking a detailed study of the maximum achievable ^{8}Li and ^{8}B fluxes, we will present the results for three fluxes, as defined in Sec. 4.3. As we will see, this is the key factor limiting the sensitivity of the setup, since its very long baselines limit the statistics at the detectors. We have also studied the impact of the beam-induced background and of the systematic errors on the performance of the experiment. We will show that these uncertainties do not affect significantly the physics reach of the setup.

[9] These oscillations however occur in atmospheric neutrinos and could be studied in the detectors for the two setups considered here. The combination of this data with the study of the golden channel of the β-beam could provide some sensitivity to these unknowns (see, *e.g.*, Refs. [265, 326–328]).

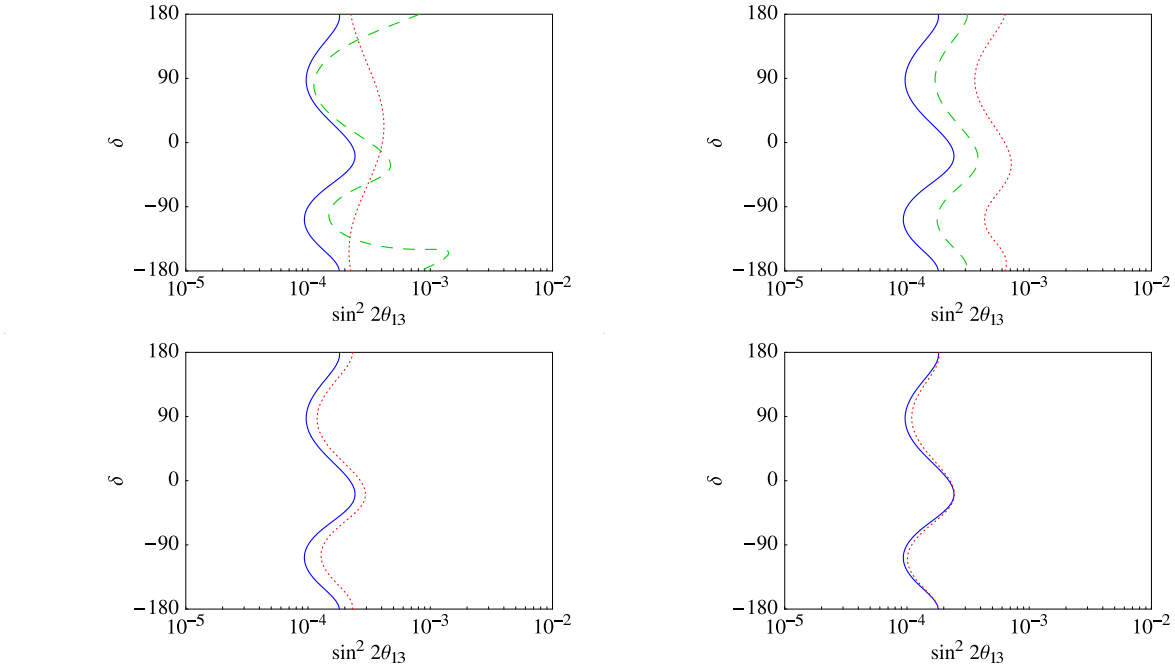

Figure 4.2: Sensitivity to θ_{13} at 3σ. Top left: comparison of baselines for a flux of 1×10^{19} useful ion decays per year. Dashed stands for $L = 2000$ Km; dotted for $L = 7000$ Km and solid for the combination of the two; Top right: the impact of the flux for the combination of the two baselines. Dotted stands for 2×10^{18}, dashed for 5×10^{18} and solid for 1×10^{19} useful ion decays per year; Bottom left: the impact of the beam-induced background for the combination of the two baselines and a flux of 1×10^{19} useful ion decays per year. Dotted stands for a background of 10^{-4} times the non-oscillated events, solid for 10^{-5} times the non-oscillated events; Bottom right: the impact of systematic errors for the combination of the two baselines and a flux of 1×10^{19} useful ion decays per year. Solid stands for systematics of 2.5% and 5% on the signal and the background, respectively: dotted for systematics of 10% and 20% on the signal and the background, respectively.

Sensitivity to θ_{13}

In Fig. 4.2 we present our results for the sensitivity to θ_{13}, defined in the following way: the values of θ_{13} and δ in the plots represent the "true" values of these parameters, i. e. the input values assumed to generate the number of events that would be measured at the detector. A "true" normal hierarchy is also assumed. For each of these input values, the χ^2 for $\theta_{13} = 0$ (marginalized in the rest of the parameters) was computed. If the value of the $\chi^2 > 9$, then the hypothesis that $\theta_{13} = 0$ can be rejected at 3σ for those "true" values of θ_{13} and δ.

In the top left panel we present the sensitivities to θ_{13} of the two baselines considered. The (green) dashed line corresponds to the sensitivity to θ_{13} with the detector at 2000 Km. The maximal sensitivity, $\sin^2 2\theta_{13} \geq 1.5 \times 10^{-4}$, is achieved for $\delta = 90°$ and $\delta = -90°$, when event rates for neutrinos and antineutrinos peak, respectively. The (red) dotted line is the sensitivity to θ_{13} with the detector at 7000 Km. Notice that, in spite of the longer baseline, the sensitivity is similar to the one achievable with the 2000 Km detector. This can be understood from the resonant enhancement of the mixing angle through matter effects at this baseline. Notice also that the δ dependence of the sensitivity is much milder, since the detector is located near the magic

baseline, where the terms involving δ vanish. Eventually, the (blue) solid curve is the sensitivity to θ_{13} for the combination of the two baselines. In this case, θ_{13} can be measured for any value of δ provided that $\sin^2 2\theta_{13} > 2 \times 10^{-4}$.

In the top right panel we study the dependence of the θ_{13}-sensitivity on the neutrino flux. Fluxes of 2×10^{18} (red dotted line), 5×10^{18} (green dashed line) and 1×10^{19} (blue solid line) useful ion-decays per year per baseline have been considered, for the combination of the two baselines. The more or less linear increase of the sensitivity with the flux indicates that the experiment performance is statistics-dominated.

The bottom left panel shows the impact of the beam-induced background on the θ_{13}-sensitivity for the combination of the two baselines for a flux of 1×10^{19} useful ion decays per year. Backgrounds of 10^{-5} (blue solid line) and 10^{-4} (red dotted line) of the total unoscillated events are considered. Notice that even increasing the background by an order of magnitude the loss of sensitivity is very small. On the other hand, decreasing the fractional background below 10^{-5} has no effect whatsoever. This background is thus equivalent in practice to no background.

Eventually, in the bottom right panel we present the impact of the systematic errors on the θ_{13}-sensitivity for the combination of the two baselines for a flux of 1×10^{19} useful ion decays per year. The systematic errors are increased from 2.5% and 5% (blue solid line) on the signal and the background, respectively, to 10% and 20% (red dotted line). It can be seen that the impact of systematic errors is negligible.

CP discovery potential

In Fig. 4.3 we present our results for the CP discovery potential, defined in the following way: the values of θ_{13} and δ in the plots represent the "true" values of these parameters. A "true" normal hierarchy is also assumed. For each of these input values, the χ^2 for $\delta = 0°$ and $\delta = 180°$ (marginalized in the rest of the parameters) were computed. If the value of the $\chi^2 > 9$, then the hypothesis that CP is conserved can be rejected at 3σ for those "true" values of θ_{13} and δ. Obviously this can never happen if the "true" value of δ is either 0° or 180°, hence no sensitivity is found in stripes around those values of δ.

In the top left panel we present the CP discovery potential for the three different fluxes at the 2000 Km baseline. Notice that for the "nominal flux", 2×10^{18} useful ion decays per year (red dotted line), the low statistics at the detector and the presence of degeneracies at CP-conserving values of δ spoil the discovery potential of the experiment. In this case there is no sensitivity to CP violation whatsoever. For the intermediate flux, 5×10^{18} useful ion decays per year (green dashed line), some areas in which CP violation can be discovered appear. Sensitivity is again lost around $\sin^2 2\theta_{13} = 4 \times 10^{-3}$ for negative δ and for $\sin^2 2\theta_{13} < 10^{-3}$ for positive δ. Even for the "ultimate flux", 1×10^{19} useful ion decays per year (blue solid line), the CP discovery potential for negative values of δ around $\sin^2 2\theta_{13} = 4 \times 10^{-3}$ is lost. This is because sign degeneracies at $\delta = 180°$ appear and do not allow to unambiguously determine CP violation, even if the true value of δ is CP-violating. This is the so called "π-transit" which also spoils the sensitivity of the $L \sim 3000$ Km detector of a NF for negative values of δ and $\sin^2 2\theta_{13} = 3 \times 10^{-4}$ (see Fig. 8 of [329]).

However, as we will see in the next subsection, excellent sensitivities to the mass hierarchy can be achieved at the far detector observing the resonant enhancement of the neutrino or antineutrino oscillation probability depending on whether the hierarchy is normal or inverted. The combination of the data taken at the two detectors can thus solve the sign degeneracy at π-transit and provide sensitivity to CP violation also for that region of the parameter space. Moreover, at the $L = 7000$ Km, close to the "magic baseline", the effects of CP violation vanish providing a clean measurement of θ_{13} that can greatly improve the CP discovery potential when combined with

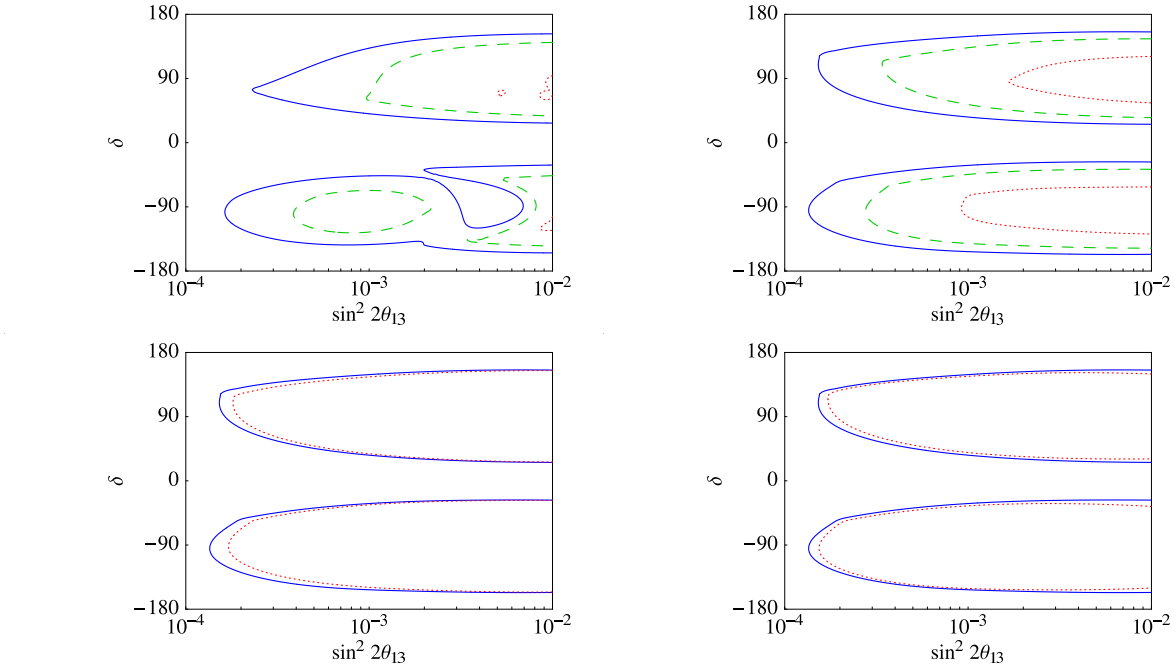

Figure 4.3: 3σ CP discovery potential. Top left: the impact of the flux for the $L = 2000$ Km baseline. Dotted stands for 2×10^{18}, dashed for 5×10^{18} and solid for 1×10^{19} useful ion decays per year; Top right: the same, for the combination of the two baselines. Bottom left: the impact of the beam-induced background for the combination of the two baselines and a flux of 1×10^{19} useful ion decays per year. Dotted stands for a background of 10^{-4} times the non-oscillated events, solid for 10^{-5} times the non-oscillated events; Bottom right: the impact of systematic errors for the combination of the two baselines and a flux of 1×10^{19} useful ion decays per year. Solid stands for systematics of 2.5% and 5% on the signal and the background, respectively: dotted for systematics of 10% and 20% on the signal and the background, respectively.

the data at 2000 Km. This combination is depicted in the top right panel of Fig. 4.3, where now very good sensitivities to CP violation can be obtained for $\sin^2 2\theta_{13} > 1.5 \times 10^{-4}$. Notice that we would get the same results for the combination of the two baselines in case an inverted hierarchy were assumed.

In the bottom panels the impact of the beam-induced background (left) and of the systematic errors (right) on the CP discovery potential is studied, finding again that their effect is marginal.

Sensitivity to the mass hierarchy

In Fig. 4.4 we present our results for the sensitivity to the mass hierarchy, defined in the following way: the values of θ_{13} and δ in the plots represent the "true" values of these parameters. A given "true" hierarchy is also assumed. For each of these input values, the χ^2 for the opposite mass hierarchy (marginalized in the rest of the parameters) was computed. If the value of the $\chi^2 > 9$, the wrong hierarchy can be rejected at 3σ for those "true" values of θ_{13} and δ.

In the top panels we present the sensitivity to the sign of the atmospheric mass difference for the combination of the two baselines and three different fluxes, for normal (left) and inverted (right) hierarchy. Notice that at 7000 Km either the neutrino or the antineutrino oscillation probability

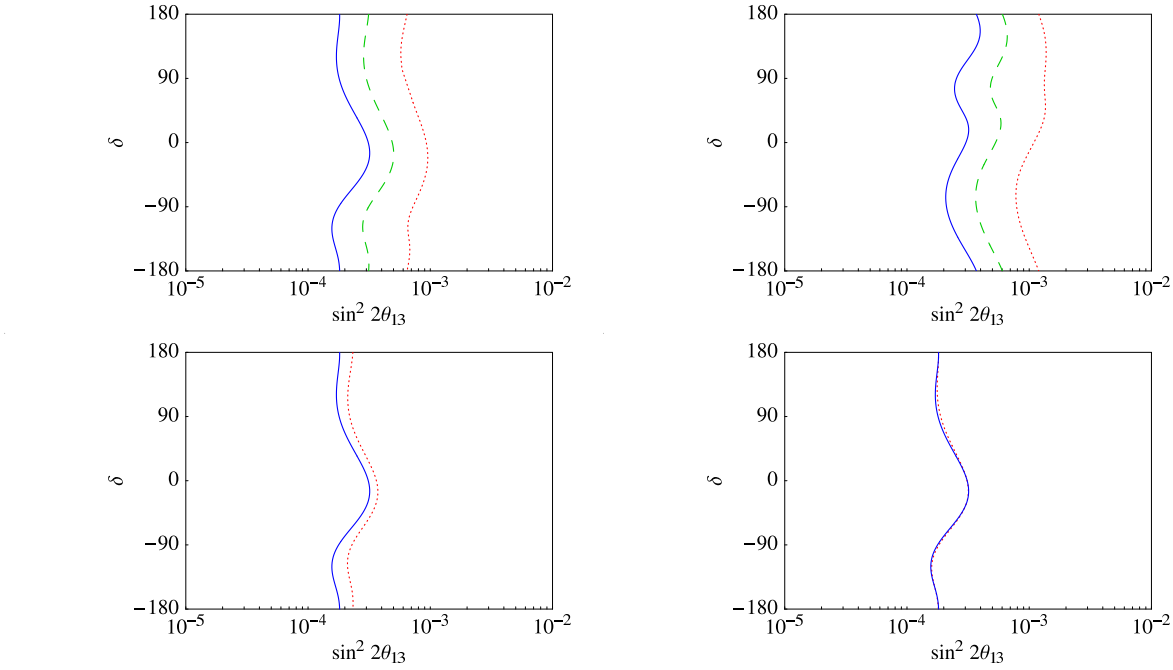

Figure 4.4: 3σ sensitivity to the mass hierarchy. Top left: the impact of the flux for the combination of the two baselines and normal hierarchy. Dotted stands for 2×10^{18}, dashed for 5×10^{18} and solid for 1×10^{19} useful ion decays per year; Top right: the same, for inverted hierarchy. Bottom left: the impact of the beam-induced background for the combination of the two baselines and a flux of 1×10^{19} useful ion decays per year. Dotted stands for a background of 10^{-4} times the non-oscillated events, solid for 10^{-5} times the non-oscillated events; Bottom right: the impact of systematic errors for the combination of the two baselines and a flux of 1×10^{19} useful ion decays per year. Solid stands for systematics of 2.5% and 5% on the signal and the background, respectively: dotted for systematics of 10% and 20% on the signal and the background, respectively.

becomes resonant [185, 283], depending on the mass hierarchy. As a consequence, the sensitivity to the sign of the atmospheric mass difference at this baseline is excellent: in Ref. [184], indeed, sensitivity to s_{atm} at 3σ down to $\sin^2 2\theta_{13} \geq 1\times10^{-3}$ (for $\gamma = 350$ and "standard" fluxes) is achieved. In our setup, due to the combination of the two baselines, a slightly better sensitivity is at reach for "nominal flux", down to $\sin^2 2\theta_{13} = 8\times10^{-4}(1\times10^{-3})$ for normal (inverted) true hierarchy, whereas sensitivity down to $\sin^2 2\theta_{13} = 2\times10^{-4}(4\times10^{-4})$ is achievable for the "ultimate flux". These sensitivities are enough to lift the sign degeneracy at the π-transit that causes the loss of sensitivity to CP violation for negative values of δ (compare top left and top right panels in Fig. 4.3).

In the bottom panels, we again show the impact of the background (left) and of systematic errors (right), respectively. The effect of both is found to be very small also in this case.

Asymmetric detectors

Up to this moment we have considered a symmetric setup in which two identical MIND-like 50 Kton detectors are located at $L = 2000$ Km and $L = 7000$ Km. The far detector is exploited, as explained in Sec. **??**, to solve the sign degeneracy in a CP-independent environment. To perform

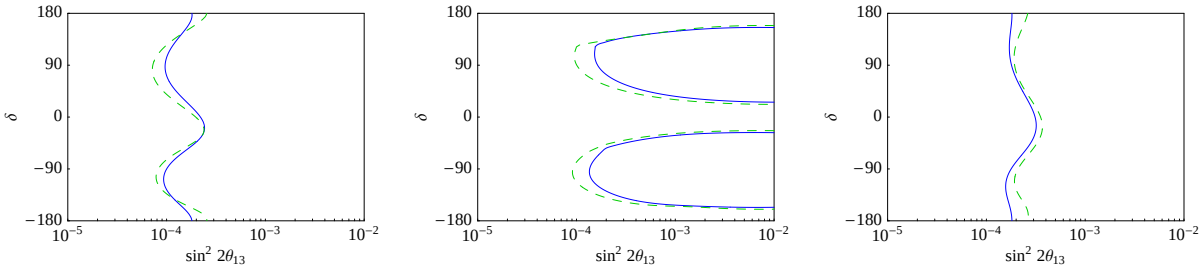

Figure 4.5: Comparison at 3σ between the performance of two detectors with equal masses (50 Kton each) and an alternative setup considering an 80 Kton near detector and a 20 Kton far one. In all plots, solid lines correspond to the symmetric setup and dashed lines to the asymmetric one. The left, middle and right panels show the sensitivity to θ_{13}, the CP discovery potential and the sensitivity to the mass hierarchy, respectively. Results have been obtained considering a flux of 1×10^{19} ion decays per year per straight section of the storage ring, a 10^{-5} fractional background and a systematic error of 2.5% on the signal and 5% on the background.

this task, however, it is not necessary to have such a large detector mass, due to the resonant effect in oscillation probabilities in matter for 6 GeV neutrinos at this baseline. At the price of losing some sensitivity to the hierarchy, thus, we can move some of the far detector mass to the near detector, increasing in this way the sensitivity to θ_{13} and δ.

This is shown in Fig. 4.5, where we present our results for the sensitivity to θ_{13}, δ and the mass hierarchy for an asymmetric setup with a 20 Kton MIND-like far detector and an 80 Kton (otherwise identical) near one. The left, middle and right panels show the sensitivity to θ_{13}, the CP discovery potential and the sensitivity to the mass hierarchy, respectively. The results have been obtained considering the "ultimate" flux, a 10^{-5} fractional background and a systematic error of 2.5% on the signal and 5% on the background. Solid lines stand for the symmetric 50 Kton case and dashed for the 80/20 Kton option.

As it was expected, we can see that the sensitivity to the hierarchy is slightly worse. In particular, we lose some sensitivity for $\delta = 0, \pi$, going from $\sin^2 2\theta_{13} \leq 2 \times 10^{-4}$ to $\sin^2 2\theta_{13} \leq 3 \times 10^{-4}$. The sensitivity loss for other values of δ is less significant. The same sensitivity loss for $\delta = 0, \pi$ is observed in the sensitivity to θ_{13}. However, we can see that an increase in the θ_{13}-sensitivity is achieved for $|\delta| = \pi/2$: we go from $\sin^2 2\theta_{13} \leq 1 \times 10^{-4}$ to $\sin^2 2\theta_{13} \leq 7 \times 10^{-5}$. This can be easily understood from the top left panel of Fig. 4.2. The sensitivity to θ_{13} at 2000 Km peaks for $|\delta| = \pi/2$ due to the increase in the neutrino (antineutrino) oscillation probability for $\delta = \pi/2$ ($\delta = -\pi/2$). On the other hand, at the magic baseline the δ dependence of the sensitivity is very mild and it is more strongly constraining θ_{13} near the CP-conserving values of δ. The CP-violation discovery potential, depicted in the middle panel, improves for any value of δ. In particular, for $|\delta| \sim \pi/2$ we go from $\sin^2 2\theta_{13} \leq 1.5 \times 10^{-4}$ to $\sin^2 2\theta_{13} \leq 9 \times 10^{-5}$.

Therefore, depending on the specific interest in a given physics observable, a symmetric setup or an asymmetric one should be adopted. Adding mass to the near detector favors the sensitivity to CP-violation, whereas increasing the size of the far detector favors the sensitivity to the mass hierarchy.

4.4.2 Results for the optimized two-baseline β-beam (setup B)

In Fig. 4.6 the black lines show the sensitivity reach of our proposed setup in terms of the three performance indicators defined above. We also compare its performance with three other high γ

β-beam setups, the sensitivity reaches for which are also shown. To make a fair comparison, we (re)calculate the sensitivities for each of the benchmark setups assuming the same total number of radioactive ions injected in the storage ring(s) and the same total number of years of running of the experiment. We assume that, at a given time, only one source ion is accelerated and fed into a storage ring. Expected performance of each of these benchmark setups is shown by a particular line type, and they are defined as follows:

1. Blue, dotted lines: These correspond to setup A (Sec. 4.4.1), where neutrino beams from decay of ^{8}B and ^{8}Li with boost factor $\gamma = 350$ are detected in two 50 kton magnetized iron detectors located at 2000 km and 7000 km.

2. Solid, black lines: These correspond to setup B. Neutrino beams produced by ^{18}Ne and ^{6}He decays, each accelerated to $\gamma = 350$ and detected in a 500 kton water Čerenkovdetector located at 650 km. A second set of beams from ^{8}B and ^{8}Li decays with $\gamma = 656$ and $\gamma = 390$, respectively, are detected at 7000 km by a 50 kton magnetized iron detector.The straight sections of storage ring of the ^{8}B and ^{8}Li source ions are 60% *shorter* than in the original ring design, and the total ^{8}B and ^{8}Li fluxes at the far detector is 40% smaller.

3. Orange, dashed lines: The two-baseline β-beam setup proposed in [320]. Here all four ions are used. Beams from decays of ^{18}Ne and ^{6}He accelerated to $\gamma = 575$ are detected in a 50 kton TASD detector at 730 km. Beams from decays of ^{8}B and ^{8}Li accelerated to $\gamma = 656$ are detected in a 50 kton magnetized iron detector at 7000 km.

4. Purple, dot-dashed lines: The one-baseline β-beam setup proposed in [274, 275]. Neutrino beams produced by ^{18}Ne and ^{6}He decays, each accelerated to $\gamma = 350$ are detected in a 500 kton water Čerenkovdetector located at 650 km.

For all the four setups we assume that there are 10^{19} *total decays per year*, irrespective of the choice of the ion [302]. Of these, only ions which decay along the straight section of the storage ring aimed at one of the two detectors are useful. For the "standard" storage ring considered in setups 2, 3 and 4, the livetime is $l = 0.28$. We have, thus, used 3×10^{18} *useful decays per year* for each ion species to reproduce the reach to the three observables for these earlier proposals. However, the storage ring for the ^{8}B and ^{8}Li ions in setup B has straight sections which are shorter by 60%, giving a livetime that is 40% smaller than for the standard storage ring. Accordingly, for the ^{8}B and ^{8}Li generated fluxes, we have only $0.6 \times 3 \times 10^{18}$ *useful decays per year*. We conservatively assume that only one type ion can be accelerated at a time and consider a total runtime of 10 years for all the setups we compare. We thus consider 5 years run per source ion for the experiments with two ions[10], and 2.5 years run per ion for those with four ions. We have considered 2.5% and 5% systematic errors on the signal and on the beam-induced background, respectively. They have been included as "pulls" in the statistical χ^2 analysis. The following 1σ errors for the oscillation parameters were also considered: $\delta\theta_{12} = 1\%$, $\delta\theta_{23} = 5\%$, $\delta\Delta m^2_{21} = 1\%$ and $\Delta m^2_{31} = 2\%$. Eventually, an error $\delta A = 5\%$ has been considered for the Earth density given by the PREM model [?, 180, 182]. Marginalization over these parameters has been performed for all observables. The GLoBES 3.0 [254, 255] software was used to perform the numerical analysis.

[10]For setup 2 where we have two ions but two baselines, we are therefore assuming that both detectors are irradiated simultaneously with neutrino beams from each ion for 5 years each. This can be done, as suggested in Setup A, using a triangular geometry storage ring, with a total livetime $l = 0.46$, *i.e.*with a flux aimed at each detector of 0.23×10^{19} useful decays per year.

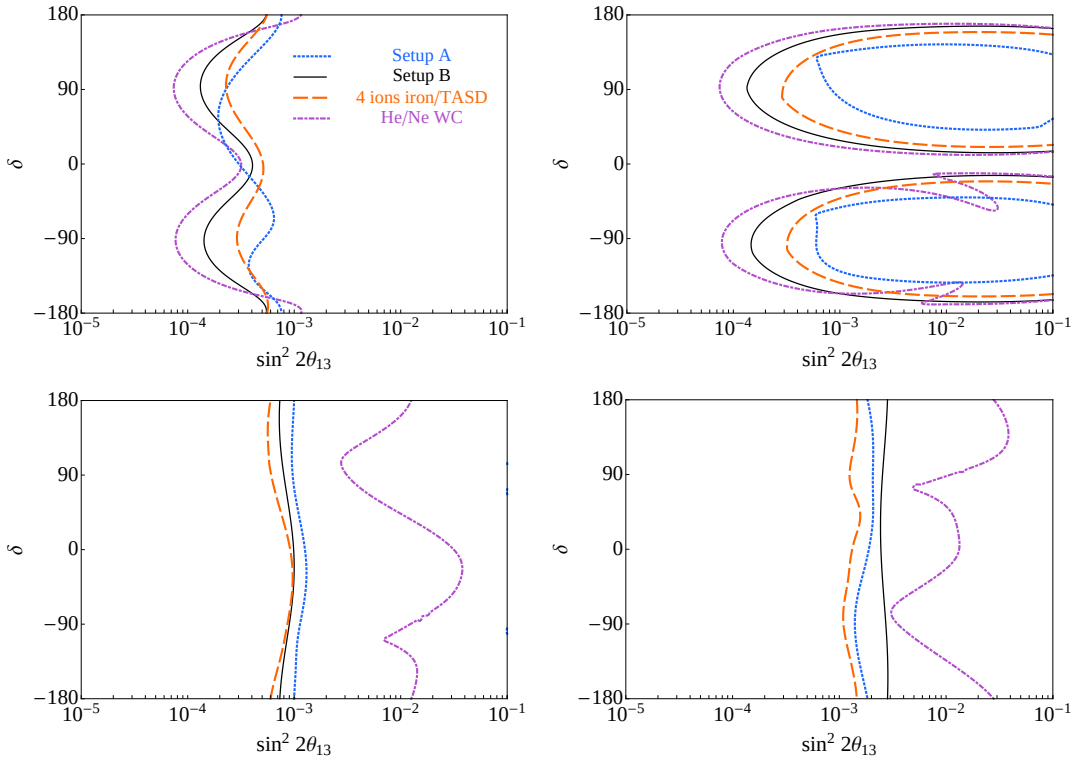

Figure 4.6: Sensitivity reach of the different β-beam setups in terms of the three performance indicators defined in the text. The upper left hand panel shows the sensitivity to , the upper right hand panels shows the CP discovery potential, while the lower panels show the sensitivity to the mass hierarchy. The lower left hand panel assumes normal hierarchy while the lower right hand panel shows the corresponding results for inverted hierarchy. The different line types are for different β-beam setups as described in the text. Note that the black lines are for setup B, which has the ^{8}B and ^{8}Li storage ring with straight sections shorter by 60% compared to all other setups (*i.e.*, a 40% smaller flux at the far detector).

Sensitivity to θ_{13}

The upper left hand panel of Fig. 4.6 shows the discovery reach. As it can be seen, the four setups perform in a very similar way. While for particular values of $\delta \simeq \pm 90°$, the best reach comes from setup 4, with ^{6}He/^{18}Ne ions and water Čerenkovdetector (purple dot-dashed line), $\leq 7 \times 10^{-5}$, its δ-marginalized sensitivity is seen to be the poorest. This happens due to the very strong δ-dependence of the probability at $L = 650$ km. On the other hand, the two baseline setups 2 (blue dotted line) and 3 (orange dashed line) which involve the magic baseline as well, show very little δ-dependence. Setup B (black solid line) apparently shows some δ-dependence despite having one of the detectors at the magic baseline because the near detector in this case is 10 times larger than the near detectors for setups 2 and 3. Therefore, while the δ-marginalized discovery reach of our proposed setup is similar to that for both the earlier two baseline setups, we see more δ-dependence here due to the 10 times larger detector at the shorter baseline. Note that while the flux is comparatively lower at the magic baseline, the probability is higher. The latter therefore compensates the effect of the former and we expect the same statistics per kton of the detector at both baselines. However, the detector size for water Čerenkovhas been taken as 10 times larger compared to magnetized iron or TASD. Therefore, the statistics at the water Čerenkovdetector at $L = 650$ km is 10 times larger compared to the statistics at the magnetized iron detector at $L = 7000$ km. For this reason, the results of setup 1 follows closely those of setup 4: the ultimate reach for our setup $\leq 2 \times 10^{-4}$, is also obtained for $\delta \simeq \pm 90°$.

CP discovery potential

The upper right hand panel shows the CP violation discovery potential. This is best at the shorter baselines. Thus, the facilities with larger number of events at short baseline outperform the others in their CP violation reach. This means that setup 4,from [274,275] has sensitivity to CP violation for the smallest values of , since the short baseline water Čerenkovdetector is exposed to the beam for ten years(*i.e.*, all the considered runtime). Unsolved sign degeneracies due to the lack of events at longer baselines, however, spoil the sensitivity for negative values of δ around $\sin^2 2\theta_{13} \sim 10^{-2}$ (the so-called "π-transit" [329]). This problem is solved when a magic baseline detector is added to the on-peak one. For this reason, no loss in the discovery potential is found for setups 1, 2 and 3 for particular values of θ_{13}. Notice that setup B has the next-to best performance (the near detector is exposed to the beam for five years instead of ten) and no π-transit problem. Finally ,the worst performance for CP violation is that of the setups 2 and 3, in which the near detector has a fiducial mass of 50 kton, only.

Sensitivity to the mass hierarchy

The lower panels show the sensitivity to the mass hierarchy. This is best at the far detectors and thus, the facilities with larger number of events at the magic baseline perform best. That explains the much smaller sensitivity of setup 4 from [274, 275] with no events at the longer baseline. The best sensitivities are in this case achieved for setup 3 from [320] due to the higher statistics granted by the larger gamma factor assumed of $\gamma = 656$ for both ^{8}B and ^{8}Li . This plots shows the advantage of accelerating the ions to higher energies. Since for the setup we propose here we restrict to the maximum γ attainable at the SPS+, which for ^{8}Li is $\gamma = 390$, the difference between the two setups is larger for the inverted hierarchy (lower right hand panel), where the sensitivity stems mainly from the antineutrinos from ^{8}Li decays. The ultimate sensitivity to the mass hierarchy for our setup is $\leq 1 \times 10^{-3} (4 \times 10^{-3})$ for normal (inverted) hierarchy, independently from δ. This must be compared with $\leq 6 \times 10^{-4} (1 \times 10^{-3})$ for normal (inverted) hierarchy, achievable with setup 3 [320].

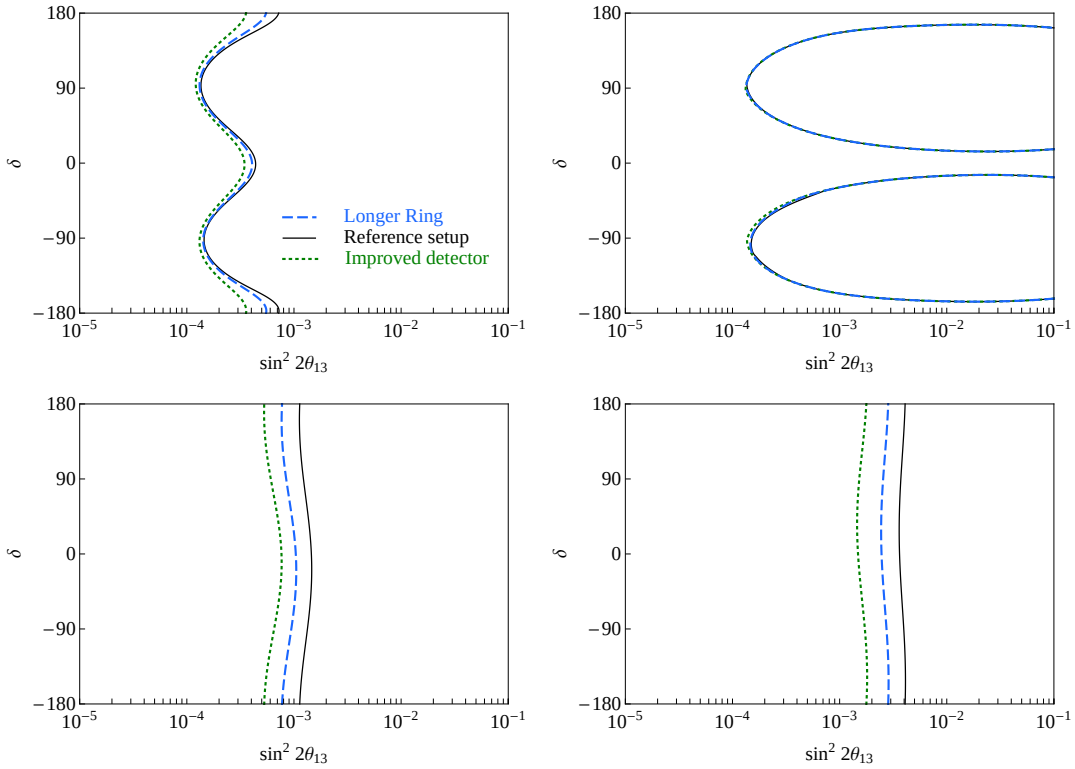

Figure 4.7: Comparison of setup B (black solid lines) with the setup with longer decay rings (blue dashed lines) and longer decay plus improved detector characteristics (green dotted lines). Comparisons are shown for the three performance indicators and the layout of the panels are as for Fig. 4.6.

Detector and decay ring specification dependence

In this subsection we study how stable the results presented here are to modifications of the experimental setup described. In particular, we focus on two effects. The first is the gain in number of useful ion decays by increasing the length of the straight sections of the storage ring. The second is the uncertainty on the achievable low energy threshold, efficiency and background at the iron detector. The sensitivity reach of our proposed setup is shown in Fig. 4.7 by the black solid lines. We first probe the effect of increasing the number of useful ion decays by increasing the length of the straight sections of the storage ring for ^{8}B and ^{8}Li ions. This is shown by the blue dashed lines where we restore the straight sections to 2500 km. This increases the ^{8}B and ^{8}Li flux at the far detector by 40% compared to the black reference lines of our setup. As it can be seen from the figure the impact of increasing the flux at the far detector is mainly on the sensitivity to the mass hierarchy (that becomes $\leq 8 \times 10^{-4} (3 \times 10^{-3})$ for normal and inverted hierarchy, respectively), but is still mild even for that observable. Smaller and more feasible designs of the decay rings are therefore possible without affecting significantly the physics reach of the proposed facility.

The second effect concerns the detector specifications. For the reference setup (black solid lines) we have assumed the same efficiencies and backgrounds as a function of the neutrino energy as those derived for the MIND detector when exposed to a NF beam in Ref. [313]. As we argued

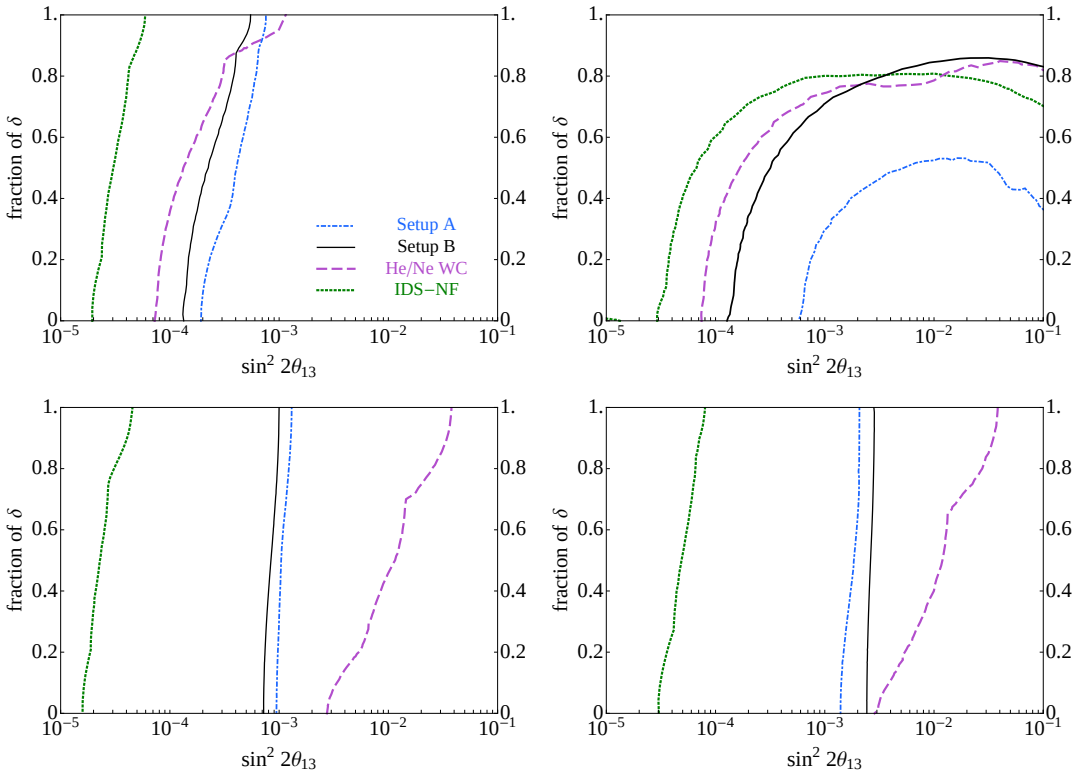

Figure 4.8: Comparison between setups A and B, the IDS-NF and the high-γ ^{6}He /^{18}Ne β-beam from Refs. [274, 275]. The upper left hand panel shows the sensitivity to , the upper right hand panels shows the CP discovery potential, and the lower panels show the sensitivity to the mass hierarchy. The lower left hand panel is obtained assuming normal hierarchy while the lower right hand panel shows the corresponding reach when inverted hierarchy is assumed.

above, this is a conservative choice for the β-beam , since this purer beam does not demand charge ID. Also, the spectrum is not as wide in energy as that of the NF and hence the problems with neutral current backgrounds are also less severe. However, the task of the iron detector at the long baseline is to determine the mass hierarchy and this will be achieved as long as the efficiency at around $6 - 7$ GeV is high enough to observe the matter resonance enhancement. The effect that a more optimistic assumption of a lower energy threshold of 1.5 GeV with a flat efficiency of 70% and background of 10^{-4} would imply for the different observables is shown in Fig. 4.7 by the green dotted lines. For these lines we also work with the longer decay ring with 40% more fluxes at the far detector. As it can be seen from the figure the gain is not very significant for any of the observables, this confirms that the challenging efficient discrimination of the lowest energy events mandatory for a NF, is not as critical for the setup proposed here.

4.4.3 Comparison with other high-energy future proposals

It is important to study how the sensitivities of the proposed set-ups compare with other facilities of the next-to-next generation proposals. We compare the performance of our two-baseline β-beam proposals (both setups A and B) with the other two facilities typically considered for the

small θ_{13} regime: the IDS-NF baseline design [322][11] and the high γ β-beam based on ^{6}He and ^{18}Ne of Refs. [274, 275]. For this comparison we present in Fig. 4.8 the same observables as in the previous figures but as a function of the fraction of the values of δ for which they can be discovered instead of the true values of δ.

From Fig. 4.8 it is clear that the facility with sensitivity to the different observables down to smallest values of is the Neutrino Factory. This can be understood from the very large fluxes assumed for the IDS baseline as compared to the ones assumed here for the β-beam set-ups: 10^{21} useful muon decays per year to be compared to the 3×10^{18} assumed for the β-beams . This translates into much higher statistics that provide sensitivities to smaller values of θ_{13}. On the other hand, the high energy of the Neutrino Factory beams implies a very small value of L/E_ν. This translates in a stronger suppression of the CP violating term of the oscillation probability with respect to the one suppressed by two powers of θ_{13} for large values of this parameter. Therefore, the CP discovery potential of β-beams outperforms that of the Neutrino Factory in Fig. 4.8 when $\sin^2 2\theta_{13} > 10^{-3}$. Since this large values of $\sin^2 2\theta_{13}$ also guarantee a discovery of the mass hierarchy and regardless of the value of δ, this makes β-beams the better option when $\sin^2 2\theta_{13} > 10^{-3}$. Furthermore, even if the statistics in the near β-beam detector is reduced by half in the present set-up compared to the one in Ref. [274, 275] in order to illuminate the second detector, the CP-discovery potential for $\sin^2 2\theta_{13} > 10^{-3}$ is better in the two-baseline set-up due to the lifting of the degeneracies that can mimic CP-conservation when combining the information from the two detectors.

[11] More recently, the mass of the detector placed at 4000 km in the baseline design has been changed from 50 kton to 100 kton [299]. However, a dramatic improvement in the performance of the facility is not expected from such upgrade, since the IDS-NF is not limited by statistics but by systematics.

5

NSI at Neutrino Factories

In this chapter, we present the results obtained in Ref. [24]. As it was already explained in Ch. 1, Non-Standard Interactions (NSI) can be studied from a top-down or a bottom-up approach. In the top-down approach, a given model of NP is studied, and the corresponding set of low-energy effective operators are derived systematically. Being these operators derived from a fundamental theory, their coefficients are related and (usually) stringent bounds exist between them. In the bottom-up approach, on the other hand, all the effective four-fermion operators which can affect neutrino oscillations are included in the analysis, and the experimental bounds are used to constrain their coefficients independently of the model. This latter approach is clearly model independent, in the sense that no assumption is made regarding the model of NP behind and, consequently, the possible relations between operators. Bounds obtained in this way are looser than in the top-down approach, but apply to a wide variety of high-energy extensions of the Standard Model.

In the bottom-up approach, NSI that modify neutrino production, propagation and detection processes must be included [330–333]. Such a large number of new parameters in the analysis, however, makes it extremely difficult to extract any useful information from the results. It is a standard strategy, thus, to separate the study of NSI in neutrino propagation in matter from the NSI effects in production and detection. The latter can be studied using near detectors [334, 335][1]. This is the strategy that we follow in this chapter. We introduce all the operators that modify neutrino propagation in matter at once, adding nine new parameters (six moduli and three phases) to the existing νSM parameter space. A complete analysis with such a huge number of parameters is extremely demanding, from both the numerical and analytical point of view. For this reason the effects of NSI in matter propagation have been widely explored in the literature turning on only one new parameter in the analysis, or two at most (one modulus and one phase) [337–339]. In this work, we try to achieve two main goals: (1) We attempt a first complete phenomenological analysis of the potential of HENF to constrain all the NSI parameters which can contribute to propagation in matter; (2) We illuminate complicated correlations between the effects of NSI and νSM CP violating phases.

In order to illustrate which features of the particular NF setup will be helpful in disentangling the correlations between the different NSI parameters and which features will be more relevant in order to observe a CP violating signal, the results will be presented for three different NF-based setups. These correspond to the standard IDS-NF setup, and two modified options where neutrinos are produced from the decay of muons with $E_\mu = 50$ GeV: the first one corresponds to a higher energy version of the standard IDS-NF setup; while for the second one only one baseline is considered, and a small detector provided with τ detection capability is added to the standard

[1] Notice, however, that near detectors will necessarily put bounds on the combination of NSI in production and detection processes. Several near detectors with different sources and/or target materials could be used to disentangle them [336].

MIND detector considered in the IDS-NF standard setup.

This chapter is structured as follows. Sec. 5.1 is dedicated to introduce the formalism of NSI in neutrino propagation, and the main features of the analytical probabilities (in presence of NSI) in App. B. In Sec. 5.2, the three NF setups under study are explained in detail, whereas in Sec. **??** the input values and the marginalization procedure used in Secs. 5.4 and 5.5 are introduced. In Secs. 5.4 and 5.5, the sensitivities to θ_{13} (in presence of NSI) and to all NSI parameters are studied. Throughout the study, we paid special attention to existing correlations between the whole set of parameters, and we found that these can be divided in two sectors which are mainly uncorrelated from each other. In Sec. 5.4 we present the sensitivities to θ_{13}, $\epsilon_{e\mu}$ and $\epsilon_{e\tau}$, which are achieved mainly through the $P_{e\mu}$ and $P_{e\tau}$ oscillation channels, whereas in Sec. 5.5 we summarize our results for the sensitivities to $\epsilon_{\mu\tau}$ and the diagonal NSI parameters, which are achieved mainly through the $P_{\mu\mu}$ disappearance channel. Finally, in Sec. 5.6 we study the CP discovery potential of the three setups in presence of NSI. In doing so, we pay special attention to complicated correlations existing between the standard and non-standard CP violating phases. A generalization of the CP-fraction concept for the case where there are several CP violating phases is introduced, and the synergy between detectors and baselines is analyzed for the different setups. For technical details related to the statistical approaches that have been followed throughout this chapter, we refer the interested reader to App. C.

5.1 Neutrino Oscillations with Non-Standard Interactions

Following the model independent approach, NSI in neutrino propagation (from here on, we will refer to them simply as NSI) are described through the inclusion of the four fermion effective operators in Eq. (1.29). Nevertheless, from neutrino oscillations we have no information on the separate contribution of a given operator with coefficient $\varepsilon^{fP}_{\alpha\beta}$, but only on their sum over flavours and chirality. The effects of these operators appear in the neutrino evolution equation, in the flavour basis[2], as:

$$i\frac{d}{dt}\begin{pmatrix}\nu_e\\ \nu_\mu\\ \nu_\tau\end{pmatrix} = \left[U\begin{pmatrix}0&0&0\\0&\Delta_{21}&0\\0&0&\Delta_{31}\end{pmatrix}U^\dagger + A\begin{pmatrix}1+\epsilon_{ee}&\epsilon_{e\mu}&\epsilon_{e\tau}\\ \epsilon^*_{e\mu}&\epsilon_{\mu\mu}&\epsilon_{\mu\tau}\\ \epsilon^*_{e\tau}&\epsilon^*_{\mu\tau}&\epsilon_{\tau\tau}\end{pmatrix}\right]\begin{pmatrix}\nu_e\\ \nu_\mu\\ \nu_\tau\end{pmatrix}, \qquad (5.1)$$

where $\Delta_{ij} = \Delta m^2_{ij}/2E$, U is the PMNS matrix, $A \equiv 2\sqrt{2}G_F n_e$ and $\epsilon_{\alpha\beta} \equiv (1/n_e)\sum_{f,P} n_f \varepsilon^{fP}_{\alpha\beta}$, with n_f the f-type fermion number density. The three diagonal entries of the modified matter potential are real parameters. Only two of them affect neutrino oscillations: we will consider the combinations $\epsilon_{ee} - \epsilon_{\tau\tau}$ and $\epsilon_{\mu\mu} - \epsilon_{\tau\tau}$, subtracting $\epsilon_{\tau\tau} \times \mathbf{I}$ from the Hamiltonian. The three complex NSI parameters $\epsilon_{e\mu}, \epsilon_{e\tau}$ and $\epsilon_{\mu\tau}$ will be parametrized as [3] $\epsilon_{\alpha\beta} = |\epsilon_{\alpha\beta}|e^{-i\phi_{\alpha\beta}}$.

In order to understand the impact of different NSI parameters in various oscillation channels it is useful to obtain approximate analytical expressions for the oscillation probabilities. In Ref. [341] approximate formulæ were derived for all the oscillation probabilities up to order ε^2 (ε^3 for the golden channel) by making a perturbative expansion in $\Delta m^2_{21}/\Delta m^2_{31} \equiv \varepsilon$ and $\epsilon_{\alpha\beta} \sim \theta_{13} \sim \varepsilon$. In App. B the approximate expressions for $P_{e\mu}, P_{e\tau}, P_{\mu\mu}$ and $P_{\mu\tau}$ are presented up to second order in ε, expanding in $\Delta m^2_{21}/\Delta m^2_{31}, \epsilon_{\alpha\beta}, \theta_{13}$ and $\delta\theta_{23} \equiv \theta_{23} - \pi/4$, too.

Let us review very briefly the main conclusions which can be extracted from this analytical study:

[2] If production or detection NSI were present, though, the effective production and detection flavour eigenstates would not coincide with the standard flavour ones [340].

[3] This is the prescription used in the MonteCUBES software. In the section devoted to CP violation, though, the prescription is precisely the opposite, $\epsilon_{\alpha\beta} \equiv |\epsilon_{\alpha\beta}|e^{i\phi_{\alpha\beta}}$.

- Up to second order in ε, $P_{e\mu}$ and $P_{e\tau}$ depend only on $\epsilon_{e\mu}$ and $\epsilon_{e\tau}$ but not on the rest of the NSI parameters (see Eq. (B.4) and Eq. (B.5) in App. B). The precise determination of these two NSI elements is only possible in the golden and the silver channels. However, it is well-known that already in the νSM case a combination of data, either from different oscillation channels or different baselines, is needed in order to avoid the well known degeneracy problem [168, 169, 171]. This problem is even more difficult to solve in presence of NSI, because four extra parameters (2 moduli and 2 phases) appear simultaneously in the golden and silver channels and severe correlations are expected to exist, not only between NSI parameters but also between them and the νSM ones.

- The $P_{\mu\mu}$ and $P_{\mu\tau}$ oscillation probabilities show a leading $\mathcal{O}(\varepsilon)$ dependence on the real part of $\epsilon_{\mu\tau}$ (which provides a very high sensitivity to this parameter), in addition to the usual quadratic dependence on $\epsilon_{e\mu}$ and $\epsilon_{e\tau}$ as in the golden and silver channels. On the other hand, the sensitivity to the imaginary part of $\epsilon_{\mu\tau}$ is expected to be much worse, since it comes only through $\mathcal{O}(\varepsilon^2)$ terms in the probability. The dependence on the diagonal combination $(\epsilon_{\mu\mu} - \epsilon_{\tau\tau})$ appears in $P_{\mu\mu}$ and $P_{\mu\tau}$ at $\mathcal{O}(\varepsilon^2)$, too. Terms proportional to $\delta\theta_{23}(\epsilon_{\mu\mu} - \epsilon_{\tau\tau})$ lead to important correlations between these two parameters.

- The dependece on $(\epsilon_{\mu\mu} - \epsilon_{\tau\tau})$ and $\epsilon_{\mu\tau}$ in $P_{\mu\mu}$ and $P_{\mu\tau}$ is the same. Therefore, the $\nu_\mu \to \nu_\tau$ channel may be useful only because it adds further statistics at the detector. However, the sensitivities to $\epsilon_{\alpha\alpha}$ and $\epsilon_{\mu\tau}$ are not limited by statistics, since the disappearance channel alone already provides enough events at the detector. As a consequence, the sensitivities to these parameters are mainly achieved through the $P_{\mu\mu}$ channel.

- The dependence on the diagonal combination $(\epsilon_{ee} - \epsilon_{\tau\tau})$ appears at third order in ε in the oscillation probabilities. Therefore, it is hard to expect a good sensitivity to this parameter. Moreover, as we can see in Eq. (5.1), when all NSI parameters vanish except for the combination $(\epsilon_{ee} - \epsilon_{\tau\tau})$, $A\,(\epsilon_{ee} - \epsilon_{\tau\tau})$ can be interpreted as a small perturbation on the standard νSM matter effect. Therefore, our sensitivity to $(\epsilon_{ee} - \epsilon_{\tau\tau})$ will be ultimately limited by uncertainties of the earth matter density.

In view of the features listed above, in the following we are going to distinguish two different groups of oscillation parameters: (i) θ_{13}, $\epsilon_{e\mu}$ and $\epsilon_{e\tau}$, that will be studied in Sec. 5.4, and (ii) $(\epsilon_{ee} - \epsilon_{\tau\tau})$, $(\epsilon_{\mu\mu} - \epsilon_{\tau\tau})$ and $\epsilon_{\mu\tau}$, that will be studied in Sec. 5.5. This classification is the natural consequence of the fact that, in practice, $P_{e\mu}$ and $P_{e\tau}$ are sensitive to (i), while the sensitivity to (ii) comes mainly from $P_{\mu\mu}$. The only possible exception to this classification is $(\epsilon_{ee} - \epsilon_{\tau\tau})$, for which the golden channel also plays an important role. Because of this structure, strong correlations between (i) and (ii) are not expected, as it has indeed been found in our numerical simulations. For this reason, we will study in Sec. 5.6 the CP discovery potential of the HENF for all the parameters belonging to (i) simultaneously (as strong correlations are expected between them), whilst neglecting parameters belonging to (ii).

5.2 The Neutrino Factory

In a Neutrino Factory (NF), muons are accelerated from an intense source to energies of several tens of GeV and injected into a storage ring with very long straight sections [342–345]. These muons decay through the processes $\mu^+ \to e^+\nu_e\bar{\nu}_\mu$ and $\mu^- \to e^-\bar{\nu}_e\nu_\mu$, providing a very well known flux (see Fig. 5.1) of neutrinos with energies up to the muon energy itself. In the laboratory frame,

the neutrino fluxes, boosted along the muon momentum vector, are given by [325]:

$$\begin{aligned}
\frac{d^2N_{\bar{\nu}_\mu,\nu_\mu}}{dyd\Omega} &= \frac{4n_\mu}{\pi L^2 m_\mu^6}\; E_\mu^4 y^2\,(1-\beta\cos\varphi)\;\left\{\left[3m_\mu^2-4E_\mu^2 y\,(1-\beta\cos\varphi)\right]\right. \\
&\quad \left.\mp\,\mathcal{P}_\mu\left[m_\mu^2-4E_\mu^2 y\,(1-\beta\cos\varphi)\right]\right\}\,, \\
\frac{d^2N_{\nu_e,\bar{\nu}_e}}{dyd\Omega} &= \frac{24n_\mu}{\pi L^2 m_\mu^6}\; E_\mu^4 y^2\,(1-\beta\cos\varphi)\;\left\{\left[m_\mu^2-2E_\mu^2 y\,(1-\beta\cos\varphi)\right]\right. \\
&\quad \left.\mp\,\mathcal{P}_\mu\left[m_\mu^2-2E_\mu^2 y\,(1-\beta\cos\varphi)\right]\right\}\,. \qquad (5.2)
\end{aligned}$$

Here, $\beta=\sqrt{1-m_\mu^2/E_\mu^2}$, E_μ is the parent muon energy, $y=E_\nu/E_\mu$, n_μ is the number of useful muons per year obtained from the storage ring, $\mathcal{P}_\mu$ is the polarization of the decaying muon and L is the distance to the detector. φ is the angle between the beam axis and the direction pointing towards the detector, assumed to be located in the forward direction of the muon beam. The angular divergence will be taken as constant, $\delta\varphi\sim 0.1$ mr.

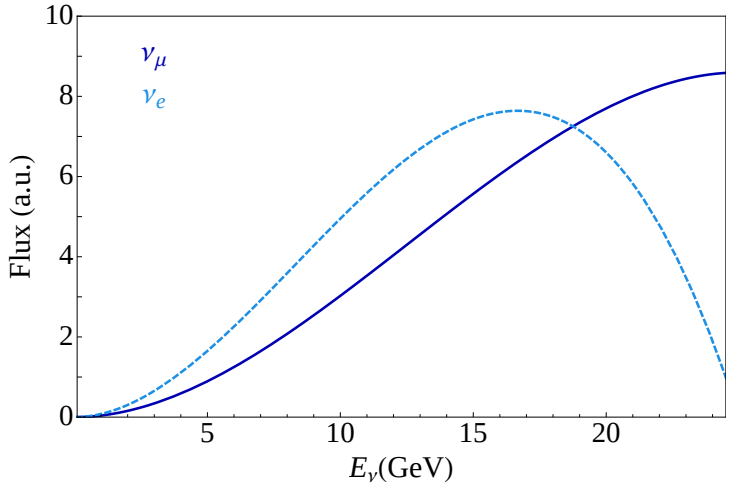

Figure 5.1: Electron and muon neutrino fluxes for a 25 GeV NF, measured at 100 km from the source, as a function of the neutrino energy.

Neutrino Factory designs have been proposed in Europe, US and Japan. The conclusion of these studies is that an accelerator complex capable of providing $\sim 10^{21}$ muon decays per year can be built.

One of the most striking features of the Neutrino Factory is the precision with which the characteristics of all components of the beam would be known. In addition to this, a total of twelve oscillation processes can be studied using the Neutrino Factory, which can store beams of both positive and negative muons. In order to take full advantage of this flavour-richness, the optimal detector should be able to perform both appearance and disappearance experiments, providing lepton identification and charge discrimination: for example, a 50-Kton MINOS-like magnetised-iron detector to study the golden channel, plus a 5-10 Kton emulsion cloud chamber or a 15 Kton magnetised liquid-argon TPC detector to look for $\nu_e\to\nu_\tau$ and $\nu_\mu\to\nu_e$ oscillations.

The $\nu_e\to\nu_\mu$ transition appears to be particularly attractive at the Neutrino Factory. It can be studied in appearance mode, by looking for muons with charge opposite to that of the stored

muon beam, thus strongly reducing the dominant background ("right-sign muons" and charmed-meson decays). This yields an impressive sensitivity to $\sin^2\theta_{13}$ and sensitivity to the leptonic CP-violating phase δ. Another important feature of the Neutrino Factory is that it is the only facility that could exploit the $\nu_e \to \nu_\tau$ and the $\nu_\mu \to \nu_\tau$ channels, as the average energy of neutrinos produced must be high enough to produce τ CC events if we want to study these oscillation channels. The "standard" Neutrino Factory refers to a facility in which a 50 GeV stored-muon beam delivers a luminosity of 1×10^{21} muon decays per year.

5.2.1 Neutrino Factory setups

At a NF, intense ν_e and ν_μ beams are available as decay products of muons (with both polarities) circulating in storage ring(s). As a consequence, a total of twelve different oscillation channels could in principle be studied. The *International Design Study for a Neutrino Factory* [346], as already mentioned, has undertaken the task of defining the optimal setup to have good sensitivity to θ_{13}, δ, and to the neutrino mass hierarchy, sign(Δm^2_{23}). This resulted in what we will refer to as the IDS25 setup hereafter: a HENF with a muon beam energy of 25 GeV, and 10^{21} useful muon decays per year aimed at two identical 50 kton MIND detectors located at two different baselines to look for ν_μ appearance events[4]. The detector located at $L = 4000$ km (which will be referred to as "intermediate baseline" from now on, to distinguish it from the short baseline where a near detector will be located[5]) is optimized to have sensitivity to the CP-violating phase δ. It, however, suffers from a severe degeneracy problem [168, 169, 171], that can be solved locating an additional "far" detector at the so-called "magic" baseline (7500 km) [168,179]. This second detector increases significantly the potential of the NF to measure the mass hierarchy, taking advantage of matter effects.

If a HENF is to be optimized to detect effects of NSI, several issues must be understood: which energy and baseline would be the best; how and to what extent the synergy between two detectors help; and, if there are any ways of optimization in order to achieve good sensitivities to both νSM and NSI parameters. Some of these problems were addressed in [347], concluding that a setting similar to IDS25 but with higher muon energies (such as 50 GeV) would be preferred to look for NSI. This is easily explained by the fact that, since NSI in propagation are introduced as an effective matter potential, an increase in the average neutrino energy will improve the relative significance of the NSI with respect to the leading standard oscillations in vacuum. This was indeed confirmed in Ref. [337] where, however, it was found that the improvement with respect to the 25 GeV setup was not very large (see, also, Ref. [339]). All of these works were performed within the ad-hoc assumption of having only one $\epsilon_{\alpha\beta}$ at a time. One of the goals of this work is indeed to check if the results obtained in these analyses survive when correlations between the various NSI parameters are taken into account. Armed with MonteCUBES, we examine this problem by comparing the sensitivity to NSI of the IDS25 and of a variant of the IDS setup with the same detectors but with parent muon energy $E_\mu = 50$ GeV when all NSI parameters are turned on simultaneously. The new setup, for obvious reasons, will be called as IDS50.

We will also check the potential of the two detectors to reduce the strong correlations between νSM and NSI parameters and within different NSI parameters, to test if this detector combination can be optimized or not for NP searches. For this reason, the performance of the two setups above, in which two identical detectors looking for $\nu_e \to \nu_\mu$ and $\nu_\mu \to \nu_\mu$ oscillations are located at different baselines, will be compared with the performance of a HENF setup in which two different detectors, one of which is equipped with τ-identification capability (that could, thus, profit of the $\nu_e \to \nu_\tau$ and $\nu_\mu \to \nu_\tau$ channels), are located at one single baseline at 4000 km. Initially, $L = 2000$

[4] Notice that, in the latest IDS design, the MIND located at the intermediate baseline is 100 kton.
[5] We will not consider such a near detector in our analysis, though.

and $L = 3000$ km were also considered as alternative baselines. They give similar results, although the 4000 km performs slightly better, and therefore will not be considered here. This setup will be called 1B50. Notice that the parent muon energy for the 1B50 setup has to be large enough to overcome the smallness of the $\nu_\tau N$ cross-section due to the τ production threshold below 4 GeV [348] and get larger statistics at the detector. For this reason, also for this setup we fix $E_\mu = 50$ GeV. Notice that the advantage of aiming at one site is two-fold: on one side, we avoid the technical difficulties of aiming one of the beams at a detector located al $L = 7500$ km (with a tilt angle of the storage ring of $\sim 36^\circ$ [349]); on the other side, as only one storage ring is needed all muon decays are aimed to the same site, therefore doubling the statistics at the detector.

The characteristic features of the three setups (IDS25, IDS50 and 1B50) are resumed in Tab. 5.1, where we remind the parent muon energy, the detectors location and technologies and the neutrino flux aiming at each detector per year. For all setups we consider 5 years of data taking for each muon polarity[6].

	IDS25	IDS50	1B50
E_μ	25 GeV	50 GeV	50 GeV
D_1	MIND@4000 km	MIND@4000 km	MIND@4000 km
D_2	MIND@7500 km	MIND@7500 km	MECC@4000 km
Φ_1	5×10^{20}	5×10^{20}	1×10^{21}
Φ_2	5×10^{20}	5×10^{20}	1×10^{21}

Table 5.1: The characteristics of the three considered setups. From top to bottom: the parent muon energy E_μ; the technology and location of the two detectors, D_1 and D_2; the number of useful muon decays per year aiming at each of the two detectors, Φ_1 and Φ_2.

The characteristic features of the two types of detector are summarized in Tab. 5.2. For technical details on these parameters, we address the interested reader to Refs. [313] and [350,351].

	$\sigma(E)$	f_S	f_B	Mass
MIND	$0.55\sqrt{E}$	2.5%	20%	50 kton
MECC	$0.2E$	15%	20%	4 kton

Table 5.2: Main characteristics of the two detectors technologies. From left to right: energy resolution, $\sigma(E)$; systematic error over the signal, f_S; systematic error over the background, f_B; detector mass.

In the analyses of Secs. 5.4 and 5.5, data have been distributed in bins of the reconstructed neutrino energy with the following size: $\Delta E_\nu = 1$ GeV for $E_\nu \in [1, 10]$ GeV; $\Delta E_\nu = 2.5$ GeV

[6] We assume that the experiment is run on the two polarities separately. This means that we are considering a total number of useful muon decays per baseline and polarity of $5 \times 5 \times 10^{20} = 2.5 \times 10^{21}$. Notice that this is completely equivalent to consider 10 years of data taking per polarity but with 2.5×10^{20} useful muon decays per baseline, year and polarity. This last option corresponds to the setup where muons of both polarities are circulating at the same time in the decay ring(s).

for $E_\nu \in [10, 15]$ GeV; $\Delta E_\nu = 5$ GeV for $E_\nu \geq 15$ GeV. This binning applies to all setups and detector technologies. In Sec. 5.6, on the other hand, data have been distributed in bins of equal size: $\Delta E_\nu = 5$ GeV for the IDS25; $\Delta E_\nu = 10$ GeV for the IDS50, 1B50 (both for the MIND and the MECC technologies).

The efficiencies for the MIND and the MECC detector technologies as a function of the reconstructed neutrino energy are shown in Fig. 5.2. The ν_μ identification efficiency at MIND has been taken from Ref. [313]. The ν_τ identification efficiency at MECC corresponds to the efficiency of the ECC for the silver channel $\nu_e \to \nu_\tau$ as computed in Ref. [352] multiplied by a factor of five to take into account the capability of the MECC to look for taus not only through their decay into muons (as for the ECC) but also into electrons and hadrons (see a detailed discussion in Ref. [350] regarding this point). The cross-sections have been taken from Refs. [266, 267].

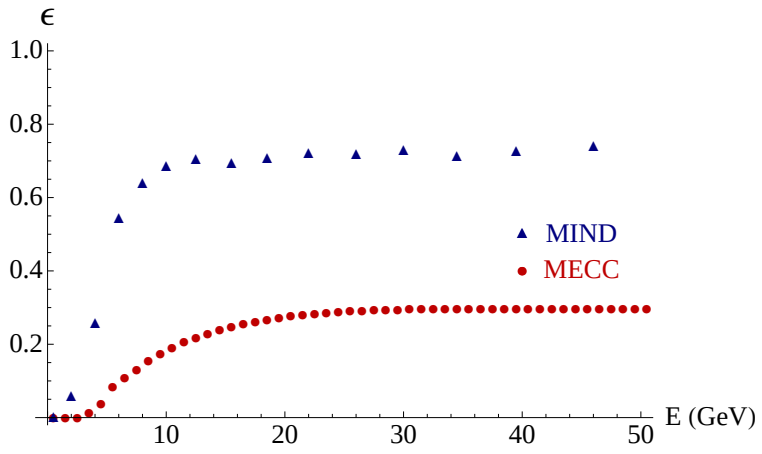

Figure 5.2: Efficiency of the MIND (blue triangles) and MECC (red circles) detectors as a function of the neutrino energy. The MIND efficiency has been taken from Ref. [313]. The MECC efficiency corresponds to the ECC efficiency [352] multiplied by a factor of five (see text for details).

Table 5.3 shows the number of events in the golden (silver) channel per kton×year at a MIND (MECC) detector with perfect efficiency, located at 4000 km from the source, for a 50 GeV NF. Normal hierarchy has been assumed, and results are shown for $\delta = \pm 90°$, and for two different values of $\theta_{13} = 0, 3°$. In order to illustrate the effect when NSI are included in the analysis, we show the total number of events at the detector also in presence of NSI, $\epsilon_{e\mu} = \epsilon_{e\tau} = 10^{-2}$. The two NSI CP violating phases have been set to zero. As it can be seen from the table, the number of events in the silver channel is very small for vanishing θ_{13}.

5.3 Input parameters and marginalization procedure

Unless otherwise stated, the input values taken in this chapter for the atmospheric and the solar parameters are: $\Delta\bar{m}^2_{21} = 7.59 \times 10^{-5}\text{eV}^2$, $\bar{\theta}_{12} = 34°$, $\Delta\bar{m}^2_{31} = 2.45 \times 10^{-3}\text{eV}^2$, $\bar{\theta}_{23} = 45.5°$ [152]. In all the simulations, the matter density has been taken according to the PREM density profile [181] assuming a 5% error. The sign of the atmospheric mass difference, $sgn(\Delta m^2_{31})$, has been chosen to be positive throughout the paper and marginalization over it will not be considered.

In all the simulations presented in Secs. 5.4 and 5.5 we have marginalized over the whole set

δ	Channel	$\theta_{13}=0$ $\epsilon_{\alpha\beta}=0$	$\theta_{13}=0$ $\epsilon_{e\mu}=\epsilon_{e\tau}=10^{-2}$	$\theta_{13}=3^\circ$ $\epsilon_{\alpha\beta}=0$	$\theta_{13}=3^\circ$ $\epsilon_{e\mu}=\epsilon_{e\tau}=10^{-2}$
$+90^\circ$	$\nu_e \to \nu_\mu$	2.75	44.93	66.70	108.54
	$\nu_e \to \nu_\tau$	1.08	7.97	15.63	22.60
-90°	$\nu_e \to \nu_\mu$	2.75	44.93	41.69	83.96
	$\nu_e \to \nu_\tau$	1.08	7.97	23.77	30.56

Table 5.3: Total number of events per year for the golden (silver) channel, measured at a 1 kton MIND (MECC) detector with perfect efficiency located at $L = 4000$ km from the source, for a 50 GeV NF. Normal hierarchy has been assumed. Results are presented for $\delta = \pm 90^\circ$ and for two different values of $\theta_{13} = 0, 3^\circ$, with and without including NSI effects in the golden sector. The two NSI CP violating phases have been set to zero: $\phi_{e\mu} = \phi_{e\tau} = 0^\circ$.

of νSM parameters. A gaussian prior distribution centered on the input values given above with variance $\sigma = 0.08(0.03)$ has been assumed for the atmospheric (solar) parameters. On the other hand, marginalization over θ_{13} and δ has also been performed assuming a flat prior distribution.

In Secs. 5.4 and 5.5 we have also marginalized over the NSI parameters $\epsilon_{\alpha\beta}$, that is, over both their moduli $|\epsilon_{\alpha\beta}|$ and phases $\phi_{\alpha\beta}$. Gaussian priors, in agreement with the bounds computed in Ref. [71], are taken into account for all the moduli of the NSI parameters around their input values, which have been set to zero throughout the next two sections. Notice that for the NSI phases no prior knowledge has been taken into account (*i.e.*, $\pi(\theta) = 1$), since we do not have any information about these phases yet. We will refer the above procedure involving νSM and NSI parameters as the *"standard marginalization procedure"* hereafter.

5.4 Sensitivities achieved mainly through the $\nu_e \to \nu_\mu$ and $\nu_e \to \nu_\tau$ channels

As we stressed in Sec. 5.1, the sensitivity to NSI parameters comes from different oscillation channels depending on the considered parameter. In this section, we study the sensitivities to $\epsilon_{e\mu}$ and $\epsilon_{e\tau}$ which would be achieved mostly through the golden (and, to a lesser extent, also through the silver) channel for the three setups under study. Since the sensitivity to the νSM parameter θ_{13} (which is the key to the measurement of δ and of the mass hierarchy, too) is also achieved through the same oscillation channels, we will examine first the question of how and to what extent the inclusion of NSI affects the sensitivity to θ_{13} (Sec. 5.4.1). We will, then, study the sensitivities to the moduli of $\epsilon_{e\mu}$ and $\epsilon_{e\tau}$ as a function of their respective CP violating phases, through which some features of the synergy between two detectors/baselines will be illuminated depending upon the settings (Sec. 5.4.2). To show the effect of the correlations between the NSI parameters and with θ_{13}, the standard marginalization procedure defined in App. C will not be always used. We will specify in each case the procedure adopted. We remind the readers that $sgn(\Delta m^2_{31})$ is kept fixed throughout this work. This point has to be kept in mind when interpreting the results.

To conclude the preamble, we describe the layout of the figures: in figures with three

columns, the left, middle and right panels correspond to the results for the IDS25, IDS50 and 1B50 settings, respectively. Red, green and blue lines correspond to 68%, 90% and 95% 2 d.o.f.'s CL contours, respectively. Whenever we depart from the standard format we will give a note in the caption of the corresponding figure to specify the layout.

5.4.1 Impact of the NSI on the measurement of θ_{13}

In Fig. 5.3 we show the sensitivity to θ_{13} as a function of δ when the NSI parameters, in addition to the νSM ones, are also taken into account during marginalization. In top panels, marginalization over $\epsilon_{\alpha\alpha}$ ($\alpha = e, \mu, \tau$), $\epsilon_{e\mu}$ and $\epsilon_{e\tau}$ is performed; in bottom panels, the marginalization procedure is done over $\epsilon_{\alpha\alpha}$ and $\epsilon_{\mu\tau}$. As a reference, we also present the 68% CL sensitivity to θ_{13} obtained without considering NSI in the analysis, represented by the dotted black lines[7]. It can be clearly seen that the impact of the presence of NSI degrees of freedom on sensitivity to θ_{13} is much more significant in top panels than in bottom panels. When marginalization is performed over $\epsilon_{e\mu}$ and $\epsilon_{e\tau}$, the degree of sensitivity loss ranges from a factor 3 (IDS50) to almost an order of magnitude (1B50) with respect to the νSM result. On the other hand, the effects of marginalization over $\epsilon_{\alpha\alpha}$ and $\epsilon_{\mu\tau}$ are quite mild, leading to a sensitivity loss of a factor of 3 (1B50), at most. We have checked that the above sensitivity loss comes from the marginalization over $\epsilon_{\alpha\alpha}$, and not over $\epsilon_{\mu\tau}$ which is effectively decoupled from θ_{13}. Approximate decoupling between the two parameter sets (θ_{13}, $\epsilon_{e\mu}$, $\epsilon_{e\tau}$) and ($\epsilon_{\alpha\alpha}$, $\epsilon_{\mu\tau}$) is consistent with the expectation from the perturbative analysis [341] (see App. B), as explained in Sec. 5.1: in a nutshell, the golden (and silver) channel oscillation probabilities (that dominate the sensitivity to θ_{13}) only depend on $\epsilon_{e\mu}$ and $\epsilon_{e\tau}$ up to second order in ε.

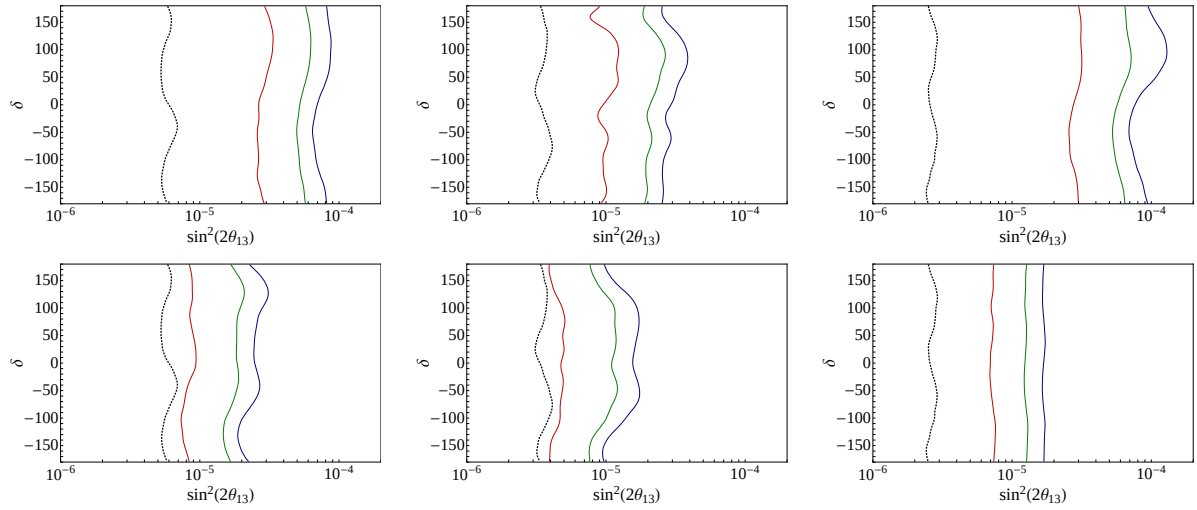

Figure 5.3: 68%, 90% and 95% CL contours for the sensitivity to θ_{13} as a function of δ for the case with NSI, compared to the 68% CL contour for the sensitivity to θ_{13} in the absence of NSI (represented by the black dotted line). Marginalization was performed over the νSM parameters, the diagonal NSI parameters $\epsilon_{\alpha\alpha}$ and either $\epsilon_{e\mu}$ and $\epsilon_{e\tau}$ (top panels) or $\epsilon_{\mu\tau}$ (bottom panels). The left, middle, and right panels show the results obtained for IDS25, IDS50, and 1B50 setups, respectively.

[7] We have checked that our results for the νSM θ_{13}-sensitivity are in reasonable agreement with those reported in the literature (see, for example, Ref. [322]).

A careful comparison between the three upper panels reveals an interesting feature: the severe impact on the sensitivity to θ_{13} observed at the 1B50 setup is largely (moderately) overcome in the IDS50 (IDS25) setups. Sensitivity to θ_{13} at the two baseline settings is robust against inclusion of NSI because they probe generalized matter effects at two different distances, a particular type of the synergy between the intermediate and far detectors [347].

In summary, in spite of the fact that the 1B50 setup apparently yields the best sensitivity to θ_{13} in absence of NSI (which is likely to be due to the doubled flux with respect to the IDS25 and IDS50 setups), its worsening after marginalization over $\epsilon_{e\mu}$ and $\epsilon_{e\tau}$, strongly correlated with θ_{13}, is much more severe due to the lack of the magic baseline detector.

5.4.2 Sensitivity to $\epsilon_{e\mu}$ and $\epsilon_{e\tau}$

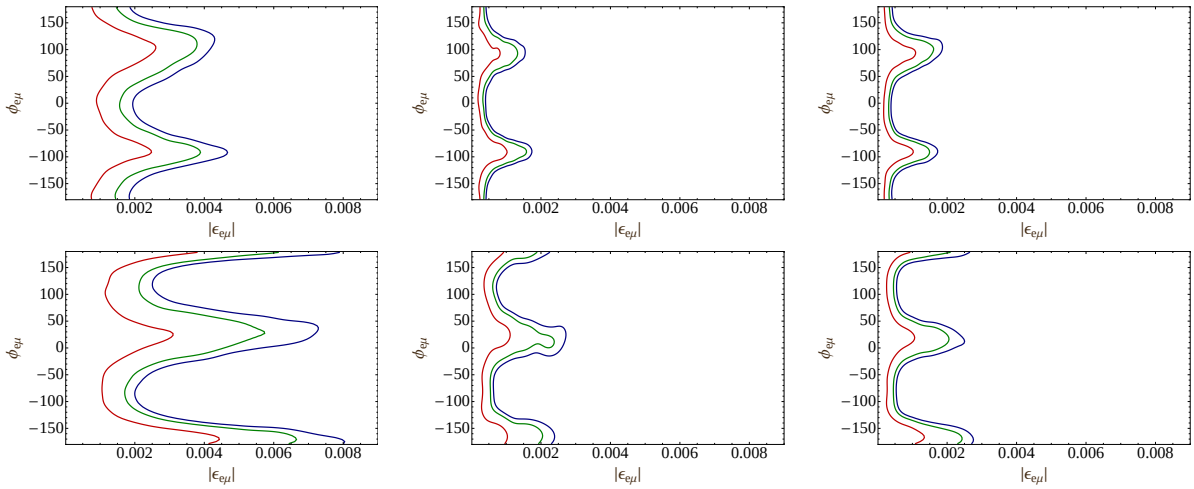

Figure 5.4: 68%, 90% and 95% CL contours for the sensitivity to $\epsilon_{e\mu}$ as a function of $\phi_{e\mu}$ for $\bar{\theta}_{13} = 0$ (upper panels) and $\bar{\theta}_{13} = 3°; \bar{\delta} = -\pi/2$ (lower panels). Marginalization has been performed over the νSM parameters, the diagonal NSI parameters $\epsilon_{\alpha\alpha}$ and $\epsilon_{e\tau}$. The left, middle, and right panels show the results obtained for IDS25, IDS50, and 1B50 setups, respectively.

In Fig. 5.4 (5.5) we present the sensitivity to $|\epsilon_{e\mu}|$ ($|\epsilon_{e\tau}|$) for $\bar{\theta}_{13} = 0$ (upper panels) and $\bar{\theta}_{13} = 3°; \bar{\delta} = -\pi/2$ (lower panels) as a function of $\phi_{e\mu}$ ($\phi_{e\tau}$), respectively. For all panels, the standard marginalization procedure defined in Sec. 5.3 is carried out, albeit neglecting marginalization over $\epsilon_{\mu\tau}$ (which is totally uncorrelated from $|\epsilon_{e\mu}|$ and $|\epsilon_{e\tau}|$, as we have checked).

We first discuss the results in Fig. 5.4. The most important remark is that both high-energy setups (IDS50 and 1B50) present similar performances, with sensitivities that are much better than that of IDS25 both for $\bar{\theta}_{13} = 0$ and $\bar{\theta}_{13} = 3°$. The fact that both IDS50 and 1B50 give sensitivities to $|\epsilon_{e\mu}|$ that are extremely similar implies that the improvement with respect to the IDS25 is due to the increase in energy, in agreement with our expectation for preferring higher energies for NSI searches. It can also be seen that the dependence of the sensitivity to $|\epsilon_{e\mu}|$ on $\phi_{e\mu}$ is stronger for $\bar{\theta}_{13} \neq 0°$ (bottom panels) than in the case of $\bar{\theta}_{13} = 0$.

In Fig. 5.5 we can see that the results obtained for the sensitivity to $|\epsilon_{e\tau}|$ are quite different from those found for $|\epsilon_{e\mu}|$. For vanishing $\bar{\theta}_{13}$, it can be seen that the IDS50 setup is better than the IDS25 and the 1B50 by a factor of $\simeq$1.7 and a few, respectively. When $\bar{\theta}_{13}$ is increased to

$\bar{\theta}_{13} = 3°$, the sensitivity to $\epsilon_{e\tau}$ becomes worse by a factor of $\simeq$2 or so, independently on the setups: the relative performance of the three setups remains almost the same as in the case of $\bar{\theta}_{13} = 0$. Notice that for the sensitivity to $|\epsilon_{e\tau}|$, unlike for $|\epsilon_{e\mu}|$, the synergy between the two detectors plays a key role [337, 339, 347], improving the sensitivity up to an order of magnitude when a second detector at the magic baseline is considered. An additional improvement is achieved due to the increase in energy, as expected.

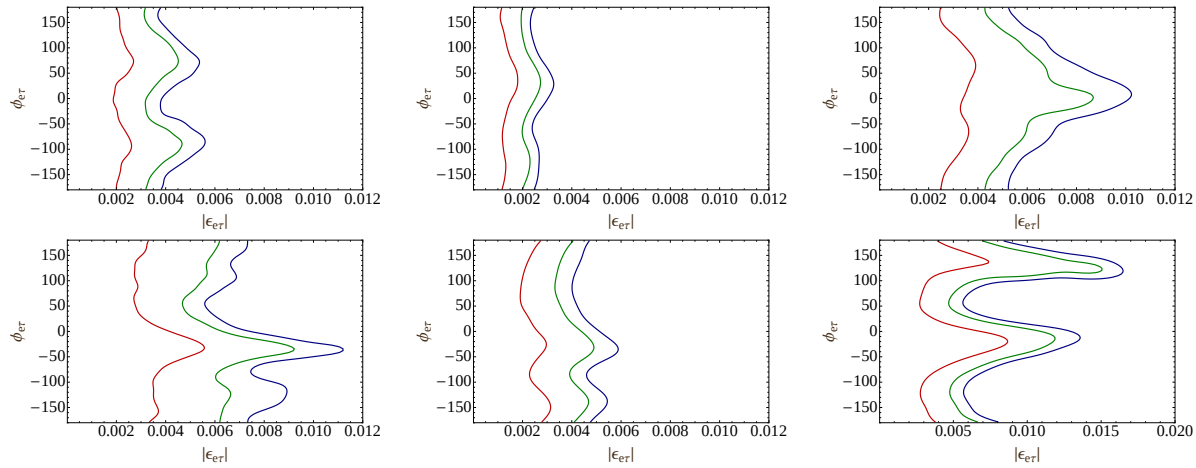

Figure 5.5: 68%, 90% and 95% CL contours for the sensitivity to $\epsilon_{e\tau}$ as a function of $\phi_{e\tau}$ for $\bar{\theta}_{13} = 0$ (upper panels) and $\bar{\theta}_{13} = 3°; \bar{\delta} = -\pi/2$ (lower panels). Marginalization has been performed over the νSM parameters, the diagonal NSI parameters $\epsilon_{\alpha\alpha}$ and $\epsilon_{e\mu}$. The left, middle, and right panels show the results obtained for IDS25, IDS50, and 1B50 setups, respectively. Notice the different scale for the lower right panel, for which the sensitivity is much worse than for the rest of setups.

The oscillation probabilities presented in App. B can help us to understand further the results presented in Figs. 5.4 and 5.5. In the first line of $P_{e\mu}$ in Eq. (B.4) we can observe that the two terms proportional to $\epsilon_{e\mu}$ appear with the same sign, while the ones proportional to $\epsilon_{e\tau}$ have opposite sign and tend to cancel. We have checked that, in the energy range relevant for the three setups under consideration, the coefficient of the $\epsilon_{e\mu}$ term can be one order of magnitude larger than the corresponding coefficient of the $\epsilon_{e\tau}$ term. For this reason, the golden channel is more sensitive to $\epsilon_{e\mu}$ than $\epsilon_{e\tau}$, as it can be seen by comparing Figs. 5.4 and 5.5. For the same reason, the $\epsilon_{e\mu}$ sensitivity is only mildly affected by marginalization over $\epsilon_{e\tau}$, whereas the sensitivity to $\epsilon_{e\tau}$ is strongly affected by the marginalization over $\epsilon_{e\mu}$. This explains why the detector at the magic baseline plays an important role for the sensitivity to $|\epsilon_{e\tau}|$, whereas for $\epsilon_{e\mu}$ the energy is the key parameter independently of the number of baselines. Notice that the features of $P_{e\tau}$ are quite the opposite: terms proportional to $\epsilon_{e\tau}$ add up, while those proportional to $\epsilon_{e\mu}$ tend to cancel (see the first line of Eq. (B.5) in App. B). One could naively think, then, that a better sensitivity is expected for $\epsilon_{e\tau}$ instead of $\epsilon_{e\mu}$ in the 1B50 setup due to its ability to detect τ's. This is not the case, however, because the statistics in MECC is poor compared to that in MIND. The good $\epsilon_{e\mu}$ sensitivity observed at the 1B50 depends on the doubled flux at the MIND section of the detector[8].

A last interesting remark can be drawn in the phase dependence of the results of Figs. 5.4 and 5.5. If we compare the sensitivity contours for $\bar{\theta}_{13} = 0$ (upper panels) and $\bar{\theta}_{13} = 3°$ (lower

[8]We will see in Sec. 5.6 that the silver channel can, however, play an important role in the discovery of CP violation due to NSI.

panels), we can see a shift of locations of the sensitivity minima. This feature is a result of the complicated correlations between $\delta, \phi_{e\mu}$ and $\phi_{e\tau}$ in the golden channel probability. The key factor for this effect to take place is the CP-violating value we have chosen for $\bar{\delta}$, which maximizes the effect.

5.5 Sensitivities achieved mainly through the $\nu_\mu \to \nu_\mu$ channel

As we have mentioned in Sec. 5.1, sensitivity to the rest of the NSI parameters, *i.e.* the diagonal elements $\epsilon_{\alpha\alpha}$ and $\epsilon_{\mu\tau}$, mainly comes from the $\nu_\mu \to \nu_\mu$ channel[9]. In this section, we will study first the expected sensitivity to $|\epsilon_{\mu\tau}|$ as a function of its CP-violating phase $\phi_{\mu\tau}$ (Sec. 5.5.1). The sensitivity to the diagonal NSI parameters will be studied next (Sec. 5.5.2), taking particular care to unveil the correlations between $\epsilon_{\alpha\alpha}$, θ_{13} and θ_{23}.

5.5.1 Sensitivity to $\epsilon_{\mu\tau}$

In Fig. 5.6 the sensitivity to $\epsilon_{\mu\tau}$ for $\bar{\theta}_{13} = 0$ is shown only for the IDS50 setup, since we have found remarkably similar results for the rest of setups under study. The standard marginalization procedure is employed as usual. The most significant feature in this figure is the extremely high sensitivity to the real part of $\epsilon_{\mu\tau}$ (better than 10^{-3}). The high sensitivity is driven by the leading NSI correction to the disappearence oscillation probability in Eq. (B.6):

$$P_{\mu\mu} = P^{\rm SI}_{\mu\mu} - |\epsilon_{\mu\tau}| \cos\phi_{\mu\tau} (AL) \sin(\Delta_{31} L) + \mathcal{O}(\varepsilon^2) + \ldots \tag{5.3}$$

When $\epsilon_{\mu\tau}$ is mostly imaginary, $\phi_{\mu\tau} \sim \pm 90°$, we observe a significant sensitivity loss of more than an order of magnitude, as expected from the fact that the leading dependence on $\mathrm{Im}(\epsilon_{\mu\tau})$ appears at $\mathcal{O}(\varepsilon^2)$ in the probability, as seen in Eq. (B.6). We have explicitly verified that fixing $\epsilon_{e\mu}$ and $\epsilon_{e\tau}$ during marginalization does not produce any appreciable change in the sensitivity to $\epsilon_{\mu\tau}$. This confirms the numerical results presented in Sec. 5.4.2 where no correlation between $\epsilon_{e\mu}$ (or $\epsilon_{e\tau}$) and $\epsilon_{\mu\tau}$ was found. Eventually, we have checked that the $\epsilon_{\mu\tau}$ sensitivity does not vary significantly for nonzero $\bar{\theta}_{13}$, in agreement with the discussion in Sec. 5.4.1.

5.5.2 Sensitivity to the diagonal NSI parameters

In Fig. 5.7 we show the sensitivities to the NSI diagonal parameters obtained with the IDS50 setup for different input values of $\bar{\theta}_{13}$ and $\bar{\theta}_{23}$. As for the $\epsilon_{\mu\tau}$ case, the results are extremely similar for the other two setups under study, and hence their results are not shown. Top panels correspond to $\bar{\theta}_{13} = 0$, the bottom ones to $\bar{\theta}_{13} = 3°$. Left panels are obtained for $\bar{\theta}_{23} = 45°$, in which the red, green and the blue lines stand for the 68%, 90% and 95% CL contours, respectively. In the right panels only the 95% CL contours are drawn, for $\bar{\theta}_{23} = 43°$ by the purple dashed lines and $\bar{\theta}_{23} = 47°$ by the black solid lines. The standard marginalization is adopted here too.

First of all, we see that all panels show that the sensitivity to $(\epsilon_{ee} - \epsilon_{\tau\tau})$ is about an order of magnitude worse than the sensitivity to $(\epsilon_{\mu\mu} - \epsilon_{\tau\tau})$. This behaviour is in agreement with the fact that the leading dependence on the latter combination appears at $\mathcal{O}(\varepsilon^2)$ in the oscillation probabilities, while for the former one it appears at $\mathcal{O}(\varepsilon^3)$ (see [341]). Notice, nonetheless, that

[9]The $\nu_\mu \to \nu_\tau$ channel only increases the statistics at the detector. However, the sensitivity to $\epsilon_{\alpha\alpha}$ and $\epsilon_{\mu\tau}$ is not limited by statistics thanks to the disappearance channel. As a consequence, the $\nu_\mu \to \nu_\tau$ channel is not very useful in this context since it does not add any additional information.

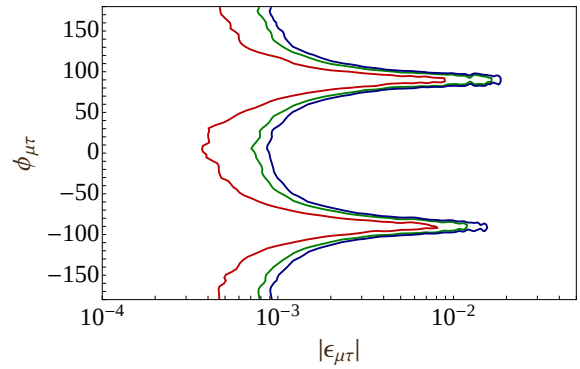

Figure 5.6: 68%, 90% and 95% CL contours for the sensitivity to $\epsilon_{\mu\tau}$ as a function of $\phi_{\mu\tau}$ for $\bar{\theta}_{13} = 0$. Marginalization has been performed over the νSM parameters, the matter density and the rest of NSI parameters. The 50 GeV IDS setup has been assumed.

the sensitivity to $(\epsilon_{ee} - \epsilon_{\tau\tau})$ (approximately $\simeq 10\%$ and $\simeq 20\%$ at 95%CL, 2 d.o.f.'s, for $\bar{\theta}_{13} = 3°$ and 0, respectively) is better than the sensitivity achieved at any other facilities considered in the literature. It improves as $\bar{\theta}_{13}$ increases, probably due to the effect of the golden channel, as we can see by comparing top and bottom panels. On the other hand we have observed, in agreement with the discussion in Sec. 5.1, that the $(\epsilon_{ee} - \epsilon_{\tau\tau})$ sensitivity is mainly limited by the matter uncertainty, which has been set to 5% in our simulations. In other words, unless the PREM error on the matter density is improved, a $\sim 10\%$ sensitivity to $(\epsilon_{ee} - \epsilon_{\tau\tau})$ would be the limiting accuracy that could be reached[10].

The impact of a non-maximal atmospheric mixing angle can be seen in the right panels in Fig. 5.7: two narrow strips appear at both sides of the central region. By looking into the disappearance probability, $P_{\mu\mu}$ in Eq. (B.6), it is easy to realise that the sensitivity in the central region of the plots is driven through the term proportional to $(\epsilon_{\mu\mu} - \epsilon_{\tau\tau})^2$ in the disappearence channel, being the only one which does not vanish to order ε^2 for maximal mixing in the atmospheric sector. The narrow bands at both sides appear as a consequence of the non-maximal input for the atmospheric mixing angle, and they are driven by the terms proportional to $\delta\theta_{23}(\epsilon_{\mu\mu} - \epsilon_{\tau\tau})$ in $P_{\mu\mu}$. Indeed, the fact that these two strips appear both for $\bar{\theta}_{23} = 43°$ and $\bar{\theta}_{23} = 47°$ indicates the existence of an "octant" degeneracy between $\delta\theta_{23}$ and $(\epsilon_{\mu\mu} - \epsilon_{\tau\tau})$.

It is also remarkable that no significant correlations among $\epsilon_{\alpha\alpha}$, $\epsilon_{e\mu}$ and $\epsilon_{e\tau}$ have been found, as expected from the results presented in Sec. 5.4.2.

5.6 Discovery potential for CP violation in the $(\phi_{e\mu}, \phi_{e\tau}, \delta)$ space

One of the most interesting aspects of any system involving NSI is the possible existence of multiple sources of CP violation. It is important to understand characteristic features of CP violation such as correlations between the phases or possible degeneracies arising between them. In this section we focus on the study of CP violation associated with the two NSI CP-violating phases $\phi_{e\mu}$ and

[10] An alternative method to constrain ϵ_{ee}, which is free from this problem and is complementary to our method, is to use solar neutrinos, whose sensitivity to ϵ_{ee} appears to reach $\sim 20\%$ at 1 σCL (1 d.o.f.) [353].

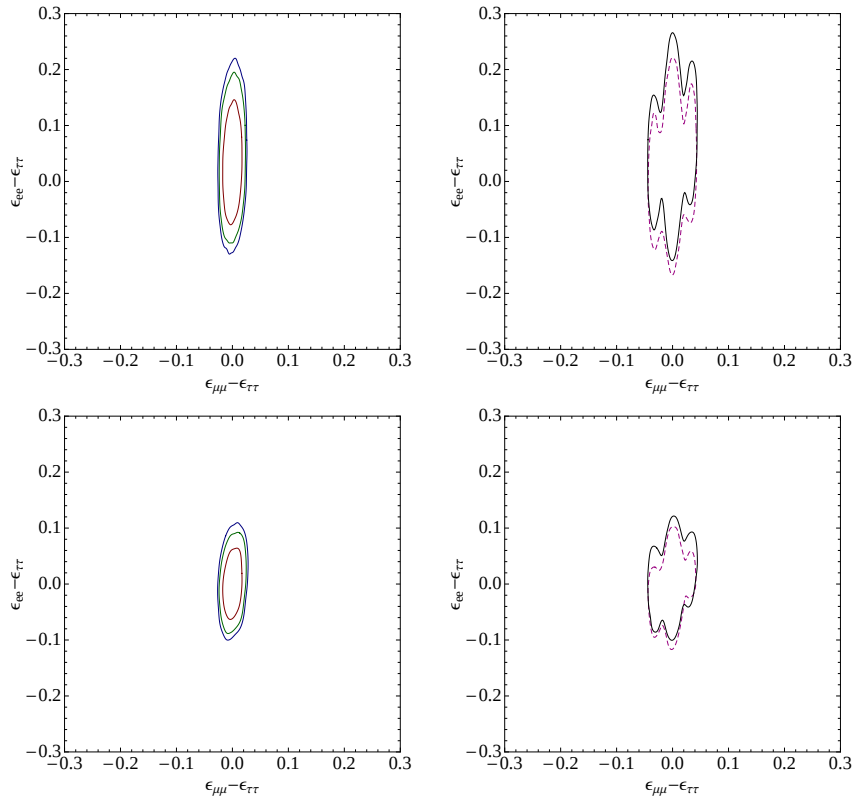

Figure 5.7: Sensitivity to (ϵ_{ee}-$\epsilon_{\tau\tau}$) and ($\epsilon_{\mu\mu}$-$\epsilon_{\tau\tau}$) at the IDS50 setup.Top panels: $\bar{\theta}_{13} = 0$; bottom panels: $\bar{\theta}_{13} = 3°$. Left panels: 68%, 90% and 95% CL contours for $\bar{\theta}_{23} = 45°$; right panels: 95% CL contour for $\bar{\theta}_{23} = 43°$ (purple dotted line) and $\bar{\theta}_{23} = 47°$ (black solid line). Marginalization has been performed over θ_{23}, Δm^2_{31}, the matter density, θ_{13} and δ.

$\phi_{e\tau}$ together with the standard νSM phase δ, which appear in the golden and silver channels. Depending on the values of $\theta_{13}, |\epsilon_{e\mu}|$ and $|\epsilon_{e\tau}|$, strong and complicated correlations are expected to take place between these three phases. The third NSI phase, $\phi_{\mu\tau}$, only appears in $P_{\mu\mu}$ and $P_{\mu\tau}$ (see App. B) and is uncorrelated to the rest of the CP-phases. For this reason effects of CP violation in the $\mu - \tau$ sector will not be studied here.

For any realistic NP model giving rise to NSI at low energies, the effects are generally not expected to be larger than $\mathcal{O}(10^{-2})$. For this reason, we will focus on "reasonable" values for $|\epsilon_{e\mu}|$ and $|\epsilon_{e\tau}|$, in the range $|\epsilon_{\alpha\beta}| \in [10^{-3}, 10^{-2}]$, for which the correlations with θ_{13} can still be large[11]. For NSI moduli smaller than 10^{-3}, the effect of δ always dominates and it is very difficult to detect CP violation due to NSI. On the other hand, we will see that a very interesting structure arises in the discovery potential in the three-dimensional parameter space for the input values we have considered for the NSI moduli. In particular, we have studied three cases: (a) both moduli are "small", $|\bar{\epsilon}_{e\mu}| = |\bar{\epsilon}_{e\tau}| = 10^{-3}$, (b) both of them are "large", 10^{-2}, and finally (c)

[11]The range of values considered for the NSI moduli in this work differ significantly from that in Ref. [338], where values for $|\epsilon_{e\tau}|$ as large as unity were considered. In addition, the number of NSI parameters in the analysis is different as well. As a consequence, the comparison of the results obtained is not straightforward. Some qualitative features of the results obtained in Ref. [338] have been recovered, though.

an "asymmetric" case where $|\bar{\epsilon}_{e\mu}| = 10^{-3}; |\bar{\epsilon}_{e\tau}| = 10^{-2}$. Within these three cases, the last one is particularly interesting. Let us remind that, in the golden channel, $\epsilon_{e\mu}$ plays a leading role while $\epsilon_{e\tau}$ is subdominant (Sec. 5.4). Therefore, the difference by a factor of ten in their order of magnitudes triggers interesting three-fold correlations between $\delta, \phi_{e\mu}$ and $\phi_{e\tau}$.

5.6.1 Non-standard CP violation in the absence of νSM CP violation

The first question we address is whether it is possible to detect a new CP-violating signal due to NSI in the absence of standard CP violation. We study, therefore, the CP discovery potential (defined in Sec. C.2) in the case where the input value for the standard CP-violating phase, $\bar{\delta}$, is set to zero or π. The two cases defined in Sec. C.2 are considered. The first possibility stands for a relatively large value of θ_{13}, $\bar{\theta}_{13} = 3°$, which would be already measured by the time the HENF is built. In this case, we can safely use Eq. (C.3) to study the CP-discovery potential. The second possibility arises when no signal for a non-vanishing θ_{13} is found by the ongoing and soon-coming neutrino oscillation experiments. In this case, we can only conclude that $\theta_{13} \lesssim 3°$, and we have to use Eq. (C.4) instead. These two cases yield the best and the worst results[12] for the CP discovery potential in the $(\phi_{e\mu}, \phi_{e\tau})$ space for $\delta = 0$ and 180°.

We show in Figs. 5.8 and 5.9 the CP discovery potential in the $(\phi_{e\mu}, \phi_{e\tau})$ plane for $\bar{\delta} = 0$ and 180°, respectively. From left to right we show results for the IDS25, IDS50 and 1B50 setups, respectively. From top to bottom we present the CP discovery potential for the three choices of the two NSI moduli input values, $(|\bar{\epsilon}_{e\mu}|, |\bar{\epsilon}_{e\tau}|) = (10^{-3}, 10^{-3})$, $(10^{-3}, 10^{-2})$, and $(10^{-2}, 10^{-2})$, respectively. The shaded regions represent the area of the parameter space in which CP violation can be distinguished from CP conservation at the 99% CL (3 d.o.f.). The yellow (light gray) regions have been obtained for $\bar{\theta}_{13} = 3°$ using Eq. (C.3). The cyan (dark gray) regions, on the other hand, have been obtained after searching for intrinsic degeneracies in θ_{13} and then marginalizing over $\bar{\theta}_{13}$, using Eq. (C.4).

We first discuss the case of $\bar{\theta}_{13} = 3°$ (yellow regions). The results obtained are quite similar for $\bar{\delta} = 0$ and 180°. In both cases the CP discovery potential for small NSI parameters corresponding to $(|\bar{\epsilon}_{e\mu}|, |\bar{\epsilon}_{e\tau}|) = (10^{-3}, 10^{-3})$ (top row) vanishes for the IDS25 and the 1B50 setups, and it is non-vanishing only for two very small regions at $|\phi_{e\mu}| \simeq 90°$, independently of the value of $\phi_{e\tau}$, for the IDS50. The IDS25 setup presents no CP discovery potential at all for the case where $(|\bar{\epsilon}_{e\mu}|, |\bar{\epsilon}_{e\tau}|) = (10^{-3}, 10^{-2})$ either. For this choice of NSI parameters, on the other hand, the IDS50 and the 1B50 setups show different performances: the former is able to discover CP violation due to NSI when both NSI phases are nearly maximal, $(|\phi_{e\mu}|, |\phi_{e\tau}|) \sim (90°, 90°)$; the latter can establish NSI-induced CP violation for $|\phi_{e\tau}| \sim 90°$ (regardless of the value of $\phi_{e\mu}$). In the case of "large" NSI parameters, $(|\bar{\epsilon}_{e\mu}|, |\bar{\epsilon}_{e\tau}|) = (10^{-2}, 10^{-2})$, the three setups yield a very good CP discovery potential for $\bar{\theta}_{13} = 3°$. In this case we observe a similar pattern of the sensitivity regions for all three setups: most of the space is covered, apart from two strips around $\phi_{e\mu} = 0$ and 180° whose widths mildly vary for differing setups.

As it was already mentioned in Sec. 5.4.2, the dependence on $\epsilon_{e\mu}$ and $\epsilon_{e\tau}$ in the $\nu_e \to \nu_\mu$ oscillation probability is quite different: the coefficient of the $\epsilon_{e\mu}$ term is roughly one order of magnitude larger than the corresponding coefficient of the $\epsilon_{e\tau}$ term in the considered range of energy and baselines. Therefore, the behaviour of the CP discovery potential due to NSI at the IDS25 and IDS50 are primarily determined by $\epsilon_{e\mu}$ if $|\epsilon_{e\mu}|$ and $|\epsilon_{e\tau}|$ are comparable. This is clearly seen by the vertical bands shown in the top and bottom panels in Figs. 5.8 and 5.9: the CP discovery potential presents practically no dependence at all on $\epsilon_{e\tau}$, its behaviour being dominated by $\epsilon_{e\mu}$, since for these panels both parameters are of the same order of magnitude

[12] We have also checked that for $\bar{\theta}_{13} > 3°$ our results do not change dramatically.

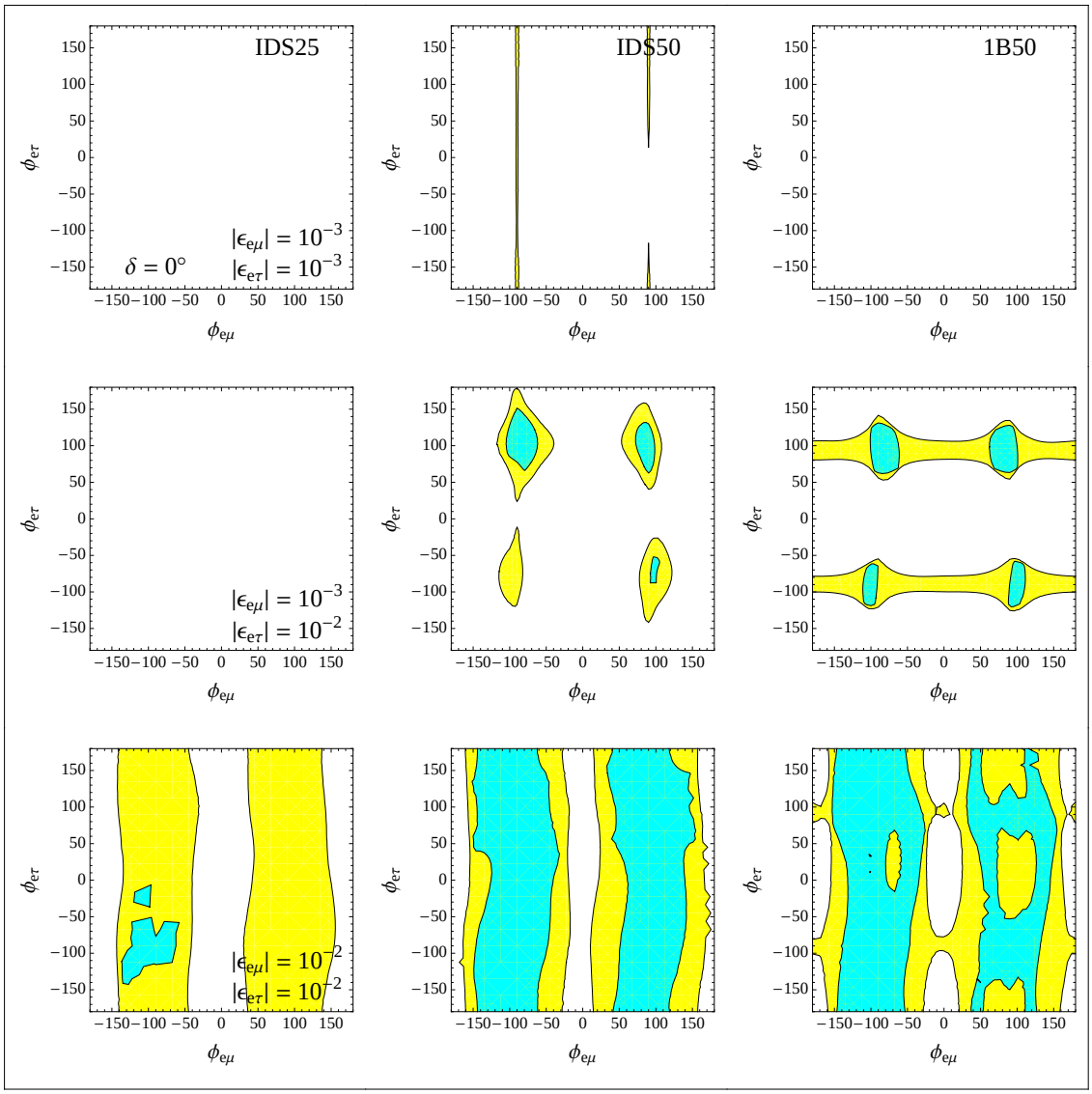

Figure 5.8: The 99% CL (3 d.o.f.'s) CP discovery potential in the $(\phi_{e\mu}, \phi_{e\tau})$ plane for $\bar{\delta} = 0$. From top to bottom: $(|\bar{\epsilon}_{e\mu}|, |\bar{\epsilon}_{e\tau}|) = (10^{-3}, 10^{-3})$, $(10^{-3}, 10^{-2})$ and $(10^{-2}, 10^{-2})$. The yellow (light gray) regions have been obtained for $\theta_{13} = \bar{\theta}_{13} = 3°$, Eq. (C.3). The cyan (dark gray) regions have been obtained after searching for intrinsic degeneracies in θ_{13} and then marginalizing over $\bar{\theta}_{13}$, Eq. (C.4).

(and, therefore, the latter is suppressed by its coefficient). In the asymmetric case, however, $(|\bar{\epsilon}_{e\mu}|, |\bar{\epsilon}_{e\tau}|) = (10^{-3}, 10^{-2})$ (middle row), these vertical bands disappear since now both parameters are competitive. A particularly interesting feature is seen in the right panels, which correspond to the performance of the 1B50 setup. In this case, due to the presence of the silver channel, the roles of $\epsilon_{e\mu}$ and $\epsilon_{e\tau}$ are interchanged: two horizontal bands appear at $|\phi_{e\tau}| = 90°$, showing that

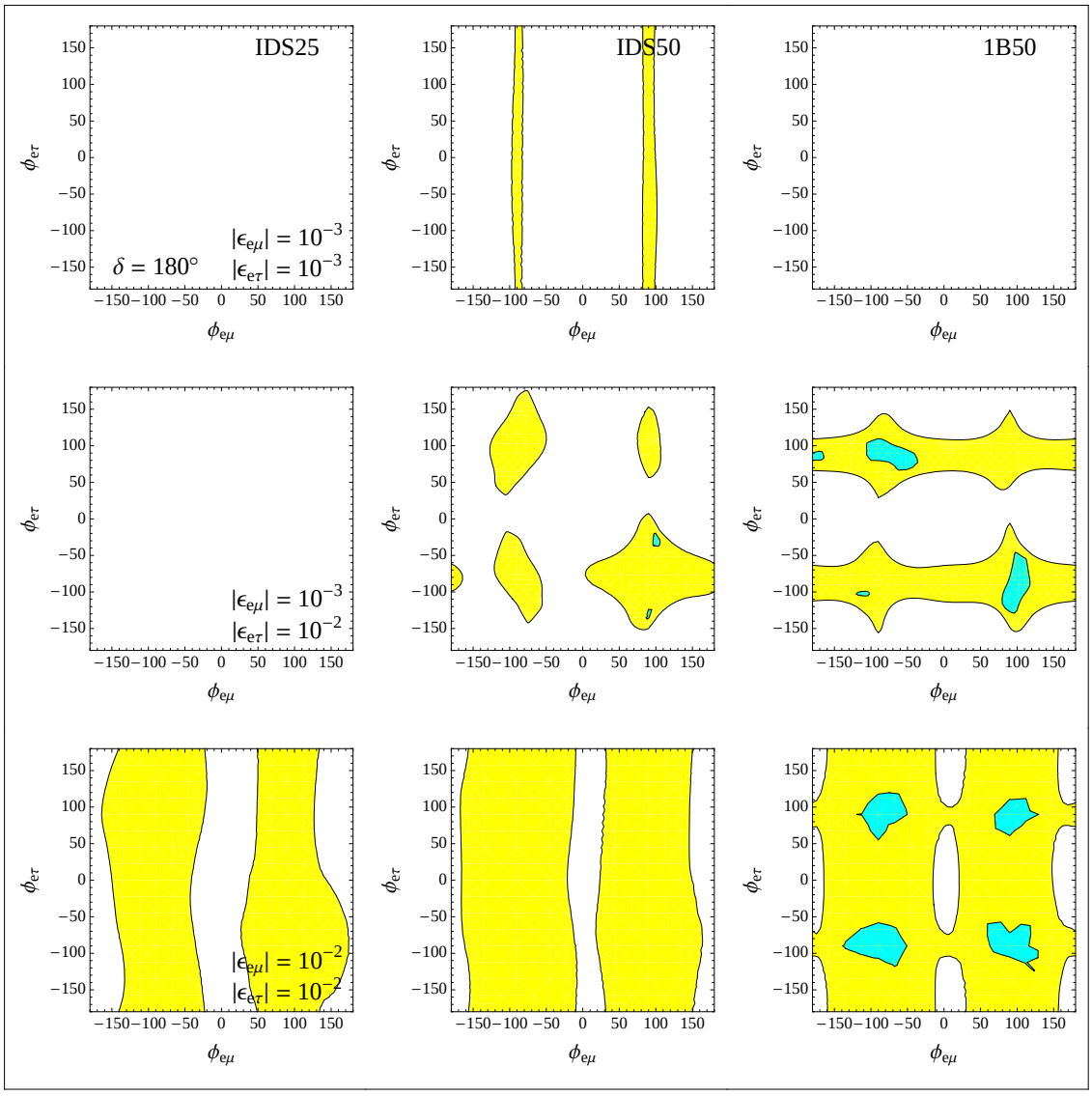

Figure 5.9: The same as Fig. 5.8 but with $\bar{\delta} = 180°$.

the behaviour of the CP discovery potential is dominated by $\epsilon_{e\tau}$ in spite of the low statistics of the silver channel. This is a consequence of the enhanced role of the silver channel due to the asymmetric choice of $\epsilon_{e\mu}$ and $\epsilon_{e\tau}$ and by the size of their corresponding coefficients (inverted with respect to the golden channel). For $|\bar{\epsilon}_{e\mu}| = 10^{-3}$ we see no significant difference for $\bar{\delta} = 0$ or $180°$ in the case $\bar{\theta}_{13} = 3°$ (yellow regions).

Now we discuss the CP discovery potential for the case of $\theta_{13} \lesssim 3°$, depicted as the cyan regions in Figs. 5.8 and 5.9. The first thing we notice is that, when marginalization over θ_{13} and $\bar{\theta}_{13}$ is performed, the CP discovery potential is partially lost for all the setups under study. This effect is due to the presence of interference terms in the form $\theta_{13}|\epsilon_{e\alpha}| \times \exp i(\delta + \phi_{e\alpha})$ in the probabilities.

Notice that this effect is much worse in the case of $\bar{\delta} = 180°$ than for $\bar{\delta} = 0$. In the former case, only small islands in the $(\phi_{e\mu}, \phi_{e\tau})$ space survive at around the maximally CP-violating values of the NSI phases only for the 1B50 setup, while the IDS25 and the IDS50 setups show no discovery potential at all for any of the considered input values of the NSI moduli. The marked difference between the shaded regions for $\bar{\delta} = 0$ and $\bar{\delta} = 180°$ illuminates very well how complicated the interplay among the three CP-phases is; once we marginalize over θ_{13}, flipping the sign of $e^{i\delta}$ leads to a cancellation between the standard and non-standard CP-violating contribution, which results in a heavy loss of the CP discovery potential of the facilities. This cancellation is less effective when the 1B50 setup is considered, as the silver channel is enhanced when the golden channel gets depleted and viceversa.

It is remarkable to see that high enough neutrino energies turn out to be of key importance in order to observe NSI-induced CP violation; the IDS50 setup always performs better than the IDS25, for all the input values we have considered for the NSI moduli.

To conclude this section, we point out the following two features: firstly, as this analysis has been performed with fixed mass hierarchy, it is expected that the CP discovery potential could become worse when the sign-Δm^2 degeneracies are taken into account[13]. Secondly, a more refined analysis of the correlations between the three phases with a proper treatment of backgrounds, systematic errors and marginalization over atmospheric parameters should be performed to confirm robustness of the observed features.

5.6.2 $\delta_{\rm CP}$ fraction: Non-standard CP violation in presence of νSM CP violation

In the previous section, we have presented the two dimensional slice of the three-dimensional "CP sensitivity volume" at the very particular points $\bar{\delta} = 0$ or $180°$. For different values of $\bar{\delta}$, the CP discovery potential changes dramatically due to the correlations between the three phases. We have indeed found very different features depending on the considered setup, the choice of the input values for the NSI moduli $(|\bar{\epsilon}_{e\mu}|, |\bar{\epsilon}_{e\tau}|)$, and the mixing angle $\bar{\theta}_{13}$; in particular, many "holes" appear indicating regions inside the three-dimensional parameter space for which we are not able to distinguish a CP-violating input from the CP-conserving points. The existence and position of these holes change for the three setups and for the considered choices of $(|\bar{\epsilon}_{e\mu}|, |\bar{\epsilon}_{e\tau}|)$ and $\bar{\theta}_{13}$. Therefore, to repeat the procedure adopted in Figs. 5.8 and 5.9 and draw infinitely many slices of the CP discovery potential for different values of $\bar{\delta}$ would neither be practical nor shed any useful light over the intimate structure of the correlations.

We therefore introduce a new quantity, the "$\delta_{\rm CP}$-*fraction* contour in the $(\phi_{e\mu}, \phi_{e\tau})$ space", to condense the information. This quantity, denoted as $F_\delta(\phi_{e\mu}, \phi_{e\tau})$, is defined as the fraction of possible values of $\bar{\delta}$ which fall into the region where CP violation can be established at the 99% CL (3 d.o.f.) for a certain point in the $(\phi_{e\mu}, \phi_{e\tau})$ space. Notice that this is nothing but the usual CP-fraction redefined on the two-dimensional plane[14] $(\phi_{e\mu}, \phi_{e\tau})$. Such contours are shown for $\bar{\theta}_{13} = 3°$ in Fig. 5.10, using Eq. (C.3), and in Fig. 5.11, using Eq. (C.4).

In Fig. 5.10, the white, yellow, cyan, pink and red regions correspond to $F_\delta(\phi_{e\mu}, \phi_{e\tau}) \leq$ 40%, 60%, 80%, 90% and 95%, respectively, for fixed $\theta_{13} = \bar{\theta}_{13} = 3°$. Globally, the IDS50 setup

[13] Notice, however, that in the two-baselines setups for measuring the νSM parameters the magic baseline detector is able to solve the sign degeneracy in most of the parameter space [322]. It is an intriguing question to examine to what extent it continues to hold with NSI. This question has been investigated in [339] but only partially and needs to be examined further.

[14] The concept of CP-fraction was introduced in Refs. [268, 269] to compare in a condensed form the performances of different proposals regarding the measurement of a given observable. It is defined as the fraction of the δ-parameter space (*i.e.*, the fraction of 2π) for which a given setup is able to perform a given task.

has the best CP discovery potential, while the IDS25 and 1B50 setups yield comparable results (the 1B50 performance being slightly better). The top and bottom panels, which correspond to $(|\bar{\epsilon}_{e\mu}|, |\bar{\epsilon}_{e\tau}|) = (10^{-3}, 10^{-3})$ and $(10^{-2}, 10^{-2})$, respectively, display similar features as those we have seen for $\bar{\delta} = 0$ or 180°. $F_\delta(\phi_{e\mu}, \phi_{e\tau})$ larger than 40% (60%) is achieved in almost the whole plane for all the setups in the case of "small" ("large") NSI parameters. A $F_\delta(\phi_{e\mu}, \phi_{e\tau})$ greater than 80% is achieved for all the setups under study around $|\phi_{e\mu}| \sim 90°$ for "large" NSI input values.

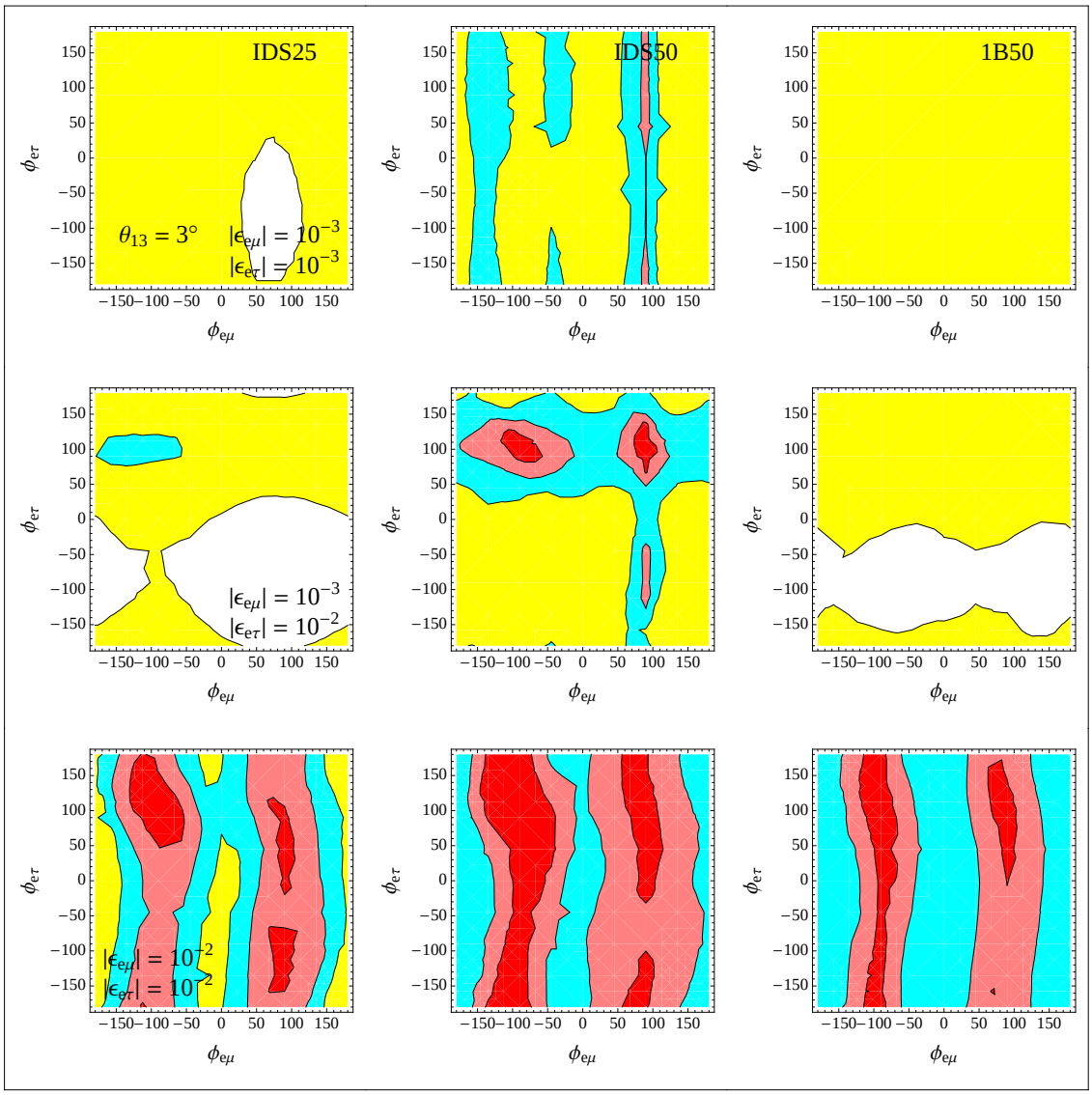

Figure 5.10: Contours for the $\delta_{\rm CP}$-fraction F_δ in the $(\phi_{e\mu}, \phi_{e\tau})$ plane (as defined in the text) for $\bar{\theta}_{13} = 3°$, obtained using Eq. (C.3). From left to right: results for the IDS25, IDS50 and 1B50 setups. From top to bottom: $(|\bar{\epsilon}_{e\mu}|, |\bar{\epsilon}_{e\tau}|) = (10^{-3}, 10^{-3})$, $(10^{-3}, 10^{-2})$ and $(10^{-2}, 10^{-2})$. The white, yellow, cyan, pink and red regions correspond to $F_\delta(\phi_{e\mu}, \phi_{e\tau}) \leq 40\%$, 60%, 80%, 90% and 95%, respectively.

On the other hand, the result for asymmetric NSI moduli, $(|\bar{\epsilon}_{e\mu}|, |\bar{\epsilon}_{e\tau}|) = (10^{-3}, 10^{-2})$, is peculiar. We can see that the CP discovery potential for the IDS25 and the 1B50 setups is worse than for "small" NSI moduli, since a larger white region with $F_\delta(\phi_{e\mu}, \phi_{e\tau}) \leq 40\%$ arises for $\phi_{e\tau} \sim -90°$. At the same time, the discovery potential for the IDS50 setup is maximal at $\phi_{e\tau} \sim 90°$. The fact that the main features of $F_\delta(\phi_{e\mu}, \phi_{e\tau})$ are determined by $\phi_{e\tau}$ rather than by $\phi_{e\mu}$ appears to be again a consequence of the asymmetric choice of NSI parameters. Having $|\bar{\epsilon}_{e\tau}|$ an order of magnitude larger than $|\bar{\epsilon}_{e\mu}|$, the two parameters play an equally important role and huge correlations arise between them, which could explain the absence of a peak in sensitivity at $\phi_{e\mu} \simeq \phi_{e\tau} \simeq -90°$ for the IDS50 setup. When the two parameters are of the same order, $\epsilon_{e\mu}$ always dominates over $\epsilon_{e\tau}$, in agreement with our previous results. A comparison between left panels in Fig. 5.10 and, for instance, Fig.12 of Ref. [354] indicates that marginalization over NSI hurts the CP sensitivity in a significant way.

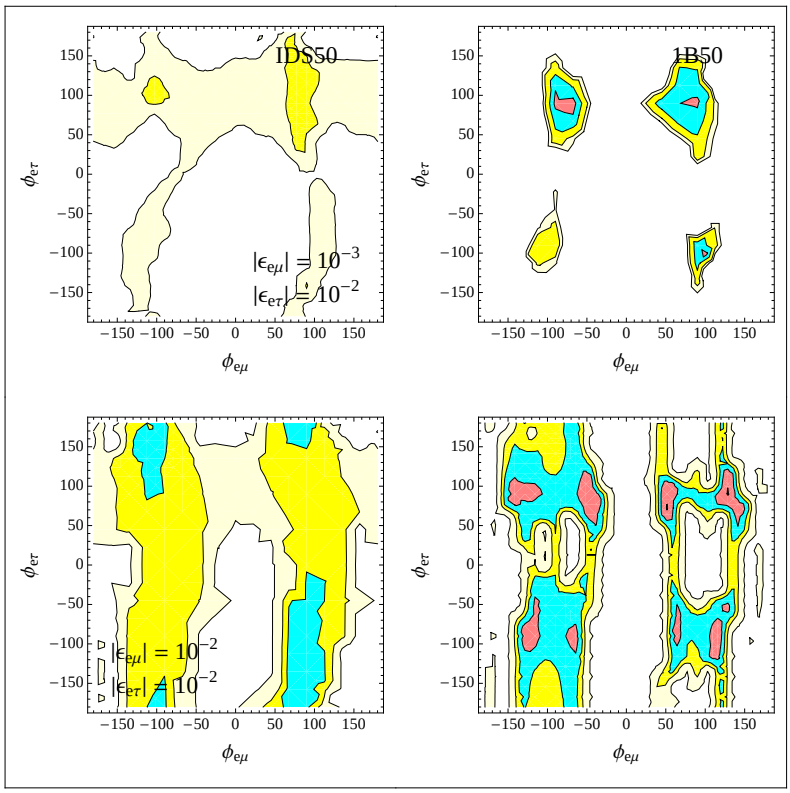

Figure 5.11: Contours for the $\delta_{\rm CP}$-fraction F_δ in the $(\phi_{e\mu}, \phi_{e\tau})$ plane (as defined in the text) after searching for intrinsic degeneracies in θ_{13} and marginalizing over $\bar{\theta}_{13}$, using Eq. (C.4). Left (right) panels: results for the IDS50 (1B50) setup. Top panels: $(|\bar{\epsilon}_{e\mu}|, |\bar{\epsilon}_{e\tau}|) = (10^{-3}, 10^{-2})$; bottom panels: $(|\bar{\epsilon}_{e\mu}|, |\bar{\epsilon}_{e\tau}|) = (10^{-2}, 10^{-2})$. The white, light yellow, yellow, cyan, pink and red regions correspond to $F_\delta(\phi_{e\mu}, \phi_{e\tau}) \leq 5\%$, 40%, 60%, 80%, 90% and 95%, respectively.

In Fig. 5.11 we show contours corresponding to $F_\delta(\phi_{e\mu}, \phi_{e\tau}) \leq 5\%, 40\%, 60\%, 80\%$ and 95% in white, light yellow, yellow, cyan, pink and red, respectively, after marginalization over θ_{13} and $\bar{\theta}_{13}$ below 3°, using Eq. (C.4). Results for the IDS25 setup are not presented because we have found vanishing F_δ for any choice of $|\bar{\epsilon}_{e\mu}|$ and $|\bar{\epsilon}_{e\tau}|$ under consideration. Similarly, we do not show any

results corresponding to $(|\bar{\epsilon}_{e\mu}|, |\bar{\epsilon}_{e\tau}|) = (10^{-3}, 10^{-3})$ either, since we have found vanishing F_δ for all the three setups. Notice that we have included in this figure an additional contour for $F_\delta < 5\%$ in order to achieve a better resolution in small F_δ regions. When we compare Fig. 5.11 to Fig. 5.10 we observe some contrived features. That is, the CP-fraction obtained for the ISD50 is not always better than that for 1B50. In certain limited regions the CP-fraction is actually larger for the 1B50 setup, but the area covered by the regions where some sensitivity to CP violation is achieved (light yellow) is larger for the IDS50 setup. It appears that this feature is an outcome of the complicated correlations between these phases.

5.6.3 CP volume fraction

If we focus on the most general possible case in which CP violation comes both from the νSM as well as from NSI, it would be interesting to understand its global features. For this purpose we define a new quantity which we call the "*CP volume fraction*". This is defined as the fraction of volume in which CP-violating signal can be distinguished, at a given CL, from a CP-conserving one in the three-dimensional parameter space spanned by $\delta, \phi_{e\mu}$ and $\phi_{e\tau}$. We use 99% CL (3 d.o.f.) to define the CP volume fraction presented in the figures in this subsection.

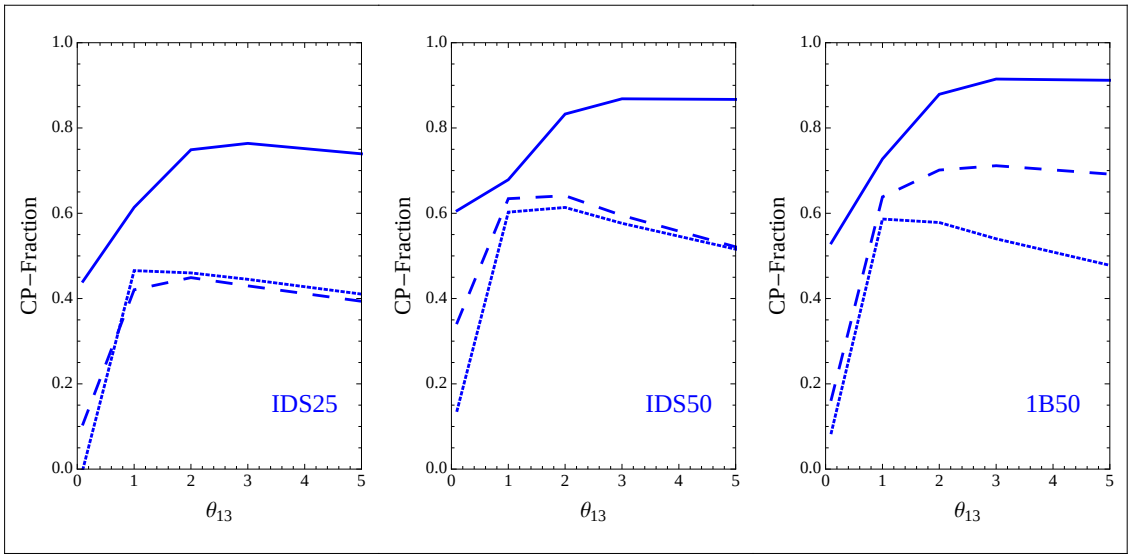

Figure 5.12: Comparison of the CP volume fractions (as defined in the text) as a function of $\bar{\theta}_{13}$, using Eq. (C.3). From left to right: IDS25, IDS50 and 1B50 setups. Results for $(|\bar{\epsilon}_{e\mu}|, |\bar{\epsilon}_{e\tau}|) = (10^{-3}, 10^{-3}), (10^{-3}, 10^{-2})$ and $(10^{-2}, 10^{-2})$ are represented by dotted, dashed and solid lines, respectively.

In Fig. 5.12, we present the results of the CP volume fraction computed using Eq. (C.3) for the three setups and the three choices ("small", "asymmetric" and "large", as usual) as a function of $\bar{\theta}_{13}$. Consider first the IDS25 and IDS50 setups: we can see that, at both setups, the CP volume fraction achievable for $(|\bar{\epsilon}_{e\mu}|, |\bar{\epsilon}_{e\tau}|) = (10^{-3}, 10^{-3})$ and $(10^{-3}, 10^{-2})$ are extremely similar. This means that the CP discovery potential for both setups is dominated by $|\bar{\epsilon}_{e\mu}|$ and the effect of $|\bar{\epsilon}_{e\tau}|$ is marginal, in agreement with the results obtained in previous sections. On the other hand, we see that when $|\bar{\epsilon}_{e\mu}| = 10^{-2}$ (solid line), the CP volume fraction rises abruptly to approximately

80% or above for $\bar{\theta}_{13} \geq 2°$.

This is not the case for the 1B50 setup: we can see that in the case of "small" NSI parameters (dotted line) it shows a similar (but slightly worse) sensitivity than that of the IDS50. The CP volume fraction is approximately 50% for $\bar{\theta}_{13} \geq 2°$. However, as soon as $|\bar{\epsilon}_{e\tau}| = 10^{-2}$, it rises to 70%, and reaches 90% for larger $|\bar{\epsilon}_{e\mu}| = 10^{-2}$ at larger θ_{13}. The behaviour clearly indicates that the 1B50 setup is taking advantage of the combination of both channels in an efficient way.

Another interesting observation that we can draw from Fig. 5.12 concerns the θ_{13}-dependence of the CP volume fraction. Firstly, the CP volume for $\theta_{13} = 0$ reflects the ability of each setup of observing CP violation exclusively due to NSI. While for the IDS25 setup the CP volume is nonzero only when $|\bar{\epsilon}_{e\mu}|$ is "large", the higher energy setups would be able to measure a CP violating signal even in the case of "small" NSI parameters. This confirms the results presented in Sec. 5.6.1 (Figs. 5.8 and 5.9). Secondly, we can see in the "small" NSI parameters case, and also in the "asymmetric" case for the IDS25 and IDS50 setups, that the CP volume fraction decreases at "large" θ_{13}, reaching a maximum for $\bar{\theta}_{13} \in [1°, 2°]$. It means that, when the NSI parameters are rather small, correlations with a "large" θ_{13} can actually reduce the CP-discovery potential of those facilities. This is no longer true when the NSI parameters are set to be "large": in this case, the CP volume fraction increases for increasing θ_{13} value but remains practically unchanged for $\theta_{13} \geq 2°$. No destructive correlations arise when the NSI parameters are sufficiently "large".

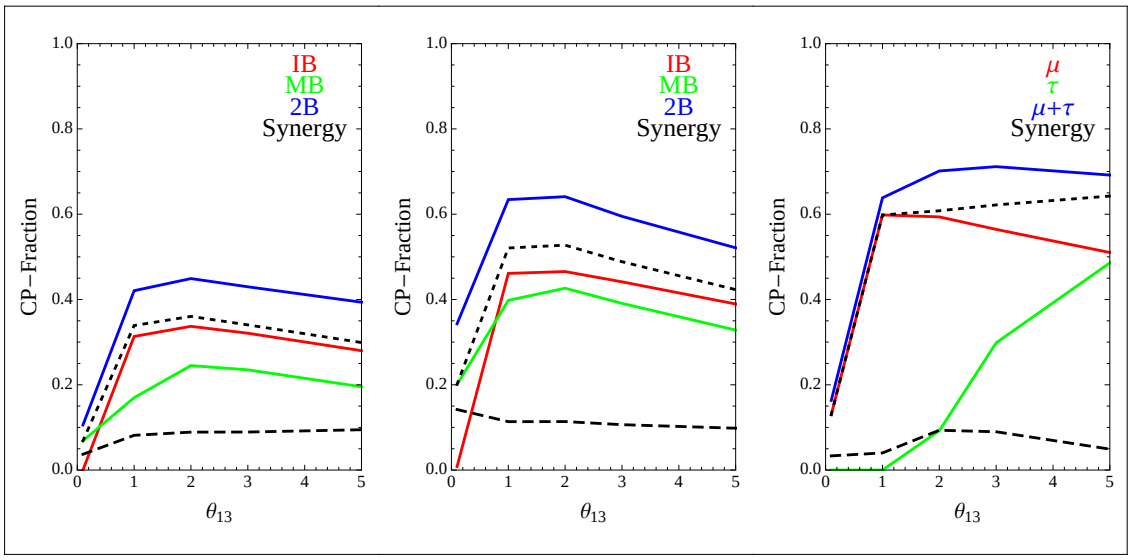

Figure 5.13: Comparison of the CP volume fractions (as defined in the text) as a function of $\bar{\theta}_{13}$ for $(|\bar{\epsilon}_{e\mu}|, |\bar{\epsilon}_{e\tau}|) = (10^{-3}, 10^{-2})$. From left to right: IDS25, IDS50 and 1B50 setups. Results for the first detector (MIND at the Intermediate Baseline) and for the second detector (either MIND at the Magic Baseline or MECC at the Intermediate Baseline) are shown in red and green, respectively. Combination of the two detectors (V_{1+2}, see text) is shown in blue. The dotted black line corresponds to the simple sum of the CP volume fractions of the separate baselines or detectors, $V_{1,2}$ (see text). The dashed black lines represent the *synergy*, *i.e.* $V_{1+2} - V_{1,2}$ (see text).

To conclude this section, we address here the issue of the relative importance of the different detectors and different baselines, and of the possible synergies between them. We present in Fig. 5.13 the CP volume fractions computed for each detector and their combinations for the

three setups. Only the case of "asymmetric" NSI parameters, $(|\bar{\epsilon}_{e\mu}|, |\bar{\epsilon}_{e\tau}|) = (10^{-3}, 10^{-2})$, is shown. Notice that it is precisely the case where the synergy between channels/detectors is most important because the two NSI parameters are equally relevant in the golden channel, which presents the largest statistics.

Let V_i be the CP volume fraction obtained by analyzing data given by a detector i, where $i = 1$ refers to the MIND detector at $L = 4000$ km and $i = 2$ to the MIND detector at $L = 7500$ km (left and middle panels) or to the MECC detector at $L = 4000$ km (right panel), respectively. The volume V_1 is represented by red lines, V_2 by green lines in all panels. The CP volume fraction obtained combining two detectors, V_{1+2}, is represented by the blue lines. Notice that V_{1+2} is not the simple sum of the CP volume fractions of the two detectors, $V_1 + V_2$. When we combine the CP volume fractions of two detectors, we must take into account that some part of the parameter space can be covered by both detectors at the same time. We call the latter volume fraction as V_{overlap}, the fraction of the three-dimensional parameter space that is covered simultaneously by both detectors. Then the correct definition of the simple sum of the CP volume fractions of two detectors is $V_{1,2} = V_1 + V_2 - V_{\text{overlap}}$. The volume $V_{1,2}$ is shown by the black dotted lines in Fig. 5.13. We can see that, in general, $V_{1,2}$ does not coincide with V_{1+2}, because the combination of the data from two detectors could in principle cover regions of the parameter space that are not accessible to each detector separately. This is nothing but the effect of the *synergy* between two detectors, an increase in the CP volume fraction due to simultaneous analysis of the data sets of two detectors, a procedure different from the simple sum of the sensitivities achieved by each one separately. The *synergy* $V_{1+2} - V_{1,2}$ is represented by the black dashed lines in Fig. 5.13.

The first thing to be noticed is that the *synergy* is never much larger than approximately 10% for any of the considered setups. In the IDS25 and IDS50 setups, $V_{1,2}$ (black solid lines) almost coincides with V_1 (red lines for the intermediate detector). This means that most of the CP volume fraction due to the magic baseline detector is already covered by the intermediate detector. In the case of 1B50 setup the situation is different. For $\bar{\theta}_{13} \leq 1^\circ$ the MECC detector does not contribute at all, as the red, black and blue lines coincide. For $\bar{\theta}_{13} \geq 1^\circ$, the MECC contribution grows linearly and it starts to cooperate with the MIND detector, as expected. However, we see that $V_{1,2}$ (black) and V_{1+2} (blue) are closer compared to the cases of IDS25/50. This means that the overlap region V_{overlap} is relatively small in this case. The two detectors are complementary, as they test different regions of the parameter space.

6

Summary and Conclusions

During the last two decades, a whole plethora of neutrino oscillation experiments has been performed in order to measure the mixing parameters in the leptonic sector. A great success has been achieved in the measurement of the solar and atmospheric parameters. However, the third mixing angle, θ_{13}, is still unknown. The CP violating phase in the leptonic sector, δ, is also unknown, as well as the hierarchy of the neutrino mass eigenstates. If θ_{13} lies beyond the reach of present and near future neutrino oscillation experiments, more powerful facilities involving larger detectors and improved beams will be needed in order to pin down this elusive mixing angle. This is precisely the physics case which has been considered in the present manuscript. A deep study of the three main proposals for the future neutrino oscillation facilities has been done in detail: Super-Beams (SB), β-beams and Neutrino Factories (NF).

The quest for θ_{13}, δ and the mass hierarchy at Super-Beams and β-beams

In case θ_{13} turns out to be extremely small ($\sin^2 2\theta_{13} \leq 10^{-4}$) the NF is, of course, the best option. However, the situation might change depending upon the value of θ_{13}. In particular, if θ_{13} turns out to be relatively large ($\sin^2 2\theta_{13} \gtrsim 10^{-3}$), a 25 GeV NF may not be needed anymore. In this case, a Low Energy NF could be helpful in order to avoid technical difficulties related to muon cooling, while it still yields a very good performance. It should be reminded, though, that in the case of relatively large θ_{13}, both SBs and β-beams offer interesting possibilities as well.

SBs offer a major advantage with respect to reactor experiments: their capability to observe CP violation and the mass hierarchy in a reasonable amount of the parameter space, if θ_{13} is not very small. Furthermore, the technology needed to produce the beam is well-known. However, their performance is tightly related to the availability of very massive detectors optimized in the low energy range and their particular specifications. At the same time, SBs are strongly limited by the intrinsic beam backgrounds. In the work presented in Ch. 3 we have studied in detail the LAGUNA-LBNO proposal, where a SB based at CERN is aimed at one of the possible locations for a neutrino observatory in Europe. Their distances to CERN range from 130 km to almost 2300 km. Different beam fluxes, optimized in order to match the first oscillation peak for each baseline, have been used. Therefore, the abilities of the different setups to explore the unknown parameters in the leptonic sector will be very different. We have considered three different very massive detectors optimized for the detection of low energy neutrinos: GLACIER, LENA and MEMPHYS. These detectors could also be used to explore neutrinos from astrophysical sources, as well as atmospheric and geoneutrinos.

This is a contribution of great interest to the community, which demonstrates that the measurement of the unknown neutrino parameters could be accomplished by the well-established SB technology together with the use of very massive neutrino detectors which have further applications

in astrophysics. Moreover, the limiting factors for each setup have been identified, providing very useful information for the optimization of the facility.

Ch. 4 has been devoted to the study of β-beams in detail. β-beams are (mainly) based in infrastructure which is already built at CERN, but they are certainly less understood and technically more challenging than SB experiments. β-beams also offer a great advantage with respect to SBs: since only one flavour is present in the beam, they are almost background-free (with the only exception of the atmospheric background, perhaps). In addition, well-known detection technologies such as the ones employed in magnetized iron or Water Čerenkov detectors can be employed. High neutrino energies, though, are mandatory in order to probe CP violation at a β-beam . These can be reached in two ways: (1) using high-Q ions; (2) going to high boost factors (a third possibility would be a combination of the two). In both cases, additional infrastructures and further research would be needed.

In particular, we have focused on two different two-baseline β-beam setups. In both cases, a β-beam produced from the decay of ^{8}Li and ^{8}B boosted at $\gamma = 350$ is aimed at a MIND detector located at 7000 km from the source. The purpose of this detector is two-fold: on one hand, it takes advantage of the resonant enhancement in the $\nu_e \to \nu_\mu$ probability which takes place only in the (anti)neutrino channel if the hierarchy is normal (inverted), providing a very clean probe of the mass ordering; on the other, due to its proximity to the magic baseline the δ-dependence disappears from the probability, providing a clean determination of θ_{13} due to the lifting of intrinsic degeneracies. The shorter baselines have been chosen so as to set the $\nu_e \to \nu_\mu$ oscillation at its first peak, where the effect of the CP violating phase is maximal. We have explored two possibilities for this baseline, depending on the ion candidates that are used to produce the beam in this case (^{6}He /^{18}Ne or ^{8}Li /^{8}B). Since both the flux and cross sections grow with γ, larger boost factors are also preferred in this case. We have restricted them to the the maximum boost factors achievable at the SPS+ at CERN (a replacement of the SPS that was proposed in a first phase within the maintainance and upgrade programme of the LHC).

We have also studied different factors that are relevant to the β-beam setups presented, such as the size of the far detector, the achievable fluxes for ^{8}Li and ^{8}B , the systematic errors and the livetime of the decay rings. In particular, we have pointed out the technical challenges involved in the construction of a decay ring aiming at 7000 km. Even though the setups considered here for a β-beam seem quite challenging from the experimental point of view, these are the kind of aggressive proposals being discussed for the next-to-next generation of facilities. Indeed, the sensitivity gain that a two-baseline β-beam would provide compared to the combination of all forthcoming reactor and accelerator experiments is remarkable. The combination of two baselines already provides good sensitivity to the three observables, whereas a more agressive proposal with a combination of four ions provides the best β-beam results. While the presently assumed β-beam fluxes cannot compete with the expectations from a NF, we find that β-beams are better optimized for regions with $\sin^2 2\theta_{13} > 10^{-3}$, providing sensitivity to the different observables in larger fractions of the parameter space.

The β-beam results presented in this thesis, together previous studies on the performance of high-γ and/or high-Q β-beams , have eventually motivated the starting of the technical study of these options. Indeed new simulations and experimental tests for the production of high-Q ions and their acceleration to high γ factors are being performed inside the EUROnu community by the experimental group at CERN in charge of the feasibility studies of a β-beam facility.

The quest for Non-Standard Interactions at Neutrino Factories

The NF is the most challenging alternative for a future neutrino oscillation facility from the technical point of view. At the same time, it is also the facility which yields the best results, with sensitivities to θ_{13}, δ and the mass hierarchy which go down to $\sin^2 2\theta_{13} \sim 10^{-5}$. In Ch. 5, we have studied the bounds that a NF could place to Non-Standard Interactions (NSI) for neutrinos propagating through matter. We have followed a completely phenomenological approach, regardless of the model of New Physics (NP) at high energies which could give rise to these low energy effective operators. Therefore, our results are completely model independent and apply to a wide variety of theories beyond the Standard Model. A comparison among three different setups has been performed keeping in mind that a possible optimization of the High-Energy NF (HENF) could be performed in order to search for NP in case θ_{13} turns out to be at reach by the ongoing (or forthcoming) neutrino experiments.

Special attention has been paid to correlations arising between the whole set of parameters associated to these new operators, and also between them and θ_{13}. We have found two uncorrelated sectors: (1) the set of parameters θ_{13}, $\epsilon_{e\mu}$ and $\epsilon_{e\tau}$, whose sensitivities are mainly achieved through the $P_{e\mu}$ and $P_{e\tau}$; (2) the $\epsilon_{\mu\tau}$ and $\epsilon_{\alpha\alpha}$, whose sensitivites are mainly achieved through the disappearance channel. Significant correlations between θ_{13}, $\epsilon_{e\mu}$ and $\epsilon_{e\tau}$ have been found at HENF setups. Such effects can be reduced placing a detector at the magic baseline, but they cannot be eliminated. The ultimate sensitivity to θ_{13} is worsened by a factor between 3 and 10 for the three setups under study when NSI are included in the analysis with respect to the standard case. The sensitivities to $\epsilon_{\mu\tau}$ and to the diagonal parameters, on the other hand, are quite independent from the setup under consideration. In the former case, we find a huge dependence on the sensitivity with $\phi_{\mu\tau}$. We also find that the sensitivity to the combination $(\epsilon_{ee} - \epsilon_{\tau\tau})$ is quite limited, since it shows up only at $\mathcal{O}(\varepsilon^3)$ in all oscillation channels. We find that the sensitivity in this case is strongly limited by the uncertainty on the matter density in the Earth.

We have also studied the possibilities of the different setups to discover CP violation due to δ, $\phi_{e\mu}$ and $\phi_{e\tau}$, and we have tried to illuminate the complicated correlations existing between them. We have studied two different cases: (1) a first possibility where CP violation is exclusively due to the presence of NSI; (2) another possibility in which CP violation could also be present in the SM. We have introduced a generalization of the CP-fraction concept for the case where several CP violating phases are involved in the analysis, and we have studied if the synergy due to the combination of different baselines/detectors helps to the measurement of CP violation. CP violation due to NSI may be observable in some cases, but strong correlations between $\phi_{e\mu}$, $\phi_{e\tau}$ and δ make it very difficult to disentangle standard and non-standard CP violation.

Among the huge amount of analysis of NSI in propagation that have been performed so far in the literature, our analysis is the most complete. We have performed a thourough study of correlations between all NSI parameters and the possibilities of observing CP violation due to simultaneous presence of several CP violating phases at a time. It should be noted that the sensitivities achieved at the high energy NF setups studied here are remarkable, and close to the edge of the effects produced by some neutrino models of NP. If NP is at the TeV scale, it is quite likely that new sources of CP violation beyond δ exist. If one interprets our exercise as an example for such generic cases, apparently, the lessons we have learned are that interplay between these phases are highly nontrivial, and any relations between them or knowledge of the right model would be of crucial importance. What we have definitely learnt in this study is that higher neutrino energies (such as 50 GeV) have proven to be crucial in order to pursue these elusive NSI effects in neutrino oscillation experiments. The work presented in this thesis demonstrates, contrary to the extended belief of the community, that a re-optimization of the NF would be needed in order to search for low energy effects of NP in the neutrino sector.

As a final remark, we have shown in this thesis how new facilities can be used to complete the measurement of the remaining unknown parameters of the leptonic mixing matrix as well as to start the study of NP beyond the three-family oscillation scenario. If any of these facilities is eventually built, it will represent a major step forward to unveil whether there is any NP beyond flavour mixing and, hopefully, to open the way towards an understanding of the flavour sector of the SM.

7

Resumen y Conclusiones

Durante las dos últimas décadas, se ha realizado toda una plétora de experimentos de oscilaciones de neutrinos para medir los parámetros de mezcla en el sector leptónico. Estos han cosechado un enorme éxito en la medida de los parámetros solares y atmosféricos, pero el tercer ángulo de mezcla, θ_{13}, es todavía desconocido, así como la fase de violación de CP, δ, y la jerarquía de los estados de masa para los neutrinos. Si θ_{13} queda fuera del rango de sensibilidad de los experimentos de oscilaciones de neutrinos actuales y de próxima construcción, será necesaria una nueva generación que nos permita determinar este elusivo ángulo de mezcla. Éste es precisamente el escenario físico que se ha considerado en el trabajo recopilado en esta tesis. Se ha realizado un estudio exhaustivo de las tres propuestas principales para futuros experimentos de oscilaciones de neutrinos: *Super-Beams* (SB), *β-beams* y *Neutrino Factories* (NF).

La búsqueda de θ_{13}, δ y la jerarquía de masas en *Super-Beams* y *β-beams*

En el caso en el que θ_{13} resultase ser extremadamente pequeño ($\sin^2 2\theta_{13} \leq 10^{-4}$) la NF es, por supuesto, la mejor opción. Sin embargo la situación podría cambiar dependiendo del valor de θ_{13}. En particular, si resultase ser relativamente grande ($\sin^2 2\theta_{13} \gtrsim 10^{-3}$), una NF a 25 GeV podría no ser necesaria. En su lugar, una NF de baja energía sería adecuada para evitar dificultades técnicas relacionadas con el *muon cooling*, al tiempo que mantendría un alto rendimiento. Aun así, debe recordarse que en este caso de θ_{13} "grande", tanto los SBs como los β-beams también ofrecen posibilidades interesantes.

Los SBs tienen una ventaja importante con respecto a los experimentos con reactores: su capacidad de observar violación de CP y la jerarquía de masas en una región razonable del espacio de parámetros, si θ_{13} no es muy pequeño. Además, la tecnología necesaria para producir el haz en este caso se conoce bien. Sin embargo, su potencial está ligado a la disponibilidad de detectores muy masivos optimizados para el rango de baja energía, y depender por tanto de las especificaciones concretas del detector. Al mismo tiempo, los SBs están fuertemente limitados por los *backgrounds* intrínsecos al haz. En el trabajo presentado en el capítulo 3 hemos estudiado en detalle la propuesta LAGUNA-LBNO, donde un SB situado en el CERN apunta a una de las posibles laboratorios capaces de alojar un observatorio de neutrinos en Europa. Las distancias de estas al CERN varían entre 130 km hasta casi 2300 km. Se han utilizado diferentes flujos para el haz, optimizados de acuerdo al primer pico de oscilación para cada distancia al detector. Por tanto, las capacidades de las diversas configuraciones para explorar los parámetros desconocidos del sector leptónico son muy diferentes para cada configuración. Hemos considerado tres detectores diferentes muy masivos, optimizados para la detección de neutrinos de baja energía: GLACIER, LENA y MEMPHYS. Estos detectores pordían usarse también para explorar neutrinos procedentes de fuentes astrofísicas, así como neutrinos atmosféricos y geoneutrinos.

Esta contribución es de gran interés para la comunidad, y demuestra que la medida de los parámetros desconocidos en el sector de los neutrinos podría alcanzarse mediante tecnología bien conocida como la de los SBs, junto con el uso de detectores muy masivos que tendrían aplicaciones adicionales en astrofísica. Además, se han identificado los factores de mayor relevancia para cada una de las configuraciones consideradas, aportando información muy útil para la optimización del experimento.

El capítulo 4 se ha dedicado al estudio de los *β-beams* en detalle. Los *β-beams* están basados, principalmente, en infraestructura que ya existe en el CERN, pero ciertamente están peor entendidos y constituyen un desafío técnico mayor que los experimentos basados en SBs. Los *β-beams* ofrecen además una gran ventaja con respecto a los SBs: puesto que sólo un sabor está presente en el haz, se encuentran prácticamente libres de *background* (con la única excepción, quizá, del *background* atmosférico). Además, para el detector se pueden emplear tecnologías bien conocidas como la del hierro magnetizado o la de los detectores de agua (*Water Čerenkov*). Por otro lado, para explorar violación de CP en un *β-beam* es necesario ir a energías más altas. Éstas pueden ser alcanzadas de dos maneras: (1) usando iones de alto *end-point* (Q); (2) acelerando los iones a alto γ (una tercera posibilidad sería una combinación de las dos). En ambos casos, serían necesarias nuevas infraestructuras y habría que realizar investigaciones adicionales.

En particular, nos hemos centrado en dos configuraciones de *β-beams* con distintas distancias al detector. En ambos casos, un *β-beam* producido por el decaimiento de ^{8}Li y ^{8}B acelerados a $\gamma = 350$ se apunta hacia un detector tipo MIND situado a 7000 km de la fuente. EL propósito de este detector es doble: por un lado, aprovecha el incremento resonante en la probabilidad para $\nu_e \to \nu_\mu$ que tiene lugar únicamente en el canal de (anti)neutrinos si la jerarquía es normal (invertida), proporcionando una evidencia clara de la ordenación de las masas; por el otro lado, debido a su proximidad a la llamada *magic baseline*, los términos que dependen de δ desaparecen de la probabilidad, proporcionando así una determinación limpia de θ_{13} debido a la ruptura de las degeneraciones intrínsecas. Por otro lado, las distancias más cortas han sido escogidas de modo que la oscilación $\nu_e \to \nu_\mu$ se encuentre en su primer pico, donde la violación de CP es máxima. Hemos explorado dos posibilidades para esta distancia, dependiendo de los iones que se usan para producir el haz en este caso (^{6}He /^{18}Ne o ^{8}Li /^{8}B). Puesto que tanto el flujo como las secciones eficaces crecen con γ, en este caso se prefieren también mayores factores de aceleración. Los hemos restringido al máximo alcanzable en el SPS+ en el CERN (un sustituto del SPS que se propuso en una primera fase dentro del plan de mantenimiento y mejoras del LHC).

Asimismo, hemos estudiado los distintos factores que resultan relevantes para las configuraciones de *β-beams* presentadas, como el tamaño del detector lejano, los flujos de ^{8}Li y ^{8}B que se podrían alcanzar, los errores sistemáticos y el *livetime* de los anillos de desintegración. En particular, hemos indicado los desafíos técnicos involucrados en la construcción de un anillo de desintegración apuntando a 7000 km. Incluso a pesar de que las configuraciones consideradas aquí para un *β-beam* parecen muy complicadas desde el punto de vista experimental, éste es el tipo de propuestas agresivas que se discuten para una segunda generación de futuros experimentos.

De hecho, la mejora en sensibilidad para un *β-beam* con dos detectores, comparada con la combinación de todos los experimentos de reactores y aceleradores venideros, es notable. La combinación de dos detectores situados a distintas distancias ya provee buena sensibilidad a los tres observables, mientras que una propuesta más agresiva que incluye la combinación de cuatro iones proporciona los mejores resultados que se pueden obtener con un en *β-beam*. Si bien los flujos asumidos actualmente para este tipo de haces no pueden competir con las expectaticas de una NF, hemos encontrado que los *β-beams* están mejor optimizados para regiones con $\sin^2 2\theta_{13} > 10^{-3}$, puesto que son sensibles a los tres observables en porciones mayores del espacio de parámetros.

Los resultados de *β-beams* presentados en esta tesis, junto con estudios previos en el rendimiento

de β-*beams* de alto γ y/o alto Q, han motivado en última instacia el estudio de estas opciones desde el punto de vista experimental. De hecho, el grupo que se ocupa de los estudios de viabilidad de un β-*beam* en el CERN ya está realizando nuevas simulaciones y pruebas experimentales en relación a la producción de iones de alto Q y su aceleración a alto γ, dentro del proyecto EUROnu.

La búsqueda de *Non-Standard Interactions* en *Neutrino Factories*

Desde el punto de vista técnico, la NF constituye la alternativa más desafiante como experimento futuro de oscilaciones de neutrinos. Al mismo tiempo, es también la que proporciona mejores resultados, con sensibilidades para θ_{13}, δ y la jerarquía de masas que llegan incluso hasta $\sin^2 2\theta_{13} \sim 10^{-5}$. En el capítulo 5 hemos estudado las cotas que una NF podría poner a *Non-Standard Interactions* (NSI) para neutrinos propagándose en materia. Hemos seguido un enfoque completamente fenomenológico, sin tener en cuenta el modelo de Nueva Física (en ingls, NP) a altas energías que pueda dar lugar a estos operadores efectivos a baja enrgía. Por tanto, nuestros resultados no dependen de la realización de ningún modelo en concreto y se aplican a una amplia variedad de teorías más allá del Modelo Estándar. Se ha elaborado una comparación entre tres posibles diseños, teniendo en cuenta que podría realizarse una posible optimización de la NF a alta energía (HENF) para la búsqueda de NP en caso de que θ_{13} resulte estar al alcance de la presente (o próxima) generación de experimentos de oscilaciones de neutrinos.

Se ha prestado especial atención a las correlaciones surgidas entre la totalidad de los parámetros asociados con estos nuevos operadores, y también entre éstos y θ_{13}. Hemos encontrado dos sectores descorrelacionados entre sí: (1) el conjunto de parámetros θ_{13}, $\epsilon_{e\mu}$ y $\epsilon_{e\tau}$, cuyas sensibilidades se consiguen principalmente a través de $P_{e\mu}$ y $P_{e\tau}$; (2) $\epsilon_{\mu\tau}$ y $\epsilon_{\alpha\alpha}$, cuyas sensibilidades se obtienen a través del canal $P_{\mu\mu}$. Hemos encontrado correlaciones significativas entre θ_{13}, $\epsilon_{e\mu}$ y $\epsilon_{e\tau}$ en NF de alta energía. Estos efectos pueden reducirse colocando un detector a la *magic baseline*, pero no eliminarse. La sensibilidad final a θ_{13} empeora en un factor entre 3 y 10 para las tres configuraciones bajo estudio cuando se incluyen NSI en el análisis, respecto al caso estándar. Las sensibilidades a $\epsilon_{\mu\tau}$ y los parámetros diagonales, por otro lado, son independientes en gran medida de la configuración considerada. En el primer caso, encontramos una gran dependencia en la sensibilidad con $\phi_{\mu\tau}$, mientras que para la combinación $(\epsilon_{ee} - \epsilon_{\tau\tau})$, la sensibilidad está bastante limitada, puesto que sólo aparece a orden $\mathcal{O}(\varepsilon^3)$ en todos los canales de oscilación. En este caso, encontramos que la sensibilidad del experimento se encuentra fuertemente limitada por la incertidumbre en la densidad de materia de la Tierra.

Hemos estudiado también las posibilidades de los distintos diseños para descubrir violación de CP debida a δ, $\phi_{e\mu}$ y $\phi_{e\tau}$, y hemos intentado esclarecer las complicacadas correlaciones existentes entre ellos. Estudiamos dos casos diferentes: (1) una primera posibilidad donde la violación de CP es debida exclusivamente a la presencia de NSI; (2) una segunda posibilidad en la que la violación de CP pueda provenir también del Modelo Estándar. Hemos introducido una generalización del concepto de la *CP-fraction* para el caso en el que varias fases de violación CP están involucradas en el análisis, y hemos estudiado si la sinergia debida a la combinación de diferentes distancias/detectores ayuda a la medida de violación de CP. Cuando ésta es producida por NSI, podría ser observable en algunos casos, pero las fuertes correlaciones entre $\phi_{e\mu}$, $\phi_{e\tau}$ y δ hacen muy difícil desentrañar el origen de la violación de CP.

Entre la vasta cantidad de análisis de NSI en propagación existente en la literatura, el nuestro es el más completo hasta ahora. Hemos realizado un estudio de las correlaciones entre todos los parámetros NSI, así como de las posibilidades de observar violación de CP debido a la presencia simultánea de varias fases que rompan CP a la vez. Se debe hacer notar que las sensibilidades obtenidas en las configuraciones de NF de alta energía aquí estudiadas son notables, y se encuentran cerca del límite de los efectos producidos en algunos modelos de NP en el sector de

los neutrinos. Si hubiera NP a la escala del TeV, es bastante probable que existieran nuevas fuentes de violación de CP más allá de δ. Si se interpreta nuestro ejercicio como un ejemplo genérico de tal caso, aparentemente, las lecciones que hemos aprendido son que la interacción entre estas fases es altamente no trivial, y que cualquie relación entre ellas o cualquier conocimiento del modelo que origina dichos operadores efectivos serían de crucial importancia. Lo que hemos aprendido definitivamente en este estudio es que resulta indispensable llegar a altas energías (50 GeV) para buscar estos elusivos efectos de NSI en experimentos de oscilaciones de neutrinos. El trabajo presentado en esta tesis demuestra, contrariamente a la creencia extendida en la comunidad, que una reoptimización de la NF sería necesaria para buscar efectos a baja energía de NP en el sector de los neutrinos.

Como observación final, en esta tesis hemos mostrado cómo los nuevos experimentos de oscilaciones de neutrinos podrían utilizarse para completar las medidas de los parámetros aún desconocidos de la matriz de mezcla leptónica, así como para comenzar el estudio de NP más allá de las oscilaciones a tres familias. Si finalmente se construyera cualquiera de estas instalaciones, representará un gran paso en dirección a revelar si hay NP detrás de la mezcla de sabores y, con suerte, podría abrirnos el camino hacia el entendimiento del sector de sabor del Modelo Estándar.

A

The acceleration and storage chain

In this Appendix we comment on some differences and similarities between the production and acceleration of ^{8}Li and ^{8}B with respect to ^{6}He and ^{18}Ne (for $\gamma = 100$ or 350). Numbers quoted here are taken from the EURISOL collaboration webpage [355, 356]. They have been computed for ^{6}He and ^{18}Ne ions boosted at $\gamma = 100$, trying to achieve the goal luminosity of 2.9×10^{18} ^{6}He and 1.1×10^{18} ^{18}Ne ion decays per year, respectively.

A.1 Proton Driver

We show in Fig. A.1 a schematic view of the infrastructure needed to produce and accelerate the ion beam. Notice that this scheme was designed for "standard" ^{6}He/^{18}Ne beams. In the baseline design, the proton driver is the proposed Super Proton Linac (SPL), a multi-MW ($\sim$ 4 MW, E_p =2.2 GeV [241] or 3.5 GeV [357, 358]) machine aimed at substituting the present Linac2 and PS Booster (PSB). Contrary to naive expectation, however, a multi-MW booster is not needed for the construction of a β-beam or an EURISOL facility[1]. Any of the possibilities currently under discussion at CERN for the upgrade of the PSB, based either on Rapid Cycling Synchrotron's or on Linac's, represents a viable solution for the production stage of a β-beam complex. In the framework of the LHC maintenance and upgrade programme, the PAF committee [359] suggested the substitution of the Linac2 with a new Linac (Linac4) that will inject protons into the PSB at 160 MeV. This would allow production of $\sim 2\times10^{13}$ ^{6}He/s for 200 kW on target, consistent with the current SPL-based design.

A.2 Ion production

The main difference between a ^{8}Li /^{8}B β-beam production and acceleration complex with respect to the baseline design (depicted in Fig. A.1) is the target. Instead of an EURISOL target station, a device in which a sustained ^{8}Li/^{8}B flux can be produced using the "ionization cooling" technique is needed. For details on the ion production, see Refs. [277, 361].

According to the latest numbers by the EURISOL collaboration [355], 5×10^{13} ^{6}He atoms/s and 2×10^{12} ^{18}Ne atoms/s can be produced using standard BeO and MgO ISOL targets, respectively. No relevant changes in these numbers are expected using a different design for the proton driver. The ^{18}Ne production rate is still low to obtain the goal luminosity 1.1×10^{18} ν_e/year.

[1] The SPL (or a similar proton driver) is mandatory, instead, for a low-energy neutrino SuperBeam [242] or for a Neutrino Factory.

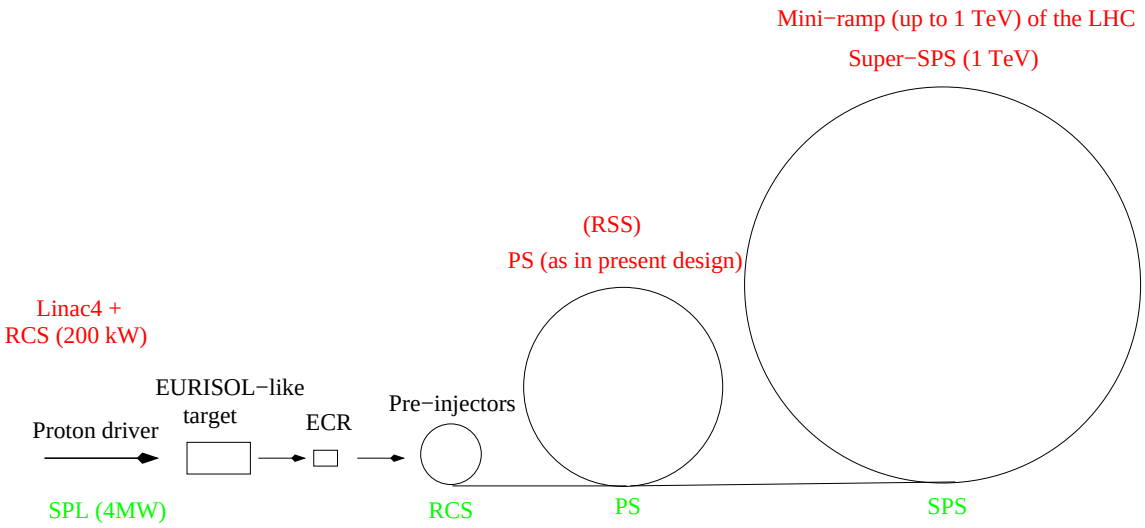

Figure A.1: The main components of the β-beam production and acceleration complex. In the lower part, the machines considered in the baseline option are indicated (where RCS stands for Rapid Cycling Synchrotron). The alternatives that profit of the LHC maintenance and upgrade programme are mentioned in the upper part. The Rapid Superconducting Synchrotron [360] (RSS) is a possible upgrade of the PS. Eventually, the Super-SPS is presently known as "SPS+".

Once isotopes are produced, they are collected and ionized using an ECR ion source. Ionization efficiency at this stage is ^{18}Ne is 29%, whereas for the ^{6}He flux is 93% [355].

A.3 Acceleration stage

In Tab. A.1 we give the relevant parameters, extracted from Ref. [355], for the acceleration stage of He/Ne ions up to $\gamma = 100$ in the standard (reference) setup. At the same time, we compute the values of the same parameters for Li/B ions injected and accelerated using the same setup up to $\gamma = 100$. We assume for Li/B the same number of ions injected per second in each stage as for He ions. Notice that no asymmetry is expected for Li/B, since both ions have similar Z, A and $T_{1/2}$ (see Tab. 4.1). This is not the case for ^{6}He and ^{18}Ne, whose production and ionization stages differ significantly.

Unfortunately, we cannot perform a similar computation of these parameters for the setups used in Ch. 4 (*i.e.* accelerating Li/B ions up to $\gamma = 350$) in the absence of a detailed technical specification of the acceleration chain.

The standard acceleration stage consists of four steps:

1. Ions are accelerated to $\gamma = 1.1$ introducing them into a LinAc (where ^{18}Ne ions get fully ionized).

2. They are then injected into the Rapid Cycling Synchrotron (RCS), where they reach $\gamma_{He} = 1.8$ and $\gamma_{Ne} = 2.8$ ($\gamma_{Li} = 1.9$ and $\gamma_{B} = 2.9$). The transfer efficiency from the LinAc to the RCS is 50%, only. The different γ reached at the end of this phase depends on the different A/Z, at fixed magnetic field, radius and acceleration time ($t_{acc} \sim 0.05$ s). No significant power losses (see, *e.g.*, Ref. [356]) are expected at this stage ($\lesssim 0.1$ KW), for any of the

considered ions. No benefit from the LHC maintenance and upgrade phase is expected.

3. After the RCS, ions are transported and injected into the PS. Once in the PS, they are accelerated up to $\gamma_{He} = 9.3$ and $\gamma_{Ne} = 15.5$ ($\gamma_{Li} = 10.3$ and $\gamma_B = 17.4$), in $t_{acc} \sim 0.8$ s. Significant power losses are expected at this stage, for any of the considered ions[2]: $P_{He} \simeq 0.8$ KW, $P_{Ne} \simeq 1.0$ KW, $P_{Li} \simeq 1.1$ KW, $P_B \simeq 1.3$ KW. This corresponds to a power loss per meter of $P_{He}/L_{PS} = 1.3$ W/m, $P_{Ne}/L_{PS} = 1.6$ W/m, $P_{Li}/L_{PS} = 1.8$ W/m, $P_B/L_{PS} = 2.1$ W/m. These values exceed the permitted upper limit, 1 W/m. This is a well known problem, see *e.g.* Ref. [287] and [355], that must be solved if we are to use the PS at CERN as a second stage ion beam accelerator.

   This acceleration stage could greatly benefit of the LHC maintenance and upgrade programme. The PS is the oldest machine in the CERN complex, and it has been proposed to replace it with a new 50 GeV synchrotron (called "PS2") [359]. Using the PS2, substantial improvements are expected.

4. After coming out of the PS, ions are transported and injected into the SPS with no significant expected losses. In this last acceleration stage, they are boosted to $\gamma = 100$ in $t_{He} = 2.5$ s and $t_{Ne} = 1.4$ s ($t_{Li} = 2.2$ s and $t_B = 1.2$ s). Power losses at this stage are: $P_{He} = 3.0$ KW, $P_{Ne} = 1.8$ KW, $P_{Li} = 3.4$ KW and $P_B = 2.2$ KW. In this case, due to the longer SPS circumference ($L = 6912$ m), the power loss per meter is: $P_{He}/L_{SPS} = 0.4$ W/m, $P_{Ne}/L_{SPS} = 0.3$ W/m, $P_{Li}/L_{SPS} = 0.5$ W/m and $P_B/L_{SPS} = 0.3$ W/m, well within acceptable limits for all considered ions.

   The SPS+ would have an enormous impact on the design of a β-beam at CERN. A detailed simulation of the acceleration and losses at this facility for any of the considered ions is lacking. Notice, however, that the proposed design fulfills simultaneously the two most relevant requirements for a high energy β-beam booster: it provides a fast ramp ($dB/dt = 1.2 \div 1.5$ T/s [362]) to minimize the number of decays during the acceleration phase and it can increase the γ boosting factor up to $\gamma \leq 600$.

The outcome of our analysis is that accelerating He/Ne or Li/B ions using the same acceleration chain up to the same final γ will give similar results for particle losses and dissipated power.

[2]We have computed the number of lost particles and the dissipated power at each acceleration stage following Ref. [356], getting good agreement with Ref. [355] for the RCS and the SPS and for the particle loss at the PS. However, our result for the power loss for ^{6}He and ^{18}Ne in the PS differ from that reported in Ref. [355]. We do not understand the source of the disagreement. Notice that our conclusion is not affected by this discrepancy, though: the total dissipated power at the PS exceeds presently allowed values.

	^{6}**He**	^{18}**Ne**	^{8}**Li**	^{8}**B**
LINAC				
(Injected ions/s)/10^{12}	17.1 [355]	5.25 [355]	17.1	17.1
γ_{final}	1.11 [355]	1.11 [355]	1.10	1.10
RCS ($L = 251$ m)				
(Injected ions/s)/10^{12}	8.53 [355]	2.62 [355]	8.53	8.53
γ_{final}	1.84 [355]	2.77 [355]	1.9	2.9
P (KW)	$\lesssim 0.1$	$\lesssim 0.1$	$\lesssim 0.1$	$\lesssim 0.1$
$t_{acc}(s)$	0.0475 [355]	0.0475 [355]	0.0475	0.0475
PS ($L = 628$ m)				
(Injected ions/s)/10^{12}	1.84 [355]	1.25 [355]	1.84	1.84
γ_{final}	9.33 [355]	15.53 [355]	10.3	17.4
P (KW)	0.8	1.0	1.1	1.3
P/L (W/m)	1.3	1.6	1.8	2.1
$t_{acc}(s)$	0.8 [355]	0.8 [355]	0.8	0.8
SPS ($L = 6912$ m)				
(Injected ions/s)/10^{12}	1.59 [355]	1.20 [355]	1.61	1.68
γ_{final}	100	100	100	100
P (KW)	3.0	1.8	3.4	2.2
P/L (W/m)	0.4	0.3	0.5	0.3
$t_{acc}(s)$	2.54 [355]	1.42 [355]	2.2	1.2

Table A.1: Relevant beam parameters at the different acceleration stages of the standard β-beam setup for ^{6}He/^{18}Ne and ^{8}Li/^{8}B.

B

Oscillation probabilities

Vacuum oscillation probabilities are relatively easy to derive from Eqs. (1.14) and (1.15). However, in matter these probabilities are much more complicated. The exact formulae where no mass difference is neglected can be found in [363]. However, physical implications of these formulae are not easily seen. On the other hand, approximated expressions of these oscillation probabilities can be worked out through perturbative expansions on small parameters. We will introduce in Sec. B.1 the approximate probabilities in matter (under the assumption of constant matter density[1]) for the $\nu_e \to \nu_{\mu,\tau}$ and $\nu_\mu \to \nu_\mu$ oscillation channels, while in Sec. B.2 we will present the approximate oscillation probabilities for the same channels in presence of NSI.

B.1 Oscillation probabilities in the standard approach

Approximate expressions for the oscillation probabilities can be worked out taking advantage of the fact that θ_{13} and $\Delta m^2_{21}/\Delta m^2_{31} \equiv \alpha \simeq 7.5 \times 10^{-5}/2.5 \times 10^{-3} \sim 0.03$ are very small parameters. Remember that for long baseline experiments, such as the ones considered here, $V \sim \Delta_{31}$. Thus, probabilities can be safely expanded up to second order in the following parameters [167]:

$$\varepsilon : \left\{\theta_{13},\, \Delta m^2_{21}/\Delta m^2_{31},\, \Delta m^2_{21}/V\right\}$$

where $V = \sqrt{2} G_F N_e$ (eV^2/GeV).

B.1.1 The $\nu_e \to \nu_\mu$ appereance channel

This channel is often referred to as the **"golden channel"** [325], because it offers the best option to find CP violation from both the theoretical and experimental point of view:

$$P^{\pm,\mathrm{mat}}_{e\mu}(\theta_{13}, \delta) = X^\mu_\pm \sin^2 2\theta_{13} + Y^\mu_\pm \cos\theta_{13} \sin 2\theta_{13} \cos\left(\pm\delta - \frac{\Delta_{31} L}{2}\right) + Z^\mu\,, \tag{B.1}$$

[1] It is important to take into account that these probabilities are not valid for neutrinos traveling through the Sun or the Earth core, where the constant matter density assumption is no longer valid. In addition, if $\Delta m^2_{21} L/2E \simeq 1$, the solar terms start oscillating and the probabilities presented here are no longer valid either.

where ± refers to neutrinos and antineutrinos, respectively, and

$$\begin{cases} X^{\mu}_{\pm} &= \sin^2\theta_{23}\left(\frac{\Delta_{13}}{B_{\mp}}\right)^2\sin^2\left(\frac{B_{\mp}L}{2}\right)\,, \\ Y^{\mu}_{\pm} &= \sin 2\theta_{12}\sin 2\theta_{23}\left(\frac{\Delta_{21}}{V}\right)\left(\frac{\Delta_{31}}{B_{\mp}}\right)\sin\left(\frac{VL}{2}\right)\sin\left(\frac{B_{\mp}L}{2}\right)\,, \\ Z^{\mu} &= \cos^2\theta_{23}\sin^2 2\theta_{12}\left(\frac{\Delta_{21}}{V}\right)^2\sin^2\left(\frac{VL}{2}\right)\,, \end{cases}$$

with $Z^{\mu} = Z^{\mu}_{+} = Z^{\mu}_{-}$, $\Delta_{ij} = \dfrac{\Delta m^2_{ij}}{2E}$, and $B_{\mp} = |V \mp \Delta_{31}|$ (with $\mp$ referring to neutrinos and antineutrinos, respectively). s_{ij} and c_{ij} stand for $\sin(\theta_{ij})$ and $\cos(\theta_{ij})$, respectively.

Its T-conjugated channel, $\nu_\mu \rightarrow \nu_e$, has the same oscillation probability, changing $\delta \rightarrow -\delta$. It is sometimes called the "**platinum channel**".

B.1.2 The $\nu_e \rightarrow \nu_\tau$ appearance channel

This probability is identical to that for the golden channel, only replacing $c_{23} \leftrightarrow -s_{23}$ and $s_{23} \leftrightarrow c_{23}$. Theoretically, it has thus the same sensitivity to δ as the "golden channel". However, taus are more difficult to detect than muons, and thus this channel is often referred to as the **"silver channel"** [173]:

$$P^{\pm,\mathrm{mat}}_{e\tau}(\theta_{13},\delta) = X^{\tau}_{\pm}\sin^2 2\theta_{13} - Y^{\tau}_{\pm}\cos\theta_{13}\sin 2\theta_{13}\cos\left(\pm\delta - \frac{\Delta_{31}L}{2}\right) + Z^{\tau}\,, \tag{B.2}$$

where ± refers to neutrinos and antineutrinos, respectively, and

$$\begin{cases} X^{\tau}_{\pm} &= \cos^2\theta_{23}\left(\frac{\Delta_{31}}{B_{\mp}}\right)^2\sin^2\left(\frac{B_{\mp}L}{2}\right)\,, \\ Y^{\tau}_{\pm} &= Y^{\mu}_{\pm}\,, \\ Z^{\tau} &= \sin^2\theta_{23}\sin^2 2\theta_{12}\left(\frac{\Delta_{21}}{V}\right)^2\sin^2\left(\frac{VL}{2}\right)\,, \end{cases}$$

with $Z^{\tau} = Z^{\tau}_{+} = Z^{\tau}_{-}$.

B.1.3 The $\nu_\mu \rightarrow \nu_\mu$ disappearance channel

The disappearance probability for muon neutrinos reads as:

$$P^{\pm,\mathrm{mat}}_{\mu\mu}(\theta_{13},\delta) = 1 - \chi_{\pm}\sin^2 2\theta_{13} - \psi_{\pm}\sin 2\theta_{13}\cos\delta - \omega\,, \tag{B.3}$$

where $\pm$ refers to neutrinos and antineutrinos, respectively, and

$$\begin{cases} \chi_\pm &= s^2_{23}\left(\frac{\Delta_{31}}{B_\mp}\right)^2 \sin\left(\frac{B_\mp L}{2}\right) - \frac{1}{4}\sin^2 2\theta_{23}\left(\frac{V}{B_\mp}\right)\left(\frac{\Delta_{31}L}{2}\right)\sin\left(\Delta_{31}L\right) + \\ & \quad + \frac{1}{2}\sin^2 2\theta_{23}\left(\frac{\Delta_{31}}{B_\mp}\right)^2 \cos\left(\frac{VL}{2}\right)\sin\left(\frac{B_\mp L}{2}\right)\sin\left(\frac{\Delta_{31}L}{2}\right), \\ \psi_\pm &= \sin 2\theta_{12}\sin 2\theta_{23}\left(\frac{\Delta_{21}}{V}\right)\left(\frac{\Delta_{31}}{B_\mp}\right)\left[\cos\left(\frac{\Delta_{31}L}{2}\right)\sin\left(\frac{VL}{2}\right)\sin\left(\frac{B_\mp L}{2}\right) + \right. \\ & \quad \left. + \cos 2\theta_{23}\sin\left(\frac{VL}{2}\right)\cos\left(\frac{B_\mp L}{2}\right)\sin\left(\frac{\Delta_{31}L}{2}\right) - \cos 2\theta_{23}\left(\frac{V}{\Delta_{31}}\right)^2 \sin^2\left(\frac{\Delta_{31}L}{2}\right)\right], \\ \omega &= \sin^2 2\theta_{23}\sin^2\left(\frac{\Delta_{31}L}{2}\right) + c^2_{23}\sin^2\theta_{12}\left(\frac{\Delta_{21}}{V}\right)^2 \sin^2\left(\frac{VL}{2}\right) - \\ & \quad - c^2_{12}\sin^2 2\theta_{23}\left(\frac{\Delta_{21}L}{2}\right)\left[\sin\left(\Delta_{31}L\right) - c^2_{12}\left(\frac{\Delta_{21}L}{2}\right)\cos\left(\Delta_{31}L\right)\right] - \\ & \quad - \frac{1}{2}\sin^2 2\theta_{12}\sin^2 2\theta_{23}\left[\left(\frac{\Delta_{21}}{V}\right)^2 \sin\left(\frac{VL}{2}\right)\cos\left(\frac{B_\mp L}{2}\right)\sin\left(\frac{\Delta_{31}L}{2}\right) - \right. \\ & \quad \left. - \frac{1}{2}\left(\frac{\Delta_{21}}{V}\right)\left(\frac{\Delta_{21}L}{2}\right)\sin\left(\Delta_{31}L\right)\right], \end{cases}$$

with $\omega = \omega_+ = \omega_-$.

All terms except the first one in ω are suppressed either by s_{13} or $\Delta m^2_{21}L/E$. This channel is then, on first approximation, only sensitive to θ_{23} and Δm^2_{32}. This is in fact the oscillation regime observed in atmospheric neutrino experiments, which have already measured the atmospheric parameters. However, the first term in Eq. (**??**) does not depend on the sign of Δm^2_{32} which remains unknown. Eq. (**??**) also shows that θ_{23} cannot be distinguished from $\pi/2 - \theta_{23}$.

B.2 Oscillation probabilities in presence of NSI

We will now show the oscillation probabilities $P_{\alpha\beta}$ in matter with constant density, in presence of NSI affecting only to propagation in matter. We start from the oscillation probability expansions derived in [341] where $\epsilon_{\alpha\beta}$, θ_{13}, and $\Delta m^2_{31}/\Delta m^2_{21}$ are considered the expansion parameters. Here we simply expand also on $\delta\theta_{23} \equiv \theta_{23} - \pi/4$, considering therefore:

$$\varepsilon : \left\{\epsilon_{\alpha\beta},\, \theta_{13},\, \Delta m^2_{21}/\Delta m^2_{31},\, \delta\theta_{23}\right\}$$

as the order ε expansion parameters.

The oscillation probabilities for golden and silver channels at quadratic order on ε are given

by the following formulae:

$$
\begin{aligned}
P_{e\mu} &= \left| \mathcal{A}^{SM}_{e\mu} + \epsilon_{e\mu} \left[\sin\left(\frac{VL}{2}\right) e^{-i\frac{\Delta_{31}L}{2}} + \left(\frac{V}{\Delta_{31}-V}\right) \sin\left(\frac{\Delta_{31}-V}{2}L\right) \right] \right. \\
&\qquad \left. - \epsilon_{e\tau} \left[\sin\left(\frac{VL}{2}\right) e^{-i\frac{\Delta_{31}L}{2}} - \left(\frac{V}{\Delta_{31}-V}\right) \sin\left(\frac{\Delta_{31}-V}{2}L\right) \right] \right|^2 \\
&= \left| \sqrt{2}\frac{\Delta_{21}}{V} + \epsilon_{e\mu} - \epsilon_{e\tau} \right|^2 \sin^2\frac{VL}{2} \\
&+ \left| \sqrt{2} e^{-i\delta} \frac{\Delta_{31}}{V} + \epsilon_{e\mu} + \epsilon_{e\tau} \right|^2 \left(\frac{V}{\Delta_{31}-V}\right)^2 \sin^2\frac{\Delta_{31}-V}{2}L \\
&+ 4\,\mathrm{Re}\left[\left(\frac{\Delta_{21}}{V} + \frac{1}{\sqrt{2}}\left(\epsilon_{e\mu} - \epsilon_{e\tau}\right) \right) \left(e^{i\delta}\frac{\Delta_{31}}{V} + \frac{1}{\sqrt{2}}\left(\epsilon^*_{e\mu} + \epsilon^*_{e\tau}\right) \right) \right] \\
&\qquad \times \frac{V}{\Delta_{31}-V} \sin\frac{VL}{2} \cos\frac{\Delta_{31}L}{2} \sin\frac{\Delta_{31}-V}{2}L \\
&+ 4\,\mathrm{Im}\left[\left(\frac{\Delta_{21}}{V} + \frac{1}{\sqrt{2}}\left(\epsilon_{e\mu} - \epsilon_{e\tau}\right) \right) \left(e^{i\delta}\frac{\Delta_{31}}{V} + \frac{1}{\sqrt{2}}\left(\epsilon^*_{e\mu} + \epsilon^*_{e\tau}\right) \right) \right] \\
&\qquad \times \frac{V}{\Delta_{31}-V} \sin\frac{VL}{2} \sin\frac{\Delta_{31}L}{2} \sin\frac{\Delta_{31}-V}{2}L + O(\varepsilon^3)\,,
\end{aligned}
\tag{B.4}
$$

$$
\begin{aligned}
P_{e\tau} &= \left| \mathcal{A}^{SM}_{e\tau} + \epsilon_{e\tau} \left[\sin\left(\frac{VL}{2}\right) e^{-i\frac{\Delta_{31}L}{2}} + \left(\frac{V}{\Delta_{31}-V}\right) \sin\left(\frac{\Delta_{31}-V}{2}L\right) \right] \right. \\
&\qquad \left. - \epsilon_{e\mu} \left[\sin\left(\frac{VL}{2}\right) e^{-i\frac{\Delta_{31}L}{2}} - \left(\frac{V}{\Delta_{31}-V}\right) \sin\left(\frac{\Delta_{31}-V}{2}L\right) \right] \right|^2 \\
&= \left| \sqrt{2}\frac{\Delta_{21}}{V} + \epsilon_{e\mu} - \epsilon_{e\tau} \right|^2 \sin^2\frac{VL}{2} \\
&+ \left| \sqrt{2} e^{-i\delta} \frac{\Delta_{31}}{V} + \epsilon_{e\mu} + \epsilon_{e\tau} \right|^2 \left(\frac{V}{\Delta_{31}-V}\right)^2 \sin^2\frac{\Delta_{31}-V}{2}L \\
&- 4\,\mathrm{Re}\left[\left(\frac{\Delta_{21}}{V} + \frac{1}{\sqrt{2}}\left(\epsilon_{e\mu} - \epsilon_{e\tau}\right) \right) \left(e^{i\delta}\frac{\Delta_{31}}{V} + \frac{1}{\sqrt{2}}\left(\epsilon^*_{e\mu} + \epsilon^*_{e\tau}\right) \right) \right] \\
&\qquad \times \frac{V}{\Delta_{31}-V} \sin\frac{VL}{2} \cos\frac{\Delta_{31}L}{2} \sin\frac{\Delta_{31}-V}{2}L \\
&- 4\,\mathrm{Im}\left[\left(\frac{\Delta_{21}}{V} + \frac{1}{\sqrt{2}}\left(\epsilon_{e\mu} - \epsilon_{e\tau}\right) \right) \left(e^{i\delta}\frac{\Delta_{31}}{V} + \frac{1}{\sqrt{2}}\left(\epsilon^*_{e\mu} + \epsilon^*_{e\tau}\right) \right) \right] \\
&\qquad \times \frac{V}{\Delta_{31}-V} \sin\frac{VL}{2} \sin\frac{\Delta_{31}L}{2} \sin\frac{\Delta_{31}-V}{2}L + O(\varepsilon^3)\,,
\end{aligned}
\tag{B.5}
$$

where $\mathcal{A}^{SM}_{\alpha\beta}$ stands for the standard oscillation amplitude.

On the other hand, since the sensitivities to $\epsilon_{e\mu}$ and $\epsilon_{e\tau}$ are mainly achieved through the golden and silver channels, for the $\nu_\mu - \nu_\tau$ sector we show here only the dependence on $\epsilon_{\alpha\alpha}$ and $\epsilon_{\mu\tau}$ of the relevant oscillation probabilities, which will be called $P^{NSI}_{\alpha\beta}$:

$$
\begin{aligned}
P_{\mu\mu}^{NSI} &= -P_{\mu\tau}^{NSI} \\
&= -\left\{\delta\theta_{23}\left(\epsilon_{\mu\mu}-\epsilon_{\tau\tau}\right)+\mathrm{Re}\left(\epsilon_{\mu\tau}\right)\right\}(VL)\sin\left(\Delta_{31}L\right) \\
&+ \left\{4\delta\theta_{23}\left(\epsilon_{\mu\mu}-\epsilon_{\tau\tau}\right)\frac{V}{\Delta_{31}}+\left(\epsilon_{\mu\mu}-\epsilon_{\tau\tau}\right)^2\left(\frac{V}{\Delta_{31}}\right)^2\right\}\sin^2\frac{\Delta_{31}L}{2} \\
&- \frac{1}{2}\left(\mathrm{Re}(\epsilon_{\mu\tau})\right)^2(VL)^2\cos\left(\Delta_{31}L\right)-\left(\mathrm{Im}(\epsilon_{\mu\tau})\right)^2\frac{V}{\Delta_{31}}(VL)\sin\left(\Delta_{31}L\right)+O(\varepsilon^3)\,.
\end{aligned}
\tag{B.6}
$$

The complete oscillation probabilities at quadratic order in presence of NSI can be found in [341], though.

C

Statistical procedure

In this section, we describe the statistical approaches used to perform the numerical analyses in Ch. 5.

C.1 The statistical procedure used in Secs. 5.4 and 5.5

It is well-known that, in order to sample a N-dimensional parameter space through χ^2 grids with n samplings per parameter, a total of $\mathcal{O}(n^N)$ evaluations of the expected number of events are required. When only three-family oscillations are considered, the computation can become heavy (if all νSM parameters are taken into account) but is still affordable within the standard frequentist approach. When the NSI parameters are also taken into account, however, the number of parameters to be fitted simultaneously increases considerably and the computation time required to perform the standard minimization procedure becomes too large. A different approach must therefore be used if we want to sample a huge number of parameters with limited computational resources. The way out is suggested by noticing that most of the points belonging to the χ^2 grids that are computed in the standard approach are useless, as they are very far from the χ^2 minimum. For this reason the standard technique used to sample large multi-dimensional manifolds is to rely on efficient (either deterministic or stochastic) algorithms that search for the global minimum and then start to sample the region near the minimum to determine its size and shape. Most of the algorithms used fall into the category of Markov Chain Monte Carlo (MCMC): using these class of algorithms, the number of evaluations required for the algorithm to converge and sample properly the desired distribution grows polynomially with N, $\mathcal{O}(N^k)$, with k some integer. We have followed this approach to scan the NSI parameter space in Secs. 5.4 and 5.5, using the MonteCUBES ("Monte Carlo Utility Based Experiment Simulator") software [70] that contains a C library plug-in to implement MCMC sampling into the GLoBES [254, 255] package. It, thus, benefits from the flexibility of GLoBES in defining different experiments while implementing an efficient scanning of large parameter spaces.

Parameter determination through MCMC methods are based on Bayesian inference. The aim is to determine the probability distribution function of the different model parameters θ given some data set d, *i.e.*, the *posterior* probability $P(\theta \mid d)$. From Baye's theorem we have:

$$\mathcal{P} = P(\theta \mid d) = \frac{P(d \mid \theta) P(\theta)}{P(d)} \equiv \frac{L_d(\theta)\pi(\theta)}{M} \,. \tag{C.1}$$

The *likelihood* $L_d(\theta) = P(d \mid \theta)$ is the probability of observing the data set d given certain values of the parameters θ. The prior $\pi(\theta) = P(\theta)$ is the probability that the parameters assume the value θ regardless of the data d, that is, our previously assumed knowledge of the parameters. Finally, the

marginal probability M is the probability $P(d)$ of measuring the values d. It does not depend on the parameters θ, and therefore it can be regarded as a normalization constant[1]. Notice that the χ^2 functions defined in GLoBES provide the logarithm of the likelihood of the data d following a Poisson distribution normalized to the distribution with mean d. Therefore, the actual probability density sampled by MonteCUBES is the posterior probability $P(\theta \mid d)$:

$$\mathcal{P} = \exp\left[-\frac{\chi^2(\theta)}{2}\right] \exp\left[-\frac{\chi^2_P(\theta)}{2}\right],$$

where $\chi^2_P(\theta) = -2\ln\pi(\theta)$. This probability distribution is equivalent to a Boltzmann weight with temperature $T = 1$ and energy $E = \chi^2(\theta) + \chi^2_P(\theta)$.

We have used ten MCMC chains in all our simulations. The convergence of the whole sample improves as $R \to 1$, with R being the ratio between the variance in the complete sample and the variance for each chain. We have checked that the chains have reached proper convergence in all cases better than $R - 1 = 2.5 \times 10^{-2}$.

A typical problem when a minimization algorithm different from the complete computation of the multi-dimensional grid is applied is the possible presence of local minima or of multiple global minima ("degeneracies"). In both cases, if the minima are deep enough the algorithm will get stuck there and sample a region that does not correspond to the global minimum or will not be able to identify the presence of degenerate minima. The MonteCUBES package includes a method to identify local minima by increasing the temperature T of the chain so that the likelihood is modified to $\mathcal{P} \propto \mathcal{P}^{1/T}$. This procedure flattens the likelihood distribution, making it possible for the chains to jump from a local minimum to another. The temperature and step sizes are then decreased in successive steps and thus the different chains get stuck around different minima, unable to move through the disfavored regions when T is too low. After this, the points where the different chains have stopped are compared to decide how many different minima the chains have fallen into. Finally, new steps are added with the correct length in the direction between the degeneracies. As a result, the algorithm is able to jump between minima and sample all of them properly.

For the implementation of the NSI probabilities in matter, we use the non-Standard Interaction Event Generator Engine (nSIEGE) distributed along with the MonteCUBES package.

The definition of confidence level (CL) in a multi-dimensional MCMC algorithm need to be clarified, as it approaches the standard definition only in the limit of infinite statistics. What is done in practice with a MCMC is to generate a given number of points distributed stochastically in the multi-dimensional parameter space around the global minimum (minima). After that, projections of that multi-dimensional "cloud" of points are performed onto any desired plane chosen accordingly to the variables under study in the analysis. The projection over a given plane corresponds to marginalization over the parameters that are no longer retained. After projection, the two-dimensional plane is divided into cells and the number of points falling into each cell is computed. For small enough cells, the resulting two-dimensional histogram can be approximated by a smooth surface, for which slices can be drawn for the desired CL (68%, 90%, or 95%, in this work).

[1] In the limit of infinite statistics, it can be shown that the Bayesian probability distribution is maximized by the same set of parameters θ that minimize the χ^2 function in the frequentist approach.

C.2 The statistical procedure used in Sec. 5.6

To explore the CP discovery potential we need a different statistical procedure from the one defined in Sec. C.1. The reason is the following: a MCMC, as described above, explores the region which is close to the global minimum (or to degenerate minima) sampling with good accuracy the χ^2 distribution around that point(s). This is the right procedure to follow if we are exploring the sensitivity that a facility has to some particular observable. Consider the particular case of the sensitivity to θ_{13} in the (θ_{13}, δ) plane with marginalization over the rest of νSM and NSI parameters (see Sec. 5.4). In this case, the MCMC algorithm scans the multi-dimensional surface corresponding to a given choice of the input parameters (with the particular choice $\bar{\theta}_{13} = 0$ for θ_{13}) and a contour at a given CL of the region compatible with vanishing θ_{13} is drawn, after projecting over the (θ_{13}, δ) plane. When we compute a discovery potential, on the other hand, we first fix the parameters to be tested and draw the corresponding CL contours. Then, we check if the condition we want to fulfill is satisfied or not at a given CL (in the case of the CP discovery potential, the condition is that the contours drawn for a given set of CP violating input parameters do not touch any CP conserving point of the parameter space). Eventually, we repeat the procedure again and again varying the input parameters. If the grid density is large enough, the distribution of the input parameters that satisfy the required condition is smooth and a "CL contour" can be drawn.

If we were to use the MCMC approach to compute a discovery potential, then, we should run the algorithm as many times as the points in the grid that we want to test. In this case, the total time required to compute the discovery potential goes as $n^{N_g} \times N^k$, with n the number of points to be tested for one parameter and N_g the dimensionality of the grid. If n is large the MCMC cannot be used and the standard frequentist approach must be adopted instead. The drawback of the frequentist approach is that, in order to keep the computational time from being rapidly divergent, we cannot marginalize over the whole νSM and NSI parameter space. For this reason, in Sec. 5.6 we will not marginalize over atmospheric and solar parameters and will consider fixed inputs for the NSI parameters.

The procedure that has been used in this work to determine the CP-discovery potential is outlined below:

1. We first compute the number of expected events at the detector(s): $N(\theta_{13}, \{\phi\})$, where $\{\phi\} \equiv \{\delta, \phi_{e\mu}, \phi_{e\tau}\}$.

2. After having computed grids of number of events as a function of $(\theta_{13}; \{\phi\})$, we compute the χ^2 as follows:

$$\chi^2(\theta_{13}, \bar{\theta}_{13}; \{\phi\}, \{\bar{\phi}\}) = \sum_{\text{polarities,bins}} \frac{(N(\theta_{13}; \{\phi\}) - N(\bar{\theta}_{13}; \{\bar{\phi}\})^2}{\left(N(\bar{\theta}_{13}; \{\bar{\phi}\})^{1/2} + f N(\bar{\theta}_{13}; \{\bar{\phi}\})\right)^2} \tag{C.2}$$

   with f an overall systematic error. In all the plots given in this section, we assume the overall systematic error for the MIND detector as $f_\mu = 0.02$, and the one for the τ-signal as $f_\tau = 0.05$. No background has been considered to compute Eq. (C.2).

3. We compute, then, for any input $(\bar{\theta}_{13}; \{\bar{\phi}\})$, the χ^2 function defined in Eq. (C.2) at the eight CP-conserving (CPC) points:

$$\{\phi\}_{CPC} = (0,0,0); (0,0,\pi); (0,\pi,0); (\pi,0,0); (0,\pi,\pi); (\pi,0,\pi); (\pi,\pi,0); (\pi,\pi,\pi)\,,$$

   taking the smallest χ^2 value found. Using this procedure, we obtain the five-dimensional surface:

$$\chi^2_{CPC}(\theta_{13}, \bar{\theta}_{13}; \{\bar{\phi}\}) = \min_{\{\phi\}_{CPC}} \left(\chi^2(\theta_{13}, \bar{\theta}_{13}; \{\phi\}_{CPC}, \{\bar{\phi}\})\right) \tag{C.3}$$

This procedure generalizes to the case of three simultaneously active phases the procedure outlined in Ref. [338], where only δ and $\phi_{e\tau}$ were considered.

4. We distinguish, then, between two cases depending on the value of $\bar{\theta}_{13}$:

   - The first possibility is that θ_{13} is already measured by the time the HENF is built. In this case, we can use the χ^2 function (C.3) computed at $\theta_{13} = \bar{\theta}_{13}$ to see the region of the phase parameter space where CP violation can be distinguished from the CP conservation hypothesis.
   - The second possibility stands for a very small (or even vanishing) θ_{13}. In this case, it is also necessary to marginalize over θ_{13} since possible CP-conserving solutions can be found for a given CP-violating input $(\bar{\theta}_{13}; \{\bar{\phi}\})$ at a different θ_{13} (what in the standard three-family oscillation scenario is called an "intrinsic degeneracy" [168]). In order to take these degeneracies into account, we minimize the χ^2 over θ_{13}:

   $$\chi^2_{\theta,CPC}(\bar{\theta}_{13}; \{\bar{\phi}\}) = \min_{\theta_{13}} \left(\chi^2_{CPC}(\theta_{13}, \bar{\theta}_{13}; \{\bar{\phi}\})\right) .$$

   However, notice that in this case the only information we have on $\bar{\theta}_{13}$ is an upper bound, $\theta_{13} \leq 3^\circ$, approximately. Therefore, marginalization over $\bar{\theta}_{13}$ in the allowed range is also required here:

   $$\chi^2_{\theta,\bar{\theta},CPC}(\{\bar{\phi}\}) = \min_{\bar{\theta}_{13}} \left(\chi^2_{\theta,CPC}(\bar{\theta}_{13}; \{\bar{\phi}\})\right) . \tag{C.4}$$

5. Eventually, we draw the three-dimensional surfaces corresponding to $\chi^2 = 11.34$. These contours represent the area of the phases parameter space in which CP violation can be distinguished from CP conservation at the 99% CL for 3 d.o.f.'s. Results will be shown for both cases in which θ_{13} is known, using Eq. (C.3), or unknown, using Eq. (C.4).

Agradecimientos

Yo creo que una tesis no está completa si no tiene una sección de agradecimientos que esté además bien surtida de recuerdos de tus años de doctorado, así que aquí va un breve resumen de los míos. En primer lugar, me gustaría dar las gracias a mis compis del mítico 512. Al final parece que tantas horas de sufrimiento conjunto durante el máster han dado sus frutos. Pero sobre todo, me gustaría que sepan que cada vez que diga un "jarl!" me acordaré de todos ellos. A decir verdad, a Javi y Fran son a los que más les ha tocado aguantarme la chapa, en especial a Fran, que no sólo me la ha aguantado en el trabajo sino también en nuestro pisito de Buenavista. Gracias, chicos, por estos cuatro años de risas.

También me gustaría darle las gracias a Jacobo. Además de un amigo, ha sido un muy buen "hermano mayor". Me ha enseñado muchas cosas durante estos cuatro años, pero además hemos compartido muchos momentos. La verdad es que me he acostumbrado a tenerlo ahí cerquita siempre, y ahora que ya no soy un "joven polluelo" me va a costar desacostumbrarme.

Me gustaría agradecerle muchas cosas a Enrique, y no sé por cuál empezar. Me ha enseñado muchísimo, y es otra de esas personas que siempre está ahí cuando lo necesitas. Gracias, porque cuando he estado a punto de tirar el ordenador por la ventana siempre ha sabido darme una pista de qué podía ir mal, o un truco super útil de esos que no se te olvidan jamás. Por supuesto, también quiero darle las gracias a Andrea. Me gustaría darle las gracias por todo lo que me ha enseñado, y por empujarme a hacer todas esas cosas que me daban un miedo terrible (y que aún me lo dan): las charlas, las escuelas, las conferencias, las estancias,... Y gracias por intentar entenderme, porque sé que no siempre es fácil.

Por supuesto, también me gustaría darle las gracias a mi familia. Gracias por la acogida que me dio Nacho en "TorreBronx" durante mi primer año en Madrid: sin su ayuda esto no habría sido posible (y lo cierto es que a veces echo de menos las cenas frente a ese ordenador cutrecillo que teníamos). Gracias a todos porque todos sabemos el esfuerzo que ha supuesto que me fuera a Madrid. Y a mi madre le doy las gracias por no rendirse nunca.

Para terminar, me gustaría darle las gracias a Roberto. Por cuidarme y saber entenderme todos los días. Porque siempre está ahí, por su paciencia infinita y porque siempre sabe cómo darme ánimos para seguir. Y a decir verdad, no tengo palabras suficientes para agradecer nada de todo eso.

Bibliography

[1] S. Glashow, "Partial Symmetries of Weak Interactions," *Nucl.Phys.* **22** (1961) 579–588.

[2] S. Weinberg, "A Model of Leptons," *Phys.Rev.Lett.* **19** (1967) 1264–1266.

[3] H. Georgi and S. L. Glashow, "Unity of All Elementary Particle Forces," *Phys. Rev. Lett.* **32** (1974) 438–441.

[4] S. Weinberg, *The Quantum Theory of Fields*. Cambridge University Press, 1995, 1996, 2003.

[5] G. F. Smoot, C. Bennett, A. Kogut, E. Wright, J. Aymon, *et al.*, "Structure in the COBE differential microwave radiometer first year maps," *Astrophys.J.* **396** (1992) L1–L5.

[6] **WMAP Collaboration** Collaboration, E. Komatsu *et al.*, "Seven-Year Wilkinson Microwave Anisotropy Probe (WMAP) Observations: Cosmological Interpretation," *Astrophys.J.Suppl.* **192** (2011) 18, arXiv:1001.4538 [astro-ph.CO].

[7] **Supernova Search Team** Collaboration, A. G. Riess *et al.*, "Observational evidence from supernovae for an accelerating universe and a cosmological constant," *Astron.J.* **116** (1998) 1009–1038, arXiv:astro-ph/9805201 [astro-ph].

[8] R. Peccei and H. R. Quinn, "CP Conservation in the Presence of Instantons," *Phys.Rev.Lett.* **38** (1977) 1440–1443.

[9] C. Baker, D. Doyle, P. Geltenbort, K. Green, M. van der Grinten, *et al.*, "An Improved experimental limit on the electric dipole moment of the neutron," *Phys.Rev.Lett.* **97** (2006) 131801, arXiv:hep-ex/0602020 [hep-ex].

[10] M. Aizenman, "Proof of the Triviality of phi d4 Field Theory and Some Mean-Field Features of Ising Models for d¿4," *Phys. Rev. Lett.* **47** (1981) 886–886.

[11] J. Frohlich, "On the Triviality of Lambda (phi**4) in D-Dimensions Theories and the Approach to the Critical Point in D $\geq$ Four-Dimensions," *Nucl. Phys.* **B200** (1982) 281–296.

[12] A. D. Sokal, "AN ALTERNATE CONSTRUCTIVE APPROACH TO THE PHI**4 in three- dimensions QUANTUM FIELD THEORY, AND A POSSIBLE DESTRUCTIVE APPROACH TO PHI**4 in four-dimensions," *Annales Poincare Phys. Theor.* **37A** (1982) 317–398.

[13] **LEP Working Group for Higgs boson searches, ALEPH Collaboration, DELPHI Collaboration, L3 Collaboration, OPAL Collaboration** Collaboration, R. Barate *et al.*, "Search for the standard model Higgs boson at LEP," *Phys.Lett.* **B565** (2003) 61–75, arXiv:hep-ex/0306033 [hep-ex].

[14] S. Weinberg, "Implications of Dynamical Symmetry Breaking: An Addendum," *Phys. Rev.* **D19** (1979) 1277–1280.

[15] E. Gildener and S. Weinberg, "Symmetry Breaking and Scalar Bosons," *Phys. Rev.* **D13** (1976) 3333.

[16] A. Sakharov, "Violation of CP Invariance, c Asymmetry, and Baryon Asymmetry of the Universe," *Pisma Zh.Eksp.Teor.Fiz.* **5** (1967) 32–35. Reprinted in *Kolb, E.W. (ed.), Turner, M.S. (ed.): The early universe* 371-373, and in *Lindley, D. (ed.) et al.: Cosmology and particle physics* 106-109, and in Sov. Phys. Usp. 34 (1991) 392-393 [Usp. Fiz. Nauk 161 (1991) No. 5 61-64].

[17] P. Minkowski, "$\mu \to e\gamma$ at a Rate of One Out of 1-Billion Muon Decays?," *Phys. Lett.* **B67** (1977) 421.

[18] T. Yanagida, "Horizontal gauge symmetry and masses of neutrinos,". In Proceedings of the Workshop on the Baryon Number of the Universe and Unified Theories, Tsukuba, Japan, 13-14 Feb 1979.

[19] R. N. Mohapatra and G. Senjanovic, "Neutrino Mass and Spontaneous Parity Violation," *Phys.Rev.Lett.* **44** (1980) 912.

[20] M. Fukugita and T. Yanagida, "Baryogenesis Without Grand Unification," *Phys. Lett.* **B174** (1986) 45.

[21] P. Coloma, A. Donini, E. Fernandez-Martinez, and J. Lopez-Pavon, "θ_{13}, δ and the neutrino mass hierarchy at a $\gamma = 350$ double baseline Li/B β-Beam," *JHEP* **05** (2008) 050, arXiv:0712.0796 [hep-ph].

[22] S. Choubey, P. Coloma, A. Donini, and E. Fernandez-Martinez, "Optimized Two-Baseline Beta-Beam Experiment," *JHEP* **0912** (2009) 020, arXiv:0907.2379 [hep-ph].

[23] P. Coloma, T. Li, and S. Pascoli. To appear soon.

[24] P. Coloma, A. Donini, J. Lopez-Pavon, and H. Minakata, "Non-Standard Interactions at a Neutrino Factory: Correlations and CP violation," arXiv:1105.5936 [hep-ph].

[25] **Particle Data Group** Collaboration, K. Nakamura *et al.*, "Review of particle physics," *J.Phys.G* **G37** (2010) 075021.

[26] V. Bednyakov, N. Giokaris, and A. Bednyakov, "On Higgs mass generation mechanism in the Standard Model," *Phys.Part.Nucl.* **39** (2008) 13–36, arXiv:hep-ph/0703280 [HEP-PH].

[27] G. Branco, P. Ferreira, L. Lavoura, M. Rebelo, M. Sher, *et al.*, "Theory and phenomenology of two-Higgs-doublet models," arXiv:1106.0034 [hep-ph]. * Temporary entry *.

[28] A. Davidson, "B-L AS THE FOURTH COLOR, QUARK - LEPTON CORRESPONDENCE, AND NATURAL MASSLESSNESS OF NEUTRINOS WITHIN A GENERALIZED WS MODEL," *Phys.Rev.* **D20** (1979) 776.

[29] M. Parida and A. Raychaudhuri, "LOW MASS PARITY RESTORATION, WEAK INTERACTION PHENOMENOLOGY AND GRAND UNIFICATION," *Phys.Rev.* **D26** (1982) 2364.

[30] V. D. Barger, E. Ma, and K. Whisnant, "GENERAL ANALYSIS OF A POSSIBLE SECOND WEAK NEUTRAL CURRENT IN GAUGE MODELS," *Phys.Rev.* **D26** (1982) 2378.

[31] **Super-Kamiokande** Collaboration, Y. Fukuda *et al.*, "Evidence for oscillation of atmospheric neutrinos," *Phys. Rev. Lett.* **81** (1998) 1562–1567, arXiv:hep-ex/9807003.

[32] **SNO** Collaboration, Q. R. Ahmad *et al.*, "Measurement of the charged current interactions produced by B-8 solar neutrinos at the Sudbury Neutrino Observatory," *Phys. Rev. Lett.* **87** (2001) 071301, arXiv:nucl-ex/0106015.

[33] M. B. Gavela, T. Hambye, D. Hernandez, and P. Hernandez, "Minimal Flavour Seesaw Models," *JHEP* **09** (2009) 038, arXiv:0906.1461 [hep-ph].

[34] P. R. M. Gell-Mann and R. Slansky, "In *Supergravity*, edited by P. van Nieuwenhuizen and D. Freedman, (North-Holland, 1979), p. 315,".

[35] R. N. Mohapatra and G. Senjanovic, "Neutrino Masses and Mixings in Gauge Models with Spontaneous Parity Violation," *Phys. Rev.* **D23** (1981) 165.

[36] S. Weinberg, "Baryon and Lepton Nonconserving Processes," *Phys.Rev.Lett.* **43** (1979) 1566–1570.

[37] M. Magg and C. Wetterich, "NEUTRINO MASS PROBLEM AND GAUGE HIERARCHY," *Phys. Lett.* **B94** (1980) 61.

[38] J. Schechter and J. W. F. Valle, "Neutrino Masses in SU(2) x U(1) Theories," *Phys. Rev.* **D22** (1980) 2227.

[39] C. Wetterich, "Neutrino Masses and the Scale of B-L Violation," *Nucl. Phys.* **B187** (1981) 343.

[40] G. Lazarides, Q. Shafi, and C. Wetterich, "Proton Lifetime and Fermion Masses in an SO(10) Model," *Nucl. Phys.* **B181** (1981) 287.

[41] R. Foot, H. Lew, X. G. He, and G. C. Joshi, "SEESAW NEUTRINO MASSES INDUCED BY A TRIPLET OF LEPTONS," *Z. Phys.* **C44** (1989) 441.

[42] W. Konetschny and W. Kummer, "Nonconservation of Total Lepton Number with Scalar Bosons," *Phys.Lett.* **B70** (1977) 433.

[43] T. Cheng and L.-F. Li, "Neutrino Masses, Mixings and Oscillations in SU(2) x U(1) Models of Electroweak Interactions," *Phys.Rev.* **D22** (1980) 2860.

[44] A. Zee, "A Theory of Lepton Number Violation, Neutrino Majorana Mass, and Oscillation," *Phys.Lett.* **B93** (1980) 389.

[45] A. Zee, "Charged Scalar Field and Quantum Number Violations," *Phys.Lett.* **B161** (1985) 141.

[46] K. Babu, "Model of 'Calculable' Majorana Neutrino Masses," *Phys.Lett.* **B203** (1988) 132.

[47] A. Abada, C. Biggio, F. Bonnet, M. Gavela, and T. Hambye, "Low energy effects of neutrino masses," *JHEP* **0712** (2007) 061, arXiv:0707.4058 [hep-ph].

[48] B. Pontecorvo, "Mesonium and antimesonium," *Sov. Phys. JETP* **6** (1957) 429.

[49] Z. Maki, M. Nakagawa, and S. Sakata, "Remarks on the unified model of elementary particles," *Prog. Theor. Phys.* **28** (1962) 870–880.

[50] B. Pontecorvo, "Neutrino Experiments and the Problem of Conservation of Leptonic Charge," *Sov.Phys.JETP* **26** (1968) 984–988.

[51] V. N. Gribov and B. Pontecorvo, "Neutrino astronomy and lepton charge," *Phys. Lett.* **B28** (1969) 493.

[52] M. C. Gonzalez-Garcia and M. Maltoni, "Phenomenology with Massive Neutrinos," *Phys. Rept.* **460** (2008) 1–129, arXiv:0704.1800 [hep-ph].

[53] P. Harrison and W. Scott, "The Simplest neutrino mass matrix," *Phys.Lett.* **B594** (2004) 324–332, arXiv:hep-ph/0403278 [hep-ph].

[54] G. Altarelli and F. Feruglio, "Models of neutrino masses and mixings," *New J.Phys.* **6** (2004) 106, arXiv:hep-ph/0405048 [hep-ph]. Submitted to the focus Issue on 'Neutrino Physics' edited by F. Halzen, M. Lindner and A. Suzuki.

[55] P. Hernandez, "Neutrino physics," arXiv:1010.4131 [hep-ph].

[56] A. G. Cohen, S. L. Glashow, and Z. Ligeti, "Disentangling Neutrino Oscillations," *Phys.Lett.* **B678** (2009) 191–196, arXiv:0810.4602 [hep-ph].

[57] C. Jarlskog, "Commutator of the Quark Mass Matrices in the Standard Electroweak Model and a Measure of Maximal CP Violation," *Phys.Rev.Lett.* **55** (1985) 1039.

[58] C. Giunti and C. W. Kim, "Quantum mechanics of neutrino oscillations," *Found.Phys.Lett.* **14** (2001) 213–229, arXiv:hep-ph/0011074 [hep-ph].

[59] E. K. Akhmedov and J. Kopp, "Neutrino oscillations: Quantum mechanics vs. quantum field theory," *JHEP* **1004** (2010) 008, arXiv:1001.4815 [hep-ph].

[60] L. Wolfenstein, "Neutrino Oscillations in Matter," *Phys.Rev.* **D17** (1978) 2369–2374.

[61] P. Langacker, J. P. Leveille, and J. Sheiman, "On the Detection of Cosmological Neutrinos by Coherent Scattering," *Phys.Rev.* **D27** (1983) 1228.

[62] R. Lewis, "COHERENT DETECTOR FOR LOW-ENERGY NEUTRINOS," *Phys.Rev.* **D21** (1980) 663.

[63] L. Wolfenstein, "Neutrino Oscillations and Stellar Collapse," *Phys.Rev.* **D20** (1979) 2634–2635.

[64] S. P. Mikheev and A. Y. Smirnov, "Resonance enhancement of oscillations in matter and solar neutrino spectroscopy," *Sov. J. Nucl. Phys.* **42** (1985) 913–917.

[65] R. Feynman, *The Theory of Fundamental Processes*. Westview Press, 1961, 1998.

[66] Z. Berezhiani and A. Rossi, "Limits on the nonstandard interactions of neutrinos from e+ e- colliders," *Phys.Lett.* **B535** (2002) 207–218, arXiv:hep-ph/0111137 [hep-ph].

[67] S. Davidson, C. Pena-Garay, N. Rius, and A. Santamaria, "Present and future bounds on nonstandard neutrino interactions," *JHEP* **0303** (2003) 011, arXiv:hep-ph/0302093 [hep-ph].

[68] M. Gavela, D. Hernandez, T. Ota, and W. Winter, "Large gauge invariant non-standard neutrino interactions," *Phys.Rev.* **D79** (2009) 013007, arXiv:0809.3451 [hep-ph].

[69] S. Antusch, J. P. Baumann, and E. Fernandez-Martinez, "Non-Standard Neutrino Interactions with Matter from Physics Beyond the Standard Model," *Nucl. Phys.* **B810** (2009) 369–388, arXiv:0807.1003 [hep-ph].

[70] M. Blennow and E. Fernandez-Martinez, "Neutrino oscillation parameter sampling with MonteCUBES," *Comput. Phys. Commun.* **181** (2010) 227–231, arXiv:0903.3985 [hep-ph].

[71] C. Biggio, M. Blennow, and E. Fernandez-Martinez, "General bounds on non-standard neutrino interactions," *JHEP* **08** (2009) 090, arXiv:0907.0097 [hep-ph].

[72] W. Buchmuller and D. Wyler, "Effective Lagrangian Analysis of New Interactions and Flavor Conservation," *Nucl.Phys.* **B268** (1986) 621.

[73] V. Cirigliano, B. Grinstein, G. Isidori, and M. B. Wise, "Minimal flavor violation in the lepton sector," *Nucl.Phys.* **B728** (2005) 121–134, arXiv:hep-ph/0507001 [hep-ph].

[74] M. Gonzalez-Garcia and J. Valle, "Fast decaying neutrinos and observable flavor violation in a new class of majoron models," *Phys.Lett.* **B216** (1989) 360.

[75] V. Lobashev, V. Aseev, A. Belesev, A. Berlev, E. Geraskin, *et al.*, "Direct search for mass of neutrino and anomaly in the tritium beta spectrum," *Phys.Lett.* **B460** (1999) 227–235.

[76] C. Kraus, B. Bornschein, L. Bornschein, J. Bonn, B. Flatt, *et al.*, "Final results from phase II of the Mainz neutrino mass search in tritium beta decay," *Eur.Phys.J.* **C40** (2005) 447–468, arXiv:hep-ex/0412056 [hep-ex].

[77] **KATRIN Collaboration** Collaboration, A. Osipowicz *et al.*, "KATRIN: A Next generation tritium beta decay experiment with sub-eV sensitivity for the electron neutrino mass. Letter of intent," arXiv:hep-ex/0109033 [hep-ex].

[78] T. Thummler and f. t. K. Collaboration, "Introduction to direct neutrino mass measurements and KATRIN," arXiv:1012.2282 [hep-ex]. * Temporary entry *.

[79] K. Assamagan, C. Bronnimann, M. Daum, H. Forrer, R. Frosch, *et al.*, "Upper limit of the muon-neutrino mass and charged pion mass from momentum analysis of a surface muon beam," *Phys.Rev.* **D53** (1996) 6065–6077.

[80] N. data center for Cosmic Microwave Background (CMB) research webpage. http://lambda.gsfc.nasa.gov/product/map/current/params/lcdm_sz_lens_mnu_wmap7_bao_h0.cfm.

[81] M. Blennow, E. Fernandez-Martinez, J. Lopez-Pavon, and J. Menendez, "Neutrinoless double beta decay in seesaw models," arXiv:1005.3240 [hep-ph].

[82] H. Klapdor-Kleingrothaus, A. Dietz, L. Baudis, G. Heusser, I. Krivosheina, *et al.*, "Latest results from the Heidelberg-Moscow double beta decay experiment," *Eur.Phys.J.* **A12** (2001) 147–154, arXiv:hep-ph/0103062 [hep-ph].

[83] **IGEX Collaboration** Collaboration, C. Aalseth *et al.*, "The IGEX Ge-76 neutrinoless double beta decay experiment: Prospects for next generation experiments," *Phys.Rev.* **D65** (2002) 092007, arXiv:hep-ex/0202026 [hep-ex].

[84] **CUORICINO Collaboration** Collaboration, C. Arnaboldi *et al.*, "Results from a search for the 0 neutrino beta beta-decay of Te-130," *Phys.Rev.* **C78** (2008) 035502, arXiv:0802.3439 [hep-ex].

[85] **NEMO Collaboration** Collaboration, R. Arnold *et al.*, "Limits on different Majoron decay modes of Mo-100 and Se-82 for neutrinoless double beta decays in the NEMO-3 experiment," *Nucl.Phys.* **A765** (2006) 483–494, arXiv:hep-ex/0601021 [hep-ex].

[86] **NEMO Collaboration** Collaboration, J. Argyriades *et al.*, "Measurement of the Double Beta Decay Half-life of Nd-150 and Search for Neutrinoless Decay Modes with the NEMO-3 Detector," *Phys.Rev.* **C80** (2009) 032501, arXiv:0810.0248 [hep-ex].

[87] S. Umehara, T. Kishimoto, I. Ogawa, R. Hazama, H. Miyawaki, *et al.*, "Neutrino-less double-beta decay of Ca-48 studied by Ca F(2)(Eu) scintillators," *Phys.Rev.* **C78** (2008) 058501, arXiv:0810.4746 [nucl-ex].

[88] F. A. Danevich, A. S. Georgadze, V. V. Kobychev, B. N. Kropivyansky, A. S. Nikolaiko, *et al.*, "Search for 2 beta decay of cadmium and tungsten isotopes: Final results of the solotvina experiment," *Phys.Rev.* **C68** (2003) 035501.

[89] R. Bernabei, P. Belli, J. Capella, R. Cerulli, C. Dai, *et al.*, "Results with the DAMA/LXe experiment at LNGS," *Nucl.Phys.Proc.Suppl.* **110** (2002) 88–90.

[90] H. Klapdor-Kleingrothaus, A. Dietz, H. Harney, and I. Krivosheina, "Evidence for neutrinoless double beta decay," *Mod.Phys.Lett.* **A16** (2001) 2409–2420, arXiv:hep-ph/0201231 [hep-ph].

[91] H. Klapdor-Kleingrothaus and I. Krivosheina, "The evidence for the observation of 0nu beta beta decay: The identification of 0nu beta beta events from the full spectra," *Mod.Phys.Lett.* **A21** (2006) 1547–1566.

[92] S. Hannestad, A. Mirizzi, G. G. Raffelt, and Y. Y. Wong, "Neutrino and axion hot dark matter bounds after WMAP-7," *JCAP* **1008** (2010) 001, arXiv:1004.0695 [astro-ph.CO].

[93] **CUORE Collaboration** Collaboration, C. Arnaboldi *et al.*, "CUORE: A Cryogenic underground observatory for rare events," *Nucl.Instrum.Meth.* **A518** (2004) 775–798, arXiv:hep-ex/0212053 [hep-ex].

[94] **NEMO Collaboration** Collaboration, A. Barabash, "The extrapolation of NEMO techniques to future generation 2beta-decay experiments," *Phys.Atom.Nucl.* **67** (2004) 1984–1988.

[95] **Majorana Collaboration** Collaboration, R. Gaitskell *et al.*, "The Majorana zero neutrino double beta decay experiment," arXiv:nucl-ex/0311013 [nucl-ex]. White paper.

[96] D. Akimov, G. Bower, M. Breidenbach, R. Conley, E. Conti, *et al.*, "EXO: An advanced Enriched Xenon double-beta decay Observatory," *Nucl.Phys.Proc.Suppl.* **138** (2005) 224–226.

[97] **GERDA Collaboration** Collaboration, S. Schonert *et al.*, "The GERmanium Detector Array (GERDA) for the search of neutrinoless beta beta decays of Ge-76 at LNGS," *Nucl.Phys.Proc.Suppl.* **145** (2005) 242–245.

[98] M. Chen, "The SNO liquid scintillator project," *Nucl.Phys.Proc.Suppl.* **145** (2005) 65–68.

[99] S. Umehara, T. Kishimoto, I. Ogawa, R. Hazama, S. Yoshida, *et al.*, "CANDLES for double beta decay of Ca-48," *J.Phys.Conf.Ser.* **39** (2006) 356–358.

[100] H. Nakamura, P. Doe, H. Ejiri, S. Elliott, J. Engel, *et al.*, "Multilayer scintillator responses for Mo observatory of neutrino experiment studied using a prototype detector MOON-1," *J.Phys.Soc.Jap.* **76** (2007) 114201, arXiv:nucl-ex/0609008 [nucl-ex].

[101] **KamLAND Collaboration** Collaboration, A. Terashima *et al.*, "Ramp;D for possible future improvements of KamLAND," *J.Phys.Conf.Ser.* **120** (2008) 052029.

[102] **NEMO and SuperNEMO Collaborations** Collaboration, H. Ohsumi, "SuperNEMO project," *J.Phys.Conf.Ser.* **120** (2008) 052054.

[103] J. Diaz, N. Yahlali, M. Ball, J. Barata, F. Borges, *et al.*, "The NEXT experiment," *J.Phys.Conf.Ser.* **179** (2009) 012005.

[104] J. Gomez-Cadenas, J. Martin-Albo, M. Sorel, P. Ferrario, F. Monrabal, *et al.*, "Sense and sensitivity of double beta decay experiments," *JCAP* **1106** (2011) 007, arXiv:1010.5112 [hep-ex].

[105] P. Lipari, "CP violation effects and high-energy neutrinos," *Phys.Rev.* **D64** (2001) 033002, arXiv:hep-ph/0102046 [hep-ph].

[106] A. Abazov, O. Anosov, E. Faizov, V. Gavrin, A. Kalikhov, *et al.*, "Search for neutrinos from sun using the reaction Ga-71 (electron-neutrino e-) Ge-71," *Phys.Rev.Lett.* **67** (1991) 3332–3335.

[107] B. T. Cleveland *et al.*, "Measurement of the solar electron neutrino flux with the Homestake chlorine detector," *Astrophys. J.* **496** (1998) 505–526.

[108] **GALLEX** Collaboration, W. Hampel *et al.*, "GALLEX solar neutrino observations: Results for GALLEX IV," *Phys. Lett.* **B447** (1999) 127–133.

[109] **SAGE** Collaboration, J. N. Abdurashitov *et al.*, "Measurement of the solar neutrino capture rate with gallium metal," *Phys. Rev.* **C60** (1999) 055801, arXiv:astro-ph/9907113.

[110] **SNO** Collaboration, S. N. Ahmed *et al.*, "Measurement of the total active B-8 solar neutrino flux at the Sudbury Neutrino Observatory with enhanced neutral current sensitivity," *Phys. Rev. Lett.* **92** (2004) 181301, arXiv:nucl-ex/0309004.

[111] **GNO COLLABORATION** Collaboration, M. Altmann *et al.*, "Complete results for five years of GNO solar neutrino observations," *Phys.Lett.* **B616** (2005) 174–190, arXiv:hep-ex/0504037 [hep-ex].

[112] **Kamiokande Collaboration** Collaboration, Y. Fukuda *et al.*, "Solar neutrino data covering solar cycle 22," *Phys.Rev.Lett.* **77** (1996) 1683–1686.

[113] **Super-Kamiokande** Collaboration, S. Fukuda *et al.*, "Solar 8B and hep Neutrino Measurements from 1258 Days of Super-Kamiokande Data," *Phys. Rev. Lett.* **86** (2001) 5651–5655, arXiv:hep-ex/0103032.

[114] **Super-Kamiokande** Collaboration, S. Fukuda *et al.*, "Determination of Solar Neutrino Oscillation Parameters using 1496 Days of Super-Kamiokande-I Data," *Phys. Lett.* **B539** (2002) 179–187, arXiv:hep-ex/0205075.

[115] **Super-Kamiokande Collaboration** Collaboration, M. Smy *et al.*, "Precise measurement of the solar neutrino day / night and seasonal variation in Super-Kamiokande-1," *Phys.Rev.* **D69** (2004) 011104, arXiv:hep-ex/0309011 [hep-ex].

[116] **Super-Kamkiokande Collaboration** Collaboration, J. Hosaka *et al.*, "Solar neutrino measurements in super-Kamiokande-I," *Phys.Rev.* **D73** (2006) 112001, arXiv:hep-ex/0508053 [hep-ex].

[117] **Super-Kamiokande** Collaboration, J. P. Cravens *et al.*, "Solar neutrino measurements in Super-Kamiokande-II," *Phys. Rev.* **D78** (2008) 032002, arXiv:0803.4312 [hep-ex].

[118] **SNO Collaboration** Collaboration, J. Boger *et al.*, "The Sudbury neutrino observatory," *Nucl.Instrum.Meth.* **A449** (2000) 172–207, arXiv:nucl-ex/9910016 [nucl-ex].

[119] **SNO** Collaboration, Q. R. Ahmad *et al.*, "Measurement of day and night neutrino energy spectra at SNO and constraints on neutrino mixing parameters," *Phys. Rev. Lett.* **89** (2002) 011302, arXiv:nucl-ex/0204009.

[120] **SNO** Collaboration, Q. R. Ahmad *et al.*, "Direct evidence for neutrino flavor transformation from neutral-current interactions in the Sudbury Neutrino Observatory," *Phys. Rev. Lett.* **89** (2002) 011301, arXiv:nucl-ex/0204008.

[121] J. N. Bahcall, M. Pinsonneault, and S. Basu, "Solar models: Current epoch and time dependences, neutrinos, and helioseismological properties," *Astrophys.J.* **555** (2001) 990–1012, arXiv:astro-ph/0010346 [astro-ph].

[122] **Borexino Collaboration** Collaboration, G. Alimonti *et al.*, "Science and technology of BOREXINO: A Real time detector for low-energy solar neutrinos," *Astropart.Phys.* **16** (2002) 205–234, arXiv:hep-ex/0012030 [hep-ex].

[123] **The Borexino Collaboration** Collaboration, C. Arpesella *et al.*, "Direct Measurement of the Be-7 Solar Neutrino Flux with 192 Days of Borexino Data," *Phys.Rev.Lett.* **101** (2008) 091302, arXiv:0805.3843 [astro-ph].

[124] **KamLAND** Collaboration, K. Eguchi *et al.*, "First results from KamLAND: Evidence for reactor anti- neutrino disappearance," *Phys. Rev. Lett.* **90** (2003) 021802, arXiv:hep-ex/0212021.

[125] **KamLAND Collaboration** Collaboration, T. Araki *et al.*, "Measurement of neutrino oscillation with KamLAND: Evidence of spectral distortion," *Phys.Rev.Lett.* **94** (2005) 081801, arXiv:hep-ex/0406035 [hep-ex].

[126] **KamLAND Collaboration** Collaboration, S. Abe *et al.*, "Measurement of the 8B Solar Neutrino Flux with KamLAND," arXiv:1106.0861 [hep-ex]. * Temporary entry *.

[127] **Super-Kamiokande Collaboration** Collaboration, K. Abe *et al.*, "Solar neutrino results in Super-Kamiokande-III," arXiv:1010.0118 [hep-ex]. Long author list - awaiting processing.

[128] **The KamLAND Collaboration** Collaboration, A. Gando *et al.*, "Constraints on θ_{13} from A Three-Flavor Oscillation Analysis of Reactor Antineutrinos at KamLAND," *Phys.Rev.* **D83** (2011) 052002, arXiv:1009.4771 [hep-ex].

[129] **Kamiokande Collaboration** Collaboration, Y. Fukuda *et al.*, "Atmospheric muon-neutrino / electron-neutrino ratio in the multiGeV energy range," *Phys.Lett.* **B335** (1994) 237–245.

[130] **Super-Kamiokande Collaboration** Collaboration, Y. Ashie *et al.*, "Evidence for an oscillatory signature in atmospheric neutrino oscillation," *Phys.Rev.Lett.* **93** (2004) 101801, arXiv:hep-ex/0404034 [hep-ex]. Press release available at: http://www.eurekalert.org/pub_releases/2004-07/bu-gto070804.php.

[131] **Super-Kamiokande** Collaboration, Y. Ashie *et al.*, "A Measurement of Atmospheric Neutrino Oscillation Parameters by Super-Kamiokande I," *Phys. Rev.* **D71** (2005) 112005, arXiv:hep-ex/0501064.

[132] **Super-Kamiokande Collaboration** Collaboration, J. Hosaka *et al.*, "Three flavor neutrino oscillation analysis of atmospheric neutrinos in Super-Kamiokande," *Phys.Rev.* **D74** (2006) 032002, arXiv:hep-ex/0604011 [hep-ex].

[133] R. Becker-Szendy, C. Bratton, D. Casper, S. Dye, W. Gajewski, *et al.*, "The Electron-neutrino and muon-neutrino content of the atmospheric flux," *Phys.Rev.* **D46** (1992) 3720–3724.

[134] **Soudan-2 Collaboration** Collaboration, W. A. Mann, "New results on atmospheric neutrinos from Soudan 2," *Nucl.Phys.Proc.Suppl.* **91** (2001) 134–140, arXiv:hep-ex/0007031 [hep-ex].

[135] **MACRO Collaboration** Collaboration, M. Ambrosio *et al.*, "Matter effects in upward going muons and sterile neutrino oscillations," *Phys.Lett.* **B517** (2001) 59–66, arXiv:hep-ex/0106049 [hep-ex].

[136] **K2K Collaboration** Collaboration, S. Ahn *et al.*, "Detection of accelerator produced neutrinos at a distance of 250-km," *Phys.Lett.* **B511** (2001) 178–184, arXiv:hep-ex/0103001 [hep-ex].

[137] **MINOS** Collaboration, E. Ables *et al.*, "P-875: A Long baseline neutrino oscillation experiment at Fermilab,". FERMILAB-PROPOSAL-0875.

[138] **K2K** Collaboration, M. H. Ahn *et al.*, "Indications of Neutrino Oscillation in a 250 km Long- baseline Experiment," *Phys. Rev. Lett.* **90** (2003) 041801, arXiv:hep-ex/0212007.

[139] **MINOS** Collaboration, D. G. Michael *et al.*, "Observation of muon neutrino disappearance with the MINOS detectors and the NuMI neutrino beam," *Phys. Rev. Lett.* **97** (2006) 191801, arXiv:hep-ex/0607088.

[140] **MINOS** Collaboration, P. Adamson *et al.*, "Measurement of Neutrino Oscillations with the MINOS Detectors in the NuMI Beam," *Phys. Rev. Lett.* **101** (2008) 131802, arXiv:0806.2237 [hep-ex].

[141] **The MINOS Collaboration** Collaboration, P. Adamson *et al.*, "Measurement of the neutrino mass splitting and flavor mixing by MINOS," arXiv:1103.0340 [hep-ex].

[142] **OPERA Collaboration** Collaboration, M. Guler *et al.*, "OPERA: An appearance experiment to search for $\nu_\mu \to \nu_\tau$ oscillations in the CNGS beam. Experimental proposal,".

[143] M. Komatsu, P. Migliozzi, and F. Terranova, "Sensitivity to theta(13) of the CERN to Gran Sasso neutrino beam," *J.Phys.G* **G29** (2003) 443, arXiv:hep-ph/0210043 [hep-ph].

[144] **OPERA Collaboration** Collaboration, R. Acquafredda *et al.*, "First events from the CNGS neutrino beam detected in the OPERA experiment," *New J.Phys.* **8** (2006) 303, arXiv:hep-ex/0611023 [hep-ex].

[145] **Collaboration for the OPERA** Collaboration, L. Esposito and for the OPERA Collaboration, "Search for $\nu_\mu \to \nu_\tau$ oscillations in appearance mode in the OPERA experiment," arXiv:1105.5239 [hep-ex]. * Temporary entry *.

[146] **CHOOZ** Collaboration, M. Apollonio *et al.*, "Search for neutrino oscillations on a long base-line at the CHOOZ nuclear power station," *Eur. Phys. J.* **C27** (2003) 331–374, arXiv:hep-ex/0301017.

[147] **CHOOZ** Collaboration, M. Apollonio *et al.*, "Limits on Neutrino Oscillations from the CHOOZ Experiment," *Phys. Lett.* **B466** (1999) 415–430, arXiv:hep-ex/9907037.

[148] A. B. McDonald, "Solar neutrinos," *New J.Phys.* **6** (2004) 121, arXiv:astro-ph/0406253 [astro-ph].

[149] T. Kajita, "Atmospheric neutrinos," *New J.Phys.* **6** (2004) 194.

[150] K. Inoue, "Reactor neutrino oscillation studies with KamLAND," *New J.Phys.* **6** (2004) 147.

[151] M. C. Gonzalez-Garcia, M. Maltoni, and J. Salvado, "Updated global fit to three neutrino mixing: status of the hints of theta13 ¿ 0," *JHEP* **04** (2010) 056, arXiv:1001.4524 [hep-ph].

[152] T. Schwetz, M. Tortola, and J. Valle, "Global neutrino data and recent reactor fluxes: status of three-flavour oscillation parameters," arXiv:1103.0734 [hep-ph]. * Temporary entry *.

[153] A. de Gouvea, J. Jenkins, and B. Kayser, "Neutrino mass hierarchy, vacuum oscillations, and vanishing —U(e3)—," *Phys.Rev.* **D71** (2005) 113009, arXiv:hep-ph/0503079 [hep-ph].

[154] A. de Gouvea and W. Winter, "What would it take to determine the neutrino mass hierarchy if theta(13) were too small?," *Phys.Rev.* **D73** (2006) 033003, arXiv:hep-ph/0509359 [hep-ph].

[155] A. de Gouvea and J. Jenkins, "Non-oscillation probes of the neutrino mass hierarchy and vanishing —U(e3)—," arXiv:hep-ph/0507021 [hep-ph].

[156] **Double Chooz** Collaboration, F. Ardellier *et al.*, "Double Chooz: A search for the neutrino mixing angle theta(13)," 2006.

[157] **Daya-Bay** Collaboration, X. Guo *et al.*, "A precision measurement of the neutrino mixing angle theta(13) using reactor antineutrinos at Daya Bay," arXiv:hep-ex/0701029.

[158] Information about the experiment available at http://neutrino.snu.ac.kr/RENO.

[159] K. Hagiwara, N. Okamura, and K.-i. Senda, "Physics potential of T2KK: An extension of the T2K neutrino oscillation experiment with a far detector in Korea," *Phys. Rev.* **D76** (2007) 093002, arXiv:hep-ph/0607255.

[160] **NOvA Collaboration** Collaboration, D. Ayres *et al.*, "NOvA: Proposal to build a 30 kiloton off-axis detector to study $\nu_\mu \to \nu_e$ oscillations in the NuMI beamline," arXiv:hep-ex/0503053 [hep-ex]. Updated version of 2004 proposal. Higher resolution version available at Fermilab Library Server.

[161] T. Schwetz, M. A. Tortola, and J. W. F. Valle, "Three-flavour neutrino oscillation update," *New J. Phys.* **10** (2008) 113011, arXiv:0808.2016 [hep-ph].

[162] **MINOS Collaboration** Collaboration, P. Adamson *et al.*, "Search for muon-neutrino to electron-neutrino transitions in MINOS," *Phys.Rev.Lett.* **103** (2009) 261802, arXiv:0909.4996 [hep-ex].

[163] **Kamiokande Collaboration** Collaboration, R. Wendell *et al.*, "Atmospheric neutrino oscillation analysis with sub-leading effects in Super-Kamiokande I, II, and III," *Phys.Rev.* **D81** (2010) 092004, arXiv:1002.3471 [hep-ex].

[164] **The MINOS Collaboration** Collaboration, P. Adamson *et al.*, "New constraints on muon-neutrino to electron-neutrino transitions in MINOS," *Phys.Rev.* **D82** (2010) 051102, arXiv:1006.0996 [hep-ex].

[165] T. Mueller, D. Lhuillier, M. Fallot, A. Letourneau, S. Cormon, *et al.*, "Improved Predictions of Reactor Antineutrino Spectra," 2011.

[166] G. Mention, M. Fechner, T. Lasserre, T. Mueller, D. Lhuillier, *et al.*, "The Reactor Antineutrino Anomaly," *Phys.Rev.* **D83** (2011) 073006, arXiv:1101.2755 [hep-ex].

[167] E. K. Akhmedov, R. Johansson, M. Lindner, T. Ohlsson, and T. Schwetz, "Series expansions for three-flavor neutrino oscillation probabilities in matter," *JHEP* **04** (2004) 078, arXiv:hep-ph/0402175.

[168] J. Burguet-Castell, M. B. Gavela, J. J. Gomez-Cadenas, P. Hernandez, and O. Mena, "On the measurement of leptonic CP violation," *Nucl. Phys.* **B608** (2001) 301–318, arXiv:hep-ph/0103258.

[169] H. Minakata and H. Nunokawa, "Exploring neutrino mixing with low energy superbeams," *JHEP* **10** (2001) 001, arXiv:hep-ph/0108085.

[170] H. Minakata, H. Nunokawa, and S. J. Parke, "Parameter degeneracies in neutrino oscillation measurement of leptonic CP and T violation," *Phys.Rev.* **D66** (2002) 093012, arXiv:hep-ph/0208163 [hep-ph].

[171] G. L. Fogli and E. Lisi, "Tests of three-flavor mixing in long-baseline neutrino oscillation experiments," *Phys. Rev.* **D54** (1996) 3667–3670, arXiv:hep-ph/9604415.

[172] V. Barger, D. Marfatia, and K. Whisnant, "Breaking eight-fold degeneracies in neutrino CP violation, mixing, and mass hierarchy," *Phys. Rev.* **D65** (2002) 073023, arXiv:hep-ph/0112119.

[173] A. Donini, D. Meloni, and P. Migliozzi, "The silver channel at the Neutrino Factory," *Nucl. Phys.* **B646** (2002) 321–349, arXiv:hep-ph/0206034.

[174] A. Donini, E. Fernandez-Martinez, P. Migliozzi, S. Rigolin, and L. Scotto Lavina, "Study of the eightfold degeneracy with a standard beta- beam and a super-beam facility," *Nucl. Phys.* **B710** (2005) 402–424, arXiv:hep-ph/0406132.

[175] D. Meloni, "Solving the octant degeneracy with the Silver channel," *Phys. Lett.* **B664** (2008) 279–284, arXiv:0802.0086 [hep-ph].

[176] A. Donini and E. Fernandez-Martinez, "Alternating ions in a beta-beam to solve degeneracies," *Phys. Lett.* **B641** (2006) 432–439, arXiv:hep-ph/0603261.

[177] M. Ishitsuka, T. Kajita, H. Minakata, and H. Nunokawa, "Resolving Neutrino Mass Hierarchy and CP Degeneracy by Two Identical Detectors with Different Baselines," *Phys. Rev.* **D72** (2005) 033003, arXiv:hep-ph/0504026.

[178] K. Hagiwara, N. Okamura, and K. ichi Senda, "Solving the neutrino parameter degeneracy by measuring the T2K off-axis beam in Korea," *Phys. Lett.* **B637** (2006) 266–273, arXiv:hep-ph/0504061.

[179] P. Huber and W. Winter, "Neutrino factories and the 'magic' baseline," *Phys. Rev.* **D68** (2003) 037301, arXiv:hep-ph/0301257.

[180] A. M. Dziewonski and D. L. Anderson, "Preliminary reference earth model," *Phys. Earth Planet. Interiors* **25** (1981) 297–356.

[181] S. V. Panasyuk, "Reference Earth Model (REM) webpage.". http://panaworks.com/lana/rem/index.htm.

[182] F. D. Stacey, "Physics of the earth," *2nd edition* **Wiley** (1977) .

[183] A. Y. Smirnov, "Neutrino oscillations: What is magic about the 'magic' baseline?," arXiv:hep-ph/0610198.

[184] S. K. Agarwalla, S. Choubey, and A. Raychaudhuri, "Unraveling neutrino parameters with a magical beta-beam experiment at INO," *Nucl. Phys.* **B798** (2008) 124–145, arXiv:0711.1459 [hep-ph].

[185] S. K. Agarwalla, S. Choubey, and A. Raychaudhuri, "Neutrino mass hierarchy and theta(13) with a magic baseline beta-beam experiment," *Nucl. Phys.* **B771** (2007) 1–27, arXiv:hep-ph/0610333.

[186] A. Donini, D. Meloni, and S. Rigolin, "The impact of solar and atmospheric parameter uncertainties on the measurement of theta(13) and delta," *Eur. Phys. J.* **C45** (2006) 73–95, arXiv:hep-ph/0506100.

[187] Y. Declais *et al.*, "Search for neutrino oscillations at 15-meters, 40-meters, and 95-meters from a nuclear power reactor at Bugey," *Nucl. Phys.* **B434** (1995) 503–534.

[188] F. Dydak *et al.*, "A Search for Muon-neutrino Oscillations in the Δm^2 Range 0.3-eV^2 to 90-eV^2," *Phys. Lett.* **B134** (1984) 281.

[189] F. Ardellier *et al.*, "Letter of intent for double-CHOOZ: A search for the mixing angle theta(13)," arXiv:hep-ex/0405032.

[190] **Double Chooz** Collaboration, I. Gil-Botella, "The Double Chooz reactor neutrino experiment," *J. Phys. Conf. Ser.* **110** (2008) 082007, arXiv:0710.4258 [hep-ex].

[191] C.-J. Lin and f. t. D. B. Collaboration, "Status of the Daya Bay Reactor Neutrino Oscillation Experiment," *PoS* **ICHEP2010** (2010) 305, arXiv:1101.0261 [hep-ex]. * Temporary entry *.

[192] **Double Chooz Collaboration** Collaboration, C. Mariani, "DoubleChooz: Experiment Status," *AIP Conf.Proc.* **1222** (2010) 475–478.

[193] **RENO Collaboration** Collaboration, Y. Oh, "Current status of RENO," *Nucl.Phys.Proc.Suppl.* **188** (2009) 109–111.

[194] **LAGUNA Collaboration** Collaboration, D. Angus *et al.*, "The LAGUNA design study-towards giant liquid based underground detectors for neutrino physics and astrophysics and proton decay searches," arXiv:1001.0077 [physics.ins-det].

[195] D. Autiero, J. Aysto, A. Badertscher, L. B. Bezrukov, J. Bouchez, *et al.*, "Large underground, liquid based detectors for astro-particle physics in Europe: Scientific case and prospects," *JCAP* **0711** (2007) 011, arXiv:0705.0116 [hep-ph].

[196] A. Rubbia, "A CERN-based high-intensity high-energy proton source for long baseline neutrino oscillation experiments with next-generation large underground detectors for proton decay searches and neutrino physics and astrophysics," arXiv:1003.1921 [hep-ph]. * Temporary entry *.

[197] "EURO-ν High intensity ν ocillation facility in Europe.". FP7-infrastructures-2007-1 project no. 212372.

[198] Information about the EUROnu project available at http://www.euronu.org/.

[199] V. Barger, S. Geer, and K. Whisnant, "Neutral currents and tests of three-neutrino unitarity in long-baseline experiments," *New J. Phys.* **6** (2004) 135, arXiv:hep-ph/0407140.

[200] J. Wotschack, "FIRST RESULTS FROM THE CDHS neutrino OSCILLATION EXPERIMENT AT CERN,".

[201] **CDHS COLLABORATION** Collaboration, C. Guyot, "HIGH PRECISION MEASUREMENT OF SIN**2THETA(W) IN SEMILEPTONIC NEUTRINO INTERACTIONS,".

[202] **CHORUS Collaboration** Collaboration, E. Eskut *et al.*, "The CHORUS experiment to search for muon-neutrino –gt; tau-neutrino oscillation," *Nucl.Instrum.Meth.* **A401** (1997) 7–44.

[203] **KARMEN Collaboration** Collaboration, B. Armbruster *et al.*, "Upper limits for neutrino oscillations muon-anti-neutrino → electron-anti-neutrino from muon decay at rest," *Phys.Rev.* **D65** (2002) 112001, arXiv:hep-ex/0203021 [hep-ex].

[204] **LSND Collaboration** Collaboration, A. Aguilar *et al.*, "Evidence for neutrino oscillations from the observation of anti-neutrino(electron) appearance in a anti-neutrino(muon) beam," *Phys.Rev.* **D64** (2001) 112007, arXiv:hep-ex/0104049 [hep-ex].

[205] **The MiniBooNE** Collaboration, A. A. Aguilar-Arevalo *et al.*, "A Search for electron neutrino appearance at the $\Delta m^2 \sim 1\mathrm{eV}^2$ scale," *Phys. Rev. Lett.* **98** (2007) 231801, arXiv:0704.1500 [hep-ex].

[206] **The MiniBooNE Collaboration** Collaboration, A. Aguilar-Arevalo *et al.*, "Event Excess in the MiniBooNE Search for $\bar{\nu}_\mu \to \bar{\nu}_e$ Oscillations," *Phys.Rev.Lett.* **105** (2010) 181801, arXiv:1007.1150 [hep-ex].

[207] **NOMAD Collaboration** Collaboration, P. Astier *et al.*, "Search for nu(mu) → nu(e) oscillations in the NOMAD experiment," *Phys.Lett.* **B570** (2003) 19–31, arXiv:hep-ex/0306037 [hep-ex].

[208] **NOMAD Collaboration** Collaboration, P. Astier *et al.*, "Final NOMAD results on muon-neutrino → tau-neutrino and electron-neutrino → tau-neutrino oscillations including a new search for tau-neutrino appearance using hadronic tau decays," *Nucl.Phys.* **B611** (2001) 3–39, arXiv:hep-ex/0106102 [hep-ex].

[209] J. Kopp, M. Maltoni, and T. Schwetz, "Are there sterile neutrinos at the eV scale?," arXiv:1103.4570 [hep-ph]. * Temporary entry *.

[210] **MINOS collaboration** Collaboration, P. Adamson *et al.*, "First direct observation of muon antineutrino disappearance," *Phys.Rev.Lett.* (2011) , arXiv:1104.0344 [hep-ex]. * Temporary entry *.

[211] E. Akhmedov and T. Schwetz, "MiniBooNE and LSND data: Non-standard neutrino interactions in a (3+1) scheme versus (3+2) oscillations," *JHEP* **1010** (2010) 115, arXiv:1007.4171 [hep-ph].

[212] C. Giunti and M. Laveder, "Hint of CPT Violation in Short-Baseline Electron Neutrino Disappearance," *Phys.Rev.* **D82** (2010) 113009, arXiv:1008.4750 [hep-ph].

[213] A. de Gouvea and Y. Grossman, "A three-flavor, Lorentz-violating solution to the LSND anomaly," *Phys. Rev.* **D74** (2006) 093008, arXiv:hep-ph/0602237.

[214] **LSND** Collaboration, C. Athanassopoulos *et al.*, "Evidence for anti-nu/mu –¿ anti-nu/e oscillation from the LSND experiment at the Los Alamos Meson Physics Facility," *Phys. Rev. Lett.* **77** (1996) 3082–3085, arXiv:nucl-ex/9605003.

[215] **LSND** Collaboration, C. Athanassopoulos *et al.*, "Evidence for nu/mu –¿ nu/e neutrino oscillations from LSND," *Phys. Rev. Lett.* **81** (1998) 1774–1777, arXiv:nucl-ex/9709006.

[216] **MiniBooNE Collaboration** Collaboration, A. Aguilar-Arevalo *et al.*, "Unexplained Excess of Electron-Like Events From a 1-GeV Neutrino Beam," *Phys.Rev.Lett.* **102** (2009) 101802, arXiv:0812.2243 [hep-ex].

[217] K. Schreckenbach, G. Colvin, W. Gelletly, and F. Von Feilitzsch, "DETERMINATION OF THE ANTI-NEUTRINO SPECTRUM FROM U-235 THERMAL NEUTRON FISSION PRODUCTS UP TO 9.5-MEV," *Phys.Lett.* **B160** (1985) 325–330.

[218] A. Hahn, K. Schreckenbach, G. Colvin, B. Krusche, W. Gelletly, *et al.*, "ANTI-NEUTRINO SPECTRA FROM PU-241 AND PU-239 THERMAL NEUTRON FISSION PRODUCTS," *Phys.Lett.* **B218** (1989) 365–368.

[219] H. Kwon, F. Boehm, A. Hahn, H. Henrikson, J. Vuilleumier, *et al.*, "SEARCH FOR NEUTRINO OSCILLATIONS AT A FISSION REACTOR," *Phys.Rev.* **D24** (1981) 1097–1111.

[220] **CALTECH-SIN-TUM COLLABORATION** Collaboration, G. Zacek *et al.*, "Neutrino Oscillation Experiments at the Gosgen Nuclear Power Reactor," *Phys.Rev.* **D34** (1986) 2621–2636.

[221] G. Vidyakin, V. Vyrodov, I. Gurevich, Y. Kozlov, V. Martemyanov, *et al.*, "DETECTION OF ANTI-NEUTRINOS IN THE FLUX FROM TWO REACTORS," *Sov.Phys.JETP* **66** (1987) 243–247.

[222] A. Afonin, S. Ketov, V. Kopeikin, L. Mikaelyan, M. Skorokhvatov, *et al.*, "A study of the reaction $\bar{\nu}_e + p \to n + e^+$ on a nuclear reactor," *Sov.Phys.JETP* **67** (1988) 213–221.

[223] A. Kuvshinnikov, L. Mikaelyan, S. Nikolaev, M. Skorokhvatov, and A. Etenko, "Measuring the $\bar{\nu}_e + p \to n + e^+$ cross-section and beta decay axial constant in a new experiment at Rovno NPP reactor. (In Russian)," *JETP Lett.* **54** (1991) 253–257.

[224] Y. Declais, H. de Kerret, B. Lefievre, M. Obolensky, A. Etenko, *et al.*, "Study of reactor anti-neutrino interaction with proton at Bugey nuclear power plant," *Phys.Lett.* **B338** (1994) 383–389.

[225] M. Abbes, B. Achkar, S. Ait-Boubker, R. Aleksan, M. Avenier, *et al.*, "The Bugey-3 neutrino detector," *Nucl.Instrum.Meth.* **A374** (1996) 164–187.

[226] C. Giunti and M. Laveder, "Short-Baseline Electron Neutrino Disappearance, Tritium Beta Decay and Neutrinoless Double-Beta Decay," *Phys.Rev.* **D82** (2010) 053005, arXiv:1005.4599 [hep-ph].

[227] J. Kopp, P. A. Machado, and S. J. Parke, "Interpretation of MINOS data in terms of non-standard neutrino interactions," *Phys.Rev.* **D82** (2010) 113002, arXiv:1009.0014 [hep-ph].

[228] J. Heeck and W. Rodejohann, "Gauged $L_\mu - L_\tau$ and different Muon Neutrino and Anti-Neutrino Oscillations: MINOS and beyond," arXiv:1007.2655 [hep-ph].

[229] R. N. Mohapatra, *Massive Neutrinos in Physics and Astrophysics, Third Edition. World Scientific Lecture Notes in Physics, Vol. 72.* World Scientific Publishing Co., 2004.

[230] G. Steigman, "Primordial Nucleosynthesis: The Predicted and Observed Abundances and Their Consequences," arXiv:1008.4765 [astro-ph.CO]. * Temporary entry *.

[231] R. H. Cyburt, B. D. Fields, and K. A. Olive, "An Update on the big bang nucleosynthesis prediction for Li-7: The problem worsens," *JCAP* **0811** (2008) 012, arXiv:0808.2818 [astro-ph].

[232] J. Hamann, S. Hannestad, J. Lesgourgues, C. Rampf, and Y. Y. Wong, "Cosmological parameters from large scale structure - geometric versus shape information," *JCAP* **1007** (2010) 022, arXiv:1003.3999 [astro-ph.CO]. * Temporary entry *.

[233] J. Hamann, S. Hannestad, G. G. Raffelt, I. Tamborra, and Y. Y. Wong, "Cosmology seeking friendship with sterile neutrinos," *Phys.Rev.Lett.* **105** (2010) 181301, arXiv:1006.5276 [hep-ph].

[234] K. Ichikawa, T. Sekiguchi, and T. Takahashi, "Probing the Effective Number of Neutrino Species with Cosmic Microwave Background," *Phys.Rev.* **D78** (2008) 083526, arXiv:0803.0889 [astro-ph].

[235] S. Galli, M. Martinelli, A. Melchiorri, L. Pagano, B. D. Sherwin, *et al.*, "Constraining Fundamental Physics with Future CMB Experiments," *Phys.Rev.* **D82** (2010) 123504, arXiv:1005.3808 [astro-ph.CO].

[236] M. V. Diwan, "The Case for a super neutrino beam," *Frascati Phys.Ser.* **35** (2004) 89–109, arXiv:hep-ex/0407047 [hep-ex].

[237] **CERN working group on Super Beams** Collaboration, J. J. Gomez-Cadenas *et al.*, "Physics potential of very intense conventional neutrino beams," arXiv:hep-ph/0105297 [hep-ph].

[238] **The T2K Collaboration** Collaboration, Y. Itow *et al.*, "The JHF-Kamioka neutrino project," arXiv:hep-ex/0106019 [hep-ex].

[239] "NOvA webpage.". http://www-nova.fnal.gov/.

[240] K. Nakamura, "Hyper-Kamiokande: A next generation water Cherenkov detector," *Int.J.Mod.Phys.* **A18** (2003) 4053–4063.

[241] B. Autin *et al.*, "Conceptual design of the SPL, a high-power superconducting H- linac at CERN,". CERN-2000-012.

[242] M. Mezzetto, "Physics potential of the SPL super beam," *J. Phys.* **G29** (2003) 1781–1784, arXiv:hep-ex/0302005.

[243] M. Diwan, S. H. Kettell, L. Littenberg, W. Marciano, Z. Parsa, *et al.*, "Proposal for an Experimental Program in Neutrino Physics and Proton Decay in the Homestake Laboratory," arXiv:hep-ex/0608023 [hep-ex].

[244] V. Barger, M. Bishai, D. Bogert, C. Bromberg, A. Curioni, *et al.*, "Report of the US long baseline neutrino experiment study," arXiv:0705.4396 [hep-ph].

[245] B. Richter, "Conventional beams or neutrino factories: The next generation of accelerator-based neutrino experiments," arXiv:hep-ph/0008222.

[246] A. Longhin, "http://irfu.cea.fr/en/Phocea/Pisp/index.php?id=72,".

[247] A. Rubbia, "Underground Neutrino Detectors for Particle and Astroparticle Science: The Giant Liquid Argon Charge Imaging ExpeRiment (GLACIER)," *J.Phys.Conf.Ser.* **171** (2009) 012020, arXiv:0908.1286 [hep-ph].

[248] L. Oberauer, "Low-energy neutrino physics after SNO and KamLAND," *Mod.Phys.Lett.* **A19** (2004) 337–348, arXiv:hep-ph/0402162 [hep-ph].

[249] T. Marrodan Undagoitia *et al.*, "LENA: A multipurpose detector for low energy neutrino astronomy and proton decay," *J. Phys. Conf. Ser.* **120** (2008) 052018.

[250] T. Marrodan Undagoitia, F. von Feilitzsch, M. Goder-Neff, K. Hochmuth, L. Oberauer, *et al.*, "Low energy neutrino astronomy with the large liquid scintillation detector LENA," *Prog.Part.Nucl.Phys.* **57** (2006) 283–289, arXiv:hep-ph/0605229 [hep-ph].

[251] **Borexino** Collaboration, C. Arpesella *et al.*, "First real time detection of Be7 solar neutrinos by Borexino," *Phys. Lett.* **B658** (2008) 101–108, arXiv:0708.2251 [astro-ph].

[252] A. de Bellefon, J. Bouchez, J. Busto, J.-E. Campagne, C. Cavata, *et al.*, "MEMPHYS: A Large scale water Cerenkov detector at Frejus," arXiv:hep-ex/0607026 [hep-ex].

[253] C. K. Jung, "Feasibility of a next generation underground water Cherenkov detector: UNO," *AIP Conf.Proc.* **533** (2000) 29–34, arXiv:hep-ex/0005046 [hep-ex].

[254] P. Huber, M. Lindner, and W. Winter, "Simulation of long-baseline neutrino oscillation experiments with GLoBES," *Comput. Phys. Commun.* **167** (2005) 195, arXiv:hep-ph/0407333.

[255] P. Huber, J. Kopp, M. Lindner, M. Rolinec, and W. Winter, "New features in the simulation of neutrino oscillation experiments with GLoBES 3.0," *Comput. Phys. Commun.* **177** (2007) 432–438, arXiv:hep-ph/0701187.

[256] E. Kozlovskaya, J. Peltoniemi, and J. Sarkamo, "The density distribution in the Earth along the CERN- Pyhasalmi baseline and its effect on neutrino oscillations," arXiv:hep-ph/0305042.

[257] V. Barger, M. Bishai, D. Bogert, C. Bromberg, A. Curioni, *et al.*, "Report of the US long baseline neutrino experiment study," arXiv:0705.4396 [hep-ph].

[258] V. Barger, P. Huber, D. Marfatia, and W. Winter, "Which long-baseline neutrino experiments are preferable?," *Phys. Rev.* **D76** (2007) 053005, arXiv:hep-ph/0703029.

[259] L. Esposito and A. Rubbia, "Private communication,".

[260] R. Mollenberg, "Reconstruction of GeV neutrino events in LENA," *Talk at NuFact 2010* (2010) .

[261] R. Mollenberg *private communication* (2010) .

[262] **LENA Collaboration** Collaboration, M. Wurm *et al.*, "The next-generation liquid-scintillator neutrino observatory LENA," arXiv:1104.5620 [astro-ph.IM].

[263] B. Choudhary, "LBNE: Physics Reach and Status," *Talk at NuFact 2010* (2010) .

[264] L. Whitehead, "Private communication,".

[265] J.-E. Campagne, M. Maltoni, M. Mezzetto, and T. Schwetz, "Physics potential of the CERN-MEMPHYS neutrino oscillation project," *JHEP* **04** (2007) 003, arXiv:hep-ph/0603172.

[266] M. D. Messier, "Evidence for neutrino mass from observations of atmospheric neutrinos with Super-Kamiokande,". Ph.D. Thesis (Advisor: James L. Stone).

[267] E. Paschos and J. Yu, "Neutrino interactions in oscillation experiments," *Phys.Rev.* **D65** (2002) 033002, arXiv:hep-ph/0107261 [hep-ph].

[268] P. Huber, M. Lindner, and W. Winter, "From parameter space constraints to the precision determination of the leptonic Dirac CP phase," *JHEP* **0505** (2005) 020, arXiv:hep-ph/0412199 [hep-ph].

[269] P. Huber, M. Lindner, M. Rolinec, and W. Winter, "Physics and optimization of beta-beams: From low to very high gamma," *Phys. Rev.* **D73** (2006) 053002, arXiv:hep-ph/0506237.

[270] C. experiment, "http://proj-cngs.web.cern.ch/proj-cngs/.,".

[271] P. Zucchelli, "A novel concept for a anti-nu/e / nu/e neutrino factory: The beta beam," *Phys. Lett.* **B532** (2002) 166–172.

[272] J. Bouchez, M. Lindroos, and M. Mezzetto, "Beta beams: Present design and expected performances," *AIP Conf. Proc.* **721** (2004) 37–47, arXiv:hep-ex/0310059.

[273] A. Donini, E. Fernandez-Martinez, and S. Rigolin, "Appearance and disappearance signals at a beta-beam and a super-beam facility," *Phys. Lett.* **B621** (2005) 276–287, arXiv:hep-ph/0411402.

[274] J. Burguet-Castell, D. Casper, J. J. Gomez-Cadenas, P. Hernandez, and F. Sanchez, "Neutrino oscillation physics with a higher gamma beta- beam," *Nucl. Phys.* **B695** (2004) 217–240, arXiv:hep-ph/0312068.

[275] J. Burguet-Castell, D. Casper, E. Couce, J. J. Gomez-Cadenas, and P. Hernandez, "Optimal beta-beam at the CERN-SPS," *Nucl. Phys.* **B725** (2005) 306–326, arXiv:hep-ph/0503021.

[276] A. Jansson, O. Mena, S. J. Parke, and N. Saoulidou, "Combining CPT-conjugate Neutrino channels at Fermilab," *Phys. Rev.* **D78** (2008) 053002, arXiv:0711.1075 [hep-ph].

[277] C. Rubbia, A. Ferrari, Y. Kadi, and V. Vlachoudis, "Beam cooling with ionisation losses," *Nucl. Instrum. Meth.* **A568** (2006) 475–487, arXiv:hep-ph/0602032.

[278] C. Rubbia, "Ionization cooled ultra pure beta-beams for long distance nu/e –¿ nu/mu transitions, theta(13) phase and CP- violation," 2006.

[279] A. Donini *et al.*, "A beta beam complex based on the machine upgrades of the LHC," *Eur. Phys. J.* **C48** (2006) 787–796, arXiv:hep-ph/0604229.

[280] A. Donini *et al.*, "Neutrino hierarchy from CP-blind observables with high density magnetized detectors," *Eur. Phys. J.* **C53** (2008) 599–606, arXiv:hep-ph/0703209.

[281] G. Rajasekaran, "India-based neutrino observatory," *AIP Conf. Proc.* **721** (2004) 243–246, arXiv:hep-ph/0402246.

[282] **INO Collaboration** Collaboration, M. Athar *et al.*, "India-based Neutrino Observatory: Project Report. Volume I.,".

[283] S. K. Agarwalla, S. Choubey, S. Goswami, and A. Raychaudhuri, "Neutrino parameters from matter effects in P_{ee} at long baselines," *Phys. Rev.* **D75** (2007) 097302, arXiv:hep-ph/0611233.

[284] S. K. Agarwalla, S. Choubey, A. Raychaudhuri, and W. Winter, "Optimizing the greenfield Beta-beam," *JHEP* **06** (2008) 090, arXiv:0802.3621 [hep-ex].

[285] T. Ota, J. Sato, and Y. Kuno, "Search for T violation in neutrino oscillation with the use of muon polarization at a neutrino factory," *Phys.Lett.* **B520** (2001) 289–297, arXiv:hep-ph/0107007 [hep-ph].

[286] T. Ota and O. Yasuda, "Solving the degeneracy by a neutrino factory with polarized muon beam," *Nucl.Phys.Proc.Suppl.* **155** (2006) 174–175.

[287] B. Autin *et al.*, "The acceleration and storage of radioactive ions for a neutrino factory," *J. Phys.* **G29** (2003) 1785–1796, arXiv:physics/0306106.

[288] L. Ekstrm and R. Firestone, "WWW Table of Radioactive Isotopes.". Database version 2/28/99 from URL http://ie.lbl.gov/toi/index.htm.

[289] E. W. webpage. http://j2eeps.cern.ch/beta-beam-fp7-parameters/.

[290] O. Tengblad, "Private communication.". http://www.targisol.csic.es/intro_database.html.

[291] C. Volpe, "What about a beta beam facility for low energy neutrinos?," *J. Phys.* **G30** (2004) L1–L6, arXiv:hep-ph/0303222.

[292] S. K. Agarwalla, P. Huber, and J. M. Link, "Constraining sterile neutrinos with a low energy beta-beam," *JHEP* **1001** (2010) 071, arXiv:0907.3145 [hep-ph].

[293] F. Terranova, A. Marotta, P. Migliozzi, and M. Spinetti, "High energy beta beams without massive detectors," *Eur. Phys. J.* **C38** (2004) 69–77, arXiv:hep-ph/0405081.

[294] O. Bruning *et al.*, "LHC luminosity and energy upgrade: A feasibility study.". CERN-LHC-PROJECT-REPORT-626, 2002.

[295] M. Lindroos, "Talk at the second plenary IDS meeting.". http://www.hep.ph.ic.ac.uk/ids/communication/RAL-2008-01-16/agenda.html.

[296] P. Lipari, "Private communication,".

[297] E. Fernandez-Martinez and D. Meloni, "Importance of nuclear effects in the measurement of neutrino oscillation parameters," *Phys.Lett.* **B697** (2011) 477–481, arXiv:1010.2329 [hep-ph].

[298] M. S. Zisman, "Experimental tests of cooling: Expectations and additional needs," *PoS* **NUFACT08** (2008) 079.

[299] S. Choubey, R. Gandhi, S. Goswami, J. Berg, R. Fernow, *et al.*, "International Design Study for the Neutrino Factory, Interim Design Report,".

[300] S. Geer, O. Mena, and S. Pascoli, "A Low energy neutrino factory for large θ_{13}," *Phys. Rev.* **D75** (2007) 093001, arXiv:hep-ph/0701258.

[301] A. D. Bross, M. Ellis, S. Geer, O. Mena, and S. Pascoli, "A Neutrino factory for both large and small θ_{13}," *Phys.Rev.* **D77** (2008) 093012, arXiv:0709.3889 [hep-ph].

[302] A. Donini and M. Lindroos, "Optimisation of a beta beam," *PoS* **NUFACT08** (2008) 051.

[303] A. Fabich, 2007. Talk at NuFact07.

[304] W. T. Winter *et al.*, "Determination of the B-8 neutrino spectrum," *Phys. Rev. Lett.* **91** (2003) 252501.

[305] M. Mezzetto, "Physics reach of the beta beam," *J. Phys.* **G29** (2003) 1771–1776, arXiv:hep-ex/0302007.

[306] E. Fernandez-Martinez, "The gamma = 100 beta-Beam revisited," *Nucl.Phys.* **B833** (2010) 96–107, arXiv:0912.3804 [hep-ph].

[307] A. Donini, E. Fernandez-Martinez, D. Meloni, and S. Rigolin, "nu/mu disappearance at the SPL, T2K-I, NOnuA and the neutrino factory," *Nucl. Phys.* **B743** (2006) 41–73, arXiv:hep-ph/0512038.

[308] A. Guglielmi, M. Mezzetto, P. Migliozzi, and F. Terranova, "Measurement of three-family neutrino mixing and search for CP violation," arXiv:hep-ph/0508034.

[309] J. Sato, "Monoenergetic neutrino beam for long baseline experiments," *Phys. Rev. Lett.* **95** (2005) 131804, arXiv:hep-ph/0503144.

[310] J. Bernabeu, J. Burguet-Castell, C. Espinoza, and M. Lindroos, "Monochromatic neutrino beams," *JHEP* **12** (2005) 014, arXiv:hep-ph/0505054.

[311] M. Rolinec and J. Sato, "Neutrino beams from electron capture at high gamma," *JHEP* **08** (2007) 079, arXiv:hep-ph/0612148.

[312] J. Bernabeu, C. Espinoza, C. Orme, S. Palomares-Ruiz, and S. Pascoli, "CP violation from a combined Beta Beam and Electron Capture neutrino experiment," *AIP Conf.Proc.* **1222** (2010) 174–178.

[313] **ISS Detector Working Group** Collaboration, T. Abe *et al.*, "Detectors and flux instrumentation for future neutrino facilities," *JINST* **4** (2009) T05001, arXiv:0712.4129 [physics.ins-det].

[314] M. Mezzetto, "Physics potential of the gamma=100,100 beta beam," *Nucl.Phys.Proc.Suppl.* **155** (2006) 214–217, arXiv:hep-ex/0511005 [hep-ex].

[315] D. Meloni, O. Mena, C. Orme, S. Palomares-Ruiz, and S. Pascoli, "An intermediate gamma beta-beam neutrino experiment with long baseline," *JHEP* **07** (2008) 115, arXiv:0802.0255 [hep-ph].

[316] S. K. Agarwalla, A. Raychaudhuri, and A. Samanta, "Exploration prospects of a long baseline beta beam neutrino experiment with an iron calorimeter detector," *Phys.Lett.* **B629** (2005) 33–40, arXiv:hep-ph/0505015 [hep-ph].

[317] A. Donini, E. Fernandez, P. Migliozzi, S. Rigolin, L. Scotto Lavina, *et al.*, "Perspectives for a neutrino program based on the upgrades of the CERN accelerator complex," arXiv:hep-ph/0511134 [hep-ph].

[318] R. Adhikari, S. K. Agarwalla, and A. Raychaudhuri, "Can R-parity violating supersymmetry be seen in long baseline beta-beam experiments?," *Phys.Lett.* **B642** (2006) 111–118, arXiv:hep-ph/0608034 [hep-ph].

[319] S. K. Agarwalla, S. Rakshit, and A. Raychaudhuri, "Probing Lepton Number Violating Interactions with Beta-beams," *Phys.Lett.* **B647** (2007) 380–388, arXiv:hep-ph/0609252 [hep-ph].

[320] S. K. Agarwalla, S. Choubey, and A. Raychaudhuri, "Exceptional Sensitivity to Neutrino Parameters with a Two Baseline Beta-Beam Set-up," *Nucl. Phys.* **B805** (2008) 305–325, arXiv:0804.3007 [hep-ph].

[321] A. Cervera, A. Laing, J. Martin-Albo, and F. Soler, "Performance of the MIND detector at a Neutrino Factory using realistic muon reconstruction," *Nucl.Instrum.Meth.* **A624** (2010) 601–614, arXiv:1004.0358 [hep-ex].

[322] **ISS Physics Working Group** Collaboration, A. Bandyopadhyay *et al.*, "Physics at a future Neutrino Factory and super-beam facility," *Rept. Prog. Phys.* **72** (2009) 106201, arXiv:0710.4947 [hep-ph].

[323] A. B. Laing, "Optimisation of detectors for the golden channel at a neutrino factory,". Ph.D. Thesis (Advisor: F. J. Paul Soler).

[324] A. Cervera, F. Dydak, and J. Gomez Cadenas, "A large magnetic detector for the neutrino factory," *Nucl. Instrum. Meth.* **A451** (2000) 123–130.

[325] A. Cervera *et al.*, "Golden measurements at a neutrino factory," *Nucl. Phys.* **B579** (2000) 17–55, arXiv:hep-ph/0002108.

[326] S. Choubey and P. Roy, "Probing the deviation from maximal mixing of atmospheric neutrinos," *Phys. Rev.* **D73** (2006) 013006, arXiv:hep-ph/0509197.

[327] P. Huber, M. Maltoni, and T. Schwetz, "Resolving parameter degeneracies in long-baseline experiments by atmospheric neutrino data," *Phys. Rev.* **D71** (2005) 053006, arXiv:hep-ph/0501037.

[328] P. Coloma, A. Donini, P. Migliozzi, L. Lavina, and F. Terranova, "A minimal Beta Beam with high-Q ions to address CP violation in the leptonic sector," arXiv:1004.3773 [hep-ph]. * Temporary entry *.

[329] P. Huber, M. Lindner, and W. Winter, "Superbeams versus neutrino factories," *Nucl. Phys.* **B645** (2002) 3–48, arXiv:hep-ph/0204352.

[330] Y. Grossman, "Nonstandard neutrino interactions and neutrino oscillation experiments," *Phys. Lett.* **B359** (1995) 141–147, arXiv:hep-ph/9507344.

[331] M. C. Gonzalez-Garcia, Y. Grossman, A. Gusso, and Y. Nir, "New CP violation in neutrino oscillations," *Phys. Rev.* **D64** (2001) 096006, arXiv:hep-ph/0105159.

[332] T. Ota, J. Sato, and N. aki Yamashita, "Oscillation enhanced search for new interaction with neutrinos," *Phys. Rev.* **D65** (2002) 093015, arXiv:hep-ph/0112329.

[333] P. Huber, T. Schwetz, and J. Valle, "Confusing nonstandard neutrino interactions with oscillations at a neutrino factory," *Phys.Rev.* **D66** (2002) 013006, arXiv:hep-ph/0202048 [hep-ph].

[334] J. Tang and W. Winter, "On near detectors at a neutrino factory," *AIP Conf.Proc.* **1222** (2010) 88–92, arXiv:0909.4667 [hep-ph].

[335] R. Alonso, S. Antusch, M. Blennow, P. Coloma, A. de Gouvea, *et al.*, "Summary report of MINSIS workshop in Madrid," arXiv:1009.0476 [hep-ph].

[336] S. Antusch, M. Blennow, E. Fernandez-Martinez, and T. Ota, "New physics searches at near detectors of neutrino oscillation experiments," *JHEP* **1006** (2010) 068, arXiv:1005.0756 [hep-ph].

[337] J. Kopp, T. Ota, and W. Winter, "Neutrino factory optimization for non-standard interactions," *Phys. Rev.* **D78** (2008) 053007, arXiv:0804.2261 [hep-ph].

[338] W. Winter, "Testing non-standard CP violation in neutrino propagation," *Phys.Lett.* **B671** (2009) 77–81, arXiv:0808.3583 [hep-ph]. * Temporary entry *.

[339] A. M. Gago, H. Minakata, H. Nunokawa, S. Uchinami, and R. Zukanovich Funchal, "Resolving CP Violation by Standard and Nonstandard Interactions and Parameter Degeneracy in Neutrino Oscillations," *JHEP* **01** (2010) 049, arXiv:0904.3360 [hep-ph].

[340] P. Langacker and D. London, "LEPTON NUMBER VIOLATION AND MASSLESS NONORTHOGONAL NEUTRINOS," *Phys.Rev.* **D38** (1988) 907.

[341] T. Kikuchi, H. Minakata, and S. Uchinami, "Perturbation Theory of Neutrino Oscillation with Nonstandard Neutrino Interactions," *JHEP* **03** (2009) 114, arXiv:0809.3312 [hep-ph].

[342] M. Apollonio *et al.*, "Oscillation physics with a neutrino factory. ((G)) ((U))," 2002.

[343] S. Geer, "Neutrino beams from muon storage rings: Characteristics and physics potential," *Phys. Rev.* **D57** (1998) 6989–6997, arXiv:hep-ph/9712290.

[344] A. De Rujula, M. B. Gavela, and P. Hernandez, "Neutrino oscillation physics with a neutrino factory," *Nucl. Phys.* **B547** (1999) 21–38, arXiv:hep-ph/9811390.

[345] J. Gomez-Cadenas and D. A. Harris, "Physics opportunities at neutrino factories," *Ann.Rev.Nucl.Part.Sci.* **52** (2002) 253–302.

[346] I. homepage, "https://www.ids-nf.org/wiki/FrontPage,".

[347] N. Ribeiro, H. Minakata, H. Nunokawa, S. Uchinami, and R. Zukanovich-Funchal, "Probing Non-Standard Neutrino Interactions with Neutrino Factories," *JHEP* **0712** (2007) 002, arXiv:0709.1980 [hep-ph].

[348] P. Lipari, M. Lusignoli, and F. Sartogo, "The Neutrino cross-section and upward going muons," *Phys. Rev. Lett.* **74** (1995) 4384–4387, arXiv:hep-ph/9411341.

[349] **ISS Accelerator Working Group** Collaboration, M. Apollonio *et al.*, "Accelerator design concept for future neutrino facilities," *JINST* **4** (2009) P07001, arXiv:0802.4023 [physics.acc-ph].

[350] A. Donini, K. ichi Fuki, J. Lopez-Pavon, D. Meloni, and O. Yasuda, "The discovery channel at the Neutrino Factory: $\nu_\mu \to \nu_\tau$ pointing to sterile neutrinos," *JHEP* **08** (2009) 041, arXiv:0812.3703 [hep-ph].

[351] L. Scotto Lavina, "Design and performance of ECC-MECC," *PoS* **NUFACT08** (2008) 049.

[352] D. Autiero *et al.*, "The synergy of the golden and silver channels at the Neutrino Factory," *Eur. Phys. J.* **C33** (2004) 243–260, arXiv:hep-ph/0305185.

[353] H. Minakata and C. Pena-Garay, "Solar Neutrino Observables Sensitive to Matter Effects," arXiv:1009.4869 [hep-ph].

[354] J. Bernabeu, M. Blennow, P. Coloma, A. Donini, C. Espinoza, *et al.*, "EURONU WP6 2009 yearly report: Update of the physics potential of Nufact, superbeams and betabeams," arXiv:1005.3146 [hep-ph].

[355] M. Lindroos. http://beta-beam-parameters.web.cern.ch/beta-beam-parameters/.

[356] E. Wildner *et al.*, "Optimization of neutrino rates from the EURISOL beta-beam accelerator complex,". CERN-AB-2007-015.

[357] R. Garoby, "The SPL at CERN," *AIP Conf. Proc.* **773** (2005) 239–243.

[358] J. E. Campagne and A. Cazes, "The theta(13) and delta(CP) sensitivities of the SPL-Frejus project revisited," *Eur. Phys. J.* **C45** (2006) 643–657, arXiv:hep-ex/0411062.

[359] I. working group webpage, "Proton Accelerator for the Future (PAF).". http://pofpa.web.cern.ch/pofpa/.

[360] R. Garoby and W. Scandale, "Plans for the future of proton accelerators at CERN," *Nucl. Phys. Proc. Suppl.* **147** (2005) 16–19.

[361] "Workshop on "Radioactive beams for nuclear physics and neutrino physics" 37^{th} Rencontre de Moriond, Les Arcs (France) March 17-22nd, 2003.". http://moriond.in2p3.fr/radio/index.html.

[362] P. Fabbricatore, S. Farinon, M. Greco, U. Gambardella, and G. Volpini, "Rapid cycling superconducting magnets," *Nucl. Phys. Proc. Suppl.* **154** (2006) 157–162.

[363] H. Zaglauer and K. Schwarzer, "THE MIXING ANGLES IN MATTER FOR THREE GENERATIONS OF NEUTRINOS AND THE MSW MECHANISM," *Z.Phys.* **C40** (1988) 273.